Solid-state Polymer Nanofoams

Huimin Guo

A dissertation
submitted in partial fulfillment of the
requirements for the degree of

Doctor of Philosophy

University of Washington
2015

Reading Committee:
Vipin Kumar, Chair
Nicholas Boechler
John Weller

Program Authorized to Offer Degree:
Mechanical Engineering

University of Washington

Abstract

Solid-state Polymer Nanofoams

Huimin Guo

Chair of the Supervisory Committee:

Vipin Kumar, Professor

Department of Mechanical Engineering

This work explores the fabrication and properties of solid-state polymer nanofoams. Polymer nanofoams, which are expected to be the next generation cellular materials, have attracted much attention in the past decade. Nanoscale dimension of the bubbles could potentially render the nanofoams to have improved properties or some novel properties never observed before. There existed substantial challenges in creating polymer nanofoams and their properties were very poorly understood. This dissertation was set out to develop a versatile fabrication technique for creating polymer nanofoams, and to gain a better understanding their properties.

Two approaches are initially investigated for enhancing cell nucleation and reducing cell size: varying intrinsic viscosity (or equivalently molecular weight) and varying glass transition temperature. Molecular weight and glass transition temperature are two of the most important parameters of polymers; however, their effect on cell nucleation was not reported previously in literature. In this study, it is found that the polymer with a higher molecular weight or higher glass transition temperature has a higher cell nucleation density and smaller cell size. These two approaches, however, show no success in creating nanofoams.

A novel solid-state foaming process based on low-temperature carbon dioxide saturation is discovered and studied in this work. Using this novel process, nanofoams with cell size less than 100 nm are created for the first time in four polymers – polycarbonate (PC), polymethylmethacrylate (PMMA), polysulfone (PSU), and polyphenylsulfone (PPSU). Since the low-temperature saturation regime was never studied, fundamental aspects regarding to the solubility and diffusivity of carbon dioxide in polymers, as well as the glass transition temperature depression are first discussed. Lowering the saturation temperature (down to -30 °C) is found to increase the carbon dioxide solubility substantially. The increased solubility depresses the glass transition temperature of the polymers significantly, even to below 0 °C.

Processing space has been established for each of the four polymers that relate process parameter (e.g. saturation temperature and foaming temperature) to cellular structures. Nanofoams are created with a smallest cell size around 20 nm and maximum cell nucleation density on the order of 10^{15} cells per cubic centimeter. Also, a critical carbon dioxide concentration is observed, above which the cell nucleation density increases much more rapidly and the cell size drops drastically. In addition, it is discovered that above certain carbon dioxide concentration, as the foaming temperature increases the closed-cellular structure transitions to a porous, interconnected nanoporous structure.

Several properties of PC nanofoams are investigated in this work. It is found that both tensile and impact properties are a strong function of foam density. Cell size doesn't seem to play a significant role. Reducing cell size results in much lower thermal conductivity, which enables the nanofoams to be potentially used as better insulation materials. Also, nanofoams are found to have a higher glass transition temperature and much improved light transmittance. This suggests the possibly of creating transparent nanofoams.

DEDICATION

To my beloved family,

mom, dad, and sisters,

for their endless love, support, and encouragement.

ACKNOWLEDGMENTS

I would like to express the deepest appreciation to my committee chair and academic advisor, Professor Vipin Kumar. Without your guidance and support this dissertation would not have been possible. I am very thankful for the freedom you gave me so that I could explore the research that fascinated me. I am also grateful for the amount of opportunities you provided to me to improve my technical and communication skills. Also, thank you for being such a great role model for me to learn how to be a good and patient man.

I would like to thank my committee members, Professor Rene Overney, Professor Nicholas Boechler, Prof. Jiangyu Li, and Dr. John Weller, for your useful suggestions and feedback on my research.

I would like to thank Prof. Keith Elder for his support and encouragement. Working with you in teaching ME395 was always a great joy for me. I would like to thank Prof. John Kramlich for giving me many TA opportunities to practice my teaching skills.

I also would like to thank members of MicroGREEN Polymers, Inc. for their support. In particular, I would like to thank Krishna Nadella, Xiaoxi Wang, John Lu, Blake Ragland, and Shawna Lamoree for all of your support and help.

I would like to acknowledge the past and present members of Microcellular Plastics Laboratory: Dustin Miller, James Hanks, Shieng Liu, Brian Aher, Andrei Nicolae, Nathan Olson, Gaurav Mahamuni, Viktoriya Dolomanova, Javier Pinto, Javier Escudero, and Belen Notario. It was a great pleasure and honor to work with each of you. Special thanks to Andrei Nicolae who helped me greatly with my various experiments.

I would like to express appreciation to the staff in the Mechanical Engineering Department: Bill Kuykendall, Eamon McQuaide, Kevin Soderlund, Michelle Hickner, Wanwisa Kisalang, Sue Chen, Nancy Moses, and Carey Purnell. I appreciate all of your help in the past several years.

I am grateful to United States National Science Foundation, University of Washington Center for Commercialization, and MicroGREEN Polymers Inc. for funding my dissertation work.

Last but not least, I would like to thank my family and friends. I would like to thank my mom, dad, and sisters for all of your support and encouragement. I am very grateful to my mom for teaching me to believe in myself and to be patient when I felt frustrated with my research. I am also grateful to my three lovely nieces for bringing fun and laugh to my life. I am very thankful to have so many great friends who encouraged and supported me in my graduate studies, including Chen Chen, Zhou Yang, Xingbo Peng, Chuan Luo, Yue Gong, Yuanzheng Gong, Qing Guo, Rui Gao, Peiqi Wang, Di Zhang, Ya Zhao, Zhe Bai, Geoffery Hohn, Cory Moore, Mahdi Ashrafi, Garren family, and many other friends.

TABLE OF CONTENTS

LIST OF TABLES

LIST OF FIGURES

Chapter 1

Introduction

1.1 Background and Motivation

Microcellular and Nanocellular Foams

Micrcocellular polymer foams, or microcellular foams, are polymer foams with cell size in the micrometer range. In the 1950's, McIntire [1] and Amos [2] reported foams with cell size around 100 μm, when processing polystyrene with gaseous alkyl halide (e.g. methyl chloride) and ammonia (added to regulate cell size). In the early 1980's, Martini et al. [3, 4] developed a much cleaner and more controllable solid-state microcellular foaming technique as a means to decrease the amount of material required by the food packaging industry. The new technique used gaseous blow agents, such as nitrogen and carbon dioxide. The cell size reported was on the order of 10 μm, and in a cubic centimeters (cm^3) volume, there could be more than 10^8 cells. It was envisioned that void size will be required to be in the micrometer range for thin wall application, where part thicknesses are in the range of 1 mm [4]. Since then, microcellular foams have been produced from a very wide variety of thermoplastic polymers, including PVC [5], ABS [6], PC [7], PET [8], and PLA [9, 10], to name a few. Compared to traditional foams, which have cell sizes larger than 500 μm, microcellular foams have much more predictable and improved properties [8, 11-16]. Also, unlike processing traditional foams which involves chemical blowing agent, the processing of microcellular foams which uses physical blowing agent such as carbon dioxide and nitrogen, is more environmentally friendly.

Nanocellular polymer foams, or nanofoams, are polymer foams with cell size in the nanometer range. When cell size is in the range of 100 nm – 1 μm, names such as "supermicrocellular", "ultramicrocellular" or "submicrocellular" structures have been used in literature [17-19]. During the past decade, nanofoams have drawn tremendous attention from researchers in academia and various industries, such as the aerospace, building, insulation, electronics and membrane industries. Nanofoams can be regarded in concept as an extension of microcellular foams. Figure 1.1 shows an example of cellular structures of microcellular and nanocellular foams. Average cell size is 12 μm and 28 nm, respectively.

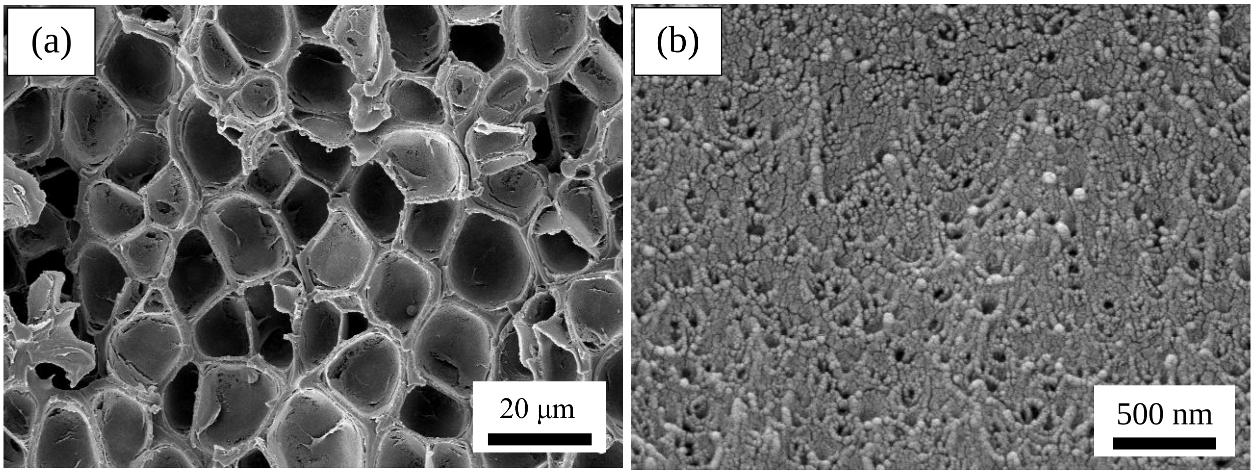

Figure 1.1 Cellular structure of a) microcellular and b) nanocellular polycarbonate foams [20].

Solid-state Foaming Process

Solid-state foaming is a process by which foaming occurs while the polymer remains in the solid state throughout the entire process. This is different from conventional polymer foaming processes where the polymer is heated to molten state. Martini et al. [3, 4] developed a solid-state foaming process to create microcellular structure in high impact polystyrene (HIPS). The process is shown in Figure 1.2. Such technique tends to increase the cell density, i.e., the number of cells per unit volume of the parent material, and to produce much smaller cell sizes than those in conventional cellular structures [4]. The first step of the process involves saturating the virgin polymer under high pressures of an inert gas such as CO_2 in a pressure vessel. The high pressure gas will then start to diffuse into the polymer, causing a mass increase of the polymer. The gas will continue to saturate the polymer until equilibrium is reached. Then, the saturated sample is then removed from the pressure vessel and transferred to a foaming station. In the second step, the polymer-gas system is heated to an elevated temperature, which causes the nucleation of cells. The foaming temperature is typically around the glass transition temperature of the polymer, well below the melting point. In a variation of this 2-step process, microcellular foams have been created by a sudden drop in gas pressure that causes a solubility drop resulting in a cell nucleation [21]. This one-step process is frequently called as pressure quench method.

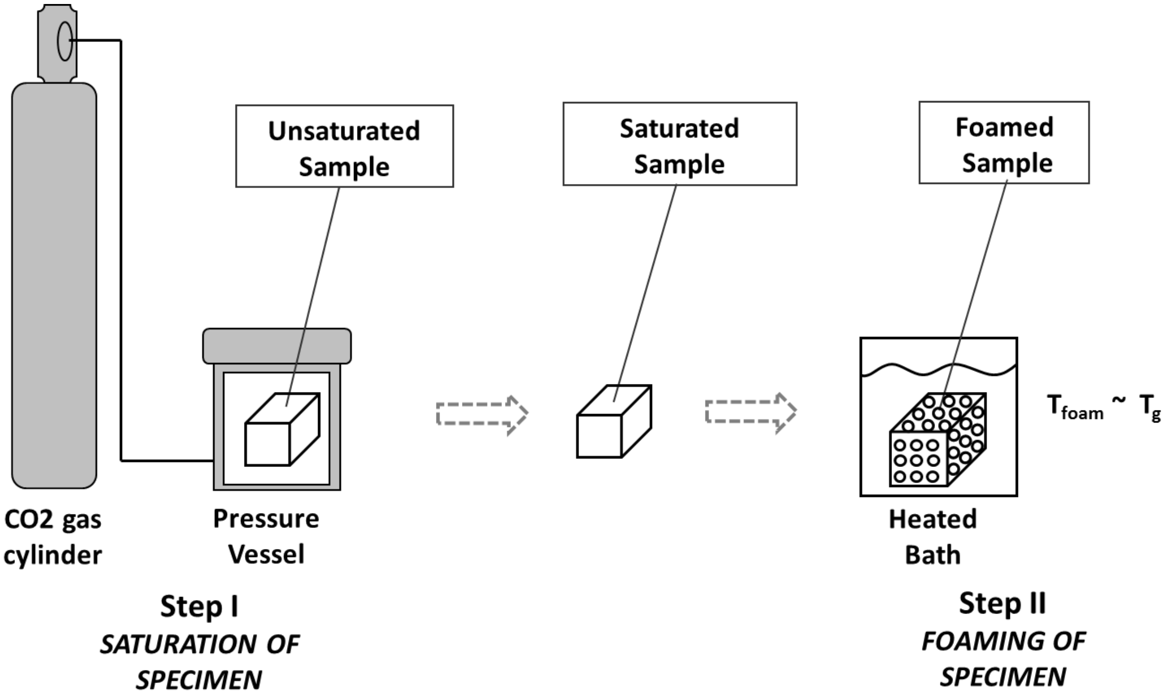

Figure 1.2 Schematic of solid-state foaming process.

Motivation

The research in this dissertation was mainly motivated by the huge potential of polymer nanofoams. Nanofoams have been deemed as the next generation cellular materials [22, 23]. It has been widely expected that nanofoams would offer many properties that are superior to existing materials, and present a unique combination of properties not seen before. Miller and Kumar [24] showed that PEI nanofoams had a significantly higher strain to failure, resulting in an improvement in the tensile toughness by 350% compared to microcellular foams. They also found a brittle-to-ductile transition in PEI nanofoams resulting in impact energies that are up to 600% higher compared to microcellular foams. Zhou et al. [25] showed that PEI nanofoams had higher specific flexural strength and specific flexural modulus than microcellular PEI and unfoamed PEI. Very recently, Notario et al. [22] reported a higher elastic modulus in PMMA nanofoams compared to microcellular foams.

It has been hypothesized that nanofoams will have much lower thermal conductivity than microcellular foams due to reduced gas phase heat conduction, when cell size is close to the mean free path of air molecules at ambient temperature and pressure (about 70 nm). This is called Knudsen effect and has been demonstrated in organic aerogels [26] and very recently in PMMA-based nanofoams with cell sizes down to 100 nm by Pinto et al. [27] and Notario et al. [28]. They showed that gaseous phase heat conduction was reduced in the nanofoams following Knudsen equation. In addition, they found that a reduction of cell size below 1 µm decreased the thermal conductivity of the solid phase, possibly due to the increased tortuosity of solid phase and/or confinement effect with the presence of the nanocells [28].

Another popular hypothesis suggests that nanofoams based on clear amorphous polymers, such as PMMA and PC, could present transparency when cell size is significantly smaller than the light wavelength. Such materials can be potentially used to create thermally insulative yet transparent windows, which can lead to huge energy savings for buildings [20]. Szymanski [29] used light scattering method to determine the size information of the air bubbles in polymer media, and found an increased transmission ratio when the cell sizes were below 1 µm under the wavelengths of 500 nm and 700 nm. Miller [30] compared the optical transmissivity of PEI foams with varying cell sizes over a range of void fractions. Using infrared incident light with a wavelength of 940 nm, he found that nanocellular PEI (cell size 20-60 nm) showed higher transmissivity than microcellular PEI (cell size 2-5 µm). This preliminary result supports the hypothesis of creating optically transparent foams by reducing cell size.

In addition, if pores are open and interconnected in the nanofoams, then we have an open nanoporous material. Open nanoporous materials have been widely used in filtration, gas separation, energy storage, and catalysis supports [31].

1.2 **Literature Review on the Fabrication of Polymer Nanofoams**

Polymer nanofoams have been created via various methods and in various polymers/polymer systems. The following is a review of previous studies on fabricating polymer nanofoams. This serves as a background for the approaches undertaken in this study to create nanofoams.

Hedrick et al. [32-34] used a thermolysis method to make thin film polyimide nanofoams with a low dielectric constant for microelectronics applications. The polyimide nanofoams are prepared from block copolymers consisting of thermally stable and thermally labile blocks, the latter being the dispersed phase. Foam formation is via the thermolysis of the thermally labile block, leaving pores of the size and shape corresponding to the initial copolymer morphology. Nanopores with an average size of tens of nanometers were generated. The schematic in Figure 1.3 shows this process.

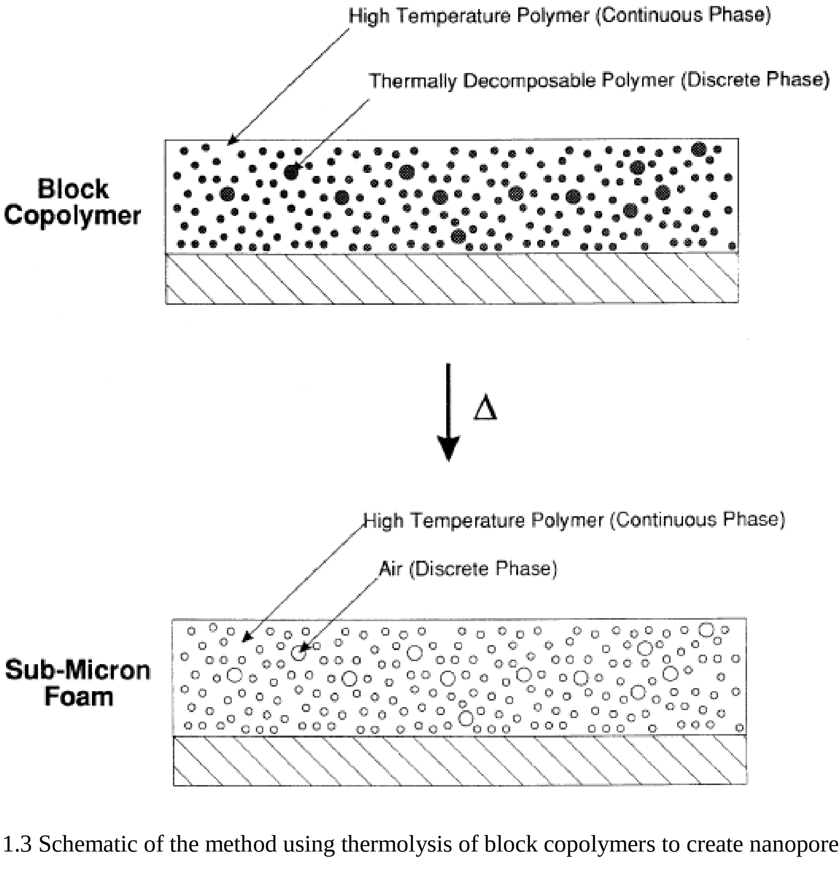

Figure 1.3 Schematic of the method using thermolysis of block copolymers to create nanopores [34].

Solid-state gas foaming process has shown a great utility in creating polymeric nanofoams. The gas used is mainly CO_2. Using this method, polymer nanofoams have been produced from *homopolymers, copolymers, polymer blends,* and *polymer nanocomposites*.

For **homopolymers**, Baldwin et al. [17] first reported using supercritical CO_2 to create supermicrocellular structures in polymers. Using a saturation condition of 20.7 MPa and 43 ℃, they successfully created nanofoams with a cell size of 800 nm, 100nm, 200 nm, and cell densities of 2×10^{12} cells/cm^3, 5×10^{14} cells/cm^3, 6×10^{13} cells/cm^3 in PVC, LDPE, HDPE, respectively.

Handa et al. [18, 19] utilized the retrograde behavior of PMMA to obtain nanofoams. By saturating PMMA in CO_2 at -0.2 ℃ and 3.4 MPa, they made PMMA nanofoams with an average cell size of 350 nm, a cell density of 4.4×10^{13} cells/cm^3 and a relative density of about 10%.

Murray et al. [6] saturated ABS at 26.7 ℃ and at a pressure of 4 MPa and above, and created ABS nanofoams with a cell size about 500 nm and cell nucleation density about 10^{13} cells/cm^3. Nawaby et al. [35] later showed that using a lower temperature and lower pressure (0 ℃ and 3.4 MPa), ABS nanofoams with a cell size of 470 nm and cell density of 2.8×10^{12} cells/cm^3 were created. The success with the lower temperature and pressure was due to the retrograde behavior of ABS.

Krause et al. [36] first reported making nanofoams in high temperature polymers. Using 5 MPa and 25 ℃ saturation condition, they made nanofoams with cell size below 100 nm and cell density over 10^{14} cells/cm^3 in PEI and PES thin films. Later, using similar conditions, PI nanofoams were created with cell size in the range of 20-50 nm [37]. Instead of making nanofoams in PEI thin films, Miller et al. [38] investigated the processing space for making nanofoams in PEI thick sheets (~1.5mm). Under subcritical condition (5 MPa and 21 ℃), PEI nanofoams with cell size in the range of 30-120 nm and cell density on the order of 10^{14} cells/cm^3 were created. Later, Zhou et al. [25] used supercritical CO_2 at 6-10 MPa and 21-55 ℃ to saturate PEI and after foaming achieved nanofoams with a cell size of 50-200 nm. Aher et al. [39] used supercritical CO_2 at 20 MPa and 45 ℃ to saturate PEI, and subsequently utilized a different heating method - hot press technique to produce PEI nanofoams with a cell size of 40-100 nm and cell density about 10^{15} cells/cm^3

For **copolymers**, nanofoams have been created mainly in 1) PMMA based copolymers and 2) PS based copolymers with fluorinated blocks. Costeux et al. [40] investigated a family of PMMA copolymers. With the high molecular weight copolymer Poly(MMA-co-EMA), they achieved foams with cell size about 80 nm, cell nucleation density exceeding 10^{16} cells/cm^3, and relative density less than 20%, by saturating the copolymer in supercritical CO_2 at 30 MPa and 35 ℃. Under similar processing conditions, Poly(MMA-co-tBMA) nanofoams with a cell size of 145 nm and cell nucleation density of 10^{15} cells/cm^3 were created.

Yokoyama et al. [41-44] reported creation of nanofoams in PS when copolymerized with CO_2-philic fluorinated blocks. The presence of high CO_2-philic perfluoro blocks, in the form of submicrometric separated domains in the PS matrix, acts as nucleating agents during the foaming process. In one study, they created PS-b-PFMA nanofoams with cell size of 10-30 nm and cell density of 10^{16} cells/cm^3, by using quench method and with the saturation condition of 7.5-30 MPa and 60 ℃. In another study, they reported nanofoams PS-b-PFS nanofoams with cell size of 20-40 nm and cell density of 5×10^{15} cells/cm^3 using quench method and with the saturation condition of 10-30 MPa and 60 ℃. Later, also using pressure quench method, Reglero-Ruiz [45] fabricated nanofoams in PS-b-PFDA with fluorinated block (1,1,2,2-tetrahydroperfluorodecyl acrylate, PFDA). With a depressurization rate of 5 MPa/min from 30 MPa and 0 ℃, PS-b-PFDA nanofoams with cell size on the order of 100 nm and cell density 7.3×10^{14} cells/cm^3 were achieved.

For polymer blends, a great success in creation of nanofoams has been achieved. The concept for these polymer blends nanofoams was similar: one phase acted as the matrix, the other dispersed phase served as a template for bubble nucleation, and the differences in properties between the matrix and dispersed phase were exploited to control cell nucleation and growth. Krause et al. [37] investigated PSU/PI blends with

50% and 80% weight percentage of PI under the saturation condition of 5 MPa and 25 ℃. They fabricated nanofoams with an open nanoporous morphology and the openings were well below 500 nm.

Nemoto et al. [46, 47] investigated foaming of polypropylene (PP)/propylene-ethylene copolymer (PER) blend with 25%-75% PER composition. Nanofoams with cell size around 0.5 μm and cell nucleation density 10^{10} - 10^{11} cells/cm^3 were created when using a pressure quench method and with a saturation condition of 20 MPa and 25 ℃. Under similar conditions, polypropylene/thermoplastic polystyrene elastomer (PP/TPS) nanofoams were created with cell size in the range of 200-400 nm and cell nucleation density of 6-8 $\times 10^{13}$ cells/cm^3.

Nemoto et al. [48] also studied PEEK/PEI blend to create nanofoams. With the saturation condition of 20 MPa and 40 ℃, nanofoams with a cell size around 100 nm were created, and it was found that bubble location was highly controlled in the PEI domain.

Reglero-Ruiz et al. [49-51] studied the poly(methyl methacrylate)/methylmethacrylate-co-butylacrylate-co-methylmethacrylate (MAM) blend, in which 10% MAM (triblock copolymer) was added to PMMA. Using the pressure quench method with the saturation condition of 30 MPa and room temperature, they achieved nanofoams with an average cell size of 200 nm, a cell density of 4.5×10^{14} cells/cm^3 and a relative density of 40%. An increase of the number of nucleation sites appeared due to the presence of the nanostructured polymer formed by the butyl acrylate groups, which were not miscible in the PMMA matrix.

Costeux et al. [52] synthesized a series of styrenic-acrylic polymer blends. Using a saturation condition of 33 MPa and 30 ℃, PEMA/SAN nanofoams with a cell size of 95-110 nm and cell nucleation density of 3×10^{15} cells/cm^3 were created. Under similar conditions, PMMA-co-EA/SAN nanofoams with a cell size of 86-110 nm and cell nucleation density of 2-5 $\times 10^{15}$ cells/cm^3, were created.

Polymer nanocomposites, which have some amount of nanoparticles dispersed in the polymer matrix, have been shown to generate nanofoams. In the nanocomposites, the boundaries between the added nanoparticles and polymer matrix serve as nucleation sites and greatly enhanced cell nucleation. Fujimoto et al. [53] studied foaming of PLA/SBE nanocomposites, where SBE is a layered silicate with a particle length of ~100 nm. Using supercritical carbon dioxide at 140-165 ℃ and 10 MPa to saturate this nanocomposite and subsequently foamed it in oil bath, they created nanofoams with a cell size of 360 nm, cell density of 1.2×10^{14} cells/cm^3, and density about 0.57 g/cm^3. In contrast, neat PLA foams showed a non-uniform cellular morphology with a large cell size of 230 μm. Costeux and Zhu [54] found an enhanced cell nucleation with the addition of nanoparticles with a particle size less than 30 nm in PMMA-based copolymers. For Poly(MMA-co-EA) with 0.5% wt nanosilica, nanofoams with an average cell size of 95 nm, a cell density 8.6×10^{15} cells/cm^3, and a relative density of 20.5% were achieved, by saturating the polymer nanocomposite in supercritical CO_2 at 30 MPa and 40 ℃. For Poly(MMA-co-EMA) with 0.25% wt POSS nanoparticles, foams with an average cell size of 100 nm, a cell density of 10^{16} cells/cm^3, and a relative density of 15% were achieved, by saturating the polymer nanocomposite in supercritical CO_2 at 33 MPa and 50 ℃.

1.3 **Research Objectives**

One interesting observation that can be made from the literature review is that most of the success in creating nanofoams relied on modifying the neat polymers - copolymerization, blending with another polymer, and adding nanoparticles to polymer matrix. Although effective, these methods have three disadvantages. First, these methods typically involve tedious synthesis and blending process [55], which can lead to a longer product cycle and drive up the cost of production. Secondly, there exists the uniformity issue [56, 57]. The non-uniformity of blending and non-uniform dispersion of nanoparticles can severely affect the final foam morphology and foam quality. Thirdly, these methods may alter the properties of neat polymers in an undesired way. For example, the clarity of neat polymers might be comprised by the incorporation of other polymer phases or nanoparticles, such as carbon nanotubes. The disadvantages prevent the wide usage of these methods, and thus there exists a need for a simple and more scalable process. The other observation from the literature review is that most polymer nanofoams have cell size between 100 nm and 1 μm. Nanoscale effects are most obvious when the cell size is below 100 nm.

Therefore, the major objective of this research is to synthesize a relatively simple and scalable process to produce polymer nanofoams with cell size < 100 nm. The new process should be fully characterized with the process space well established. Then, the fundamentals behind the process need to be understood. Another objective is to understand the properties of nanofoams. Once the process space is established, property tests of nanofoams will be carried out.

1.4 Organization of This Dissertation

This dissertation is organized into several chapters with a specific focus in each chapter. The structure of this dissertation is as follows:

Chapter 1 provides a brief introduction to the microcellular and nanocellular foams, solid-state foaming process, and a literature review of the methods for fabricating nanofoams. Motivation and objectives of this research are also stated.

Chapter 2 and **Chapter 3** present two approaches explored to enhance cell nucleation in order to create nanofoams: Chapter 3 – varying intrinsic viscosity (or equivalently molecular weight) of polyethylene terephthalate (PET); Chapter 4 - varying glass transition temperature (T_g) of cyclic olefin copolymer (COC). Molecular weight and glass transition temperature are two of the most important parameters of polymer, and yet their effects haven’t been well studied.

Chapter 4 describes the low-temperature saturation solid-state foaming process and the rationale for using low-temperature saturation. The low-temperature saturation process is then used to screen a number of polymers to look for candidates for creating nanofoams.

Chapter 5 presents the detailed study on creating polycarbonate (PC) nanofoams using the low-temperature saturation solid-state foaming process.

Chapter 6 and **Chapter 7** present the detailed study on creating poly(methyl methacrylate) (PMMA) nanofoams using the low-temperature saturation solid-state foaming process. Chapter 7 describes low-temperature CO_2 sorption, diffusion, and depression of T_g of PMMA by the absorbed CO_2. Chapter 8 describes the foaming results and cellular morphologies of PMMA nanofoams.

Chapter 8 presents the detailed study on creating polysulfone (PSU) nanofoams using the low-temperature saturation solid-state foaming process.

Chapter 9 presents the study on polyphenylsulfone (PPSU) nanofoams using the low-temperature saturation solid-state foaming process.

Chapter 10 discusses some of the properties of nanofoams using PC as an example. Tensile test, impact test, thermal conductivity measurement, glass transition temperature measurement, and light transmittance measurement are performed.

Chapter 11 summarizes the work presented in this dissertation regarding to both fabrication and properties of nanofoams. Several recommended research work are also specified for further investigation.

The diagram in Figure 1.4 shows the structure of this dissertation and relationship between different chapters.

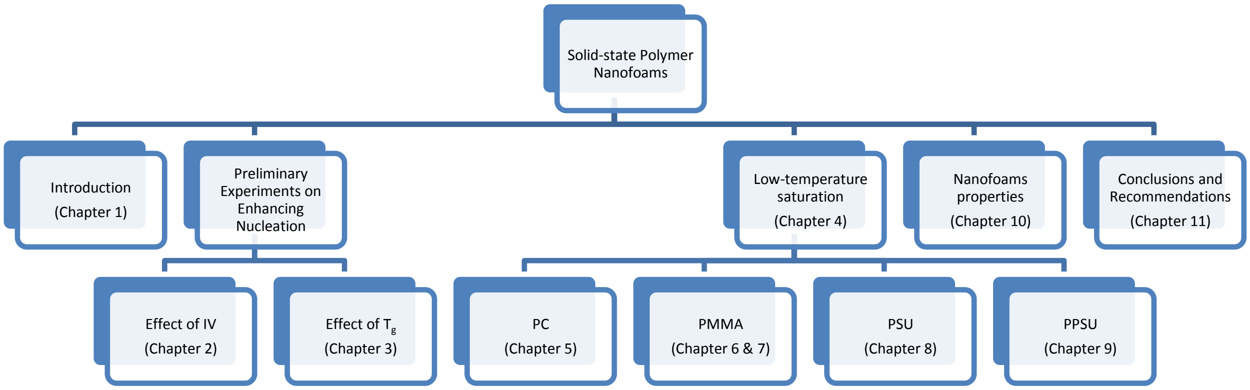

Figure 1.4 Structure of the dissertation and relationship between chapters.

1.5 **Nomenclature and Acronyms**

The following is a list of nomenclature and acronyms used in this dissertation.

N_f (cell density): number of cells per cm^3 of foam, cells/cm^3

N_0 (cell nucleation density): number of cells nucleated per cm^3 of original unfoamed polymer, cells/cm^3

t_{sat} : saturation time, ℃

T_{sat} : saturation temperature, ℃

T_f : foaming temperature, ℃

T_g : glass transition temperature, ℃

S: solubility

D: diffusivity, cm^2/s

R: gas constant, 8.314 J K^{-1} mol^{-1}

ΔH_s: heat of sorption, J/mol

IV: Intrinsic viscosity, dL/g

M_w: weight average molecular weight, g/mol

M_n: number average molecular weight, g/mol

PC: polycarbonate

PI: polyimide

PS: polystyrene

PMMA: polymethyl methacrylate

PSU: polysulfone

PPSU: polyphenyl sulfone

PET: polyethylene terephthalate

CPET: crystallizable PET

PEEK: polyether ether ketone

TPU: thermoplastic polyurethane

COC: cyclic olefin copolymer

PLA: polylactic acid

PEI: polyetherimide

PES: polyethersulfone

PP: polypropylene

ABS: acrylonitrile butadiene styrene

LDPE: low density polyethylene

HDPE: high density polyethylene

UHMWPE: ultra-high molecular weight polyethylene

PTFE: polytetrafluoroethylene

1.6 **References**

1. McIntire OR. Manufacture of cellular thermoplastic products. The Dow Chemical Company, 1948.
2. Amos JL. Method of making cellular thermoplastic products. The Dow Chemical Company, 1951.
3. Martini JE, Suh NP, and Waldman FA. Microcellular closed cell foams and their method of manufacture. Google Patents, 1984.
4. Martini JE. The production and analysis of microcellular foam. Mechanical Engineering, vol. Master of Science: Massachusetts Institute of Technology, 1981.
5. Kumar V and Weller JE. International Polymer Processing 1993;8(1):73-80.
6. Murray RE, Weller JE, and Kumar V. Cellular Polymers 2000;19(6):413-425.
7. Kumar V and Weller J. Journal of Manufacturing Science and Engineering 1994;116(4):413-420.
8. Shimbo M, Higashitani I, and Miyano Y. Journal of Cellular Plastics 2007;43(2):157-167.
9. Richards E, Rizvi R, Chow A, and Naguib H. Journal of Polymers and the Environment 2008;16(4):258-266.
10. Xiaoxi W, Kumar V, and Wei L. Cellular Polymers 2007;26(1):1-25.
11. Barlow C, Kumar V, Flinn B, Bordia RK, and Weller J. Journal of Engineering Materials and Technology 2000;123(2):229-233.
12. Juntunen RP, Kumar V, Weller JE, and Bezubic WP. Journal of Vinyl and Additive Technology 2000;6(2):93-99.
13. Kumar V, Juntunen RP, and Barlow C. Cellular Polymers 2000;19(1):25-37.
14. Kumar V, VanderWel M, Weller J, and Seeler KA. Journal of Engineering Materials and Technology 1994;116(4):439-445.
15. Kumar V, Weller JE, Ma M, Montecillo R, and Kwapisz R. Cellular Polymers 1998;17(5):350-361.
16. Bureau MN and Kumar V. Journal of Cellular Plastics 2006;42(3):229-240.
17. Baldwin DF, Suh NP, Park CB, and Cha SW. Supermicrocellular foamed materials. Massachusetts Institute of Technology, 1994.
18. Handa YP and Zhang Z. Journal of Polymer Science Part B: Polymer Physics 2000;38(5):716-725.
19. Handa YP, Zhang Z, and Wong B. Cellular Polymers 2001;20(1):1-16.
20. Guo H and Kumar V. Polymer 2015;56:46-56.
21. Goel SK and Beckman EJ. Cellular Polymers 1993;12(4):251-274.
22. Notario B, Pinto J, and Rodríguez-Pérez MA. Polymer 2015;63:116-126.
23. Reglero-Ruiz JA, Dumon M, Pinto J, and Rodriguez-Pérez MA. Macromolecular Materials and Engineering 2011;296(8):752-759.
24. Miller D and Kumar V. Polymer 2011;52(13):2910-2919.
25. Zhou C, Vaccaro N, Sundarram SS, and Li W. Journal of Cellular Plastics 2012;48(3):239-255.
26. Lu X, Caps R, Fricke J, Alviso CT, and Pekala RW. Journal of Non-Crystalline Solids 1995;188(3):226-234.
27. Pinto J, Solorzano E, Rodriguez-Perez M, de Saja J, and Dumon M. Thermal conductivity transition between microcellular and nanocellular polymeric foams: experimental validation of the Knudsen effect. SPE FOAMS. Barcelona, Spain, 2012.
28. Notario B, Pinto J, Solorzano E, de Saja JA, Dumon M, and Rodríguez-Pérez MA. Polymer 2015;56:57-67.

29. Szymanski WW. Journal of Aerosol Science 1996;27(1001):537-538.
30. Miller D. Characterization of polyetherimide carbon dioxide system and mechanical properties of high relative density polyetherimide nanofoams. Mechanical Engineering, vol. Master of Science: University of Washington, 2007.
31. Lu GQ and Zhao XS. Nanoporous materials: science and engineering. London: Imperial College Press, 2004.
32. Hedrick JL, Russell TP, Labadie J, Lucas M, and Swanson S. Polymer 1995;36(14):2685-2697.
33. Hedrick JL, Carter KR, Cha HJ, Hawker CJ, DiPietro RA, Labadie JW, Miller RD, Russell TP, Sanchez MI, Volksen W, Yoon DY, Mecerreyes D, Jerome R, and McGrath JE. Reactive and Functional Polymers 1996;30(1–3):43-53.
34. Hedrick JL, Carter KR, Labadie JW, Miller RD, Volksen W, Hawker CJ, Yoon DY, Russell TP, McGrath JE, and Briber RM. Nanoporous Polyimides. In: Kricheldorf HR, editor. Progress in Polyimide Chemistry II, vol. 141: Springer Berlin Heidelberg, 1999. pp. 1-43.
35. Nawaby AV, Handa YP, Liao X, Yoshitaka Y, and Tomohiro M. Polymer International 2007;56(1):67-73.
36. Krause B, Sijbesma HJP, Münüklü P, van der Vegt NFA, and Wessling M. Macromolecules 2001;34(25):8792-8801.
37. Krause B, Diekmann K, van der Vegt NFA, and Wessling M. Macromolecules 2002;35(5):1738-1745.
38. Miller D, Chatchaisucha P, and Kumar V. Polymer 2009;50(23):5576-5584.
39. Aher B, Olson NM, and Kumar V. Journal of Materials Research 2013;28(17):2366-2373.
40. Costeux S, Khan I, Bunker SP, and Jeon HK. Journal of Cellular Plastics 2014.
41. Li L, Yokoyama H, Nemoto T, and Sugiyama K. Advanced Materials 2004;16(14):1226-1229.
42. Li L, Nemoto T, Sugiyama K, and Yokoyama H. Macromolecules 2006;39(14):4746-4755.
43. Yokoyama BH, Li L, Nemoto T, and Sugiyama K. Advanced Materials 2004;16(17):1542-1546.
44. Yokoyama H and Sugiyama K. Macromolecules 2005;38(25):10516-10522.
45. Reglero-Ruiz JA, Cloutet E, and Dumon M. Journal of Applied Polymer Science 2012;126(1):38-45.
46. Nemoto T, Takagi J, and Ohshima M. Macromolecular Materials and Engineering 2008;293(7):574-580.
47. Nemoto T, Takagi J, and Ohshima M. Macromolecular Materials and Engineering 2008;293(12):991-998.
48. Nemoto T, Takagi J, and Ohshima M. Polymer Engineering & Science 2010;50(12):2408-2416.
49. Reglero-Ruiz JA, Dumon M, Pinto J, and Rodriguez-Pérez MA. Macromolecular Materials and Engineering 2011;296(8):752-759.
50. Regelero-Ruiz JA, Pedros M, Tallon JM, and Dumon M. The Journal of Supercritical Fluids 2011;58(1):168-176.
51. Reglero-Ruiz JA, Tallon JM, Pedros M, and Dumon M. The Journal of Supercritical Fluids 2011;57(1):87-94.
52. Costeux S, Bunker SP, and Jeon HK. Journal of Materials Research 2013;28(17):2351-2365.
53. Fujimoto Y, Ray SS, Okamoto M, Ogami A, Yamada K, and Ueda K. Macromolecular Rapid Communications 2003;24(7):457-461.
54. Costeux S and Zhu L. Polymer 2013;54(11):2785-2795.
55. Reglero-Ruiz JA, Pedros M, Tallon JM, and Dumon M. The Journal of Supercritical Fluids 2011;58(1):168-176.
56. Khare HS and Burris DL. Polymer 2010;51(3):719-729.
57. Ma P-C, Siddiqui NA, Marom G, and Kim J-K. Composites Part A: Applied Science and Manufacturing 2010;41(10):1345-1367.

Chapter 2

Preliminary Experiments on Enhancing Nucleation to Create Nanofoams - Effect of Intrinsic Viscosity on Solid-state Microcellular Foaming of Polyethylene Terephthalate (PET)

2.1 **Abstract**

Microcellular foams, with cells of order 10 µm, have been studied for over two decades. But little research has been done to study the effect of molecular weight on solid-state microcellular foaming. In this study, polyethylene terephthalate (PET) with a range of intrinsic viscosity (IV) 0.68-0.81dL/g was used to investigate the effect of molecular weight on microcellular foaming process and resulting foam microstructures and properties. In the saturation step, IV showed negligible effect on sorption and desorption of CO_2 in PET for all the conditions explored. In the foaming step, we found relative density increased with increasing IV. Also, as IV increased, cell size decreased, and cell nucleation density increased. We hypothesize that lower chain mobility in higher IV samples led to more localized cell nucleation, resulting in a higher nucleation density, and also more constraints for cell growth, resulting in a smaller cell size. In addition, higher IV foams were found to have smaller skin thicknesses.

2.2 **Introduction**

Microcellular foams refer to thermoplastic foams with cells on the order of 10 µm. The idea to incorporate such small bubbles in thermoplastics goes back to early work at MIT [1, 2]. The basic solid-state batch process used for polystyrene [1] has been used to created microcellular foams from a number of amorphous and semi-crystalline polymers, such as polyvinyl chloride (PVC) [3], polycarbonate (PC) [4], acrylonitrile-butadiene-styrene (ABS) [5],and polylactic acid (PLA) [6], to name a few.

This chapter has been published in Journal of Materials Research, 2013, 28: 2374-2379.

There are two basic steps in the solid-state foaming of thermoplastic polymers. The first step is saturating the virgin polymer under high pressures of an inert gas such as CO_2 in a pressure vessel. The high pressure gas will then start to diffuse into the polymer, causing a mass increase of the polymer. The gas will continue to saturate the polymer until equilibrium is reached. In the second step, bubbles are nucleated in the gas-polymer system by creating a thermodynamic instability. This is achieved by either a sudden drop in pressure [7] or sudden increase in temperature [3, 4]. Both methods suddenly reduce the solubility of the gas, driving the gas out of the polymer matrix and into nucleated bubbles.

Molecular weight is known to influence mechanical properties of polymers [8, 9]. But little research has been done to examine its effect on the solid-state microcellular foaming process. Lee [10] studied the effect of molecular weight on foam melt extrusion process, and found cell size and degree of foaming decreased with increasing molecular weight. Stafford [11] studied the effect of molecular weight on supercritical CO_2 foaming of polystyrene, and found that molecular weight did not significantly affect cell size and cell densities. However, the effects of molecular weight on each step of the solid-state microcellular foaming process and resulting foam properties are still largely unexplored.

PET has good strength, ductility, gas barrier properties and food compatibility. As the most recycled plastic, it has been widely used for various packaging applications. The sponsor of this research which makes microcellular products from recycled PET, was concerned with the variability of intrinsic viscosity (IV) in incoming recycled sheets. The PET recycling stream is mainly from water bottles and soft drink bottles, in which IV typically ranges from 0.7 dL/g to 0.85 dL/g [12]. IV range investigated in this study (0.68-0.81 dL/g) reflected the typical IV variations in recycled PET stream. In this paper, we investigated the effect of IV (an indirect measure of molecular weight) on sorption, desorption, and foaming of PET, and final foam properties including relative density, microstructure and skin thickness.

2.3 **Experimental**

2.3.1 **Materials**

PET resins were supplied by Phoenix Technologies International, LLC. These resins were made with four different IV levels by different degrees of chain extending. Resins were compression molded into 50.8 mm diameter disk-shaped samples with thickness 0.82 mm using a hydraulic hot press. IV of the molded sheets was then determined according to ASTM D4603 by dissolving polymer in solvent 60/40 phenol/TCE at temperature 30°C. Average molecular weight (MW), density, glass transition temperature (T_g), and percent crystallinity (Cr%) are all shown in Table 2.1 for corresponding IV levels. Average molecular weights were calculated from IV values using Mark-Houwink equation with the parameters $K=2.64\times10^{-4}$ and $a=0.73$, which were suggested by the materials provider. The differences in density, T_g and Cr% are negligible compared to the IV or molecular weight. Notice that molecular weight and its range are shown here, but IV will be used as major and more accurate distinguishing parameter for samples in this study.

Differential scanning calorimetry (DSC) measurements were performed on a TA Instruments Q20 setup. The DSC procedure followed the ASTM D3418-08 technique using a heat rate of 10°C/min, and T_g and Cr% were determined from DSC plots.

Table 2.1 Intrinsic viscosity, average molecular weight, density, T_g and crystallinity of PET samples.

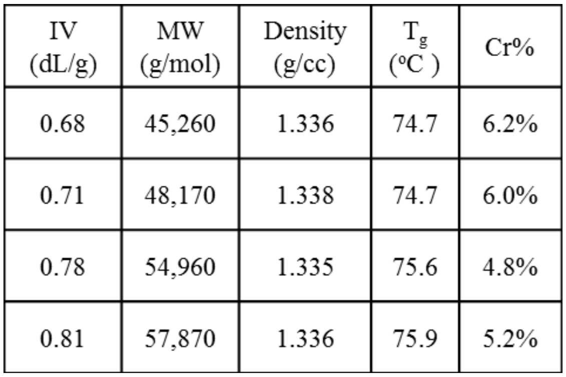

IV (dL/g)	MW (g/mol)	Density (g/cc)	T_g (°C)	Cr%
0.68	45,260	1.336	74.7	6.2%
0.71	48,170	1.338	74.7	6.0%
0.78	54,960	1.335	75.6	4.8%
0.81	57,870	1.336	75.9	5.2%

2.3.2 **Sorption and Desorption**

Disk-shaped samples with diameter 50.8 mm and thickness 0.82 mm were put in stainless steel pressure vessel and introduced to industrial grade CO_2 at 3 MPa, 4 MPa and 5 MPa. The pressure was controlled within ±0.1 MPa by a pressure controller. The temperature was maintained at room temperature. During saturation, the samples were periodically removed from the pressure vessel and weighed on METTLER AE240 balance which has an accuracy of ±10 µg. Sorption experiments were carried out until the mass of the sample didn't change between measurements, indicating that the CO_2 concentration had reached equilibrium. After samples were fully saturated with gas in the sorption step, they were removed from the pressure vessel and placed in room temperature environment. Mass of the samples was periodically measured.

2.3.3 **Foaming**

The saturation time used in this study for 3, 4, and 5 MPa is 240, 144, and 48 hours, respectively. After full saturation, samples with different IV were taken out from the pressure vessel and transferred to an oil bath. After 2 min transfer time, samples were immersed into the oil bath for 30 seconds. A range of foaming temperatures were chosen: 80, 90, 95, 100, 105 and 110^{o}C. After foaming, samples were quenched in room temperature water to stop further foaming from the residual hot oil on the sample surface. Samples were then washed and dried for further characterizations.

2.3.4 **Characterizations**

Density of foamed samples was measured according to ASTM D792 using a Mettler AE240 analytical scale. A representative set of samples were imaged with a scanning electron microscope (FEI Sirion SEM) to characterize the microstructures produced. The obtained SEM images were analyzed using software ImageJ for cell size, cell nucleation density and skin thickness. Cell size was reported as average value of the cell diameters of at least 50 cells within a single micrograph. Cell nucleation density and skin thickness were determined using the methods developed by Kumar and Weller [3, 13].

2.4 **Results and Discussions**

2.4.1 **Sorption and Desorption**

Figure 2.1 shows the sorption of CO_2 in PET at 4 MPa and room temperature. Each data point in the plot represents an average value of two samples. We can see that different IV PET's have essentially the same sorption behavior. The maximum difference of CO_2 concentration between different IV PET's at each point was calculated, and the average value of these maximum differences was only 2%, which is about the same as possible experimental errors. Figure 2.2 shows the desorption plot of CO_2 in PET immediately after 4 MPa full saturation. Each data point represents an average value of two samples. It can be seen that different IV PET have the same desorption behavior. The average of maximum differences was only 0.5%. Similar results were found for 3 MPa and 5 MPa conditions (not shown due to page limit). The average maximum differences in CO_2 concentration were 1.6% and 2% for 3 MPa and 5 MPa sorption, respectively; and 0.4% and 1.8% for 3 MPa and 5 MPa desorption, respectively. Therefore, for the IV range investigated and at room temperature condition, PET's of different IV have essentially the same sorption and desorption behaviors.

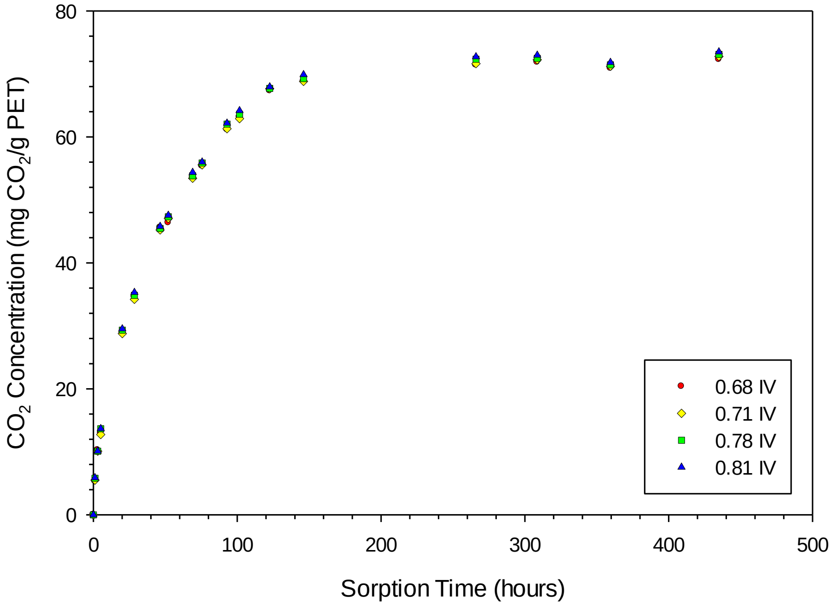

Figure 2.1 Sorption plot of CO_2 in different IV samples (thickness 0.82 mm) at 4 MPa saturation pressure and room temperature.

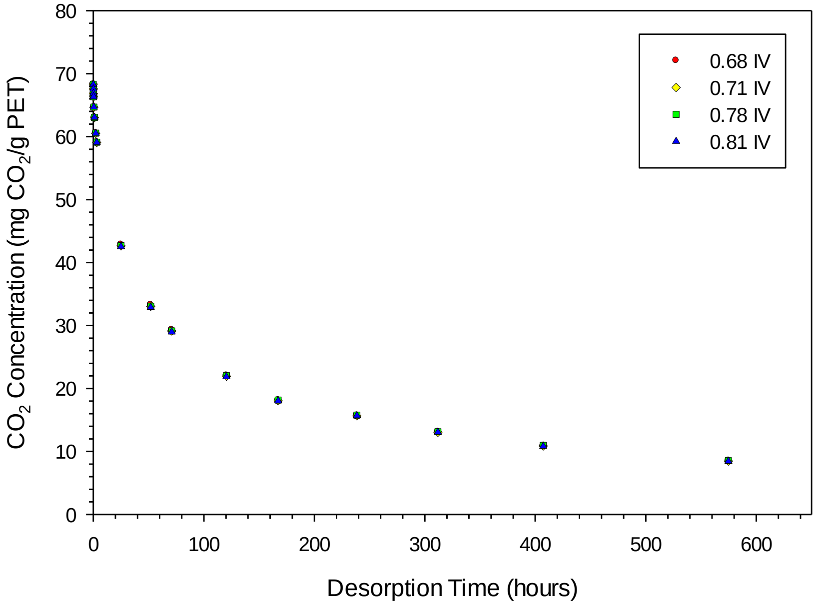

Figure 2.2 Desorption plot of CO_2 in different IV samples (thickness 0.82 mm) in room temperature environment immediately after 4 MPa full saturation.

2.4.2 **Relative Density**

Relative density is defined as the ratio of foam density to the density of unfoamed material. Macroscopically, under the same foaming condition, different IV PET had different degrees of expansion. This is verified by data in Figure 2.3, which shows relative density of different IV PET foams as a function of foaming temperature. All samples were saturated at 4 MPa and then processed at various temperatures. Each data point represents the average relative density of three samples. We can see that under identical processing conditions relative densities increase as IV increases. For all foaming temperatures, an increase of 0.1 dL/g in IV brings an average 4% absolute increase in relative densities. Also, from the graph, as foaming temperature increases, the relative densities of foamed PET decrease for all the different IV PET's. This observation agrees with results on PET in literature [14]. Similar results of IV effects were found for 3 MPa and 5 MPa conditions. In summary, under identical processing condition, higher IV PET foamed samples have higher relative densities. The lower relative density in low IV samples is due to the larger cells they possess, which will be discussed in the microstructure section.

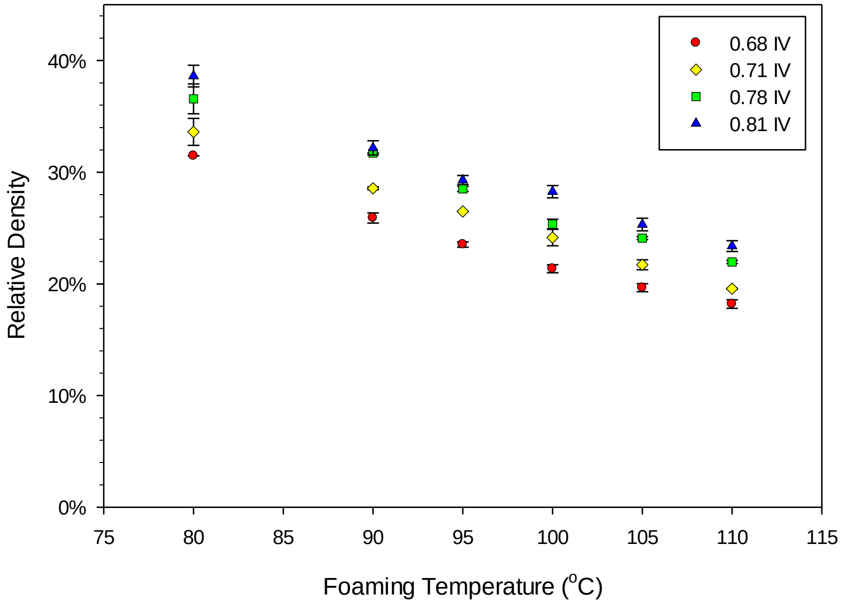

Figure 2.3 Relative density of different IV PET foams as a function of foaming temperature. All samples were initially saturated at 4 MPa.

2.4.3 **Microstructure**

Figure 2.4 shows the average cell size of foamed PET as a function of IV at various foaming temperatures. We can see the average cell size decreases with increasing IV. At different foaming temperatures, IV seems to have different degrees of effect: at 80°C, cell size has a larger change, from 33 µm for 0.68 IV sample to 21 µm for 0.81 IV sample; at 110°C, the cell size changes from 25 µm for 0.68 IV sample to 22 µm for 0.81 IV sample. The energy input to the gas-polymer system at the higher temperature seems to neutralize any variations in cell size and cell nucleation density on account of IV difference. On average, the cell size has about 20% reduction for a 0.1 dL/g increase in IV.

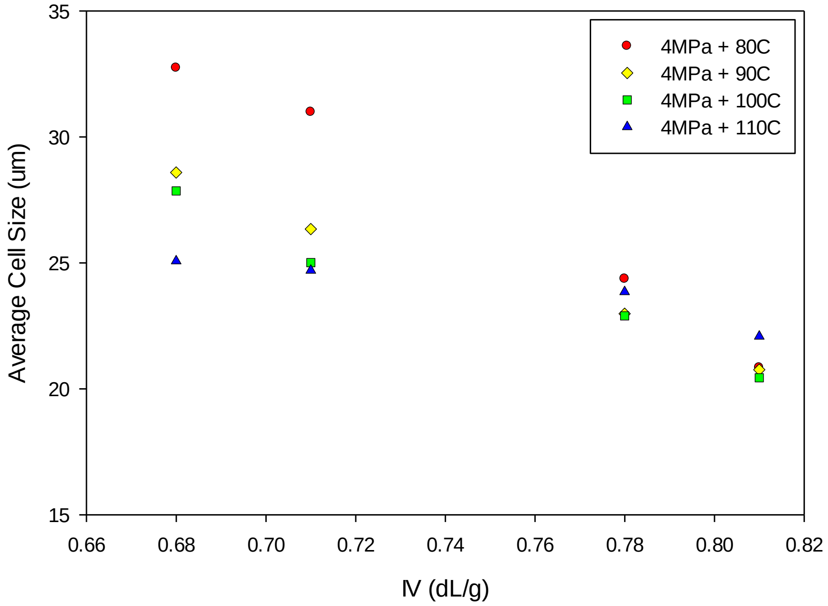

Figure 2.4 Average cell size of foamed PET as a function of IV at various foaming temperatures. All samples were initially saturated at 4 MPa.

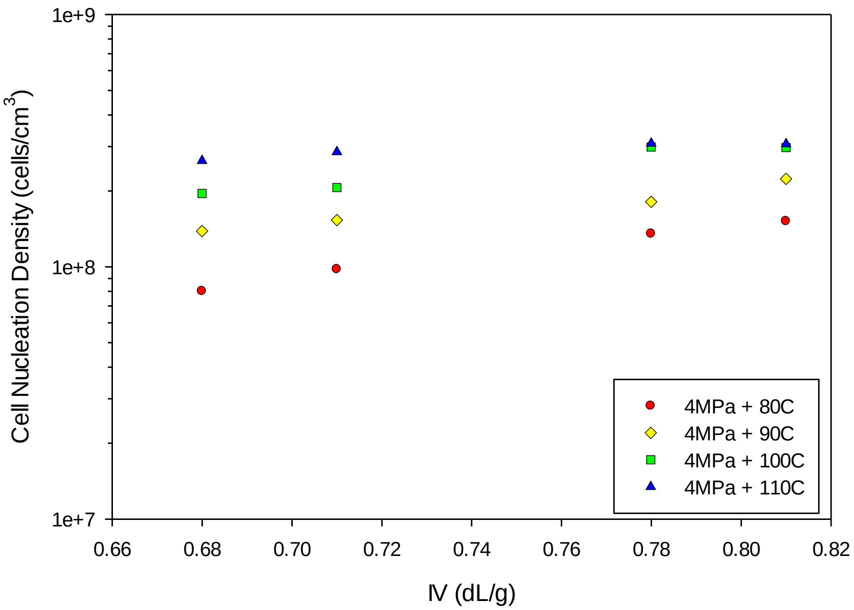

Figure 2.5 Cell nucleation density of foamed PET as a function of IV at various foaming temperatures. All samples were initially saturated at 4 MPa.

Cell nucleation density results are shown in Figure 2.5. As the IV increases, so do the cell nucleation density. Similar to cell size case, IV shows different degrees of effect on cell nucleation density under different foaming temperatures. On average, for a 0.1 dL/g increase in IV, cell nucleation density has an increase of 40%. Also, notice that in the plot, logarithm of cell nucleation density seems to have a linear relationship with IV. Figure 2.6 shows the microstructure of different IV PET foams processed at 4 MPa and 80^{o}C. There are visible differences in the images even the imaged areas are as small as 0.0028 cm^2. Clearly, the bottom two images have more cells than the top two. Similar results were found for PET samples saturated at 3 MPa and 5 MPa.

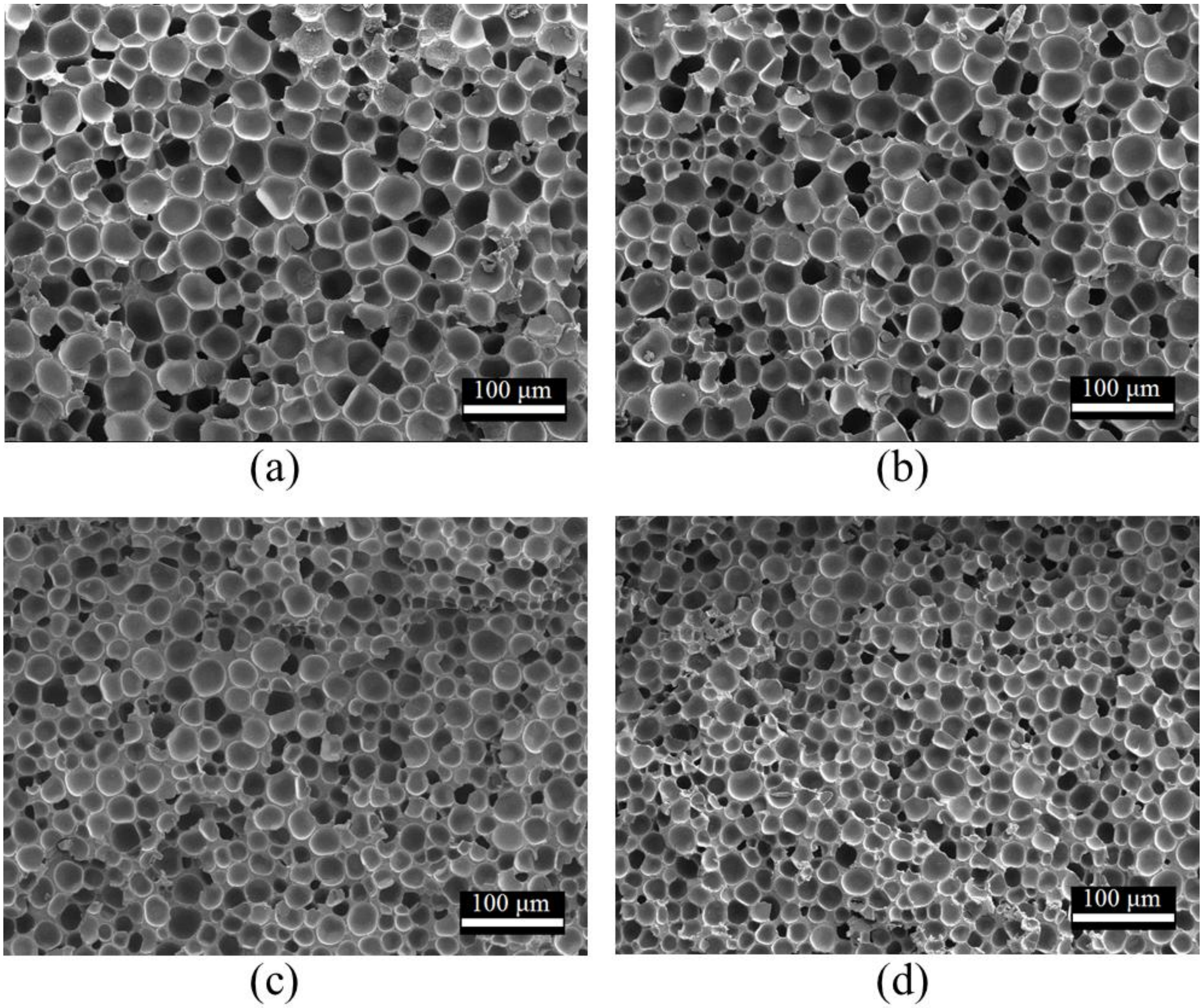

(a) (b) (c) (d)

Figure 2.6 Microstructure of different IV PET foams (all saturated at 4 MPa and foamed at 80 ℃): (a) 0.68 IV, 241 cells; (b) 0.71 IV, 287 cells; (c) 0.78 IV, 379 cells; (d) 0.81 IV, 427 cells. The magnification is 200x.

The classical nucleation theory has been used in solid-sate microcellular foaming research to understand the general trends. The homogeneous nucleation rate N_0 is given by [15]

$$N_0 = C_0 f_0 \exp(-\frac{\Delta G_{crit}}{kT}) \tag{1}$$

$$\Delta G_{crit} = \frac{16\pi\sigma^3}{3\Delta P^2} \tag{2}$$

where ΔG_{crit} is the free energy of critical nucleus formation (or activation energy), C_0 is the concentration of gas molecules, f_0 is the frequency factor of gas molecules joining a nucleus, k is the Boltzmann constant, T is the absolute temperature, σ is the surface energy at the polymer-cell interface, and ΔP is gas saturation pressure.

Under identical processing conditions, different IV samples had the same C_0, T, and ΔP. Literature [16-18] shows that the surface energy σ typically increases as the molecular weight increases. This would result in a lower activation energy and thus a higher nucleation density in lower IV samples, which contradicts the results in this study. This suggests that the classical nucleation theory may not be suitable for explaining the IV effects on solid-state microcellular foaming.

Upon nucleation, gas molecules have two possibilities: one is to go into a critical nucleus to stabilize it; the other is to diffuse into an already created cell to aid the cell growth. These two processes compete for the finite amount of gas molecules in the polymer. Our hypothesis for the fact that higher IV shows a higher nucleation density is this: in higher IV samples, polymer chains have lower mobility and thus the gas molecules tend to go into local critical nuclei instead of overcoming the polymer chain hindrance to diffuse a long path into cells relatively far away to aid the cell growth. Also, due to its longer polymer chains and larger intermolecular forces, thus lower chain mobility, the higher IV samples have higher resistance to cell growth or expansion. Thus, higher IV samples show smaller cell sizes.

It’s expected that in higher IV specimens there would be a larger resistance for small cells to coalesce to form larger cells. Thus, one might expect that the higher IV specimens will show smaller cells and a higher cell density. However, the uniformity of microstructures of the specimens indicated that no significant coalescence happened. This is likely due to the rather narrow range of IV’s explored in this study.

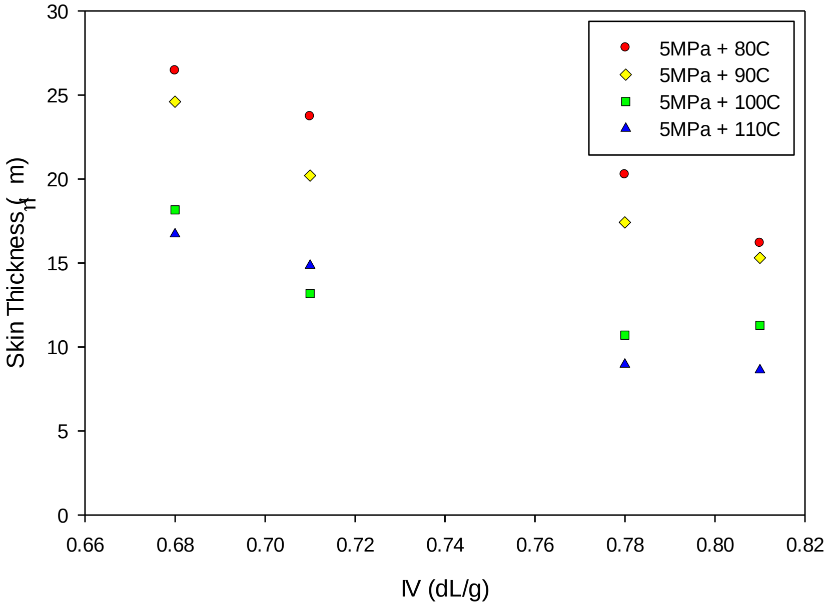

Figure 2.7 Skin thickness of foamed samples as a function of IV under various foaming temperatures. Desorption time was fixed at 2 min.

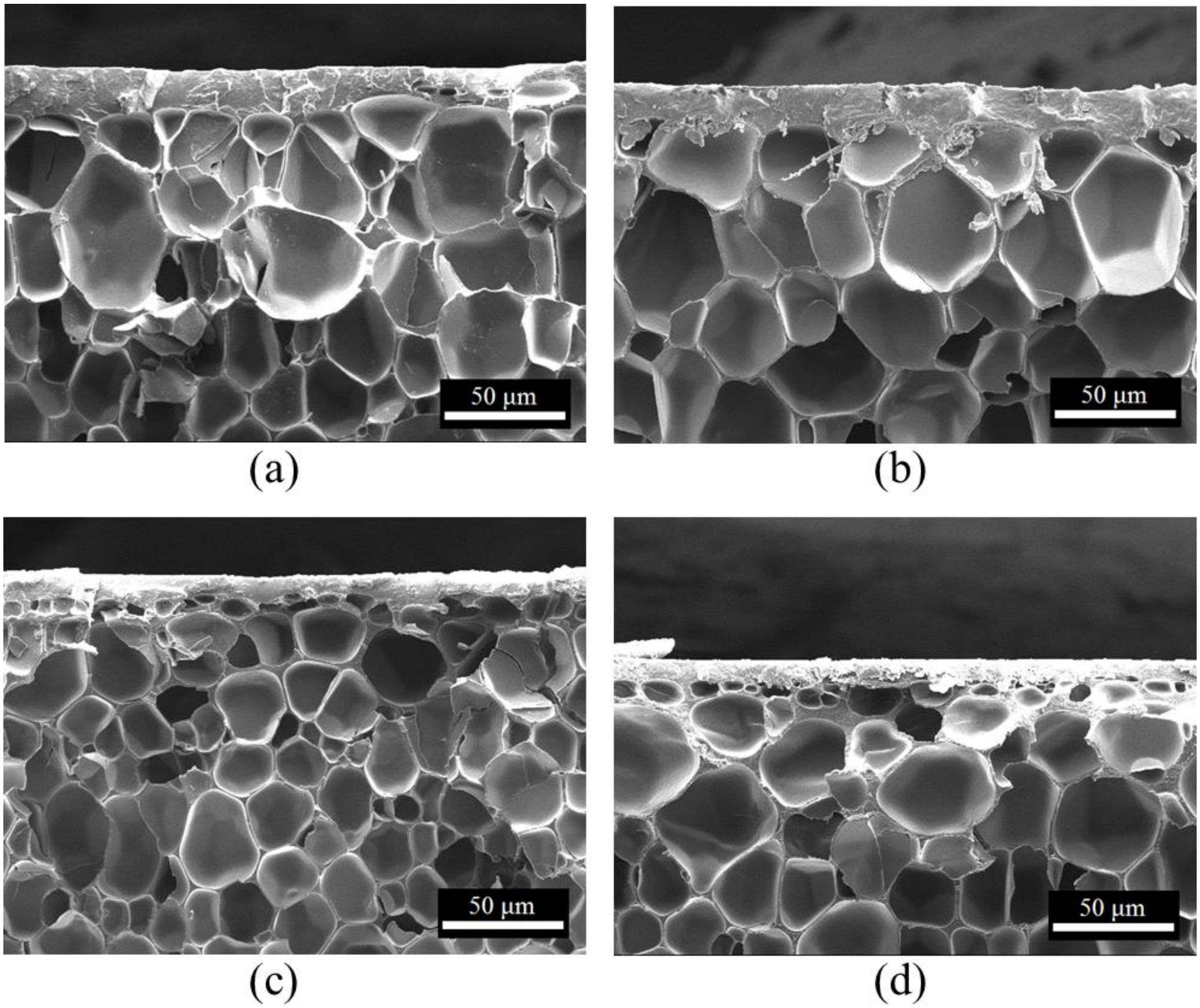

(a) (b) (c) (d)

Figure 2.8 Skin of different IV PET foams (all saturated at 5 MPa and foamed at 110 ℃): (a) 0.68IV, skin thickness 16.7 µm; (b) 0.71IV, skin thickness 14.9 µm; (c) 0.78IV, skin thickness 9.0 µm; (d) 0.81IV skin thickness 8.7 µm. The magnification is 500x.

2.4.4 **Skin Thickness**

Skin is an integral part of skin-core sandwich structure, which typically results in higher specific mechanical properties [19]. Among all the foamed samples, samples saturated at 5 MPa showed solid skins, which were used to investigate the effect of IV on skin thickness. Figure 2.7 shows skin thickness of 0.68, 0.71, 0.78 and 0.81IV PET foams as a function of IV under various foaming temperatures. Desorption time was fixed at 2 min. We can see from the plot that as IV increases skin thickness decreases for all conditions. For a 0.1 dL/g increase in IV, skin thickness has an average reduction about 30%. Figure 2.8 shows examples of skins of different IV PET foams.

As discussed above, the higher IV samples had higher cell nucleation density attributed to enhanced local nucleation. In the same manner, this enhanced local nucleation due to lower chain mobility in the higher IV samples leads to nucleation in a larger volume of the specimen, leading to smaller skin thickness.

2.5 **Conclusions**

We investigated the effect of IV on microcellular foaming of PET and final foam properties, including relative density, cell size, cell nucleation density and skin thickness. In the sorption and desorption, IV showed negligible effects on the diffusion rate and final equilibrium CO_2 concentration in PET. High IV foams had higher relative densities than low IV foams under the same saturation and foaming conditions. An increase of 0.1 dL/g in IV brought about an average of 4% increase in absolute values of relative density for 4 MPa samples. Microstructure characterization showed that high IV foams had smaller cell size and higher cell nucleation densities. For a 0.1 dL/g increase in IV, in 4 MPa samples, there were an average of 20% reduction in cell size and 40% increase in cell nucleation density. We hypothesize that lower chain mobility (due to the longer polymer chains) in higher IV samples led to more localized cell nucleation, resulting in a higher nucleation density, and also more constraints for cell expansion, resulting in a smaller cell size. In addition, with 5 MPa saturation condition, high IV foams were found to have smaller skin thicknesses than low IV foams. For a 0.1 dL/g increase in IV, skin thickness has an average reduction about 30%. The smaller skin thickness in higher IV samples is also hypothesized to be due to a lower chain mobility. This study showed that IV had effects on various aspects of the final product, including density, cell size and skin thickness. These effects can be significant depending on how well the final product quality needs to be controlled. In order to have a very consistent final product quality, the IV of the incoming raw material needs to be well controlled. Also, the knowledge of IV effects from this study enables us to tailor processing conditions to achieve desired structure and properties.

2.6 **Acknowledgments**

This study was supported by MicroGREEN Polymers, Inc. Their support is gratefully acknowledged.

2.7 **References**

1. Martini J, Suh NP, and Waldman FA. Microcellular Closed Cell Foams and Their Method of Manufacture. vol. #4473665. USA: Massachusetts Institute of Technology, 1984.
2. Martini J, Waldman FA, and Suh NP. The Production and Analysis of Microcellular Thermoplastic Foam. SPE ANTEC, vol. 28. San Francisco, CA, 1982. pp. 674.
3. Kumar V and Weller JE. International Polymer Processing 1993;VIII(I):73-80.
4. Kumar V and Weller JE. Journal of Engineering in Industry 1994;116:413-420.
5. Nawaby V and Handa P. Fundamental Understanding of the ABS-CO2 Interactions, its Retrograde Behavior and Development of Nanocellular Structures. ANTEC, vol. 2. Chicago, IL, 2004. pp. 2532-2536.
6. Wang X, Kumar V, and Li W. Cellular Polymers 2007;26(1).
7. Goel SK and Beckman EJ. Cellular Polymers 1993;12(4):251.
8. Wool RP. Polymer Interfaces: Structure and Strength. Munich: Hanser Publisher, 1995.
9. Nielsen LE and Landel RF. Mehcanical Properties of Polymers. New York: Reinhold, 1994.
10. Lee CH, Lee K-J, Jeong HG, and Kim SW. Advances in Polymer Technology 1999;19:97-112.
11. Stafford CM, Russell TP, and McCarthy TJ. Macromolecules 1999;32:7610-7616.
12. Fakirov S. Handbook of Thermoplastic Polyesters. vol. 1, 2002.
13. Kumar V and Weller J. Polymer Engineering and Science 1994;34(3):169-173.
14. Stolarczuk P. Process to Structure Characterization of Microcellular Poly(ethylene terephthalate). Mechanical Engineering, vol. Masters. Seattle: University of Washington, 1995.
15. Colton JS and Suh NP. Polymer Engineering & Science 1987;27(7):485.
16. Legrand DG and Gaines GLJ. Journal of Colloid and Interface Science 1969;31(2):162-167.
17. Dee GT and Sauer BB. Journal of Colloid and Interface Science 1992;152(1):85-103.
18. Chee KK. Journal of Applied Polymer Science 1998;70:697-703.
19. Klempner D and Sendijarevic V. Polymeric Foams and Foam Technology. Munich: Hanser Publisher, 2004.

Chapter 3

Preliminary Experiments on Enhancing Nucleation to Create Nanofoams - Effect of Glass Transition Temperature and Saturation Temperature on the Solid-state Microcellular Foaming of Cyclic Olefin Copolymer (COC)

3.1 Abstract

Effect of glass transition temperature and saturation temperature on the solid-state microcellular foaming of COC, including CO_2 solubility, diffusivity, cell nucleation and foam morphology, were investigated in this study. COCs of low T_g (78 ℃) and high T_g (158 ℃) were studied. Solubilities are 20%-50% higher in high T_g COC than the low T_g COC across the saturation temperature range. Diffusivities are about 15% higher on average in high T_g COC for temperatures up to 50 ℃. A much faster increase of diffusivity beyond 50 ℃ is observed in low T_g COC due to it being in the rubbery state. Under similar gas concentration, high T_g COC starts foaming at a higher temperature. And the foam density decreases faster in low T_g COC with foaming temperature. Also, high T_g COC foams show about two orders of magnitude higher cell nucleation density than the low T_g COC foams. The effect of saturation temperature on microcellular foaming can be viewed as the effect of CO_2 concentration. Nucleation density increases and cell size decreases exponentially with increasing CO_2 concentration. Uniform ultramicrocellular structure with an average cell size of 380 nm was created in high T_g COC. A novel hierarchical structure composed of microcells (2.5 μm) and nanocells (80 nm) on the cell wall, was discovered in the very low density high T_g COC foams.

This chapter has been published in Journal of Applied Polymer Science, 2015, 132: 42226.

3.2 **Introduction**

Microcellular foams are thermoplastic foams with cells on the order of 10 μm, which was conceived at MIT three decades ago [1, 2]. In a pioneering paper, Martini et al. [2] described a two-step process to create microcellular structure in high impact polystyrene (HIPS), that involved saturating the polymer with a non-reacting gas and then heating the gas laden polymer to near the glass transition temperature. This process later became known as the solid-state process, as the polymer foam is created near the T_g of the gas-polymer system, well below the melting point. This process has been used to investigate a number of polymers, including PVC [3], ABS [4], PC [5], PET [6], and PLA [7, 8], to name a few. In a variation of this process, microcellular foams have been created by a sudden drop in gas pressure that causes a solubility drop resulting in a cell nucleation [9].

The effect of T_g on the microcellular foaming of polymers has not been studied previously. The fact that T_g of cyclic olefin copolymer (COC) can be easily customized over a wide range by altering its norbornene content provides us an opportunity to study the effect of T_g on microcellular foaming process.

COC is a family of amorphous copolymers of ethylene and norbornene. COC with a higher norbornene content has a higher T_g due to the increased chain rigidity. In contrast to polyethylene, which shows poor solid-state foaming behavior due to low gas solubility and high crystallinities, COC generally presents good foaming behaviors, due to the fact that the introduction of bulky norbornene groups into the main chains prevents the crystallization of ethylene. COC has low water absorption, excellent water vapor barrier properties, high chemical resistance, and low shrinkage. It also shows excellent optical properties, such as low birefringence and high transparency, and is a competitor to conventional engineering plastics, such as polycarbonate [10]. The current uses of COC resins include transparent moldings for optical data storage, lenses, sensors, and industrial products in the construction and lighting sectors. There is also interest in packaging for pharmaceuticals, medical devices and diagnostic disposable.

A few groups have explored microcellular foaming of COC. Processing using CO_2 as a blowing agent has been successfully done in thin films of 6013 COC (T_g of 139 °C) by Krause et al. [11]. They saturated films at room temperature with CO_2 at 5 MPa which resulted in a 4.3 % wt. CO_2. Foaming was carried out between 65 and 155 °C, and foams with a cell size less than 5 μm and cell densities on the order of 10^{11} cells/cm^3 were achieved. Sun et al. [12] saturated COC (T_g of 137 °C) in pressure up to 30 MPa at 100-180 °C, and foamed utilizing the pressure-quench method. They achieved foams with cell densities on the order of 10^{10} cells/cm^3 range and cell size about 2-5 μm for the samples that were rapidly cooled in ice-water bath. Gendron et al. [13] have explored solid-sate foaming of TOPAS COC 8007 and 5013 (T_g 78 and 135 °C respectively). The samples were saturated in a pressure ranging from 1.4 to 5.9 MPa to a CO_2 concentration of between 2% and 8% wt. Foaming was then carried out by biaxially stretching and simultaneous heating the samples. Recently, Chen et al. [14] investigated solid-state foaming of TOPAS 6017 COC (T_g of 180 °C) in the pressure range 5-10 MPa at 40 °C. The resulting COC foams had a cell size in the range of 0.3-7.5 μm and cell density ranging from 10^9 to 10^{12} cells/cm^3. Also, the transition from foaming to crazing under certain conditions due to stress field was identified.

Besides the effect of T_g, the effect of saturation temperature (T_{sat}) on the microcellular foaming and foam morphology, is not well established, especially in the sub-critical regime. In most of microcellular foaming studies, T_{sat} has been kept constant during the saturation step. Typically, room temperature has been used in the sub-critical regime. A higher T_{sat} enables a faster diffusion (thus short sorption time), which is beneficial to the production process; on the other hand, a higher T_{sat} results in a lower solubility of gas in polymer [15, 16, 17]. Solubility is known to significantly influence cell nucleation and resulting microstructures [18, 19]. Thus, to create foams with desired structures and properties, the effect of T_{sat} on the foaming and final foam morphology need to be established.

In this paper, we compare the solid-state microcellular foaming of COCs with a high and low T_g, with the T_{sat} varying from 20-80 ℃. The effect of T_g and T_{sat} on CO_2 solubility, diffusivity, cell nucleation and foam morphology are reported.

3.3 **Experimental**

3.3.1 **Materials**

Two grades of COC, grade 8007 and 6015, were provided by TOPAS Advanced Polymers Inc. 0.25 mm thick COC sheets were cut into 2.5 cm × 2.5 cm samples for sorption and foaming studies. Material information are listed in Table 3.1. 99.9% pure CO_2 was provided by Praxair, Inc.

Table 3.1 Material used in this study.

Commercial Name	T_g (℃)	Density (g/cc)	Norbornene Content (mol%)[20]	Designated In This Paper As
TOPAS 8007	78	1.02	40%	COC78
TOPAS 6015	158	1.02	54%	COC158

3.3.2 **Sorption**

Sorption experiments were conducted by placing samples in a pressure vessel maintained at 5 MPa with an accuracy of +/- 0.1 MPa. Sorption temperatures (T_{sat}) varied over a range from

20 ℃ to 80 ℃. For sorption experiment above room temperature, a heating jacket wrapped around the pressure vessel and a temperature controller was used to maintain the pressure vessel at a desired temperature. During saturation, samples were periodically taken out from the pressure vessel, and weighed on a Mettler AE240 analytical scale accurate to +/- 10 μg. Samples were then promptly put back to the pressure vessel and repressurized. The sorption experiment continued until no further weight increase was observed in the specimen.

3.3.3 **Foaming**

Specimens used for foaming studies were first wrapped in porous paper towel, and then placed in a pressure vessel which was maintained at 5 MPa. Samples were kept in the pressure vessel for 10 h to ensure the full absorption of CO_2. After full saturation, samples were immediately removed from the pressure vessel, and quickly transferred to and immersed in a hot silicone oil bath (Thermo Haake B5) set at a desired temperature. The foaming time used for all samples was 30 seconds. After foaming, the sample was immediately quenched in room temperature water to stop further foaming.

3.3.4 **Characterization**

The excess silicone oil was removed from the surface of the sample before any characterization. The density of each sample was determined according to ASTM D792 using Mettler AE240 analytical scale. Samples were allowed to desorb for at least one week before density measurement was performed in order to eliminate the effect of residual CO_2. A representative set of samples were imaged with a scanning electron microscope (SEM) to examine the microstructures produced. All images were taken on a FEI Sirion SEM. Samples were first scored with a razor blade and freeze fractured with liquid nitrogen to expose the cross section. They were then coated with Au/Pd for 90 s at a current of 18 mA. Micrographs were taken at the center of the cross section of the specimen and analyzed using software ImageJ (National Institute of Health, USA). Average cell size was calculated by taking average cell diameters of at least 50 cells in the SEM micrographs. Cell nucleation density (number of cells nucleated per cubic centimeter of the unfoamed sample) was calculated using a procedure described in literature [18].

3.4 **Results and Discussions**

3.4.1 **Effect of T_g and T_{sat} on CO_2 Solubility**

CO_2 solubility is defined as the equilibrium CO_2 concentration for each specific saturation condition. CO_2 concentration is usually expressed as a percentage of the original polymer mass, e.g. 10% CO_2 concentration means that 10% of the mass of original polymer is now absorbed into the polymer. There was a short time interval between the pressure release and weight measurement in the sorption experiment. To account for the CO_2 loss during this interval, the solubility of CO_2 in the samples was obtained by extrapolating the desorption curve to zero desorption time. Detailed procedures can be found in literature [21, 22]. Solubility for both COC78 and COC158 at different saturation temperatures are summarized in Table 3.2 and plotted in Figure 3.1.

We can see that as T_{sat} increases, the solubility for both COCs decreases. Also, we can see that the higher T_g COC has a higher solubility in every saturation temperature. Hu et al. [20] measured the solubility of four different COCs with T_g varying between 81 and 173 ℃ and conducted sorption experiments up to 3.2 MPa at room temperature. They reported higher solubilities in higher T_g COC. The higher solubility was believed to be due to the larger free volume in the higher T_g COC. Bulky norbornene on the backbone disrupt the chain packing, thereby increasing the free volume. The measured fractional free volume (FFV) at room temperature was 0.119 for 154 ℃ T_g COC, and 0.062 for 81 ℃ T_g [20].

Also, solubilities of both COCs seem to converge at high saturation temperatures. This might be due to the decreasing free volume in both COCs as the temperature increases. A higher temperature allows higher chain mobility and thus less unoccupied free volume.

The temperature dependence of solubility is typically given by Arrhenius equation [15, 16, 23],

$$S = S_0 \exp\left(-\frac{\Delta H_S}{RT}\right) \tag{1}$$

where S_0 is the pre-exponential factor, ΔH_S is the heat of sorption or enthalpy change upon solution of gas in the polymer, and R is gas constant.

Table 3.2 Summary of solubility and diffusivity for COC78 and COC158.

	Solubility		Diffusivity, cm^2/s	
T_{sat} (℃)	COC78	COC158	COC78	COC158
20	5.40%	7.80%	1.23×10^{-8}	1.43×10^{-8}
40	4.16%	5.62%	2.40×10^{-8}	2.84×10^{-8}
50	3.84%	5.05%	3.46×10^{-8}	3.80×10^{-8}
60	3.45%	4.40%	7.55×10^{-8}	4.91×10^{-8}
70	3.25%	4.04%	1.63×10^{-7}	6.83×10^{-8}
80	3.07%	3.76%	2.78×10^{-7}	9.08×10^{-8}

Figure 3.2 shows the natural logarithm of solubilities as a function of the reciprocal of saturation temperature. A linear trend can be seen for both grades of COC. From the slopes, we calculated the heat of sorption to be -8.2 kJ/mol and -10.5 kJ/mol for COC78 and COC158, respectively.

Negative values indicate the exothermic nature of the sorption of CO_2 in COC. By comparing the two heats of sorption, we observe a larger heat release from the sorption of CO_2 in higher T_g COC.

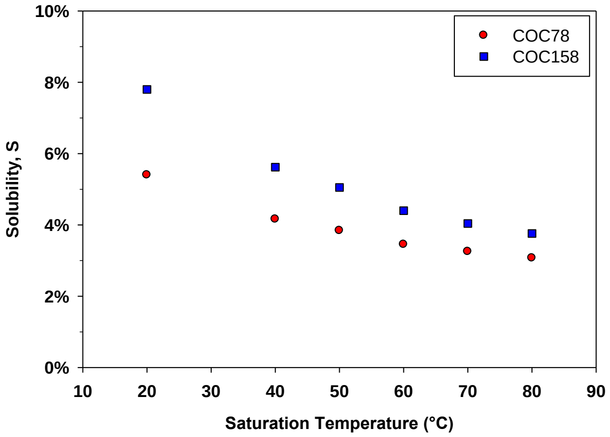

Figure 3.1 Solubility of COC78 and COC158 at different saturation temperatures.

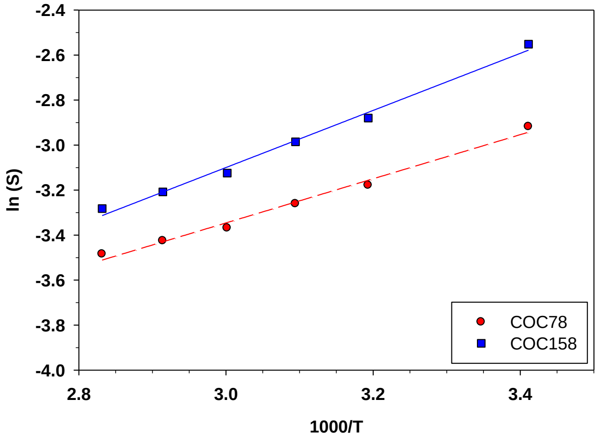

Figure 3.2 Natural logarithm of solubility as a function of reciprocal of saturation temperature for COC78 and COC158. Two best-fit lines are also included.

3.4.2 **Effect of T_g and T_{sat} on CO_2 Diffusivity**

One of the commonly used methods to determine diffusivity from a sorption plot is the initial slope method, which uses the slope of the initial part of a normalized sorption plot. At sufficiently short sorption times, the total mass uptake of gas in thin sheets can be described by [24]

$$\frac{M_t}{M_i} = \frac{4}{L}\left(\frac{Dt}{\pi}\right)^{0.5} \qquad (2)$$

where M_t is the amount of gas absorbed into polymer at time t, M_i is the equilibrium concentration, D is the diffusivity (cm^2/s), and L is the polymer thickness (cm). Diffusivity can then be calculated from the slope R of the early part of M_t/M_i vs $t^{0.5}/L$ plots.

$$D = \frac{\pi R^2}{16} \qquad (3)$$

In Figure 3.3, we have plotted the early part of the CO_2 uptake curves in COC78 with the time axis normalized for thickness, in units of ($t^{0.5}/L$), where t is in seconds and L is in cm. From the slopes, we can obtain sorption diffusivities using eqn. (3). Similarly, we can get sorption diffusivities for COC158. Both are summarized in Table 3.2.

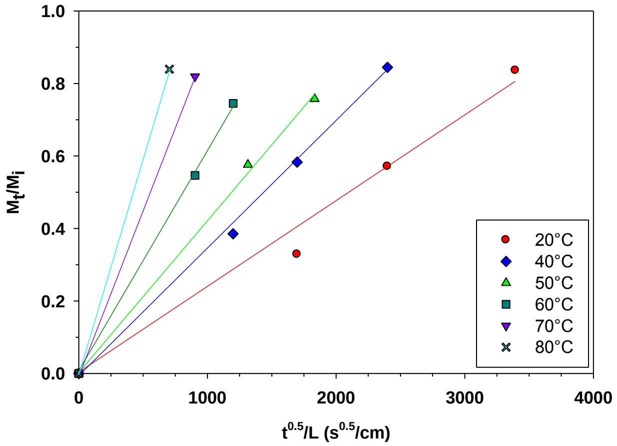

Figure 3.3 Early parts of sorption curves for COC78 at different saturation temperatures.

From the data, we see that as T_{sat} increases diffusivity also increases. The effect of temperature on the diffusivity of gas in polymers was first shown by Barrer [25] and later confirmed by others [15, 16] to be that of an activated process obeying the Arrhenius relationship:

$$D = D_0 \exp(-\frac{\Delta H_D}{RT}) \qquad (4)$$

where D_0 is the pre-exponential factor, ΔH_D is the activation energy for diffusion, R is gas constant and T is temperature in K.

Figure 3.4 shows the natural logarithm of sorption diffusivities as a function of the reciprocal of saturation temperature. A single linear trend can be observed for COC158, with an activation energy of 26.2 kJ/mol. However, for COC78, there exist two different linear lines for temperatures above and below 50 ℃, with a larger slope for above 50 ℃ case. The activation energy of diffusion is calculated to be 66.7 kJ/mol and 27 kJ/mol, for the temperature above and below 50 ℃, respectively.

When below 50 ℃, COC78 has similar diffusivities and activation energy as the COC158. Segmental chain mobility and free volume likely influence the diffusion process of CO_2 in polymer. A higher segmental chain mobility enables a faster diffusion, and larger free volume also enables a faster diffusion. Compared to COC78, COC158 has a lower segmental chain mobility, but a higher free volume. These two influence the diffusion in opposite ways. The net effect is a slightly higher diffusivity and lower activation energy in COC158.

The sudden change of activation energy at 50 ℃ for COC78 is probably due to the glass transition happening at around this temperature. Absorption of CO_2 depresses the T_g of polymer. At around 50 ℃, the amount of CO_2 absorbed sufficiently depresses T_g of COC78 to below the saturation temperature, and as a result, the polymer is in the rubbery state.

The phenomenon that a higher activation energy is needed when polymer is in rubbery state was previously reported and explained by Meares [26] in the diffusion of O_2 and Ar in polyvinyl acetate. The higher activation energy in the rubbery state is due to a larger zone of activation. Above T_g, gas molecules which dissolve in the polymer must create their own “holes” by separating the interchain polymer contacts. The penetrant then diffuses through the polymer matrix along cylindrical voids created by the synchronized rotation of polymer segments about the C-C bonds. Below T_g, the polymer consists of regions of densely packed and arranged chains which have limited freedom for rotation, separated by less dense regions of disordered chains that form the “holes” into which the gas absorbs. The gas molecule diffusion between the holes by slight compressing of localized chains in the dense regions enabling the gas molecules to pass through. The compression in the glassy state doesn’t create the long cavities common to the rubbery state, indicating the zone of chains activation is much larger in the rubbery state.

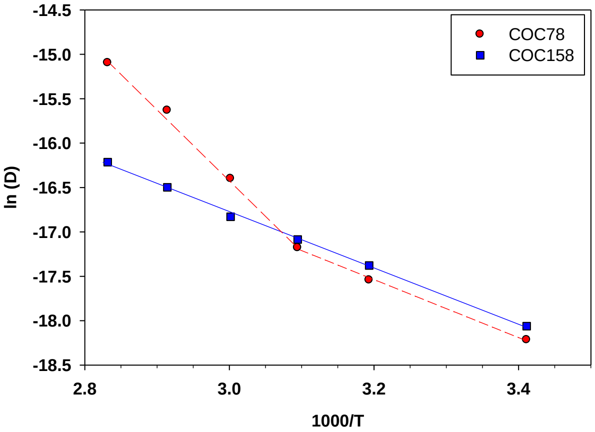

Figure 3.4 Natural logarithm of diffusivities as a function of reciprocal of saturation temperature for COC78 and COC158.

3.4.3 **Effect of T_g on Foaming and Foam Morphology**

From the solubility study above, we know that at the same saturation temperature, COC78 and COC158 have different CO_2 solubilities. Gas concentration is one of the most significant factors affecting the cell nucleation [18, 19]. In order to decouple the T_g effect and gas concentration effect, we need first saturate both grades of COC with a similar level of CO_2 concentration. COC78 was saturated at 20 ℃ to achieve a CO_2 concentration of 5.4%, and COC158 at 40 ℃ to get 5.62% CO_2 concentration.

Samples were then foamed in a range of foaming temperature. Figure 3.5 shows the relative density for both COC78 and COC158. The same general trend of decreasing density with the increasing foaming temperature up to a certain temperature is observed. Afterwards, relative density increases with a further increase in the foaming temperature. This has been previously observed in other polymer-gas systems [3, 4, 27] and was attributed to the cell collapse at higher foaming temperatures.

The threshold foaming temperature, i.e. minimum temperature for foaming to occur, is 50 ℃ for COC78 and 90 ℃ for COC158. The similar gas concentration in these two COCs introduces a similar plasticization effect. However, the high T_g COC has more rigid chain and less chain mobility to start with, thus a higher threshold foaming temperature in higher T_g COC can be expected.

The density decrease is slightly steeper in the COC78. It takes about 50 °C increase in foaming temperature to reduce the relative density from 100% down to 20%, whereas 80 °C is needed for COC158 to reach the same density reduction. The nucleated cells grow to a certain size upon heating at a giving foaming temperature. The final cell size is a complex function of gas saturation temperature and pressure, the polymer T_g, polymer matrix viscosity and extensional viscosity and its dependence on temperature, and the foaming temperature. The observation that for the higher T_g COC, a larger temperature increase is needed to reduce the density from 100% to 20% can be explained by the fact that the viscosity of the COC158 is higher than that of the COC78. Thus, a higher temperature is needed to achieve the cell growth that corresponds to a 20% relative density.

Figure 3.6 and Figure 3.7 compares the nucleation density and average cell size of COC78 and COC158 foams. An enhanced cell nucleation can be observed in the COC158. The cell nucleation density is on the order of 10^9 cells/cm^3 for COC158, whereas for COC78 nucleation density is mostly on the order of 10^7 cells/cm^3. Almost two orders of magnitude higher nucleation density is achieved in the higher T_g COC. The mechanism for a higher nucleation density in the higher T_g COC is not yet understood and is a subject of continuing investigation. Smaller cell size is seen in the higher T_g COC. Cell size of COC158 is between 3-10 μm, whereas COC78 has a cell size from10 μm up to 60 μm. SEM images of representative samples of both grades are shown in Figure 3.8. At similar densities, COC158 has a much smaller cell size than COC78.

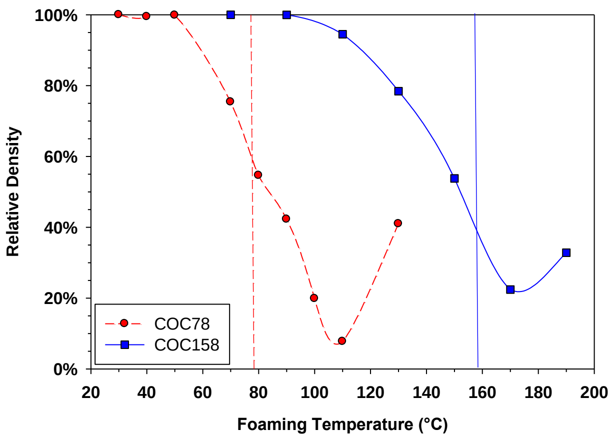

Figure 3.5 Relative density curves for COC78 and COC158, with two vertical lines indicating the two T_g's.

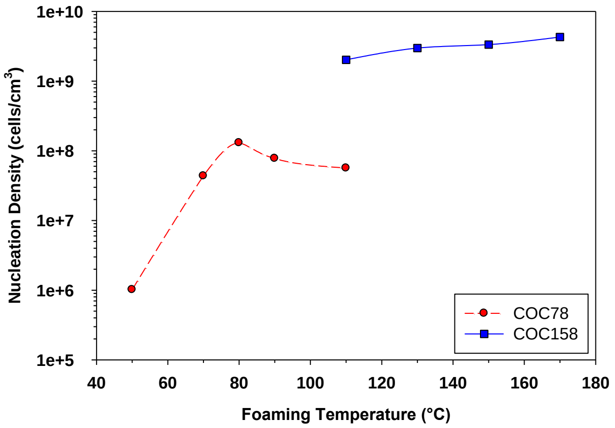

Figure 3.6 Nucleation density at different foaming temperatures for COC78 and COC158.

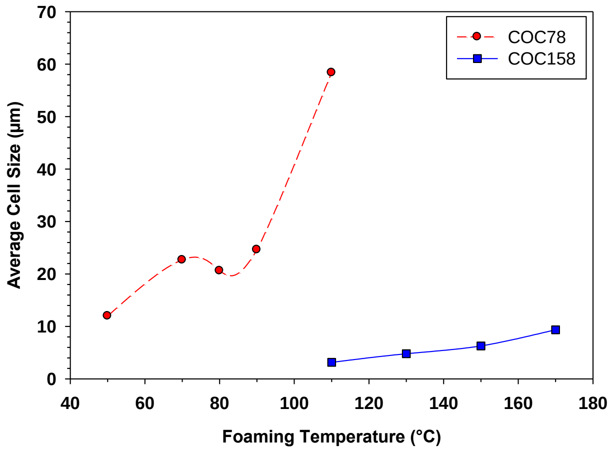

Figure 3.7 Average cell size at different foaming temperatures for COC78 and COC158.

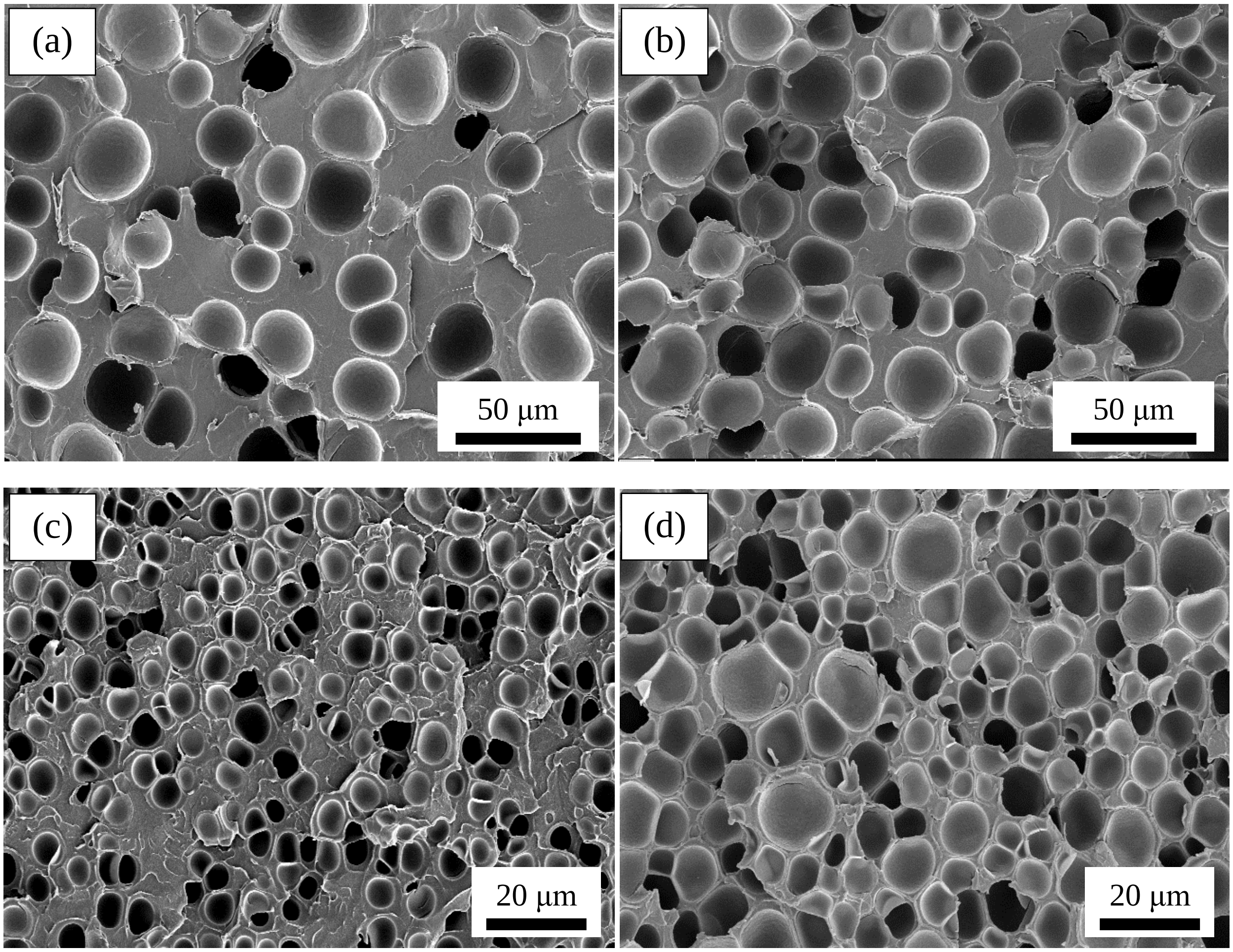

Figure 3.8 SEM images of COC78 foams with relative density and cell size of (a) 75%, 22.6 μm and (b) 55%, 20.6 μm; COC158 foams with relative density and cell size of (c) 78%, 4.8 μm and (d) 53%, 6.3 μm.

3.4.4 **Effect of T_{sat} on Foaming and Foam Morphology**

The high T_g COC158 was selected to study the effect of saturation temperature on microcellular foaming. From the sorption study, we know that saturation temperature affects the solubility (Table 3.2). The effect of saturation temperature can be viewed as the effect of gas concentration. Samples were initially saturated at 60 ℃, 40 ℃, 20 ℃, and CO_2 concentration of 4.4%, 5.62%, and 7.8% were achieved, respectively.

Figure 3.9 shows the relative density of foams saturated at different temperatures and then foamed in a range of temperatures. At higher saturation temperature, the CO_2 concentration is lower. A higher threshold foaming temperature is needed, and a more rapid decrease of relative density with foaming temperature is observed. Figure 3.10 and Figure 3.11 shows the nucleation density and average cell size as a function of CO_2 concentration. The straight trend line indicates that nucleation density increases exponentially with CO_2 concentration. Similar exponential relationship was reported in other polymer-gas systems [15, 16]. Also, average cell size decreases exponentially with increasing CO_2 concentration. At 7.8% CO_2, cell size falls below 1 μm into the ultramicrocellular region. The smallest cell size is about 380 nm. Figure 3.12 shows microstructures of representative samples that were saturated at different temperatures and then foamed at 130 ℃.

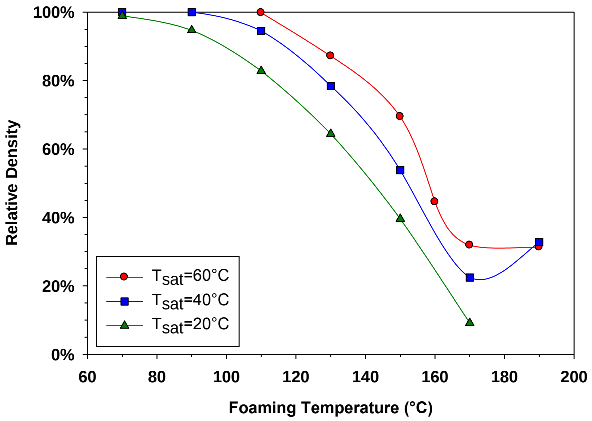

Figure 3.9 Relative density as a function of foaming temperatures for COC158 saturated at different saturation temperatures.

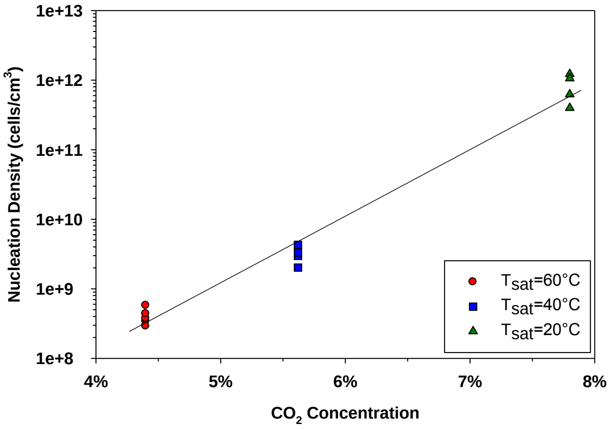

Figure 3.10 Nucleation density as a function of CO$_2$ concentration achieved via different saturation temperatures.

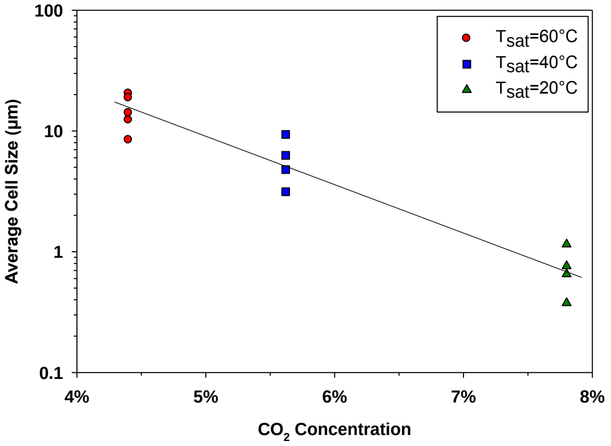

Figure 3.11 Average cell size as a function of CO$_2$ concentration achieved via different saturation temperatures.

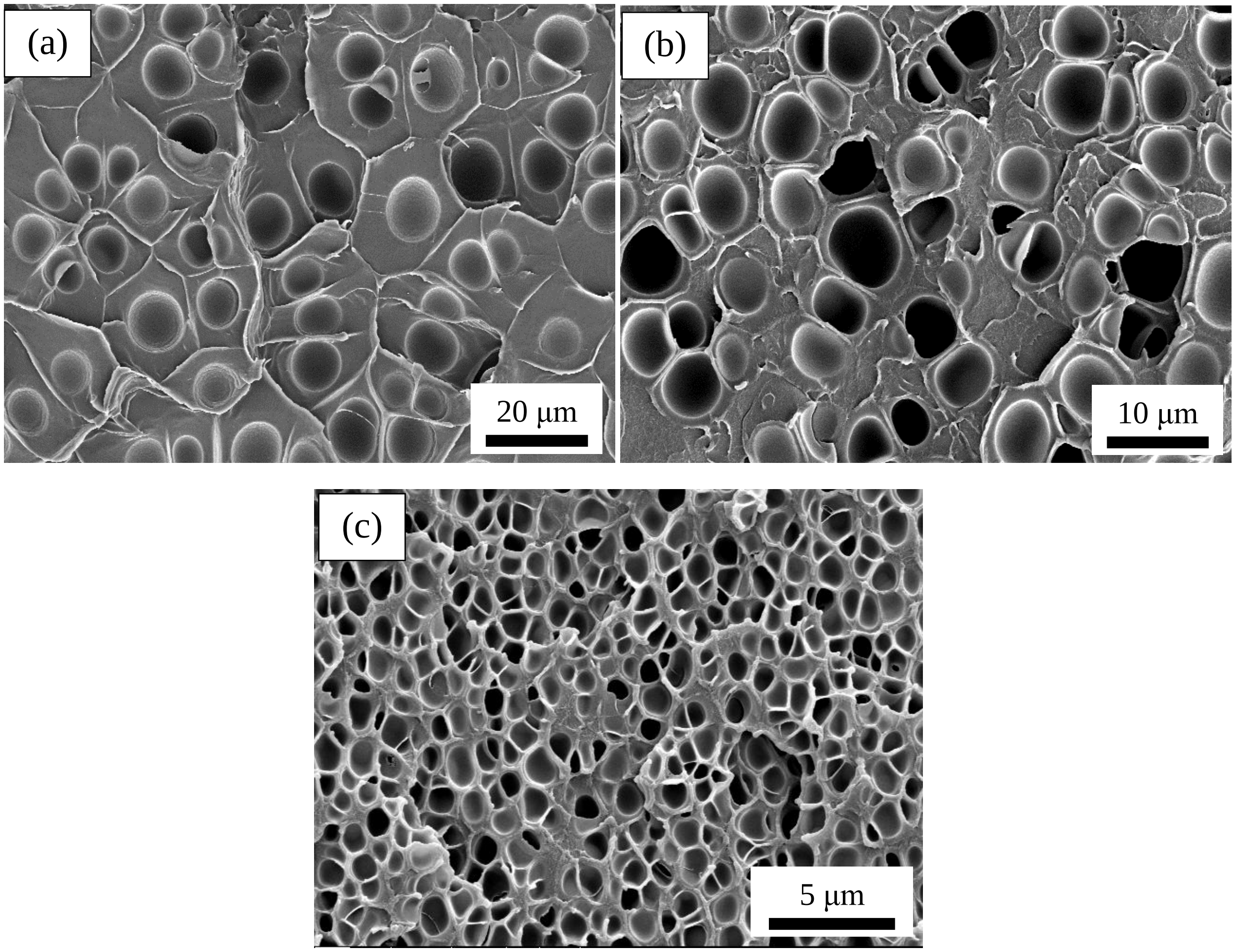

Figure 3.12 COC158 samples saturated at different temperatures and then foamed at 130 ℃: (a) T_{sat}=60 ℃, RD 87.1%, cell size 8.4 µm, (b) T_{sat}=40 ℃, RD 77.8%, cell size 4.8 µm, (c) T_{sat}=20 ℃, RD 64.4%, cell size 0.76 µm.

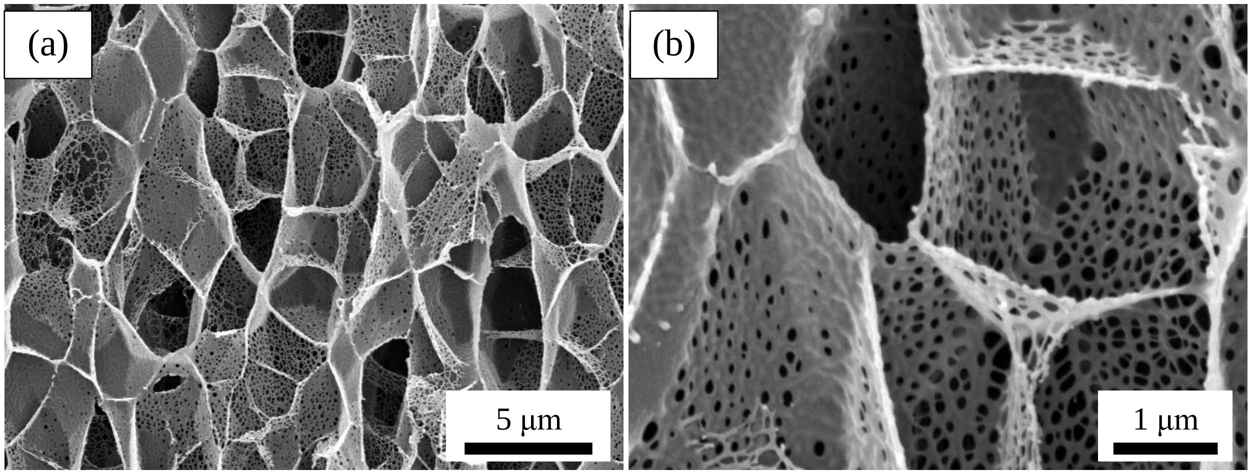

Figure 3.13 Hierarchical structure of low density (9.1% relative density) COC158 foam. (b) is a close-up of (a). Cells on the cell wall are about 80 nm in diameter.

A novel hierarchical structure (see Figure 3.13) is observed in the very low density foams. This sample was first saturated at 20 °C and then foamed at 170 °C. It has a relative density of 9.1%. The hierarchical structure consists of microcells with cell size about 2.5 μm and nanopores with cell size about 80 nm. The cell wall is only about 50 nm in thickness. The spaces enclosed by the cell walls of the microcells are interconnected through the nanopores. This novel structure may possess some unique thermal insulation, sound absorption and filtration properties. It can potentially be used in many applications, such as filtration membranes and battery separators.

Nanoporous structures on cell walls were previously reported in polyetherimide [28], polycarbonate [29] and polyethersulfone [30]. The nanoporous structures only existed on the surface of the cell wall, with solid polymer underneath the nanoporous structure and thus two neighboring microcells are not interconnected. However, in our study, the pores occupy the whole thickness of the cell wall and microcells are interconnected through these pores. The formation mechanism of the hierarchical structure is not understood at present. One possible mechanism is the stress-induced cell nucleation on the cell wall. During cell growth, the cell walls of the microcells experience a large tensile stress from the stretching. The large tensile stress can cause the residual CO_2 on the cell wall to nucleate and form new cells. The formation mechanism is currently under investigation.

3.5 **Summary**

The effect of T_g and T_{sat} on the solid-state microcellular foaming of COC, including CO_2 solubility, diffusivity, cell nucleation and foam morphology, were investigated in this study. COCs of low T_g (78 °C) and high T_g (158 °C) were used in this study. The T_g's were varied by adjusting the amount of norbornene content in the composition of copolymer, with higher norbornene content in the higher T_g COC. A temperature range of 20 ℃ to 80 ℃ was chosen to study the effect of T_{sat}.

Solubilities decrease with increasing T_{sat}, and Arrhenius relationship between solubility and saturation temperature is observed for both COCs. Solubilities are 20%-50% higher in high T_g COC than the low T_g COC across the saturation temperature range. Diffusivities increase with increasing T_{sat}. Diffusivities are about 15% higher on average in high T_g COC for temperatures up to 50 ℃. A much faster increase of diffusivity beyond 50 ℃ is observed in low T_g COC probably due to it being in the rubbery state.

We decoupled the effect of T_g and effect of gas concentration. Relationships between relative densities and foaming temperature for COC78 and COC158 are also established. Under similar CO_2 concentration, high T_g COC starts foaming at a higher temperature. And the density decreases faster in low T_g COC with foaming temperature. Also, high T_g COC foams show about two orders of magnitude higher cell nucleation density than the low T_g COC foams, and the cells are smaller in the high T_g foams.

The effect of T_{sat} on the microcellular foaming of COC was also studied using the high T_g COC. The effect of T_{sat} can be viewed as the effect of gas concentration. As the T_{sat} decreases, the gas concentration increases. As the gas concentration increases, cell nucleation density increases and cell size decreases, both exponentially. Uniform ultramicrocellular structure with an average cell size of 380 nm was created. A novel hierarchical structure with ~2.5 μm microcells and 80 nm nanopores on the cell walls was discovered in the very low density foams.

3.6 **Acknowledgments**

The authors would like to thank TOPAS Advanced Polymers for providing the materials for this study, and members of the University of Washington Cellular Composites Consortium for sponsoring the project.

3.7 **References**

1. J. Martini, N. Suh, F.A. Waldman, Microcellular closed cell foams and their method of manufacture. Patent #4473665. USA: Massachusetts Institute of Technology; 1984.
2. J. Martini, F.A Waldman, N. Suh, The production and analysis of microcellular thermoplastic foam. *SPE ANTEC*: vol. 28. San Francisco, CA; 1982. p. 674.
3. V. Kumar, J. Weller, *International Polymer Processing,* **8**, 73 (1993).
4. R.E. Murray, J. Weller, V. Kumar, *Cellular Polymers,* **19**, 413 (2000).
5. V. Kumar, J. Weller, *Journal of Engineering for Industry,* **116**, 413 (1994).
6. H. Guo, K. Nadella, V. Kumar, *Journal of Materials Research,* **28**, 2374 (2013).
7. E. Richards, R. Rizvi, A. Chow, H. Naguib, *Journal of Polymers and the Environment,* **16**, 258 (2008).
8. X. Wang, V. Kumar, W. Li, *Cellular Polymers,* **26**, 1 (2007).
9. S.K. Goel, E.J. Beckman, *Cellular Polymers,* **12**, 251 (1993).
10. J.Y. Shin, J.Y. Park, C. Liu, J. He, S.C. Kim, *Pure Appl. Chem*., **77**, 801 (2005).
11. B. Krause, R. Mettinkhof, N.F.A. van der Vegt, M. Wessling, *Macromolecules*, **34**, 874 (2001).
12. X. Sun, H. Liu, G. Li, X. Liao, J. He, *Journal of Applied Polymer Science*, **93**, 163 (2004).
13. R. Gendron, M.F. Champagne, J. Tatibouet, M.N. Bureau, *Cellular Polymers*, **28**, 1 (2009).
14. Z. Chen, C. Zeng, Z. Yao, K. Cao, *Industrial & Engineering Chemistry Research*, **52**, 9381 (2013).
15. J. Crank, G.S. Park, *Diffusion in Polymers*, London: Academic Press (1968).
16. Y.P. Handa, Z. Zhang, B. Wong, *Cellular Polymers*, **20**, 1 (2001).
17. H. Guo, V. Kumar, Solid-state Microcellular Foaming of Low- and High- T_g Cyclic Olefin Copolymer (COC), SPE FOAMS 2014 Conference, Iselin, NJ, 2014.
18. V. Kumar, J.E. Weller, *Journal of Engineering for Industry*, **116**, 413 (1994).
19. V. Kumar, N. Suh, *Polymer Engineering and Science*, **30**, 1323 (1990).
20. C. Hu, K. Lee, R. Ruaan, Y. Jean, J. Lai, *Journal of Membrane Science*, **274**, 192 (2006).
21. H. Guo, V. Kumar, *Polymer*, **56**, 46-56 (2015).
22. M. Pantoula, C. Panayiotou, *J. Supercritical Fluids* **2006**, 37, 254-262.
23. H. Guo, V. Kumar, *Polymer*, **57**, 157-163 (2015).
24. J. Crank, *The mathematics of diffusion*, New York: Oxford Science Press (1989).
25. R.M. Barrer, *Nature*, **140**, 106 (1937).
26. P. Meares, *J. Am. Chem. Soc*., **76**, 3415 (1954).
27. Y.P. Handa, B. Wong, Z. Zhang, *Polymer Engineering and Science,* **39**, 55 (1999).
28. D. Miller, V. Kumar, *Polymer,* **50**, 5576 (2009).

29. Y. Fukasawa, J. Chen, H. Saito, *Journal of Polymer Science Part B: Polymer Physics*, **46**, 843 (2008).
30. L. Sorrentino, M. Aurilia, S. Iannace, *Advances in Polymer Technology,* **30**, 234 (2011).

Chapter 4

Low-temperature Saturation Solid-state Foaming Process and Polymer Screening Study

4.1 **Introduction**

This chapter presents the rationale for using low-temperature saturation, low-temperature saturation solid-state foaming process, and some preliminary results using this process in a number of polymers.

4.1.1 **Relationship between Average Cell Size, Cell Nucleation Density and Relative Density**

In order to make nanocells with sizes below 1 μm, a very high cell nucleation density, typically higher than 10^{11} cells/cm^3, needs to be achieved. This becomes clear if we consider the relationship between average cell size, cell nucleation density, and relative density of the foams, which can be derived from the following equation:

$$N_f * \frac{\pi}{6} D^3 = V_f \tag{1}$$

where N_f is the cell density, D is the average cell size, and V_f is the void fraction of the foam.

And N_f is related to cell nucleation density N_0, and V_f is related to relative density RD by the following equations:

$$N_f = N_0 * RD \tag{2}$$

$$V_f = 1 - RD \tag{3}$$

Substitute Equation (2) and (3) into (1), we get

$$N_0 * \frac{\pi}{6} D^3 = \frac{1}{RD} - 1 \tag{4}$$

This equation applies to the case where cells are spherical. Although not all foams have perfectly spherical cells, this equation provides some useful insights regarding to how to create nanocells. In Figure 4.1, we plot this equation for three different relative densities. It's evident from the figure that in order to achieve a cell size below 1 μm cell nucleation density needs to be above 10^{11} cells/cm^3, and to achieve a cell size below 100 nm cell nucleation density needs to be above 10^{14} cells/cm^3.

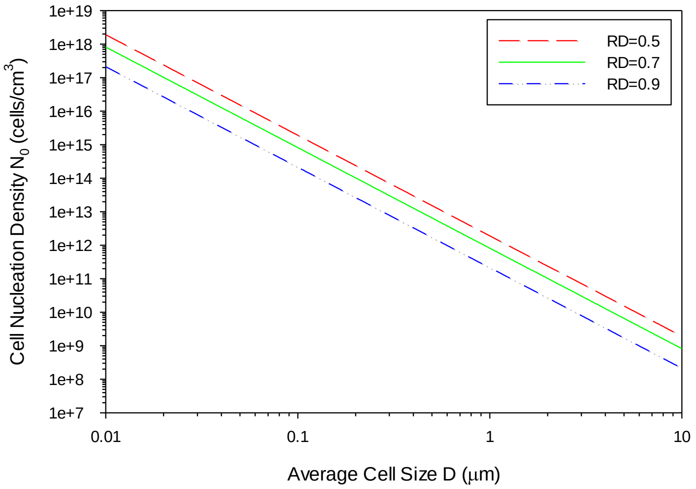

Figure 4.1 Relationship between cell nucleation density and average cell size for different relative densities. Both axes are in logarithmic scale.

4.1.2 **Vary Saturation Conditions to Enhance Cell Nucleation**

The first step in the solid-state foaming process is gas saturation. The saturation pressure, saturation temperature, and saturation time combined determine the equilibrium gas concentration (i.e. solubility). Gas concentration is known to have a significant effect on the cell nucleation. Kumar and Weller [1] reported that cell nucleation density increased exponentially with saturation pressure (equivalently, gas concentration) in polycarbonate-CO_2 system for pressure range of 2.07-6.55 MPa. In another study, Kumar reported [2] reported a similar exponential increase in cell nucleation density in polystyrene-N_2 for the pressure range of 4.13-13.79 MPa.

In order to increase gas concentration, there are three parameters that can be adjusted. The first parameter is to increase saturation time. Gas gradually diffuses into the polymer. Longer saturation time enables a larger gas concentration in the polymer. However, equilibrium state will reach at a sufficiently long time, where gas concentration reaches its maximum value. In most of cases, we leave polymer sample in pressure vessel until it is fully saturated. So this parameter is not usually used to increase gas concentration in order to enhance cell nucleation.

The second parameter is to increase saturation pressure, and this has been done in many studies [1-5]. Figure 4.2 shows the schematic of CO_2 phase diagram. Typically, in the solid-state gas foaming process, gas saturation is done in the subcritical gaseous region. Saturation pressure is usually in the range of 1 - 7 MPa. In order to achieve higher gas solubility and faster sorption, higher pressure conditions tend to be used [6, 7]. The pressures are above 7.38 MPa but usually in the range of 10-40 MPa, where CO_2 is in the supercritical region.

The third parameter is to reduce saturation temperature. Reducing saturation temperature is known to increase gas solubility in polymers [8, 9]. Most of studies in literature were carried out at room temperature or above room temperature. The saturation temperature used is the room temperature (about 20 ℃) for the subcritical gaseous region, and above 31.1 ℃ for supercritical region. Few studies in literature have been carried out at temperatures lower than the room temperature.

Although enhanced cell nucleation have been reported in many studies by increasing saturation pressure, little success have been achieved in creating nanofoams. Using lower saturation temperatures to create nanofoams is largely unexplored.

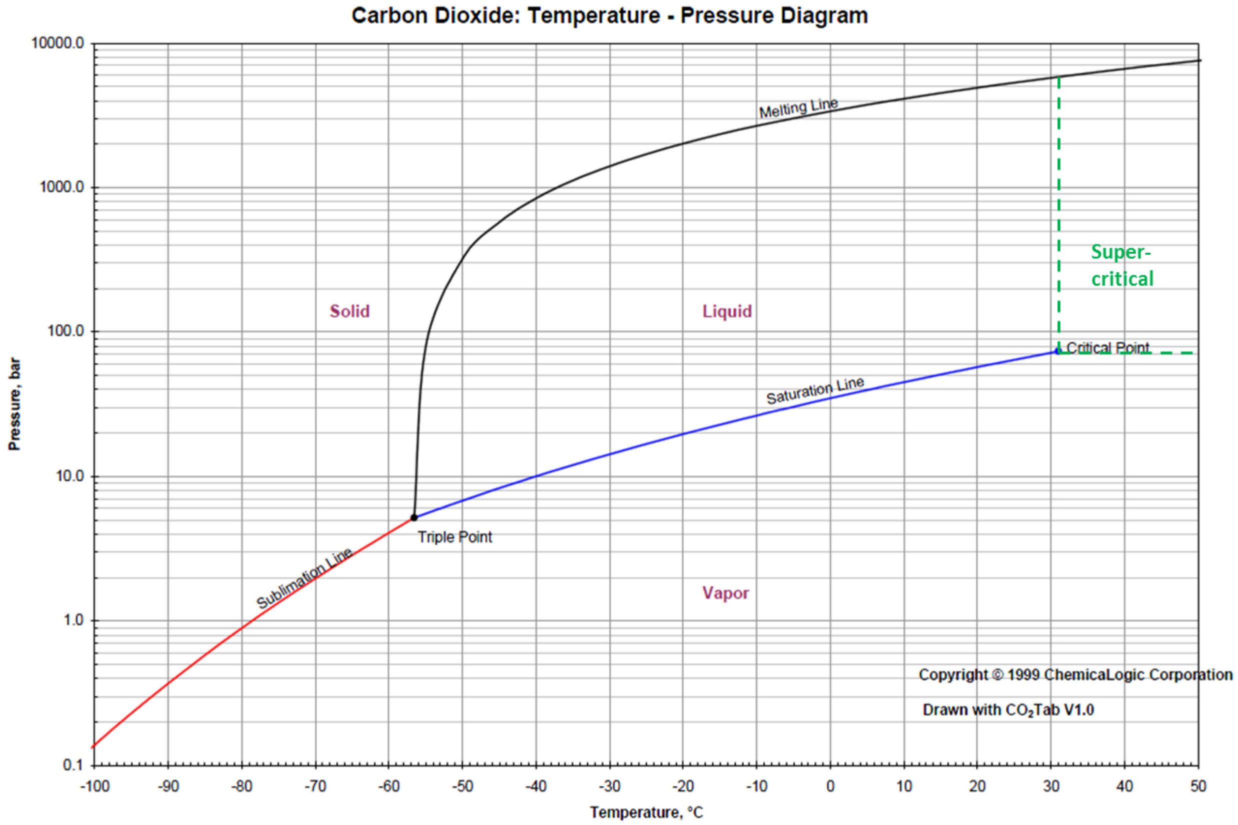

Figure 4.2 CO_2 phase diagram.

4.2 **Low-temperature Saturation Solid-state Foaming Process**

Figure 4.3 shows the schematic of the low-temperature saturation solid-state foaming process. It is very similar to the original solid-state foaming process. The only modification is the added capability to control the temperature of the pressure vessel to below room temperature. Depending on the temperature range, various means can be used to achieve the low temperature conditions. Here in the schematic we show that the pressure vessel is placed inside a freezer to achieve sub-zero temperatures.

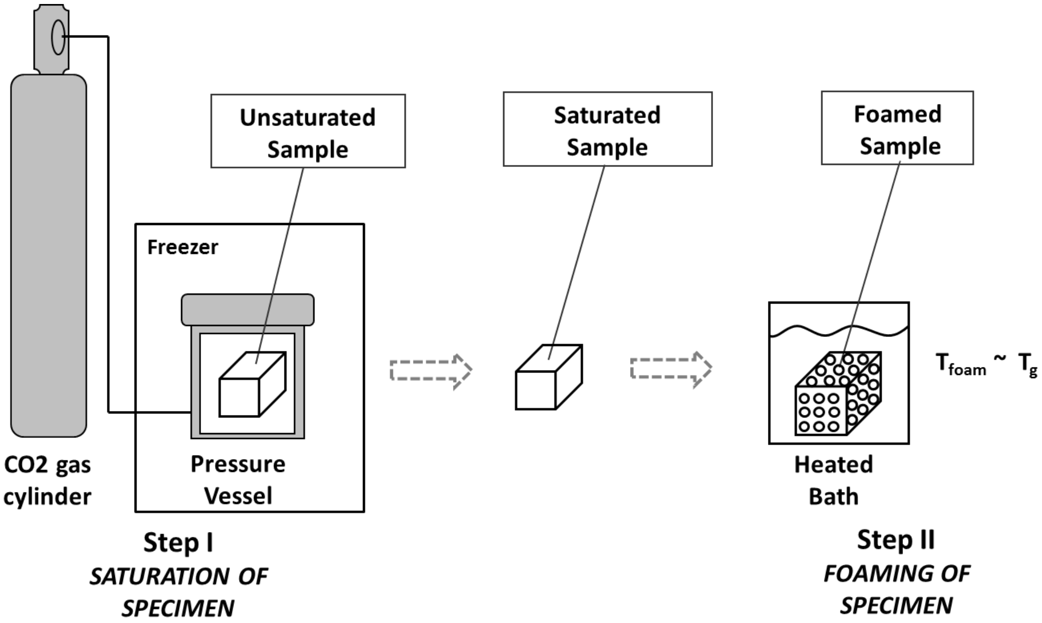

Figure 4.3 Low-temperature saturation solid-state foaming process.

The actual low-temperature saturation system is shown in Figure 4.4. There are two stainless steel pressure vessels. Each pressure vessel is seated on an aluminum cavity, which is mounted to the wooden plate. A pressure transducer, a solenoid valve, and a mechanical pressure gauge are also placed inside the freezer. Both of the pressure transducer and the solenoid valve are wrapped to eliminate the effect of moisture condensation. The pressure transducer senses the line pressure and sends signals to a PID controller, and the actual pressure is then displayed. The solenoid valve switches the connection between the pressure vessel and gas cylinder. The solenoid valve is controlled by the PID controller. When the line pressure is below a set point, the solenoid valve opens and let more gas come into the pressure vessel from the gas cylinder. Once the pressure returns to above the set point, the solenoid valve closes and no more gas can get into the pressure vessel. The mechanical pressure gauge is installed to monitor the pressure in the line, in addition to the pressure transducer. Copper tubing is used to conduct gas and connect different components.

Figure 4.4 Low-temperature saturation system. (b) is a close-up view of the freezer in (a).

4.3 **Screening of Polymers for Creating Nanofoams**

With the low-temperature saturation system set up, many different polymers were investigated to search for candidates for creating nanofoams. Solubility of CO_2 in the polymers was first measured in the first step of the process. Polymers with an appreciable amount of solubility increase were proceeded for further foaming experiments. Microstructure of the foams obtained served as the final criterion as to whether a polymer was chosen for further more detailed investigations.

4.3.1 **CO_2 Solubility in Polymers at Low Temperatures**

Many polymers have been studied in solid-state microcellular foaming process at room temperature. A majority of these polymers were collected and summarized in

Table 4.1. They are divided into four major categories: amorphous homopolymer, amorphous copolymer, highly-crystalline polymer, and semi-crystalline polymer. Nanofoams in these polymers, except PEI, ABS, PMMA, and COC, have not been previously reported. PEI nanofoams with a cell size of 30-120 nm was reported by Miller et al. [10]. ABS, PMMA and COC were reported to have cell sizes between 100 nm and 1 µm [4, 9,11-13].

Table 4.1 also shows the CO_2 concentration in various polymers at the temperature range of -40 °C to 20 °C. We can see that CO_2 solubility increases when the temperature decreases, except for highly-crystalline polymers. With the aforementioned observation that cell nucleation density increases with gas concentration, all these polymers except the highly-crystalline polymers were further pursued for creating nanofoams.

Table 4.1 CO_2 solubility in polymers at various low temperatures.

Category	Polymer	RT (~20 ℃)	0 ℃	-10 ℃	-30 ℃	-40 ℃
Amorphous homopolymer	PC	10.7%	15%	18%	20.3%	21%
	PMMA	17.5%	27%	32%	37%	41%
	PSU	10.8%		15.5%		
	PPSU	10%	13.5%	15.4%	19.9%	
	PEI	11%	15.5%	16.8%	20.3%	
	PS	9%				16.5%
Amorphous Copolymer	COC (6017)	8.4%		12%		
	ABS	12%				27%
Highly-crystalline	LDPE	2.8%		2.4%		
	HDPE	1.4%		1.6%		
	UHMWPE	2.3%		2.3%		
	PP	4%		4.1%		
	PTFE	2.3%		3%	3%	
Semi-crystalline	PET	8.5%		12%	18.5%	
	CPET	9%		12%		
	PEEK	8%			>16.5%	
	PLA	20%	30%	36%	43%	
	TPU (42D)	7.5% @27℃		10.9%		10.8%

4.3.2 **Some Preliminary Foaming Results**

Some preliminary foaming experiments were carried out. The obtained cellular structures are quite different for different polymers. PC, PMMA, PSU, and PPSU show uniform nanocellular structures with cell sizes below 100 nm. Figure 4.5, Figure 4.6, Figure 4.7, and Figure 4.8 show the SEM micrographs of PC, PMMA, PSU, and PPSU, respectively.

ABS has a cell size around 370 nm. This is about the same as that when it is saturated at room temperature and with a lower CO_2 concentration [4]. Figure 4.9 shows the cellular structure of ABS.

PLA, 42D TPU, PET, and CPET show smaller cell sizes compared to that when they are saturated at room temperature. However, cell sizes are still above 1 µm. Figure 4.10, Figure 4.11, Figure 4.12, and Figure 4.13 show the cellular structures of microcellular PLA, 42D TPU, PET and CPET, respectively.

Experiments with PS and PEI were not successful in creating nanofoams. PS was found to blister severely after the saturation process. No foaming experiments were conducted. PEI didn't blister during saturation and actually absorbed a large amount of CO_2 (20.3% at -30 ℃); however, during foaming PEI blistered severely. Due to the macro-blisters, no microstructure characterization was carried out. PEEK and COC need further investigations.

Based on these preliminary experiments, PC, PMMA, PSU, and PPSU were further investigated. Experiments under a range of saturation temperatures and with a range of foaming temperatures were carried out for these polymers. Each of them is detailed in an individual chapter.

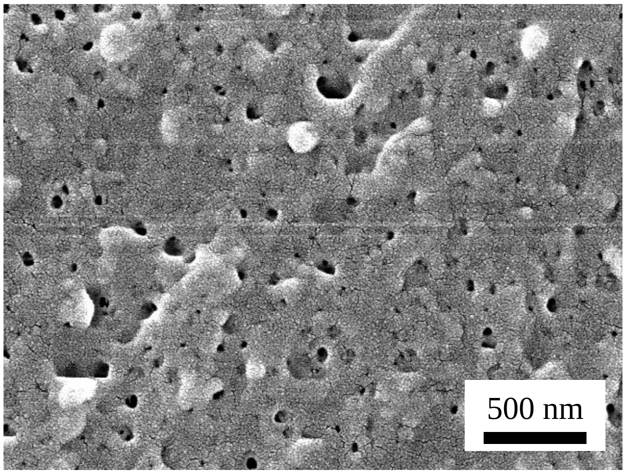

Figure 4.5 Cellular structure of PC nanofoams. Sample was saturated at 5 MPa and -30 ℃, and then foamed at 60 ℃ for 1 minute. Desorption time was 17 min. Average cell size is about 30 nm.

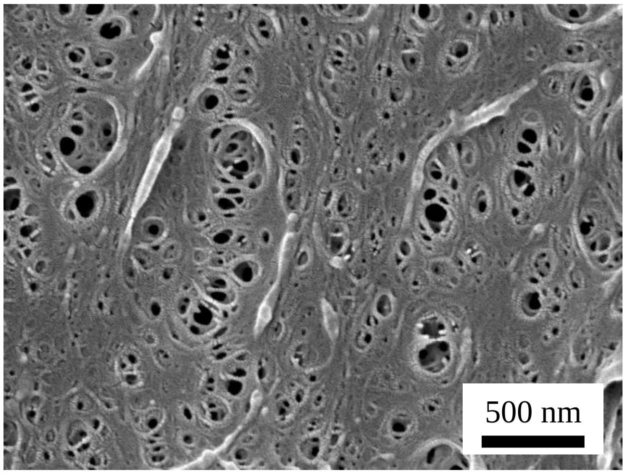

Figure 4.6 Cellular structure of PMMA nanofoams. Sample was saturated at 5 MPa and -40 ℃, and then foamed at 40 ℃ for 1 minute. Desorption time was 15 min. Average cell size is about 50 nm.

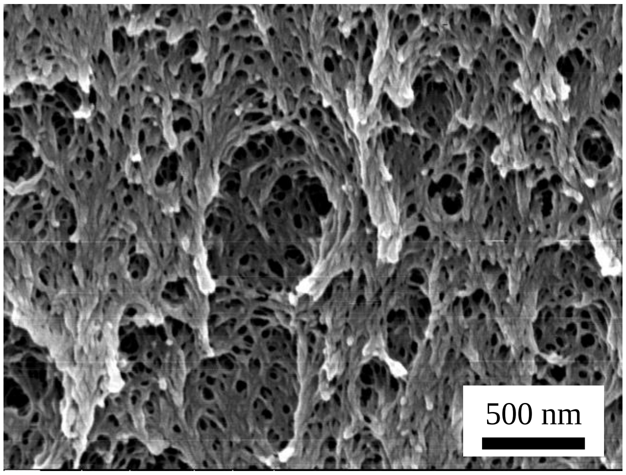

Figure 4.7 Cellular structure of PSU nanofoams. Sample was saturated at 5 MPa and -10 ℃, and then foamed at 150 ℃ for 1 minute. Desorption time was 17 min. Average cell size is about 30 nm.

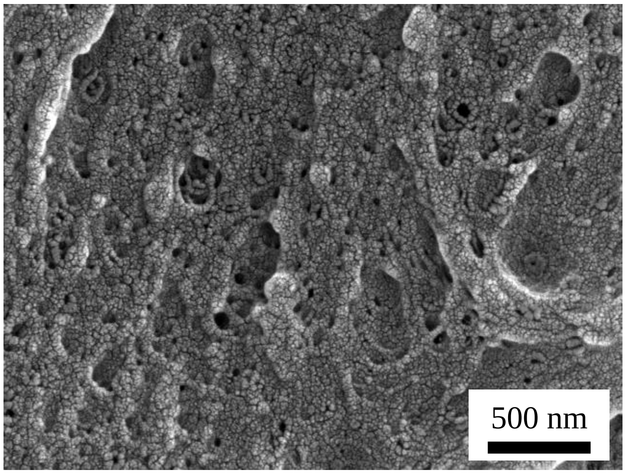

Figure 4.8 Cellular structure of PPSU nanofoams. Sample was saturated at 5 MPa and 10 ℃, and then foamed at 150 ℃ for 1 minute. Average cell size is about 28 nm.

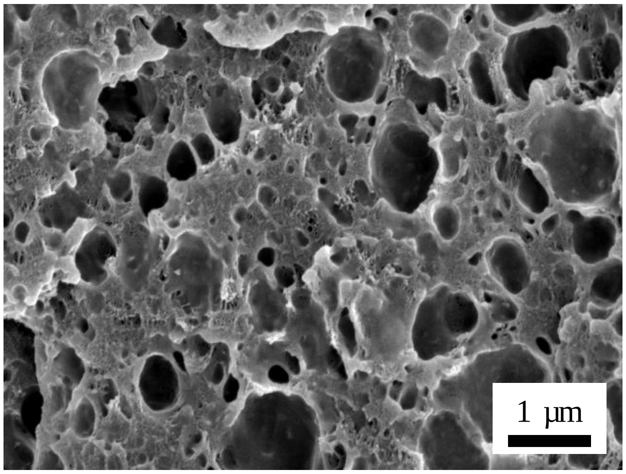

Figure 4.9 Cellular structure of ABS nanofoams. Sample was saturated at 5 MPa and -40 ℃, and then foamed at 21 ℃ for 1.5 minute. Desorption time was 11 min. Cell size ranges from 60 to 800 nm and average cell size is about 370 nm.

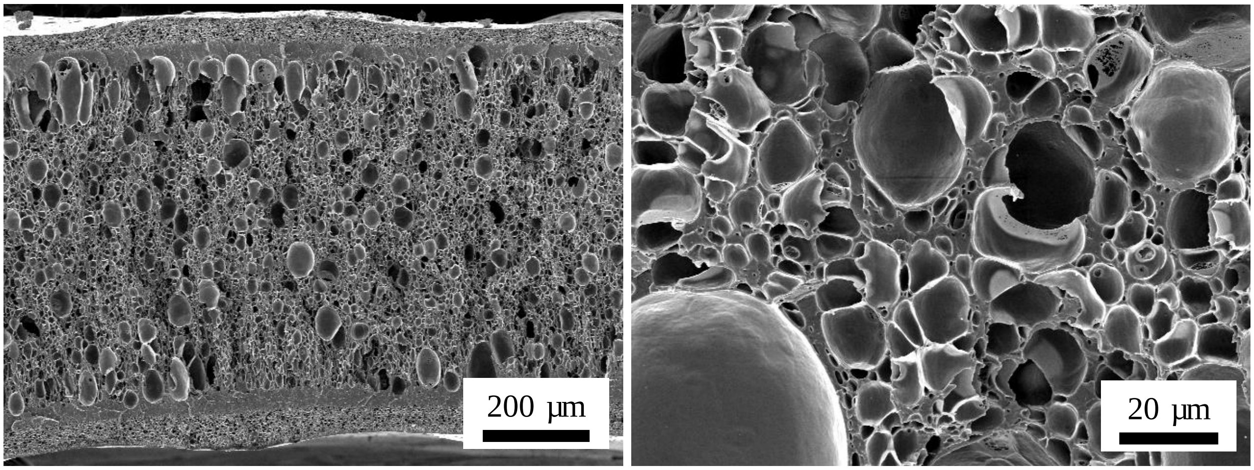

Figure 4.10 Cellular structure of PLA microcellular foams. Sample was saturated at 5 MPa and -20 ℃, and then foamed at 140 ℃ for 1 minute. Desorption time was 5 min. CO$_2$ concentration was 38%. Cell size ranges from 1 to 12 µm and average cell size is about 6 µm.

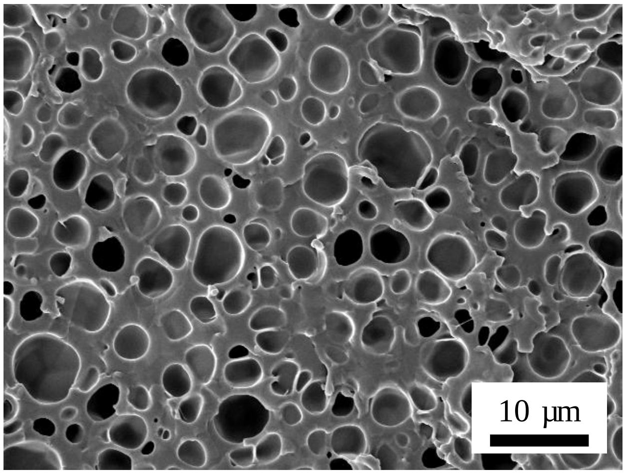

Figure 4.11 Cellular structure of 42D TPU microcellular foams. Sample was saturated at 5 MPa and -40 ℃, and then foamed at 100 ℃ for 30 seconds. Desorption time was 55 min. Average cell size is about 3 µm.

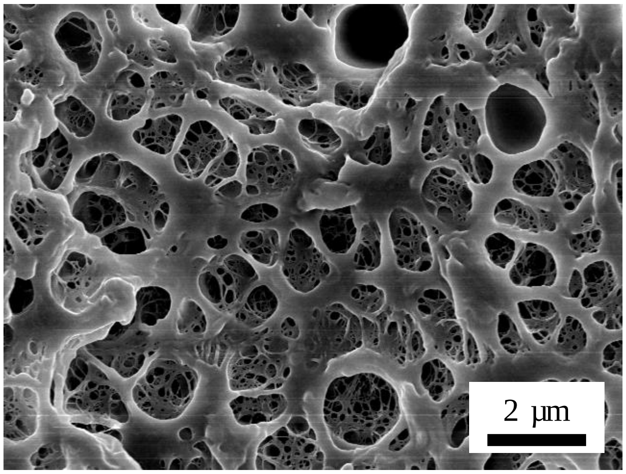

Figure 4.12 Cellular structure of PET microcellular foams. Sample was saturated at 5 MPa and -30 ℃, and then foamed at 20 ℃ for 30 seconds. Desorption time was 11 min. There are 1 μm larger cells with smaller cells inside ranging from 100 to 300 nm.

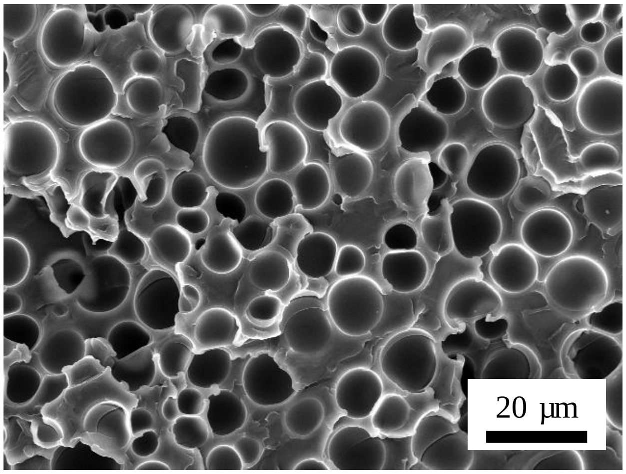

Figure 4.13 Cellular structure of CPET microcellular foams. Sample was saturated at 5 MPa and -10 ℃, and then foamed at 30 ℃ for 30 seconds. Desorption time was 7 min. Average cell size is about 6 μm.

4.4 **Conclusion**

The relationship between cell size, cell nucleation density and relative density gives us the insights that a sufficiently high cell nucleation density, typically higher than 10^{11} cells/cm^3, is needed to create nanofoams. Gas concentration is known to strongly influence cell nucleation, with a higher gas concentration leading to a higher cell nucleation density.

In order to increase gas concentration in a polymer, three different saturation parameters can be adjusted: saturation time, saturation pressure, and saturation temperature. A low-temperature solid-state foaming process was established to investigate the possibility of creating nanofoams by lowering the saturation temperature. A number of polymers were screened for candidates for creating nanofoams. CO_2 solubility is found to increase with decreasing temperatures in all the polymers, except the highly-crystalline polymers. Preliminary foaming results with polymers saturated at low temperatures show that PC, PMMA, PSU, and PPSU have nanocellular structures with cell sizes below 100 nm. Detailed studies on these polymers will be presented in separate chapters.

4.5 **References**

1. Kumar V, Weller JE. Production of microcellular polycarbonate using carbon dioxide for bubble nucleation. Journal of Engineering for Industry 1994; 116: 413-420.
2. Kumar V. Phenomenology of bubble nucleation in the solid-state nitrogen-polystyrene microcellular foams. Colloids and Surfaces A: Physiochemical and Engineering Aspects 2005; 263: 336-340.
3. Kumar V, Weller JE. A process to produce microcellular PVC. International Polymer Processing 1993; 8: 73-80.
4. Murray RE, Weller J, Kumar V. Solid-state microcellular acrylonitrile-butadiene-styrene foams. Cellular Polymers 2000; 19: 413-425.
5. Kumar V, Weller JE. Production of microcellular polycarbonate using carbon dioxide for bubble nucleation. Journal of Engineering for Industry 1994; 116: 413-420.
6. Cooper AI. Polymer synthesis and processing using supercritical carbon dioxide. Journal Material Chemistry. 2000; 10: 207-234.
7. Tsivintzelis I, Angelopoulou AG, Panayiotou C. Foaming of polymers with supercritical CO_2: an experimental and theoretical study. Polymer 2007; 48: 5928.
8. Crank J, Park GS. Diffusion in Polymers. London: Academic Press;1968.
9. Handa YP, Zhang Z, Wong B. Solubility, diffusivity, and retrograde vitrification in PMMA-CO_2, and development of sub-micron cellular structures. Cellular Polymers 2001; 20(1): 1-16.
10. Miller D, Kumar V. Microcellular and nanocellular solid-state polyethermide (PEI) foams using sub-critical carbon dioxide I. Processing and structure. Polymer 2009; 50: 5576-5584.
11. Handa YP, Zhang Z. A new technique for measuring retrograde vitrification in polymer-gas systems and for making ultramicrocellular foams from the retrograde phase. Journal of Polymer Science: Part B: Polymer Physics 2000; 38: 716-725.
12. Nawaby AV, Handa YP, Liao X, Yoshitaka Y, Tomohiro M. Polymer-CO_2 systems exhibiting retrograde behavior and formation of nanofoams. Polymer International 2007; 56: 67-73.
13. Chen Z, Zeng C, Yao Z, Cao K. Solid-state foaming of cyclic olefin copolymer by carbon dioxide. Industrial & Engineering Chemistry Research 2013; 52: 9381-9396.

Chapter 5

Some Thermodynamic and Kinetic Low-temperature Properties of the PC-CO_2 System and Morphological Characteristics of Solid-state PC Nanofoams Produced with Liquid CO_2

5.1 **Abstract**

In this paper, we describe a novel process for creating polycarbonate (PC) nanofoams with cells in the range of 20-30 nm that is based on saturating PC in liquid CO_2. We investigated the effect of saturation temperature on the solid-state processing of PC foams in the range of -30 ℃ to 80 ℃. Saturation temperature significantly affects the solubility and diffusivity, and the Arrhenius equation can describe the increase of solubility and decrease of diffusivity as the temperature decreases. We observed a drop in ΔH_s, the heat of sorption, at the transition from vapor phase to liquid phase, leading to a weaker dependence of solubility on temperature in the liquid CO_2. The dissolution of CO_2 in PC dramatically reduces its glass transition temperature in proportion to the amount of CO_2 absorbed: incorporation of 20.4% CO_2 in PC decreased the T_g from 147 ℃ down to -7.5 ℃. We have identified a critical CO_2 concentration between 15.9% and 18.9%, above which cell nucleation density rapidly increases and consequently foamed microstructure changes from microcellular to nanocellular. Nanofoams with cell nucleation densities exceeding 10^{15} cells/cm^3 and void fraction of up to 60% were achieved. The low-temperature route to enhanced cell nucleation opens up new possibilities for creating nanofoams in thermoplastics. The ability to create cells of different length scales in PC provides a unique opportunity to study the effect of cell size on mechanical and other properties of interest over a cell size range that spans several orders of magnitude.

Keywords: nanofoam, solid-state foam, low-temperature saturation, liquid CO_2

This chapter has been published in Polymer, 2015, 56: 46-56.

5.2 **Introduction**

Nanofoams, or nanocellular foams, refer to thermoplastic foams with cells of order 10 nm. Nanofoams can be regarded in concept as an extension of microcellular foams, with cells of order 10 μm, that was conceived at MIT three decades ago [1, 2]. In a pioneering paper, Martini et al. [2] described a two-step process to create microcellular structure in high impact polystyrene (HIPS), that involved saturating the polymer with a non-reacting gas and then heating the gas laden polymer to near the glass transition temperature. This process later became known as the solid-state process, as the polymer foam is created near the T_g of the gas-polymer system, well below the melting point. This process has been used to investigate a number of polymers, including PVC [3], ABS [4], PC [5], PET [6], and PLA [7, 8], to name a few. In a variation of this process, microcellular foams have been created by a sudden drop in gas pressure that causes a solubility drop resulting in a cell nucleation [9].

It has been widely expected that nanofoams would offer many properties that are superior to existing materials, and present a unique combination of properties not seen before, thus leading to a new generation of cellular polymer materials. Recently, Miller and Kumar [10] showed improved mechanical properties in nanocellular polyetherimide (PEI) when compared to microcellular PEI foams. Zhou et al. [11] reported higher flexural modulus and strength in PEI nanofoams than the unfoamed material. It has been hypothesized that nanofoams will have much lower thermal conductivity than microcellular foams due to reduced gas phase heat conduction, when cell size is close to the mean free path of air molecules at ambient temperature and pressure (about 70 nm). This is called Knudsen effect and has been demonstrated in organic aerogels [12] and very recently in polymer nanofoams with cell size down to 100 nm [13]. Another popular hypothesis suggests that nanofoams based on clear amorphous polymers, such as PMMA and PC, could present transparency when cell size is significantly smaller than the light wavelength. Such materials can be potentially used to create thermally insulative yet transparent windows, which can lead to huge energy savings for buildings. In addition, if pores are open and interconnected in the nanofoams, then we have a nanoporous material. Nanoporous materials have been widely used in filtration, gas separation, energy storage, and catalysis supports [14].

Although the idea of creating nanofoams is exciting, the methods of making nanofoams have been very limited, and only a few polymers with uniform nanocells have been discovered. Polyimide nanofoams have been produced from block copolymers consisting of thermally stable and thermally labile blocks, where the thermally labile blocks underwent thermolysis upon thermal treatment, leaving nanopores behind [15]. Solid-state gas foaming process has shown a great utility in creating polymeric nanofoams in polymer blends, such as PEEK/PEI blends [16], PP/rubber blends [17, 18], and PMMA/MAM blends [19, 20, 21]. The concept for these polymer blends nanofoams was essentially the same: one phase acted as the matrix and the other dispersed phase served as a template for bubble nucleation and growth. Nanofoams were created in PMMA and acrylic copolymers by adding small amount of nanoparticles which served as nucleation sites and greatly enhanced cell nucleation [22]. So far, in homopolymers, nanofoams have only been achieved in high glass transition temperature polymers - PEI and PES [23, 24]. In these two polymers, a critical gas concentration was reported for creating nanofoams.

As mentioned above, the first step in solid-state batch process is to saturate polymer with physical blowing agent, for example CO_2. A combination of saturation pressure and saturation temperature determines the amount of physical blowing agent absorbed, and to a large extent, the subsequent foam structure. Traditionally, the saturation temperature used is around the room temperature (20 - 30 ℃), and saturation pressure in the range of 1 - 7 MPa. In these conditions, CO_2 exist as gas. In order to achieve higher gas solubility and faster sorption, supercritical CO_2 (see Figure 5.1) is typically used [25, 26]. To achieve supercritical CO_2, saturation temperature is above 31.1 ℃ and saturation pressure above 7.3 MPa. However, saturation temperatures below room temperature have rarely been studied, and depending on the specific pressure used together, the CO_2 can be in either gaseous or liquid state. In this paper, we discovered, for the first time, the creation of nanofoams by saturation polymer at low temperatures down to -30 ℃ in the solid-state foaming process. We use polycarbonate (PC) as an example polymer for demonstrating this novel process. By sequentially lowering the saturation temperature, we've identified specific combinations of temperature and pressure that can generate PC nanofoams. Microcellular PC foams have been investigated extensively [5, 27, 28], but PC nanofoams have not been reported in literature.

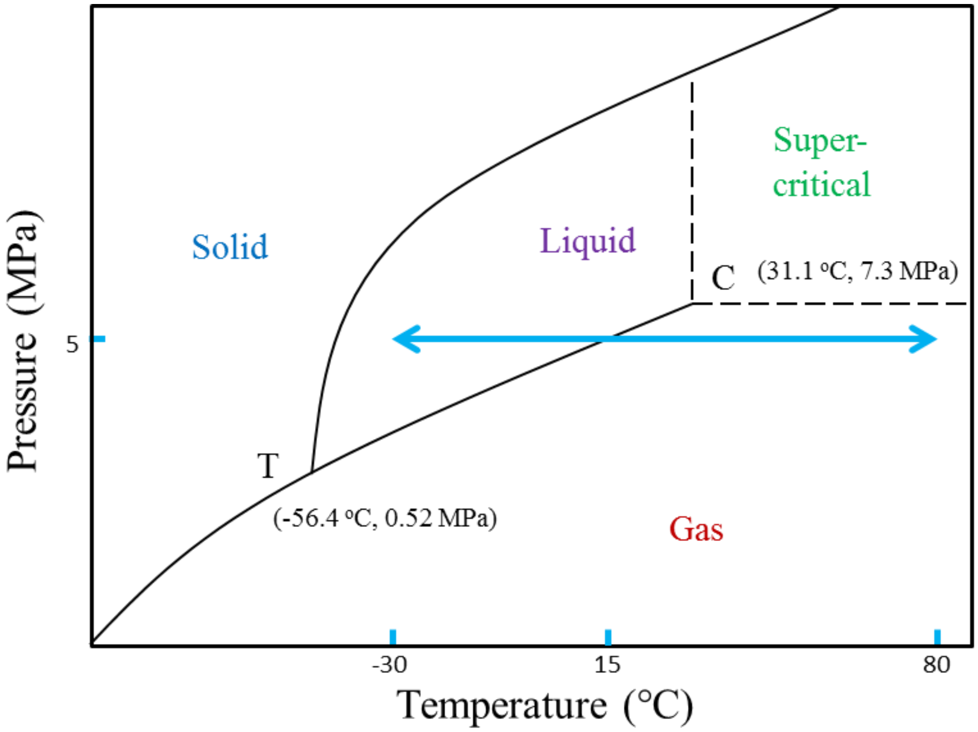

Figure 5.1 Schematic of CO_2 phase diagram. The double arrow roughly indicates the temperature range at a fixed pressure covered in this study. Notice that the range covers both the gas and liquid region, and crosses the gas-liquid boundary. *T* is the triple point and *C* is the critical point.

In this paper, we first discuss effect of saturation temperature on sorption behavior of CO_2 in PC. Over the temperature range investigated (-30 ℃ up to 80 ℃), CO_2 is in either gaseous or liquid state. Both solubility and diffusivity data are reported. Then, we show the solid-state batch foaming of samples initially saturated at various temperatures. Finally, the characterizations of density and cellular morphology of foamed samples are presented. Micrographs of uniform nanocellular structure with an average cell size of 20 – 30 nm in PC are shown.

5.3 Experimental

5.3.1 Materials

Large MAKROLON® GP polycarbonate sheets from Bayer MaterialScience LLC with a thickness of 0.80 mm were purchased. Sheets were cut into 2.5 cm × 2.5 cm samples for sorption and foaming studies. The PC has a density of 1.2 g/cm^3. Glass transition temperature (T_g) was measured to be 147 ℃ in differential scanning calorimeter (DSC) TA Instruments Q20, with a heating rate of 10^{o}C/min. T_g was determined using the half-height method. Medical grade CO_2 (99.9% purity) was purchased from Praxair, Inc.

5.3.2 Sorption

Sorption experiments were conducted by placing samples in a pressure vessel, with the CO_2 pressure inside maintained at 5 MPa with an accuracy of +/- 0.1 MPa. In order to maximize CO_2 sorption in polymer and eliminate the need of a pressure boosting device, we chose 5 MPa as the saturation pressure, which was slightly below the pressure of a full CO_2 gas cylinder. Saturation temperatures (T_{sat}) varied over a wide range from -30 ℃ to 80 ℃. For sorption experiment above room temperature, a heating jacket wrapped around the pressure vessel and a temperature controller was used to maintain the pressure vessel at a desired temperature. For low temperature sorption conditions (below 0 ℃), the pressure vessel was placed in a freezer capable of achieving -30 ℃ to 0 ℃. During saturation, samples were periodically taken out from the pressure vessel, and immediately (~ 1 min) weighed on a Mettler AE240 analytical scale accurate to +/- 10 μg. Samples were then promptly put back to the pressure vessel and repressurized. The sorption experiment continued until no further weight increase was observed in the specimen.

5.3.3 Foaming

Specimens used for foaming studies were first wrapped in porous paper towel, and then placed in a pressure vessel which was maintained at 5 MPa. Saturation temperatures selected for foaming studies were 40 ℃, 20 ℃, 0 ℃, -20 ℃, and -30 ℃. Samples were allowed to absorb CO_2 over a predetermined amount of time (based on sorption studies). After full saturation, samples were removed from the pressure vessel, and immediately immersed in a silicone oil bath (Thermo Haake B5) set at a desired foaming temperature (T_f). The foaming time used for all samples was 1 minute. After foaming, the sample was immediately quenched in an oil bath which was kept much colder than the foaming oil bath, to stop further foaming.

5.3.4 Characterization

The excess silicone oil was removed from the surface of the sample before any characterization. The density of each sample was determined according to ASTM D792 using Mettler AE240 analytical scale. Samples were allowed to desorb for at least one week before density measurement was performed in order to eliminate the effect of residual CO_2. Three measurements were performed for each sample, with a typical standard deviation of relative density about 0.2%. Solid skin on the edge of the foam was kept for the density measurement. The skin thickness was very small, on the order of 20 μm, due to very short desorption time. The calculated density of the foamed part is only about 4% smaller than bulk density, and thus the skin effect on density is negligible.

A representative set of samples were imaged with a scanning electron microscope (SEM) to examine the microstructures produced. All images were taken on a FEI Sirion SEM. Samples were first scored with a razor blade and freeze fractured with liquid nitrogen to expose the cross section. They were then coated with Au/Pd for 90 s at a current of 18 mA. Micrographs were taken at the center of the cross section of the specimen and analyzed using software ImageJ (National Institute of Health, USA). Average cell size was calculated by taking average cell diameters of at least 50 cells in the SEM micrographs. Cell nucleation density (number of cells nucleated per cubic centimeter of the unfoamed sample) was calculated using a procedure described by Kumar et al. [5].

5.4 **Results and Discussions**

5.4.1 **Solubility**

All sorption experiments were conducted at a saturation pressure of 5 MPa. Figure 5.2 shows the CO_2 uptake as a function of time at various saturation temperatures (T_{sat}). CO_2 uptake is expressed as a percentage of the original polymer mass, e.g. 10% CO_2 concentration means that 10% of the mass of original PC is now absorbed into the PC. We can see that the saturation time, time needed to reach the point where sample weight doesn't change any more, increases as the saturation temperature decreases, from 12 hrs at 40 ℃ to 72 hrs at -30 ℃.

Note that there was a short interval between the pressure release and weight measurement in the sorption experiment. Consequently, some amount of gas lost in this interval. The desorption of gas follows the one-dimensional Fickian diffusion equation [29]:

$$M_t = M_e\,[1 - \frac{4}{L}\left(\frac{Dt}{\pi}\right)^{0.5}] \tag{1}$$

where M_t is the amount of gas remained in polymer at time t, M_e is the equilibrium concentration without any desorption (or solubility), D is the diffusivity, and L is the polymer thickness.

Gas concentration values M_t were plotted versus the normalized square root of desorption time. The solubility of CO_2 in the samples can be obtained by linearly extrapolating the desorption curve to the zero desorption time. Figure 5.3 shows an example of the extrapolation of solubility value from the desorption of CO_2 in PC that were saturated at 10 ℃. The intercept of the linear fit line with Y-axis is the solubility value.

Solubility and estimated saturation time results for a wider range of temperatures are also summarized in Table 5.1. To better visualize the solubility trend, we plotted the solubility as a function of temperature in Figure 5.4 (a). It can be seen that the temperature markedly affects the solubility of CO_2 in PC. The solubility increases as the saturation temperature decreases in the whole range, approximately 5 times increase from 4% at 80 ℃ to 20.4% at -30 ℃. And 20.4% is the highest CO_2 concentration ever reported for PC. As will be revealed later, the much higher solubility at the low saturation temperature is critical for creating nanometric cells in the PC.

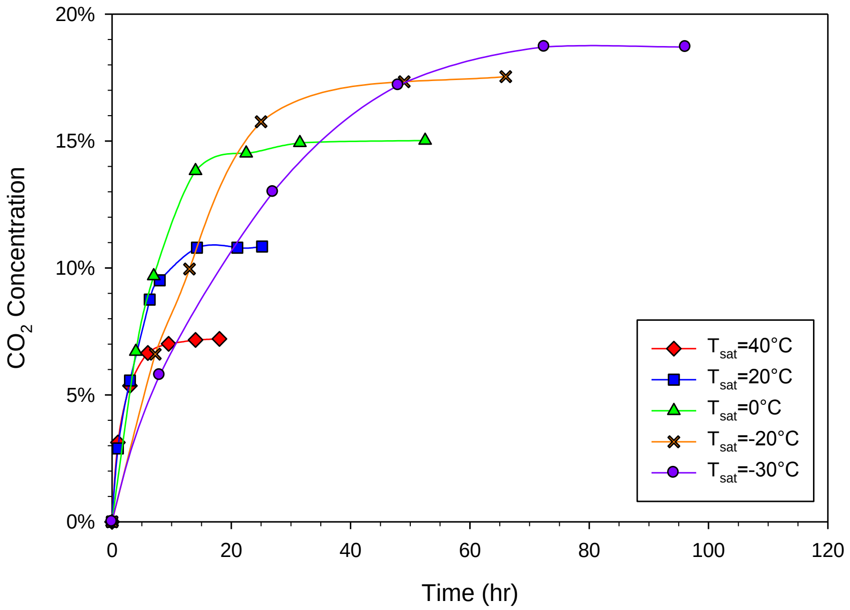

Figure 5.2 CO_2 uptake as a function of time at various saturation temperatures T_{sat}. Sample thickness was 0.80 mm.

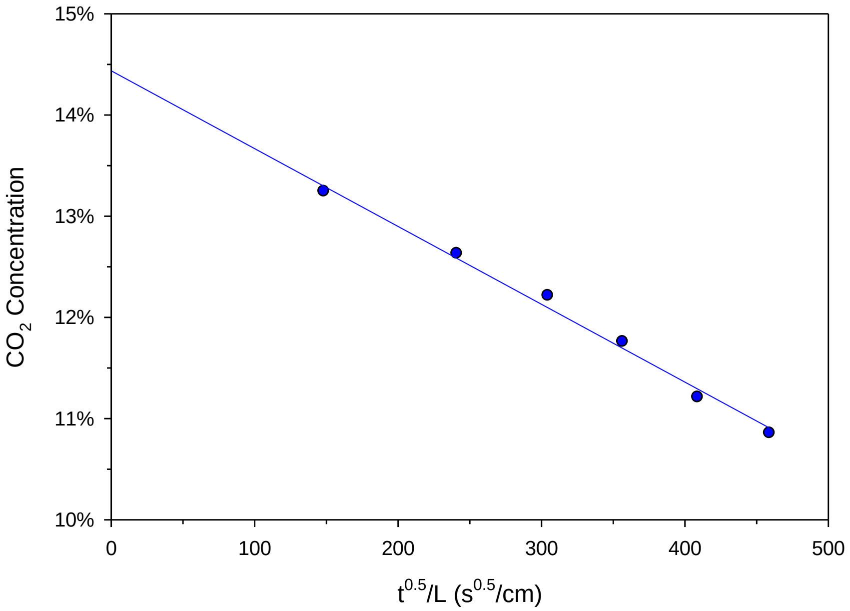

Figure 5.3 Desorption CO_2 from PC after being fully saturated at 10 ℃ and 5 MPa. A linear fit line is drawn to show the extrapolated value at t=0.

Table 5.1 Summary of solubility, diffusivity, and estimated saturation time at various saturation temperatures.

Saturation Temperature (T_{sat}) (℃)	Solubility (S)	Diffusivity (D) (cm^2/s)	Saturation Time (t_{sat}) (hr)*
80	4.0%	1.60×10^{-7}	3
60	5.5%	9.93×10^{-8}	8
40	7.8%	6.45×10^{-8}	12
20	12.1%	3.58×10^{-8}	14
15	13.3%	3.38×10^{-8}	15
10	14.4%	3.09×10^{-8}	17
0	15.9%	2.13×10^{-8}	22
-10	17.4%	1.36×10^{-8}	36
-20	18.9%	8.33×10^{-9}	49
-30	20.4%	6.36×10^{-9}	72

*for sample thickness 0.80 mm.

The temperature dependence of solubility is typically given by Arrhenius equation [30, 31],

$$S = S_0 \exp\left(-\frac{\Delta H_S}{RT}\right) \tag{2}$$

where S_0 is the pre-exponential factor, ΔH_S is the heat of sorption or enthalpy change upon solution of gas in the polymer, and R is gas constant.

Figure 5.4 (b), we plotted the natural logarithm of solubility as a function of the reciprocal of saturation temperature. Note the X-axis is 1000/T and T is in Kelvin. We can see two straight best-fit lines, together with a turning point of 15 ℃ at which the slope of the two straight lines changes. The 15 ℃ turning point coincides with the phase change temperature for CO_2 at 5 MPa. Below and above this phase changing temperature, the data follows a linear trend: below 15 °C, ΔH_S is calculated to be -5.4 kJ/mol; above 15 °C, ΔH_S is -15.7 kJ/mol. Negative heat of sorption values indicate the exothermic nature of CO_2 sorption in PC.

The difference between these two ΔH_S values is 10.3 kJ/mol. This value is essentially the same as the heat of condensation (or heat of vaporization) of CO_2, which is about 11.3 kJ/mol [32]. To explain the result, we can view the absorption of gaseous CO_2 into polymer hypothetically as follows: gaseous CO_2 first condense into CO_2 liquid at a constant temperature, which release an amount of energy equal to the heat of condensation 11.3 kJ/mol; then 5.4 kJ/mol heat is released from the absorption of CO_2 liquid into polymer; thus the net heat of sorption of gaseous CO_2 into polymer is -16.7 kJ/mol, very close to experimental data -15.7 kJ/mol.

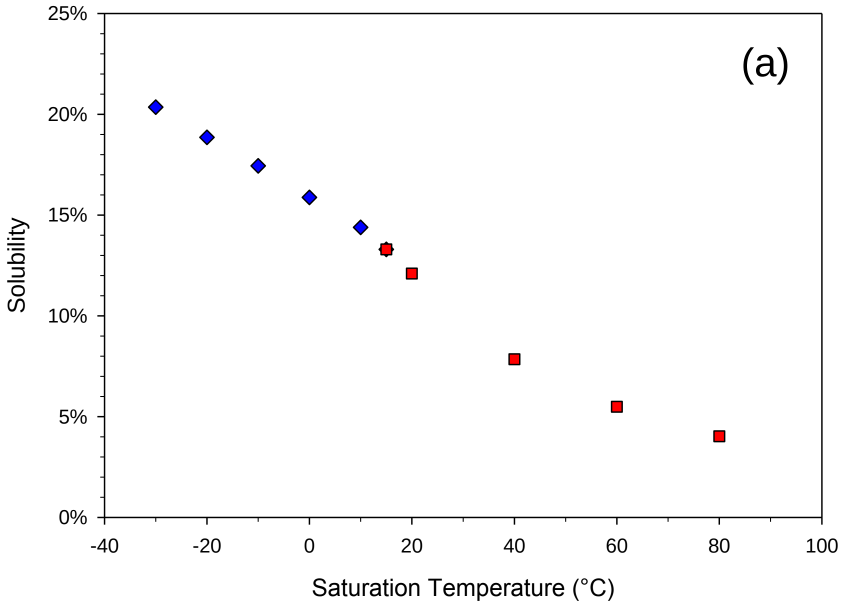

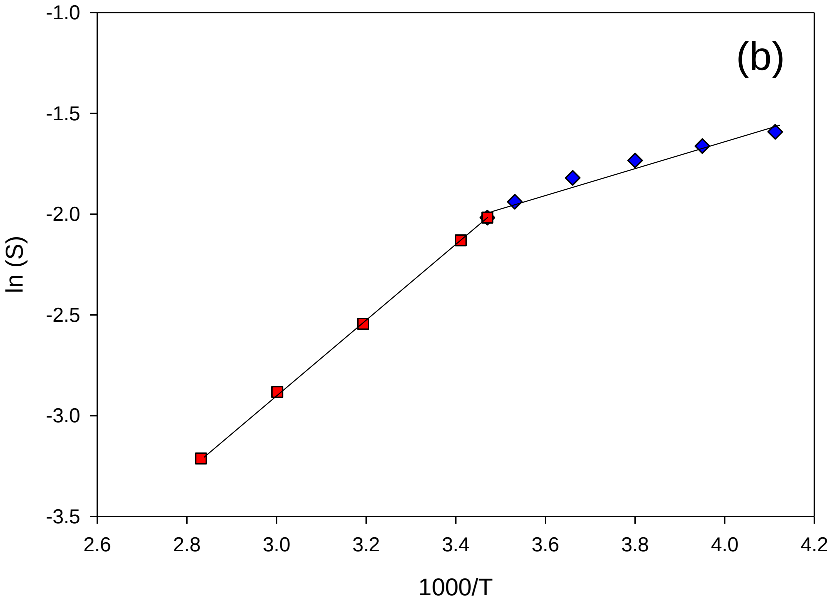

Figure 5.4 (a) solubility of CO_2 in PC as a function of saturation temperature; (b) natural logarithm of solubility as a function of reciprocal of saturation temperature with best-fit lines. Red squares – gaseous CO_2 and blue diamonds - liquid CO_2. Note the change in slope when CO_2 changes from gas to liquid at 15 ℃.

5.4.2 **Diffusivity**

One of the commonly used methods to determine diffusivity from a sorption plot is the initial slope method, which uses the slope of the initial part of a normalized sorption plot. At sufficiently short sorption times, the total mass uptake of penetrant in thin sheets can be described by [29]

$$\frac{M_t}{M_e} = \frac{4}{L}\left(\frac{Dt}{\pi}\right)^{0.5} \tag{3}$$

where M_t is the amount of gas absorbed into polymer at time t, M_e is the equilibrium gas concentration without any desorption (or solubility), D is the diffusivity, and L is the polymer thickness. Diffusivity can then be calculated from the slope R of the early part of M_t/M_e vs $t^{0.5}/L$ plots

$$D = \frac{\pi R^2}{16} \tag{4}$$

In Figure 5.5, we have plotted the early part of the CO_2 uptake curves from Figure 5.2 with the time axis normalized for thickness, in units of ($t^{0.5}/L$), where t is in seconds and L is in cm. From the slopes, we can obtain sorption diffusivities of CO_2 in PC at various temperatures using Eqn. (19).

Using this method, we've obtained the sorption diffusivities at various saturation temperatures and summarized them in Table 5.1. We can see that temperature has a profound effect on the diffusivity in PC-CO_2 system. Diffusivity decreases with the decreasing saturation temperature, nearly two orders of magnitude reduction from 1.60×10^{-7} cm^2/s at 80 ℃ down to 6.36×10^{-9} cm^2/s at -30 ℃.

The effect of temperature on the diffusivity of gas in polymers was first shown by Barrer [33] and later confirmed by others [30, 31] to be that of an activated process obeying the Arrhenius relationship:

$$D = D_0 \exp\left(-\frac{\Delta H_D}{RT}\right) \tag{5}$$

where D_0 is the pre-exponential factor, ΔH_D is the activation energy for diffusion, R is gas constant and T is temperature in K.

In Figure 5.6, we have plotted natural logarithm of sorption diffusivities in Table 5.1 as a function of the reciprocal of saturation temperature. The data follows a linear trend and the ΔH_D value obtained from the slope is 21.1 kJ/mol for PC-CO_2. In our PC-CO_2 system, a monotonic increase of diffusivity with increasing sorption temperature is observed, suggesting that in the temperature range investigated PC-CO_2 doesn't have the retrograde vitrification behavior observed in PMMA-CO_2 [31]. Also, our results suggest that phase change of CO_2 from gas to liquid, or vice versa, at around 15 ℃ doesn't bring any significant change to ΔH_D.

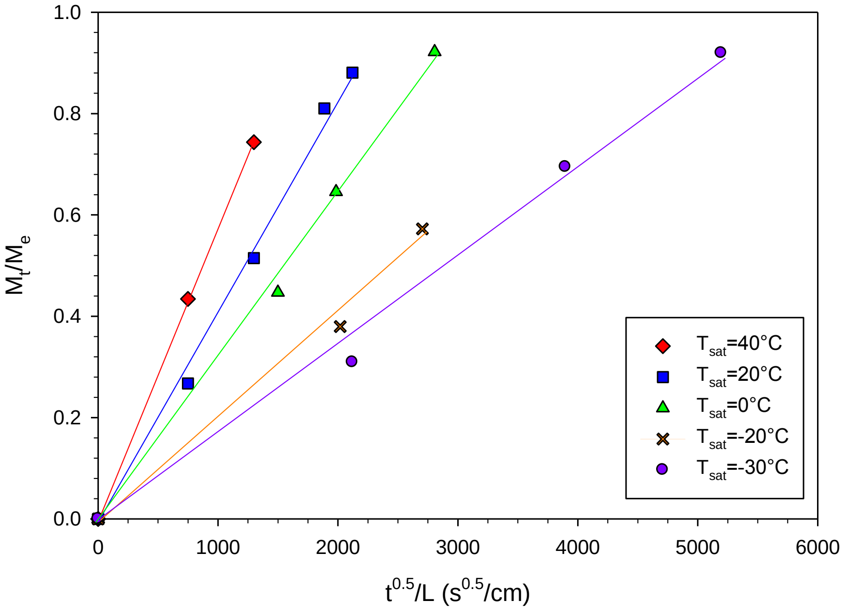

Figure 5.5 Early parts of CO_2 uptake curves with time axis normalized for thickness

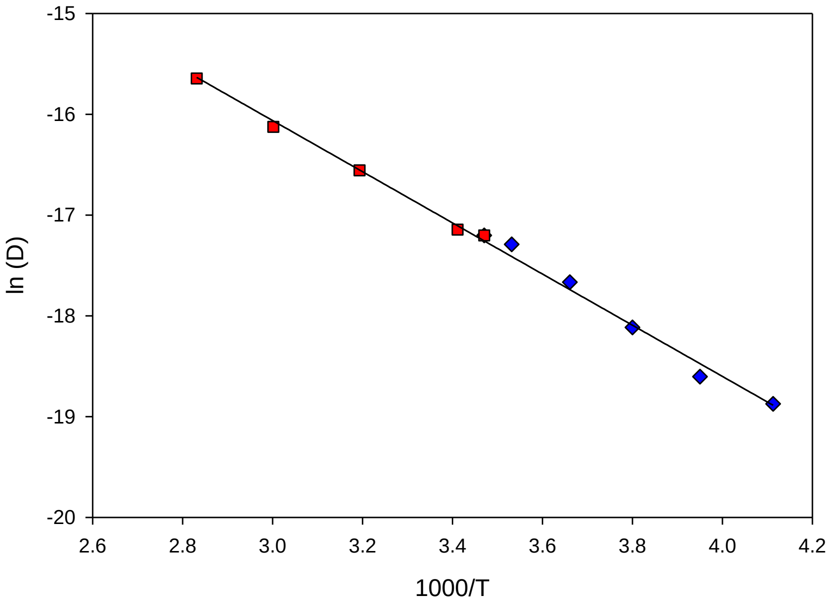

Figure 5.6 Diffusivity of CO_2 in PC at various temperatures and 5 MPa pressure. Red squares represent data points when CO_2 is gaseous, whereas blue diamonds for liquid CO_2. The best-fit line for all data points is also shown.

5.4.3 **Glass Transition Temperature Depression**

Absorption of diluent into a polymer lowers its glass transition temperature, because the diluent molecules increase polymer intermolecular distance, decreasing intermolecular interactions. The weakening of these interactions increases the segmental mobility, which leads to a lower glass transition temperature. CO_2 has very high plasticization effect and can significantly reduce T_g to a value much lower than that of the original polymer. This is one of the primary driving mechanisms in solid-state microcellular foaming. Therefore, knowledge of T_g of the polymer-diluent mixture is very important to understand and control the foaming process.

The measurement of T_g of polymer-diluent system presents great challenge, since diffusion and cell nucleation must be avoided during heating scan in regular DSC measurement. Previous studies suggested that the minimum foaming temperature and T_g of polymer-diluent system can be considered to be equivalent [34, 35]. In our study, saturated samples were foamed at increasingly higher foaming temperatures while keeping all other processing parameters the same. The minimum foaming temperature was determined as the average value of the two adjacent temperature at which foaming just did and did not happen. In addition, SEM images of these samples were prepared to confirm the formation of cells. The temperature interval of the two adjacent foaming temperatures was 5 ℃.

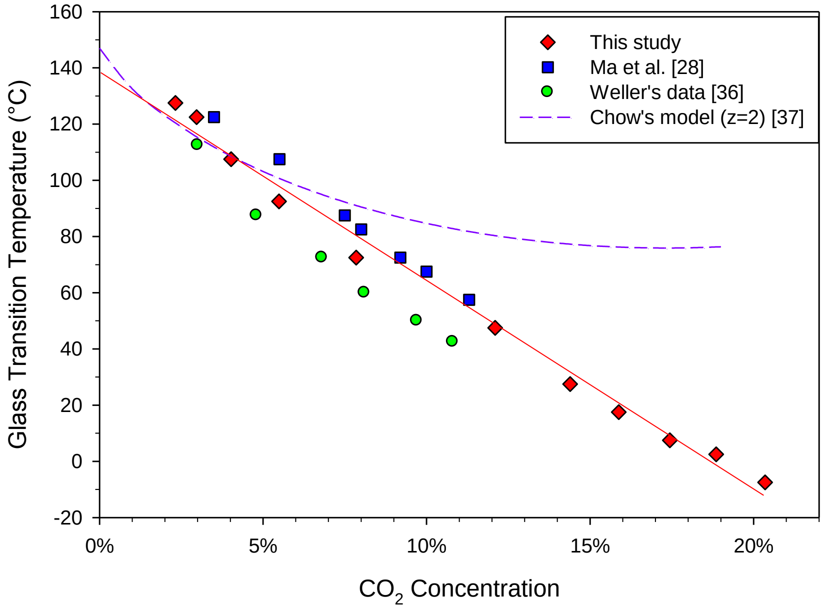

Figure 5.7 Glass transition temperature of PC as a function of CO_2 concentration. Experimental data and the best-fit line from this study and also data from Weller and Ma et al. are shown. The curve represents Chow's model prediction with z=2.

Figure 5.7 shows the T_g of PC-CO_2 mixture as a function of CO_2 solubility. We can see that CO_2 absorbed in the PC causes a significant T_g reduction; the T_g decreases down to -7.5 ℃ at 20.4% CO_2. In addition, a linear relationship between the T_g and solubility can be observed, and a 1% solubility increase results in an approximately 7.4 ℃ decrease in T_g. The intercept of a least-squares fit with y-axis (namely, when solubility is 0) corresponds to 138 ℃, which is close to the T_g (147 ℃) of unsaturated PC obtained by DSC. Weller [36] reported the T_g of PC-CO_2 up to 11% concentration and his data are close to our values. Ma et al. [28] reported the T_g of PC-CO_2 up to 12% concentration, and the reported T_g from his study is always higher than our experimental data at a similar concentration. This could be due to differences in the PC used. Nevertheless, both studies show a linear relationship and the best-fit lines are essentially parallel to each other. Similar linear relationships between T_g and solubility have also been observed in PEI, PES, PSU, and COC [23, 35].

In a previous study, Chow [37] developed a model to predict the T_g of polymer/diluent mixture using statistical mechanics. The comparison between predicted values from Chow's model and experimental data is shown in Figure 5.7. Parameters used are heat capacity associated with the glass transition ΔC_p=0.245 J $K^{-1}g^{-1}$ and lattice coordination number z=2 for PC as suggested by Chious et al. [38]. It's obvious from the graph that Chow's model cannot accurately predict T_g of PC-CO_2 mixture, especially at the high solubility range.

5.4.4 **Relative Density of Foams**

One of the most important properties of foams is the relative density, which is defined as density of foam divided by density of unsaturated polymer. Figure 5.8 shows the relative density of foamed samples as a function of foaming temperature. These samples were initially saturated at 5 MPa and at different temperatures T_{sat}, ranging from -30 ℃ to 40 ℃. The relative density-foaming temperature plot provides guidelines for creating foams of desired densities. We can see relative densities of as low as 15% in 40 ℃ saturated samples and 38% in -30 ℃ saturated samples can be produced. Also, as the foaming temperature increases, the relative density reduces due to enhanced cell nucleation and cell growth, and the rate of reduction is higher for samples saturated at higher temperatures indicated by their larger slopes.

For 0 ℃, 20 ℃ and 40 ℃ saturation temperatures, relative densities of foams decrease steadily as the foaming temperature increases in the range (up to 150 ℃) investigated. For -20 ℃ case, relative densities firstly decrease to a minimum at 130 ℃ foaming condition, and then increase at higher temperatures. Similarly, for -30 ℃ case, relative densities firstly decrease to around 40% in the range of 100 ℃ - 120 ℃, and then rapidly increase at successively higher temperatures. The reason for the increase of relative densities at higher temperatures is that at these higher temperatures, the very low viscosity and fast gas diffusion caused bubble coalescence and/or collapse, which was manifested in the severe blistering and shrinkage of the sample during foaming.

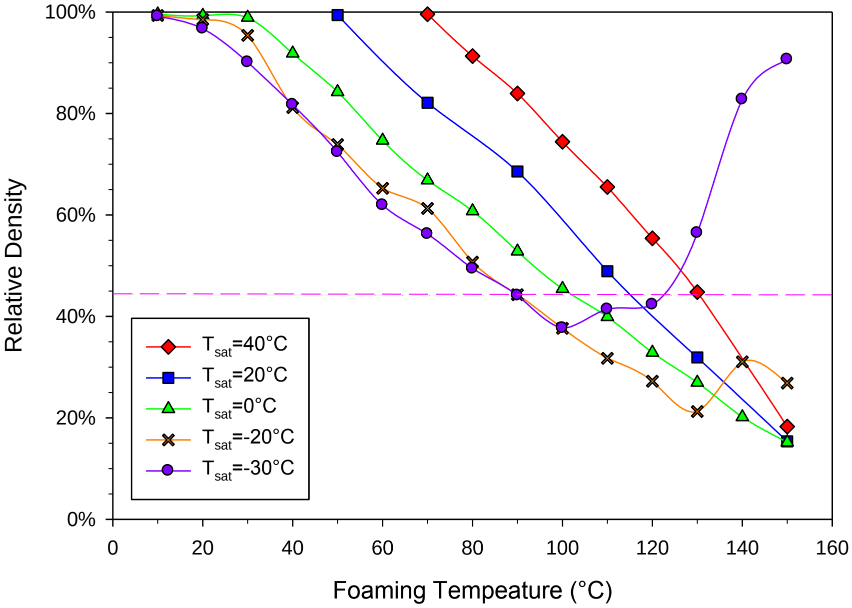

Figure 5.8 Relative density as a function of foaming temperature for samples initially saturated at various temperatures.

In addition, if we were to draw a horizontal line in the relative density plot, we can find different processing conditions to produce foams of same relative density. In the graph, a 44% relative density line is draw. To achieve this relative density, samples can be prepared by saturating at 40 ℃ and then foaming at 130 ℃ (sample #6), or by saturating at -30 ℃ and foaming at 90 ℃ (sample #23). The cellular morphologies of these two samples are very different. Sample #4 has a cell size of 12 μm, but sample #23 has a cell size of 28 nm, about 400 times smaller. Micrographs of these two samples are shown in Figure 5.9. The ability to produce foams with similar densities but vastly different cell sizes enables us to investigate cell size effect on foams properties.

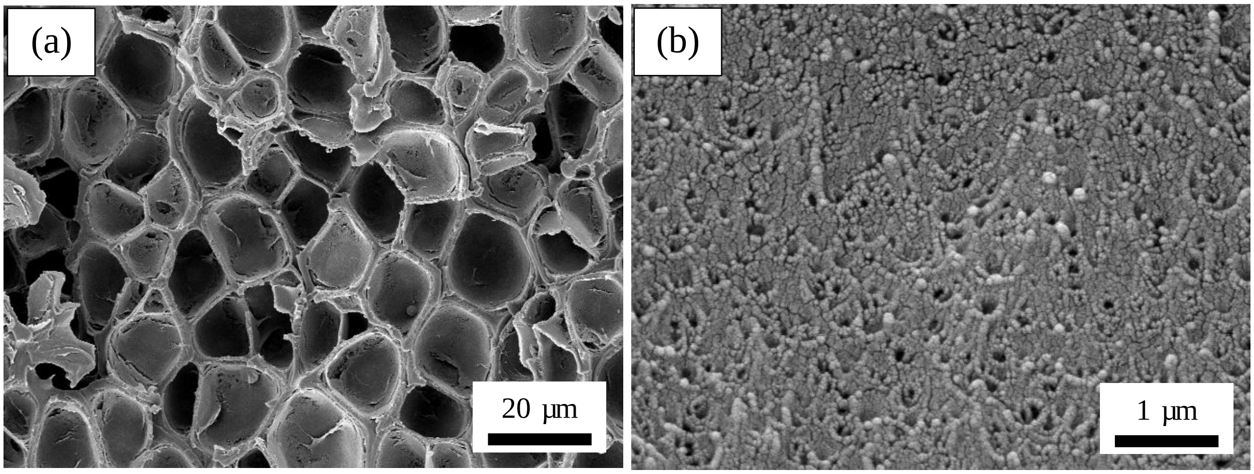

Figure 5.9 Example of microcellular and nanocellular foams with a similar density: (a) sample #6 with a relative density of 44.8% and cell size 12 µm; (b) sample #23 with a relative density of 44.1% and cell size 28 nm. The cell sizes differ by three orders of magnitude.

5.4.5 **Cellular Morphology of Foams**

5.4.5.1 Cell Nucleation Density and Average Cell Size

Representative samples were imaged by SEM to characterize the cellular structure resulting from various processing conditions. Main cellular structure characteristics investigated were average cell size and cell nucleation density. Table 5.2 summarizes the processing conditions and characteristics of the foams selected for cellular morphology investigation. The relative density, cell nucleation density and average cell size are listed. Figure 5.10 shows cell nucleation density as a function of foaming temperature for foamed samples saturated at different temperatures T_{sat}. We can see that a lower saturation temperature (thus higher CO_2 concentration from Table 5.1) results in a higher cell nucleation density. For example, the cell nucleation densities have seven orders of magnitude increase from about 10^8 cells/cm^3 for 40 ℃ samples (7.8% CO_2 concentration) to around 10^{15} cells/cm^3 for -30 ℃ samples (20.4% CO_2 concentration). Also, we can observe that the cell nucleation density is essentially not influenced by foaming temperature for saturation temperature of 0 ℃ and higher; for lower saturation temperature, approximately two orders of magnitude increase are observed over the foaming temperature range explored.

Table 5.2 Summary of processing conditions and foam characteristics.

Sample #	Saturation temperature (℃)	CO_2 concentration	Foaming temperature (℃)	Foam density (g/cm^3)	Relative density	Cell nucleation density ($cells/cm^3$)	Average cell size (μm)
1	40	7.8%	80	1.10	91.3%	2.9×10^8	7.1
2	40	7.8%	90	1.01	83.9%	4.9×10^8	8.1
3	40	7.8%	100	0.89	74.4%	6.3×10^8	8.5
4	40	7.8%	110	0.79	65.5%	7.0×10^8	9.4
5	40	7.8%	120	0.66	55.4%	6.6×10^8	10.9
6	40	7.8%	130	0.54	44.8%	6.4×10^8	12.1
7	20	12.1%	70	0.99	82.1%	4.2×10^9	3.5
8	20	12.1%	90	0.82	68.5%	6.7×10^9	4.2
9	20	12.1%	110	0.59	48.9%	8.5×10^9	4.9
10	20	12.1%	130	0.38	31.9%	6.4×10^9	6.7
11	0	15.9%	50	1.01	84.3%	2.2×10^{10}	1.1
12	0	15.9%	70	0.80	66.8%	3.8×10^{10}	1.6
13	0	15.9%	90	0.63	52.8%	3.6×10^{10}	1.7
14	0	15.9%	110	0.48	39.9%	2.8×10^{11}	1.2
15	0	15.9%	130	0.32	27.0%	1.2×10^{11}	2.2
16	-20	18.9%	50	0.89	73.9%	2.5×10^{11}	0.779
17	-20	18.9%	70	0.74	61.3%	3.6×10^{12}	0.317
18	-20	18.9%	90	0.53	44.3%	1.9×10^{13}	0.136
19	-20	18.9%	110	0.38	31.7%	3.6×10^{13}	0.201
20	-30	20.4%	60	0.74	61.9%	2.7×10^{13}	0.023
21	-30	20.4%	70	0.67	56.2%	4.1×10^{14}	0.021
22	-30	20.4%	80	0.59	49.4%	6.7×10^{14}	0.029
23	-30	20.4%	90	0.53	44.1%	8.1×10^{14}	0.028
24	-30	20.4%	100	0.45	37.7%	1.3×10^{15}	0.029
25	-30	20.4%	110	0.50	41.4%	2.0×10^{15}	0.031

Figure 5.11 shows average cell size as a function of foaming temperature for foamed samples saturated at different temperatures T_{sat}. A higher CO_2 concentration at lower saturation temperature leads to a smaller cell size, with about 500 times difference between the smallest and largest cells. For 0 ℃, 20 ℃, and 40 ℃ saturated samples, cell sizes are in the range of 1-10 μm. These are typical microcellular foams.

However, for -20 ℃ and -30 ℃ saturated samples, cell sizes fall well below 1 μm into the nanocellular region. For -30 ℃ samples, cell size is only about 20-30 nm, which is the smallest cell size ever reported in PC. Figure 5.12 and Figure 5.13 show SEM images of samples initially saturated at different temperatures and subsequently foamed at the same temperatures, 90 ℃ and 110 ℃, respectively.

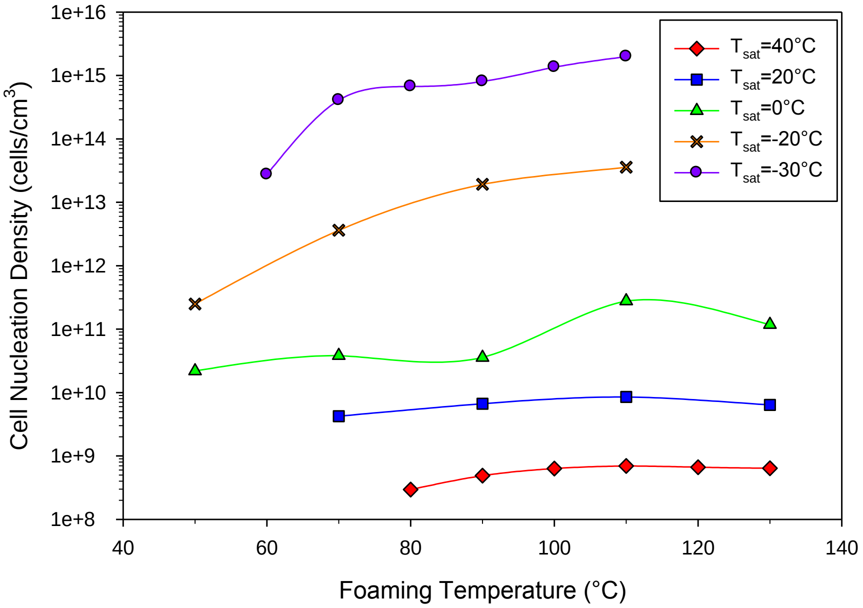

Figure 5.10 Cell nucleation density as a function of foaming temperature for foamed samples saturated at different temperatures.

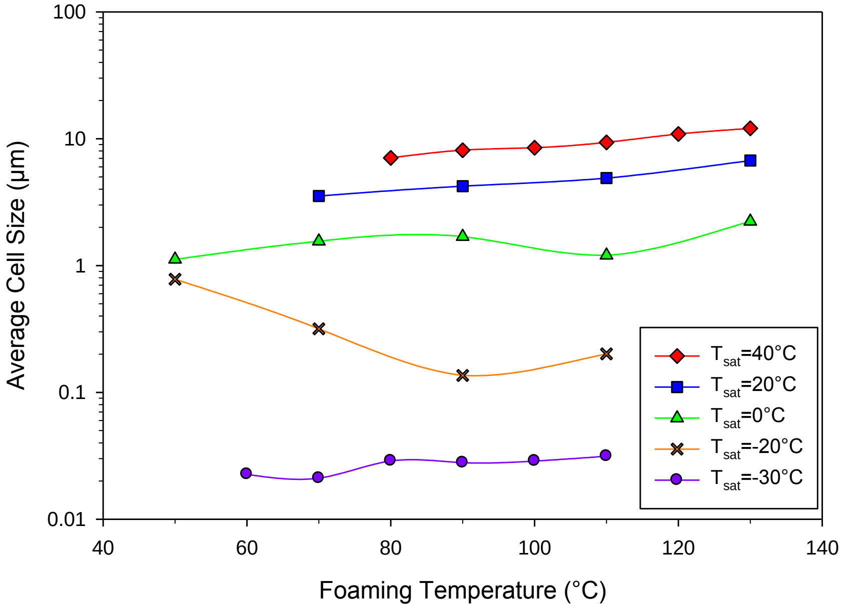

Figure 5.11 Average cell size as a function of foaming temperature for foamed samples saturated at different temperatures.

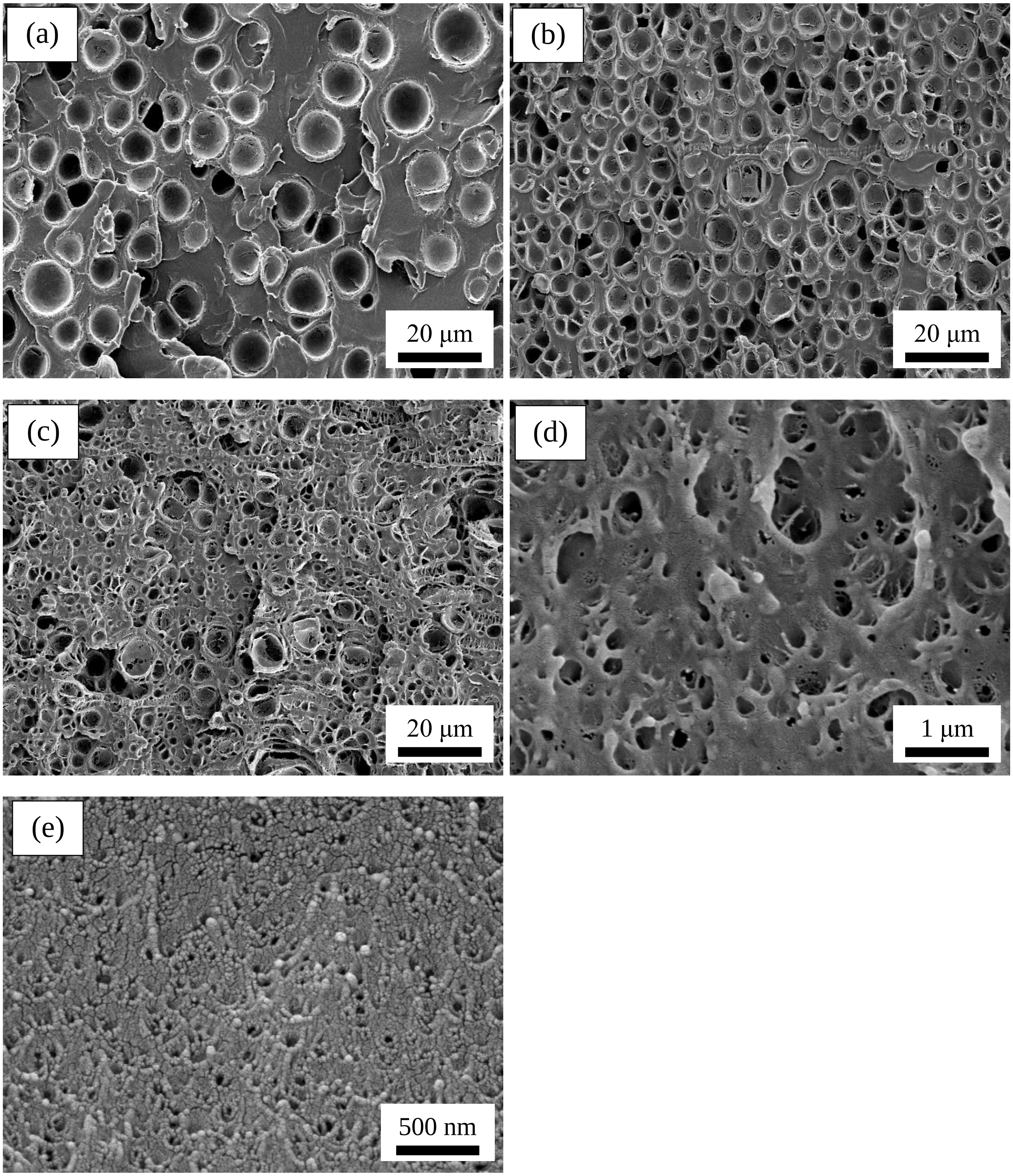

Figure 5.12 SEM micrographs of PC foams (a) sample #2, 8.1 μm, (b) sample #8, 4.2 μm, (c) sample #13, 1.7 μm, (d) sample #18, 136 nm, and (e) sample #23, 28 nm. All samples were foamed at 90 ℃. Notice the scale bars of the images are different.

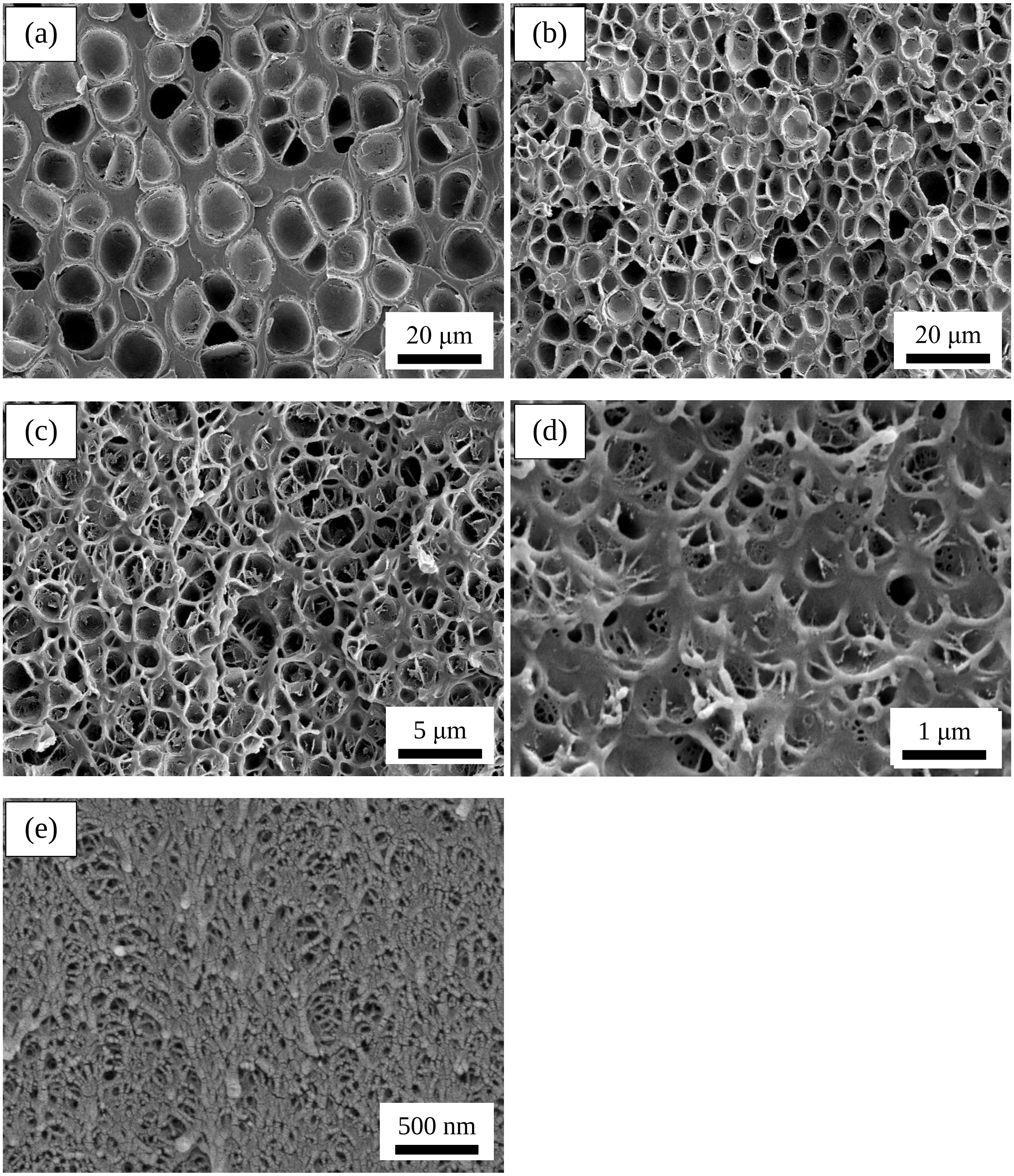

Figure 5.13 SEM micrographs of PC foams (a) sample #4, 9.4 μm, (b) sample #9, 4.9 μm, (c) sample #14, 1.2 μm, (d) sample #19, 201 nm, and (e) sample #25, 31 nm. All samples were foamed at 110 ℃. Notice the scale bars of the images are different.

5.4.5.2 Processing Window for Nanofoams

To better visualize how cell nucleation densities evolve as CO_2 concentration increases, we have plotted the cell nucleation densities at various saturation temperatures (T_{sat}) as a function of CO_2 concentration in Figure 5.14. For 7.8% - 15.9% CO_2 concentration range, cell nucleation density exponentially increases with CO_2 concentration; foamed samples show microcellular morphology. However, above 15.9% and up to 20.4%, the exponential increase of cell nucleation density is more significant (as can be seen from the much larger slope of the straight line), resulting in nanocellular morphology. In this range, a 1% - 2% increase in CO_2 concentration brings about two orders of magnitude increase in cell nucleation density, compared to only one order of magnitude increase in cell nucleation density for a 3% - 4% increase in CO_2 concentration when the CO_2 concentration is below 15.9%. Therefore, it's evident that there exists a critical CO_2 concentration, above which microcellular foams turns into nanocellullar foam, and this critical concentration for PC is between 15.9% and 18.9%. Change of cell size with CO_2 concentration can be clearly seen in Figure 5.15. In the plot, at each T_{sat}, cell sizes of foams produced from different foaming temperatures are included. There is a sudden change in the slope of the cell size vs CO_2 concentration at the critical concentration. A much more rapid decrease of cell size occurs beyond the critical concentration and the cell size falls to below 100 nm.

Critical concentrations for creating nanofoams have also been reported previously in other amorphous polymers. Krause et al. [23] reported a critical CO_2 concentration of 47-49 cm^3 CO_2 / cm^3 polymer (or equivalently 7.2-7.5%) for both PEI and PES thin films, and similarly, Miller et al. [24] found the critical CO_2 concentration to be 9.4%-11% for PEI sheets. The different critical CO_2 concentrations in PC, PEI and PES indicate that the critical CO_2 concentration is polymer dependent. This polymer-dependence is probably due to the differences in molecular structures and properties between these polymers. One common physical property we can relate the critical CO_2 concentration to is the glass transition temperature of the virgin polymers. For virgin PC, PEI and PES, T_g is 147 ℃, 218 ℃ and 230 ℃, respectively. A higher critical CO_2 concentration in the much lower T_g PC suggests that amorphous polymers with a lower T_g might need a higher critical CO_2 concentration in order to create nanofoams.

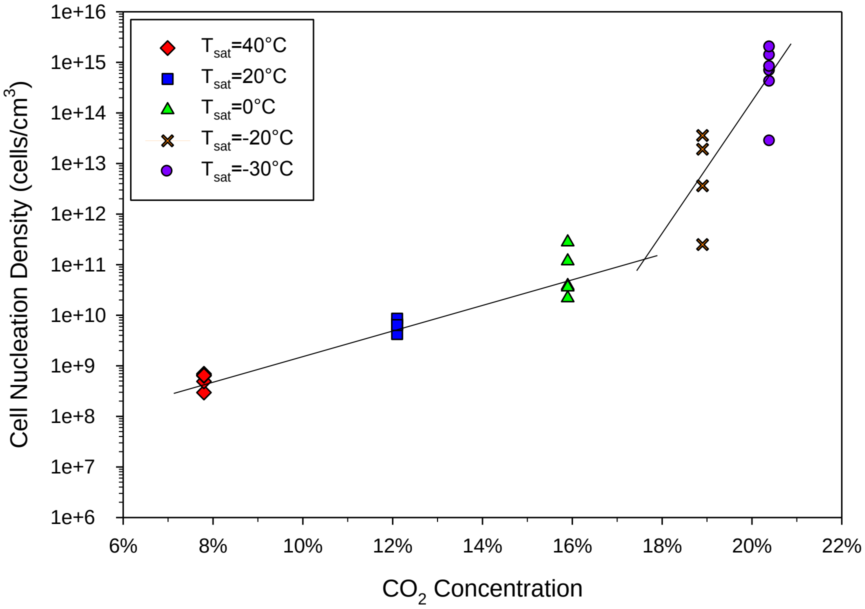

Figure 5.14 Cell nucleation density as a function of CO_2 concentration. At each T_{sat}, cell nucleation densities of foams produced from different foaming temperatures are included. Lines are drawn to show the trend. Note the more rapid increase of cell nucleation densities beyond 15.9% CO_2 concentration.

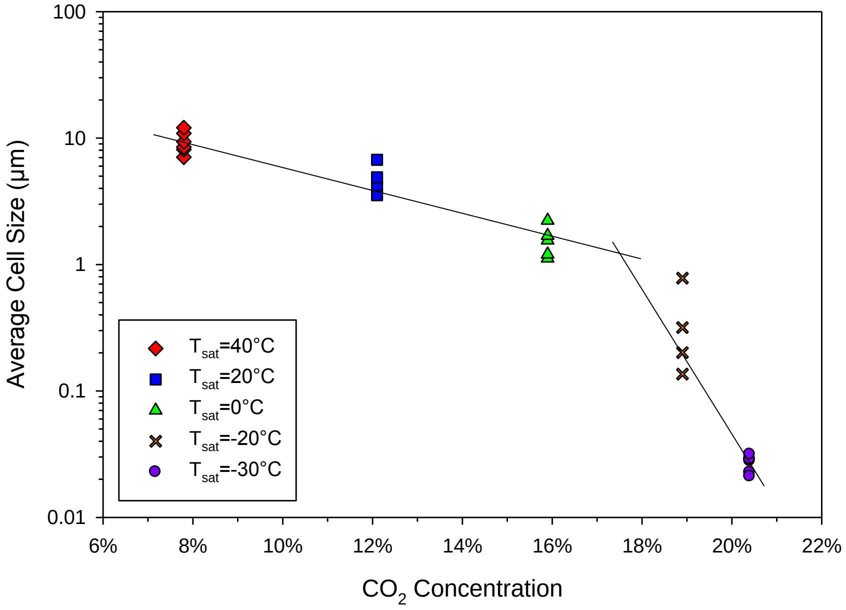

Figure 5.15 Average cell size as a function of CO_2 concentration. Lines are drawn to show the trend. Note the more rapid decrease of cell size beyond 15.9% CO_2 concentration and the cell size transitions from microscale to nanoscale.

5.4.5.3 Bicontinuous Nanoporous Structure

It appears that under certain conditions the nanocells are interconnected. A SEM of such bicontinuous nanoporous structure is shown in Figure 5.16. The sample was prepared by saturating at -30 ℃ and then foaming at 110 ℃. The relative density is 41.4%. The visible underlying struts indicate interconnectivity in the structure.

In order to verify the porous nature, a simple dye test was performed. A sample was first freeze fractured in liquid nitrogen to expose a clean cross section. Then dye/isopropanol solution was applied to the surface of this cross section for 10 minutes. Afterwards, the sample was freeze fractured again to expose the depth direction perpendicular to the cross section. Penetration of dye solution into the sample can be observed from the depth direction. For -20 ^oC saturation samples, no die penetration was observed in samples foamed up to 110 ℃; however, 130 ℃ foamed sample, die penetration was observed. Similarly, for -30 ^oC saturation samples, no die penetration was observed in samples foamed up to 100 ℃; however, 110 ℃ and 120 ℃ foamed samples, die penetration was observed. These observations indicate that sufficiently high temperatures are needed to create nanoporous structures. Krause et al. [23] also reported a change of cellular morphology from a closed cell structure to an open porous structure in PEI and PES nanofoams at higher foaming temperatures.

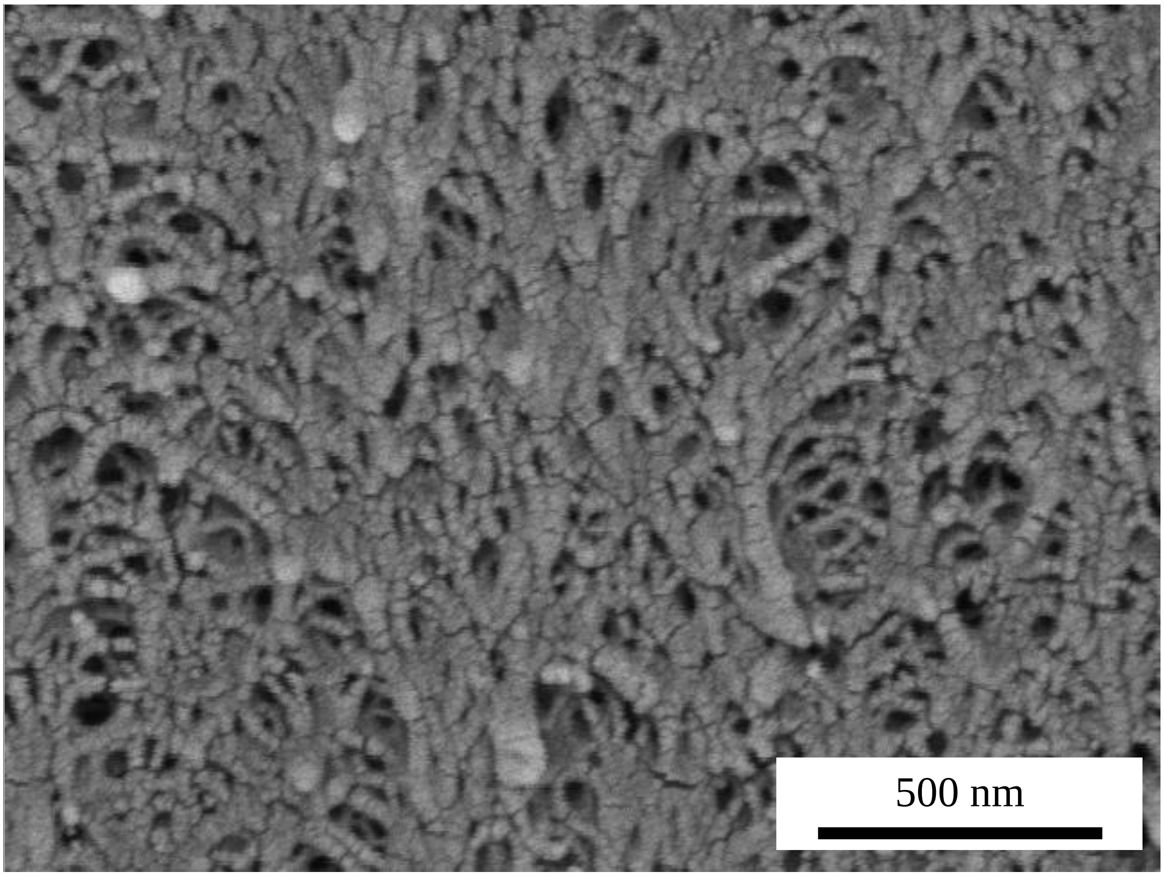

Figure 5.16 Magnified center region of Figure 5.13 (e) showing bicontinuous nanoporous structure with characteristic size about 30 nm. Magnificiation 60,000X. Note the interconnectivity in the structure as manifested by the visible underlying struts.

The phenomenon of changing from closed cell structure to open cell structure at higher foaming temperatures is interesting. From Figure 5.7, we know that T_g or minimum foaming temperature was -7.5 °C for -30 °C saturated PC sample. It's not until when the foaming temperature is 110 °C that open cellular morphology was observed. The large temperature difference (>120 °C) between T_g of saturated sample and foaming temperature results in a huge thermal instability in PC-CO_2 mixture and a large reduction in polymer viscosity. Two hypotheses are proposed to explain the morphology change. One hypothesis is based on the cell wall thinning. At high foaming temperatures, samples have relatively low viscosity and thus undergo larger expansion, resulting in lower densities. At high expansion ratio, cell walls become very thin and cells start to impinge each other. Eventually, at a sufficiently large expansion ratio, cell walls become so thin that they cannot sustain the stretching from the cell growth expansion and thus break down. As a result, cell walls disappear and cells become interconnected. Another possible mechanism is the spinodal decomposition. As opposed to the classical nucleation theory where discrete nucleation sites exist, in spinodal decomposition, the homogenous binary mixture separates into two uniform and interconnected phases: polymer rich phase and CO_2 rich phase. This phase separation results in a bicontinuous (or co-continuous) structure. These hypotheses have yet to be tested.

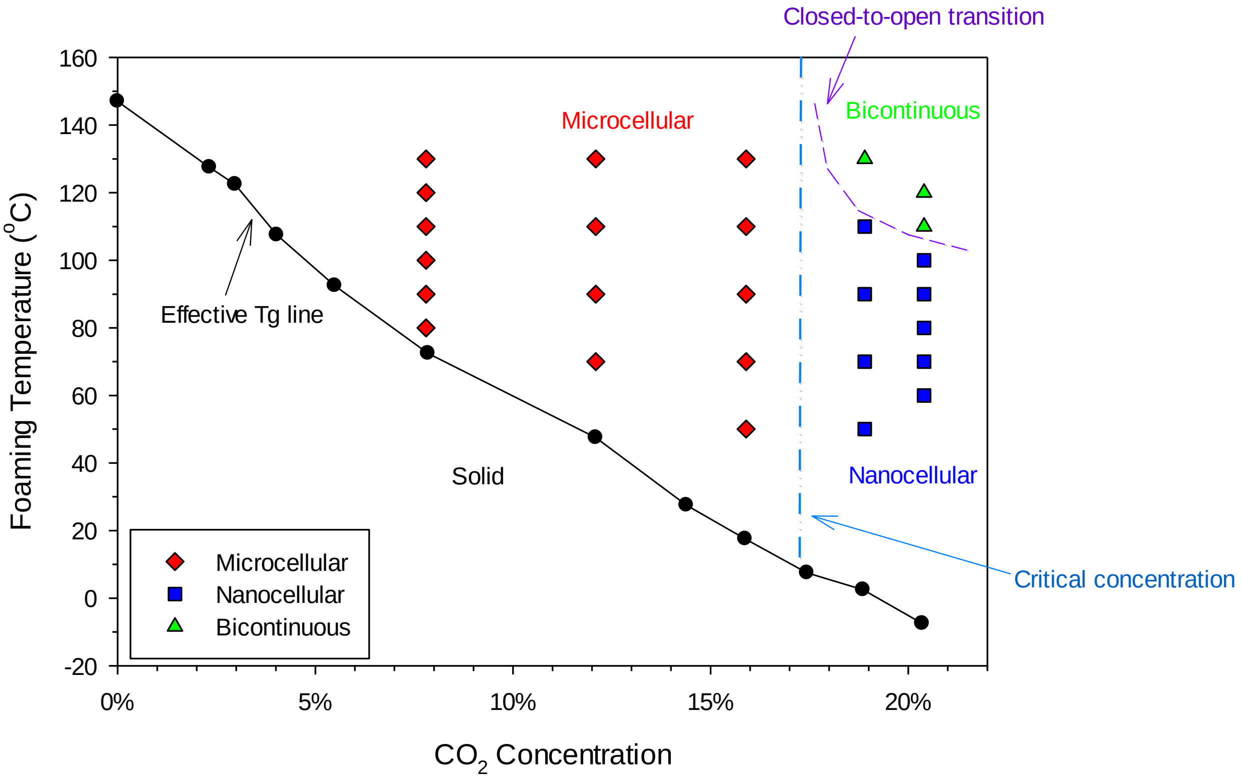

Figure 5.17 Foaming temperature - CO_2 concentration foam diagram, comprising regions of solid (S), microcellular (M), nanocellular (N), and bicontinuous nanoporous (B) structures. The effective T_g line, critical concentration line, and closed-to-open transition line are also indicated.

Figure 5.17 summarizes our results using the foaming temperature - CO_2 concentration diagram. Experimental data points from this study are shown. Four different regions are identified. Below the effective T_g line (or minimum foaming temperature line), no cellular structure is observed and samples remain solid. Above this line, either microcellular or nanocellular structure can be obtained depending on the CO_2 concentration. Below the critical concentration, microcellular foams with cell size about 1 – 10 μm are obtained, whereas above the critical concentration, nanocellular foams with cell size down to 20-30 nm are achieved. In the nanoscale region, at relatively high foaming temperature, nanocellular structures transition into bicontinuous nanoporous structures, where pores are interconnected. A line is drawn to roughly show the transition.

5.5 Summary

A low-temperature pathway to create PC nanofoams was discovered in this study. Homogenous PC nanofoams with cell size in the range of 20-30 nm, cell nucleation density over 10^{15} cells/cm^3, and relative density as low as 38% have been obtained.

The effect of saturation temperature on the solid-state foaming of PC was investigated over the range (-30 °C to 80 °C), and the resulting morphologies were characterized. Saturation temperature has significant effects on both the solubility and diffusivity. Solubility increases with decreasing saturation temperature, approximately 5 times increase from 4.0% at 80 °C to 20.4% at -30 °C. A change of heat of sorption has been found at around 15 °C, the vaporization temperature at 5 MPa for CO_2. The change of heat of sorption matches with heat of vaporization due to the vapor-liquid phase change. When CO_2 is either gas or liquid, solubility and temperature follows the Arrhenius relationship. Diffusivity decreases with decreasing saturation temperature, nearly two orders of magnitude reduction from 1.60×10^{-7} cm^2/s at 80 °C down to 6.36×10^{-9} cm^2/s at -30 °C. In contrast with solubility, diffusivity follows the Arrhenius equation with respect to temperature in the whole range (both gaseous and liquid CO_2 regions) with an activation energy of 21.1 kJ/mol.

Dissolution of CO_2 into PC dramatically plasticizes the polymer: incorporation of 20.4% CO_2 in PC decrease the T_g from 147 ℃ down to -7.5 ℃. The minimum foaming temperature, or equivalently effective T_g of mixture, shows a linear relationship with CO_2 concentration in the PC-CO_2 system.

The CO_2 concentration has a strong influence on cellular structure. As CO_2 concentration increases, cell nucleation densities increase and cell sizes reduce across the whole concentration range investigated. More importantly, we have identified a critical CO_2 concentration between 15.9% and 18.9%. Above this critical concentration, cell nucleation density increases much more rapidly with a small increase in CO_2 concentration, and consequently microcellular foams turn into nanocellular foams. The critical concentration is polymer dependent. Also, at the high CO_2 concentration (>18.9%) and a higher foaming temperature (>110 ℃), closed nanocellular foams transition into bicontinuous open nanoporous foams.

The low-temperature route to enhanced cell nucleation opens up new possibilities for creating nanofoams in thermoplastics. The ability to create cells of different length scales provides a unique opportunity to study the effect of cell size on mechanical and other properties of interest over a cell size range that spans several orders of magnitude.

5.6 **Acknowledgment**

The authors would like to acknowledge the financial support from the University of Washington CGF fund and National Science Foundation Grant CMMI 1253072. Also, we would like to thank undergraduate research assistants Varun Gupta and Ankita Sharma from IIT-Gandhinagar for their help with the experiments.

5.7 **References**

14. Martini J, Suh NP, Waldman FA. Microcellular closed cell foams and their method of manufacture. Patent #4473665. USA: Massachusetts Institute of Technology; 1984.
15. Martini J, Waldman FA, Suh NP. The production and analysis of microcellular thermoplastic foam. SPE ANTEC: vol. 28. San Francisco, CA; 1982. p. 674.
16. Kumar V, Weller JE. A process to produce microcellular PVC. International Polymer Processing 1993; 8: 73-80.

17. Murray RE, Weller J, Kumar V. Solid-state microcellular acrylonitrile-butadiene-styrene foams. Cellular Polymers 2000; 19: 413-425.
18. Kumar V, Weller JE. Production of microcellular polycarbonate using carbon dioxide for bubble nucleation. Journal of Engineering for Industry 1994; 116: 413-420.
19. Shimbo M, Higashitani I, Miyano Y. Mechanism of strength improvement of foamed plastics having fine cell. Journal of Cellular Plastics 2007; 43: 157-167.
20. Richards E, Rizvi R, Chow A, Naguib H. Biodegradable composite foams of PLA and PHBV using subcritical CO_2. Journal of Polymers and the Environment 2008; 16: 258-266.
21. Wang X, Kumar V, Li W. Low density CO_2 solid-state PLA foams. Cellular Polymers 2007; 26: 1-25.
22. Goel SK, Beckman EJ. Generation of microcellular polymers using supercritical CO_2. Cellular Polymers 1993; 12 (4): 251.
23. Miller D, Kumar V. Microcellular and nanocellular solid-state polyethermide (PEI) foams using sub-critical carbon dioxide II. Tensile and impact properties. Polymer 2011; 52 (13): 2910-2919.
24. Zhou C, Vaccaro N, Sundarram S, Li W. Fabrication and characterization of polyetherimide nanofoams using supercritical CO_2. Journal of Cellular Plastics 2012; 48 (3): 239-255.
25. Lu X, Caps R, Fricke J, Alviso CT, Pekala RW. Correlation between structure and thermal conductivity of organic aerogels. Journal of Non-crystalline Solids 1995; 188: 226-234.
26. Pinto J, Solorzano E, Rodriguez-Perez MA, de Saja JA, Dumon M. Thermal conductivity transition between microcellular and nanocellular polymeric foams: experimental validation of the Knudsen effect. Proceedings of the SPE FOAMS Conference, Barcelona, Spain (2012).
27. Lu GQ, Zhao XS. Nanoporous materials: science and engineering, London: Imperial College Press, 2004.
28. Hedrick JL, Carter KR, Cha HJ, Hawker Cj, DiPietro RA, Labadie JW, et al. High-temperature polyimide nanofoams for microelectronics applications. Reactive and Functional Polymers 1996; 30:43-53.
29. Nemoto T, Takagi J, Ohshima M. Nanocellular foams-cell structure difference between immiscible nad miscible PEEK/PEI polymer blends. Polymer Science & Engineering 2010; 50 (12): 2408-2416.
30. Nemoto T, Takagi J, Ohshima M. Control of bubble size and location in nano-/microscale cellular poly(propylene)/rubber blend foams. Macromolecular Materials and Engineering 2008; 293: 574-580.
31. Nemoto T, Takagi J, Ohshima M. Nanoscale cellular foams from a poly(propylene)-rubber blend. Macromolecular Materials and Engineering 2008; 293: 991-998.
32. Reglero Ruiz JA, Dumon M, Pinto J, Rodriguez-Perez MA. Low-density nanocellular foams produced by high-pressure carbon dioxide. Macromolecular Materials and Engineering 2011; 296: 752-759.
33. Reglero Ruiz JA, Pedros M, Tallon JM, Dumon M. Micro and nano cellular amorphous polymers (PMMA, PS) in supercritical CO2 assisted by nanostructured CO2-philic block copolymers – one step foaming. Journal of Supercritical Fluids 2011; 58: 168-176.
34. Reglero Ruiz JA, Tallon JM, Pedros M, Dumon M. Two-step micro cellular foaming of amorphous polymers in supercritical CO2. Journal of Supercritical Fluids 2011; 57: 87-94.
35. Costeux S, Zhu L. Low density thermoplastic nanofoams nucleated by nanoparticles. Polymer 2013; 54: 2785-2795.
36. Krause B, Sijbesma HJP, Munuklu P, Der Vegt Van NFA, Wessling M. Bicontinuous nanoporous polymers by carbon dioxide foaming. Macromolecules 2001; 34: 8792-8801.
37. Miller D, Kumar V. Microcellular and nanocellular solid-state polyethermide (PEI) foams using sub-critical carbon dioxide I. Processing and structure. Polymer 2009; 50: 5576-5584.
38. Cooper AI. Polymer synthesis and processing using supercritical carbon dioxide. Journal Material Chemistry. 2000; 10: 207-234.
39. Tsivintzelis I, Angelopoulou AG, Panayiotou C. Foaming of polymers with supercritical CO_2: an experimental and theoretical study. Polymer 2007; 48: 5928.
40. Collias DI, Baird DG. Impact toughening of polycarbonate by microcellular foaming. Polymer 1994; 35: 3978-83.

41. Ma Z, Zhang G, Yang Q, Shi X, Shi A. Fabrication of microcellular polycarbonate foams with unimodal or bimodal cell-size distrubtions using supercritical carbon dioxide as a blowing agent. Cellular Plastics 2014; 50 (1): 55-79.
42. Crank, J. The mathematics of diffusion. 2nd ed. New York: Oxford Science Press; 1989.
43. Crank J, Park GS. Diffusion in Polymers. London: Academic Press;1968.
44. Handa YP, Zhang Z, Wong B. Solubility, diffusivity, and retrograde vitrification in PMMA-CO_2, and development of sub-micron cellular structures. Cellular Polymers 2001; 20(1): 1-16.
45. Cengel Y, Boles M. Thermodynamics: An Engineering Approach. 7th ed. McGraw-Hill Science/Engineering/Math; 2011.
46. Barrer, RM. Nature of the diffusion process in rubber. Nature 1937; 140: 106-107.
47. Kumar V, Weller JE, Montecillo R. Microcellular PVC. ANTEC 1992; p. 1452-6.
48. Krause B, Mettinkhof R, van der Vegt NFA, Wessling M. Microcellular foaming of amorphous high-T_g polymers using carbon dioxide. Macromolecules 2001; 34: 874-884.
49. Weller, JE. The effects of processing and microstructure on the tensile behavior of microcellular foams. Ph.D dissertation. University of Washington; 1996.
50. Chow TS. Molecular interpretation of the glass transition temperature of polymer-diluent systems. Macromolecules 1980; 13: 362-364.
51. Chiou JS, Barlow JW, Paul DR. Plasticization of glassy polymers by CO_2. Journal of Applied Polymer Science 1985; 30: 2633-2642.

Chapter 6

Solid-state Poly(methyl methacrylate) (PMMA) Nanofoams. Part I: Low-temperature CO_2 Sorption, Diffusion, and the Depression in PMMA Glass Transition

6.1 **Abstract**

In this paper, we report on the solubility and diffusivity of CO_2 in PMMA in the range -30 ℃ to 100 ℃, and on the depression in the glass transition temperature when the polymer acquires an equilibrium mass% of CO_2 in this temperature range. Solubility of CO_2 in PMMA increases ten-fold from 3.9% at 100 ℃ to 39.3% at -30 °C. We observe a drop in ΔH_s, the heat of sorption, at the transition of CO_2 from vapor phase to liquid phase, leading to a weaker dependence of solubility on temperature in the liquid CO_2 regime. Four distinct diffusivity regions are identified, where diffusivity may increase or decrease with the decreasing temperature, characterized by the different activation energies. Besides the two transitions (normal vitrification and retrograde vitrification) between glassy state and rubbery state observed previously in PMMA-CO_2, we also find a new transition in the vicinity of CO_2 vaporization temperature. The dissolution of CO_2 in PMMA lowers its glass transition temperature in a non-linear fashion and the incorporation of 39.3% CO_2 in PMMA decreases its T_g from 103 ℃ to -12.5 ℃. In part II of this paper, we describe a process, based on low-temperature CO_2 saturation, that creates PMMA nanofoams with 30-40 nm cells.

Keywords: solubility; diffusivity; glass transition temperature

---

This chapter has been published in Polymer, 2015, 57: 157-163.

6.2 **Introduction**

Nanofoams are thermoplastics with nano size bubbles. In the past three decades, a number of gas-polymer systems have been studied, and foams with cell size of 100 nm and higher have been produced (see Part II of this paper for a brief review of solid-state microcellular and nanocellular foams).

The main approach to reducing cell size is based on increasing the cell nucleation density. It is well known that a higher amount of gas absorbed in the polymer leads to a higher number of cells to nucleate in a unit volume of polymer[1,2]. Thus higher CO_2 pressures have been used to reduce cell size from say 1 μm to 0.1 μm (or 100 nm). It is also known that the gas solubility in polymer increases, in general, as the saturation temperature decreases[3]. This research was undertaken to explore if the higher gas solubility at lower saturation temperature can be used to in a solid-state process[1-2, 4-5] to drive down the cell size from order 100 nm to order 10 nm. This paper addresses the solubility and diffusivity of CO_2 in PMMA at low temperatures, up to -30 °C, as well as the effect of absorbed CO_2 on the glass transition in PMMA. In Part II, we explore the process-space for solid-state foaming in PMMA-CO_2 at low temperatures, and present a processing window in which PMMA nanofoams with cells in the 30-40 nm range can be produced.

There are a number of studies on the PMMA-CO_2 system in the literature. Wissinger and Paulaitis studied sorption of CO_2 in PMMA at 32-65 °C and pressures up to 10 MPa[6,7]. Kamiya et al. investigated CO_2 sorption in PMMA in the range of 35-200 °C and pressures up to 6 MPa[8]. Shieh and Liu studied sorption and CO_2/PMMA interactions at 32 °C and pressures up to 35 MPa[9]. Rajendran et al. investigate the sorption behavior of CO_2 in PMMA at 50, 65, and 80 °C, and pressures up to 23.8 MPa[10]. Vogt et al. studied sorption of CO_2 in PMMA 60 and 100 °C, and pressures up to 12 MPa[11].

PMMA-CO_2 is known to exhibit the retrograde vitrification behavior[12-16]. At a given gas pressure, two T_gs are observed. One of the T_gs is the normally expected plasticized T_g corresponding to the glass-to-rubber transition. In addition, another T_g is observed at the same pressure, but at a lower temperature, and corresponds to the rubber-to-glass transition upon heating. This unusual behavior observed has been termed retrograde vitrification[17]. The retrograde behavior of PMMA has been utilized to create ultramicrocellular foams in the solid-state foaming process. PMMA foams with an average cell size of 350 nm, a cell density of 4.4×10^{13} cells/cm^3 and a relative density of about 10%, were obtained by saturating in CO_2 at -0.2 ℃ and 3.4 MPa[16]. One advantage of using the retrograde vitrification behavior is that gas sorption can occur much faster when the polymer-gas system is in the rubbery phase, for example, at 3.4 MPa, gas sorption occurs much more rapidly at -0.2 ℃ than at 24 ℃[16]. The other advantage is that only low pressure is required for producing foams with similar or finer microstructures[18].

In this paper, we first discuss the effect of temperature on sorption behavior of CO_2 in the range of -30 ℃ up to 100 ℃. Both solubility and diffusivity are studied. Arrhenius relationship is used to describe the effect of temperature on these parameters. Finally, glass transition temperatures of PMMA-CO_2 mixture are estimated and compared to commonly used models.

6.3 **Experimental**

6.3.1 **Material**

Acrylite FF PMMA sheets manufactured by CYRO Industries (New Jersey, USA) with a thickness of 1.48 mm were purchased. Sheets were cut into 2.5 cm × 2.5 cm samples using a band saw. The PMMA has a M_w=134,000 g/mol, M_n=71,000 g/mol, and a density of 1.19 g/cm^3. Glass transition temperature (T_g) was measured to be 103 ℃ in differential scanning calorimeter (DSC) TA Instruments Q20, with a heating rate of 10^{o}C/min. T_g was determined using the half-height method. Medical grade CO_2 (99.9% purity) was purchased from Praxair, Inc.

6.3.2 **Sorption**

Sorption experiments were conducted by placing samples in a pressure vessel, with the CO_2 pressure inside maintained at 5 MPa with an accuracy of +/- 0.1 MPa. In order to maximize CO_2 sorption in polymer and eliminate the need of a pressure boosting device, we chose 5 MPa as the saturation pressure, which was slightly below the pressure of a full CO_2 gas cylinder at room temperature. Saturation temperature (T_{sat}) varied over a wide range from -30 ℃ to 100 ℃. For sorption experiment above room temperature, a heating jacket wrapped around the pressure vessel and a temperature controller was used to maintain the pressure vessel at a desired temperature. For the temperatures between room temperature and 0 ℃, a Peltier cooling module was used. For temperatures below 0 ℃, the pressure vessel was placed in a freezer capable of achieving -30 ℃ to 0 ℃. During saturation, samples were periodically taken out from the pressure vessel, and weighed on a Mettler AE240 analytical scale accurate to +/- 10 μg. Samples were then promptly put back to the pressure vessel and repressurized. The sorption experiment continued until no further weight increase was observed in the specimen.

6.3.3 **Glass transition temperature determination**

Glass transition temperature was determined by a minimum foaming temperature approach. Specimens were first placed in a pressure vessel and then allowed to absorb CO_2 over a predetermined amount of time (based on sorption studies). After full saturation, samples were removed from the pressure vessel, and immediately immersed in a silicone oil bath (Thermo Haake B5) set at a foaming temperature (T_f) in the range of -20 ℃ - 120 ℃. The samples were kept in the oil bath for 10 minutes to allow sufficient time for foaming to happen. Saturated samples were foamed at increasingly higher foaming temperatures while keeping all other processing parameters the same. The temperature interval of the two adjacent foaming temperatures was 5 ℃. After foaming, the sample was immediately quenched in an oil bath which was kept much colder than the foaming oil bath, to stop further foaming. The minimum foaming temperature was determined as the average value of the two adjacent foaming temperatures: at the lower temperature, sample remains transparent and at the higher temperature, sample becomes opaque. Opaqueness indicates the formation of bubbles. In addition, SEM images of these samples were prepared to confirm the formation of cells. Previous studies suggested that the minimum foaming temperature and T_g of polymer-diluent system can be considered to be equivalent[19,20].

6.4 **Data Analysis, Results and Discussions**

6.4.1 **Solubility**

. shows the mass percentage (or mass%) of CO_2 in PMMA as a function of time at various saturation temperatures T_{sat}, ranging from -30 ℃ to 100 ℃. The saturation pressure was fixed at 5 MPa. Solubility is defined as the equilibrium mass% of CO_2 at a specified condition, and usually expressed as a percentage of the original polymer mass, e.g. 10% CO_2 means that 10% of the mass of original PMMA is now absorbed into the PMMA. Solubility and equilibrium mass% of CO_2 are used interchangeably in this paper. Note that there was a short time interval between the pressure release and weight measurement in the sorption experiment. To account for the CO_2 lost during this interval, the solubility of CO_2 in the samples was obtained by extrapolating the desorption curve to zero desorption time. Detailed procedures can be found in literature[21,22]. Solubility results in a wider temperature range are summarized in Table 6.1. To better visualize the solubility trend, we've also plotted the solubility as a function of saturation temperature in Figure 6.2. It is evident that the amount of CO_2 absorbed increases with decreasing temperature. By decreasing temperature from 100 ℃ to -30 ℃, the solubility increases from 3.9% to 39.3%, a ten-fold increase. To our knowledge, 39.3% is the highest amount of CO_2 ever reported absorbed in PMMA. Compared to other polymers at similar pressure and temperature conditions[2,23,24], PMMA has very high CO_2 solubility, which is probably due to the high mass density of carbonyl groups in PMMA[25].

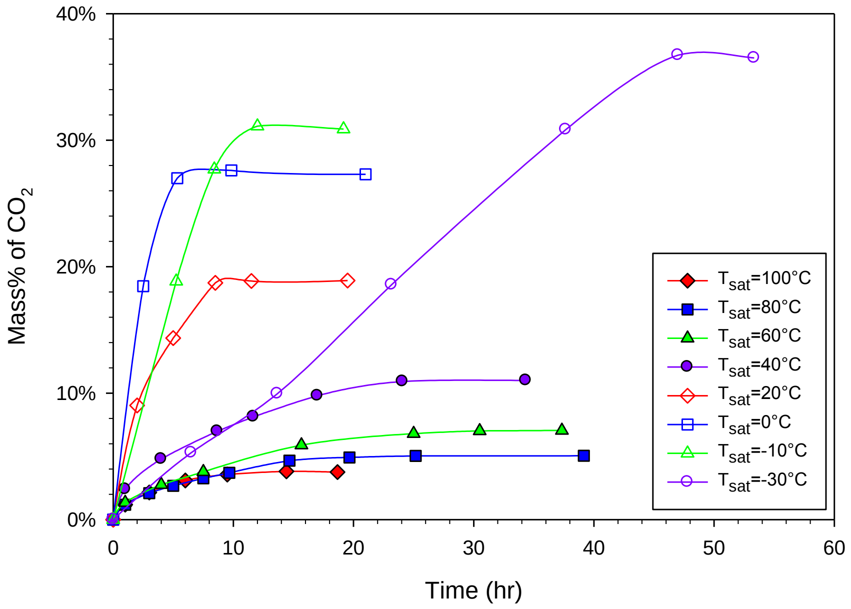

Figure 6.1 Mass% of CO_2 in PMMA as a function of time at various saturation temperatures. Sample thickness was 1.48 mm.

The temperature dependence of solubility is typically given by Arrhenius equation[3,15].

$$S = S_0 \exp\left(-\frac{\Delta H_S}{RT}\right) \qquad (1)$$

where S_0 is the pre-exponential factor, ΔH_S is the heat of sorption or enthalpy change upon solution of gas in the polymer, and R is the gas constant.

In Figure 6.3, we plotted the natural logarithm of solubility as a function of the reciprocal of saturation temperature. Note the X-axis is 1000/T where T is in Kelvin. The plot shows two distinct regions for liquid and gaseous CO_2 that intersect at 15 ℃, the phase change temperature for CO_2 at 5 MPa. Below and above this phase changing temperature, the data follows a linear trend: below 15 °C, ΔH_S is calculated to be -5.6 kJ/mol; above 15 °C, ΔH_S is -19.4 kJ/mol. Negative heat of sorption values indicate the exothermic nature of CO_2 sorption in PMMA. The difference between these two ΔH_S values is 13.8 kJ/mol. This value is close to the heat of condensation (or heat of vaporization) of CO_2, which is about

11.3 kJ/mol[26]. The change in heat of sorption at the phase changing temperature of CO_2 was also observed in our recent study of polycarbonate-CO_2 system[22].

Table 6.1 Summary of solubility (S), diffusivity (D), and saturation time (t_{sat}) at various saturation temperatures (T_{sat}).

T_{sat} (℃)	S	D (cm^2/s)	t_{sat} (hr)*
100	3.9%	1.41×10^{-7}	14
80	5.2%	7.8×10^{-8}	25
60	7.4%	5.8×10^{-8}	31
50	8.7%	5.5×10^{-8}	30
40	11.4%	6.6×10^{-8}	24
30	14.5%	7.5×10^{-8}	18
20	20.5%	1.8×10^{-7}	9
15	25.2%	2.78×10^{-7}	5
10	26.9%	3.65×10^{-7}	5
0	30.1%	2.63×10^{-7}	7
-10	32.6%	1.25×10^{-7}	12
-20	35.6%	5.5×10^{-8}	22
-30	39.3%	2.5×10^{-8}	47

* for sample thickness 1.48 mm

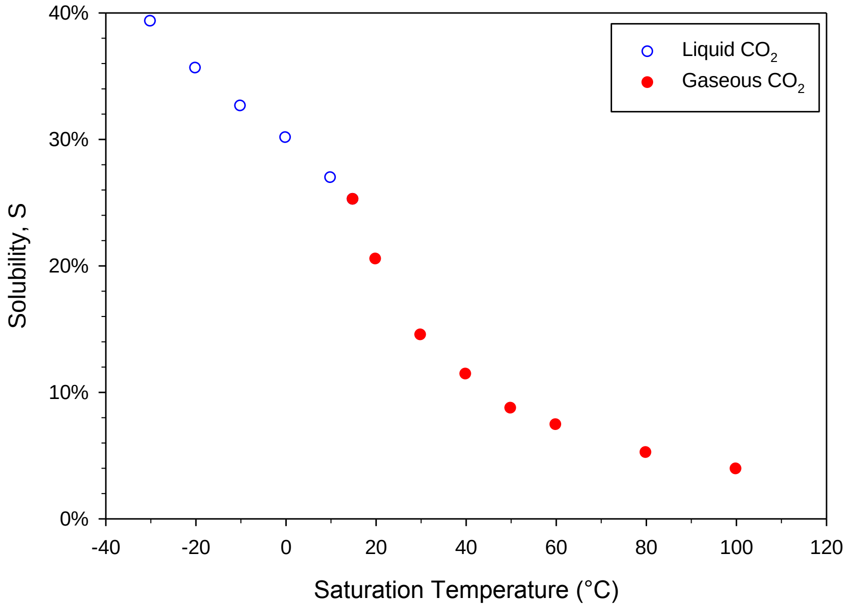

Figure 6.2 Solubility of CO_2 in PMMA as a function of saturation temperature.

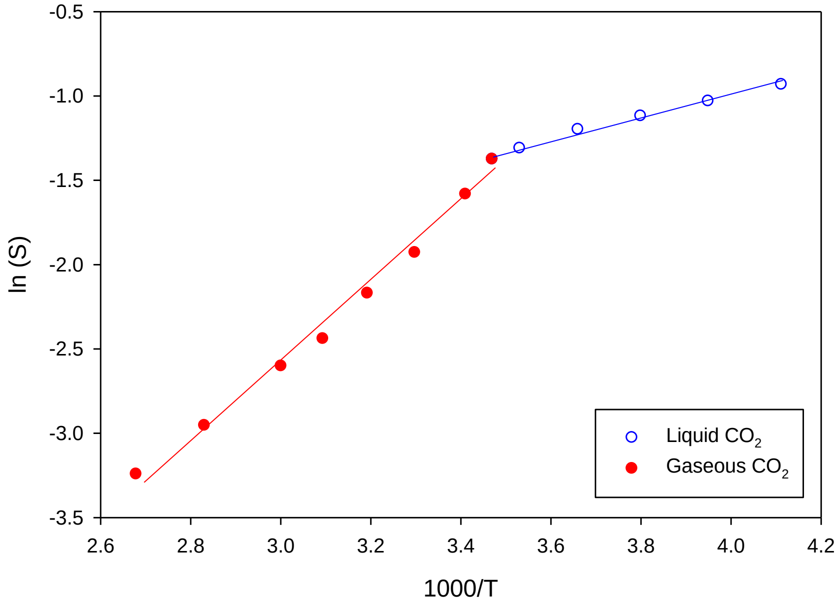

Figure 6.3 Natural logarithm of solubility as a function of reciprocal of saturation temperature with best-fit lines. Note the change in slope when CO_2 changes from gas to liquid at 15 ℃.

6.4.2 **Diffusivity**

Also, from Figure 6.1, we can see that the time needed to reach equilibrium is different for different saturation temperatures, with -30 ℃ taking the longest (~47 hrs), and 10 ℃ & 15 ℃ the shortest (~ 5 hrs). Sorption diffusivity is usually used to characterize how fast the sorption takes place. One of the methods used to determine diffusivity from a sorption plot is the hybrid method. It is a more accurate method since the model fits the data from the whole sorption curve, including both short-time and long-time data[27]. The hybrid method is described by the following equations:

$$\frac{M_t}{M_0} = \emptyset(x)f(x) + [1 - \emptyset(x)]g(x) \qquad (2)$$

$$x = Dt/L^2 \qquad (3)$$

$$f(x) = 4(x/\pi)^{0.5} \qquad (4)$$

$$g(x) = 1 - (8/\pi^2)\exp{(-\pi^2 x)} \qquad (5)$$

where M_t is the mass of CO_2 absorbed at time t, M_0 is the mass of CO_2 absorbed at equilibrium, $\emptyset(x)$ is the weighting function, f(x) is the short-time approximation, g(x) is the long-time approximation, D is the diffusivity, and L is the polymer thickness. The weighting function $\emptyset(x)$ is defined as:

$$\emptyset(x) = 1, x \leq 0.05326$$

$$\emptyset(x) = 0, x > 0.05326$$

Diffusivities are obtained by regression fitting the eqn. (2) to the sorption curves in Figure 6.1. Figure 6.4 shows an example of the model fitting to the data for sorption at 30 ℃. The model predicts the sorption data quite well. Sorption diffusivities are summarized in Table 6.1. Also, we've plotted the diffusivity data in Figure 6.5. We can see that temperature has a profound effect on the diffusivity in PMMA-CO_2 system. An order of magnitude variation can be seen, with the lowest diffusivity 2.5×10^{-8} cm^2/s at -30 ℃ and highest 3.65×10^{-7} cm^2/s at 10 ℃. More importantly, from the figure, we can see the diffusivity doesn't monotonically increase with increasing temperature over the entire temperature range, but instead, diffusivity increases with temperature in the range of -30 ℃ - 10 ℃ (region 4), decreases in the range of 10 ℃ - 30 ℃ (region 3), decrease more slowly in the range of 30 ℃ - 50 ℃ (region 2), and increases again in the range 60 ℃ – 100 ℃ (region 1). This is in contrast to many other polymer-gas systems, which typically show a monotonic increase of diffusivity with temperature.

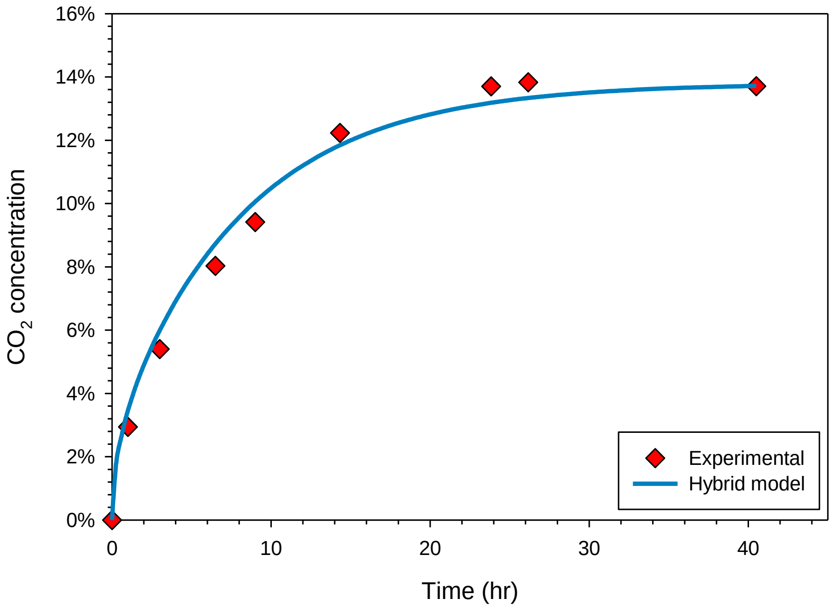

Figure 6.4 Hybrid model fitting to the experimental data of CO_2 sorption in PMMA at 30 ℃. D used is 7.5×10^{-8} cm^2/s.

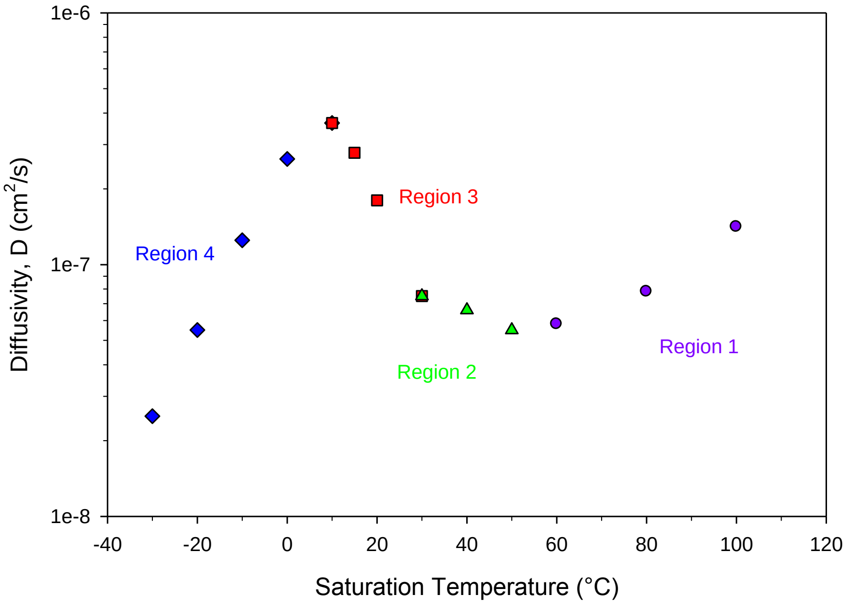

Figure 6.5 Diffusivity of CO_2 in PMMA as a function of saturation temperature. Four distinct regions are identified where diffusivity varies differently with temperature.

The effect of temperature on the diffusivity of gas in polymers was first shown by Barrer[28] and later confirmed by others[3,15] to be that of an activated process obeying the Arrhenius relationship:

$$D = D_0 \exp\left(-\frac{\Delta H_D}{RT}\right) \qquad (6)$$

where D_0 is the pre-exponential factor, ΔH_D is the activation energy for diffusion, R is gas constant and T is temperature in Kelvin.

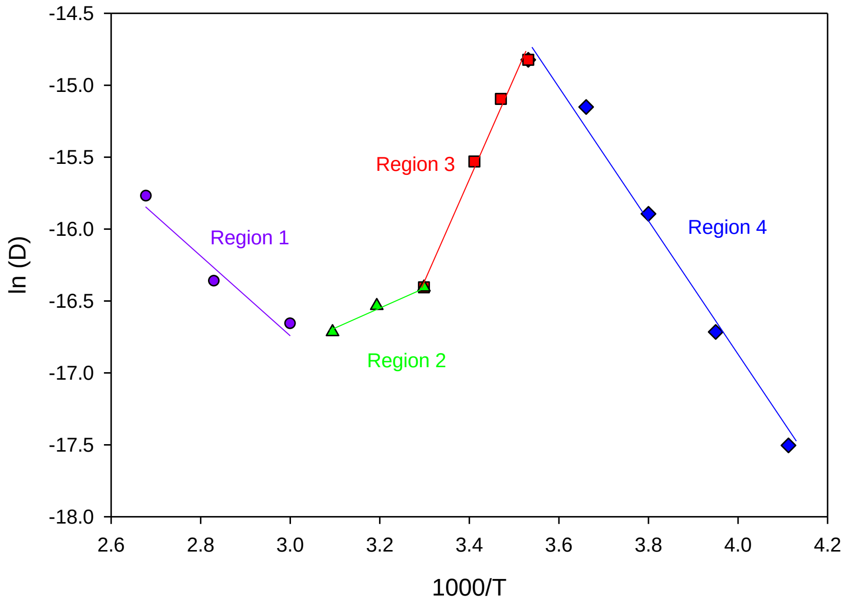

Figure 6.6 Natural logarithm of diffusivity as a function of reciprocal of saturation temperature. Four distinct regions are labeled and best-fit lines for each region are also shown.

Table 6.2 Characteristics of the four distinct diffusion regions.

Region	Temperature range	Physical state of PMMA-CO_2
Region 1	100 ℃ to 60 ℃	Rubbery
Region 2	50 ℃ to 30 ℃	Glassy
Region 3	30 ℃ to 10 ℃	Rubbery
Region 4	10 ℃ to -30 ℃	Glassy

In Figure 6.6, we have plotted natural logarithm of diffusivities in Table 6.1 as a function of the reciprocal of saturation temperature. The four distinct regions mentioned before are also labeled. Temperatures range and physical state of PMMA-CO_2 in each region are summarized in Table 6.2.

Also, within each region, a best-fit line using Arrhenius equation is shown. In region 1, as the temperature decreases, the diffusivity decreases. An activation energy barrier ΔH_D of 22.8 kJ/mol needs to be overcome for CO_2 diffusion in region 1. In region 2, as the temperature decreases, the diffusivity increases. ΔH_D is calculated to be -12.6 kJ/mol. In region 3, as the temperature decreases, the diffusivity increases, at a much faster rate than in the region 2. ΔH_D for region 3 is calculated to be -57.6 kJ/mol. In region 4, as the temperature decreases, the diffusivity decreases, at a faster rate than in region 1. ΔH_D is calculated to be 39.8 kJ/mol.

Handa et al.[15] observed that at saturation pressure of 3.4 MPa, diffusion of CO_2 in PMMA at 0 °C was faster than that at 10 °C (lower diffusivity at a higher temperature), implying a negative activation energy. Negative activation energy has been reported in chemical reactions, where the rates of reaction decreased with increasing temperature[29,30]. The proposed mechanism was the formation of an intermediate complex. Regarding to diffusion, negative activation energies have only been reported in atom and ion diffusion[31,32]. Radiation-enhanced-diffusion rates for Ag in Ni have been found to decrease at elevated temperatures and negative activation energies were reported[31]. The proposed mechanism was that at elevated temperatures the concentration of long-lived complex defects (which enhanced the atom diffusion) decreased, resulting in a slower diffusion of Ag atoms in Ni. Also, it was reported that potassium ion release from zwitterionic phosphorylcholine containing pHEMA-based hydrogels was slower at higher temperatures[32]. Temperature-dependent swelling of hydrogels was proposed to explain the negative activation energy. Neither of these proposed mechanisms is applicable to our polymer-gas system. The physical mechanism for negative activation energy of diffusion in PMMA-CO_2 system is currently under investigation.

The state of the system in terms of glassy or rubbery described in Table 6.2 can be understood in terms of the plasticization of PMMA by the dissolved CO_2 at a given temperature. In the high temperature range (region 1), some amount of CO_2 is dissolved and plasticizes the polymer, and under the high saturation temperature the PMMA-CO_2 is in the rubbery state. As the temperature is lowered, the drop in the saturation temperature dominates the increased plasticization effect from slightly more CO_2 absorption, and the PMMA-CO_2 goes into the glassy state (region 2). As the temperature is further lowered, there is a rapid increase in CO_2 solubility, resulting in a larger plasticization effect. With increased plasticization, the PMMA-CO_2 goes into the rubbery state (region 3).

The transitions from region 1 to region 2 and region 2 to region 3 have been previously reported by Handa et al. using a similar diffusivity approach[15]. They showed that for PMMA-CO_2 at 5 MPa, the rubber-to-glass transition temperature were between 50-60 ℃ and the glass-to-rubber transition (retrograde vitrification) temperature between 20-30 ℃. Our results on these two transition temperatures match well with their finding, with the rubber-to-glass transition temperature between 50-60 ℃ and the glass-to-rubber transition temperature at 30 ℃.

A new transition from region 3 to region 4 is reported here. This transition occurs at around 10 ℃, in the vicinity of the transition point (also the vaporization temperature of CO_2) in the solubility plot. As mentioned before, below the transition point, there is a change in heat of sorption ΔH_s, leading to a slower solubility increase with decreasing temperature (particularly evident from Figure 6.2). If the ΔH_s were to stay the same when temperature is lowered, the solubility of CO_2 in PMMA would be much larger at low temperatures. Suppose we could continue the same solubility trend from above 10 ℃ (without the change in ΔH_s) to below 10 ℃ in the solubility plot, the solubility would be about 70% at -30 ℃. But the measured solubility is only 39.3%. Without enough solubility and associated plasticization effect, the PMMA-CO_2 becomes glassy again.

As will be discussed in the next section, the existence of these four regions are reinforced with the comparison between glass transition temperature of PMMA-CO_2 mixture and corresponding saturation temperature used to achieve the equilibrium mass% of CO_2 in the mixture.

6.4.3 **Glass Transition Temperature**

Absorption of diluent into a polymer lowers its glass transition temperature, because the diluent molecules increase polymer intermolecular distance, decreasing intermolecular interactions. The weakening of these interactions increases the segmental mobility, which leads to a lower glass transition temperature. CO_2 has a high plasticization effect and can reduce T_g to a value significantly lower than that of the original polymer. This is one of the primary driving mechanisms in solid-state microcellular foaming. Therefore, knowledge of T_g of the polymer-diluent mixture is very important to understand and control the foaming process.

Figure 6.7 shows the glass transition temperature (T_g) of PMMA-CO_2 as a function of equilibrium mass% of CO_2. The T_g reduces from 103 ℃ to -12.5 ℃ when 39.3% CO_2 is incorporated into PMMA. Handa et al. previously reported T_g of PMMA-CO_2 mixture up to 23.5% CO_2[15]. The data are included in the plot. Both sets of data agree well for the equilibrium mass% of CO_2 between 7.5% and 23.5%. Data from our study cover a much larger range of mass% of CO_2. In PMMA, the T_g reduces from 103 ℃ to -12.5 ℃ with 39.3% CO_2, an average of 3 ℃ reduction with 1% increase in the amount of CO_2 absorbed. This plasticization effect is small in comparison to other polymers. For example, with 1% increase in CO_2 absorption, the reduction of T_g in polyethersulfone (PES), polysulfone (PSU), and cyclic olefin copolymer (COC), is 13 ℃, 16 ℃ and 18 ℃, respectively[20].

Empirical models have been developed to predict the T_g of a variety of binary mixtures, including the plasticizers in high polymers. Three of these models were used to fit our data - Fox equation[33], Jenckel & Heusche equation[34], and Gordon & Taylor equation[35]:

Fox equation: $\frac{1}{T_g(w)} = \frac{w}{T_{g1}} + \frac{1-w}{T_{g2}}$ (7)

Jenckel & Heusche equation: $T_g(w) = wT_{g1} + (1-w)T_{g2} + w(1-w)k$ (8)

Gordon & Taylor equation $T_g(w) = \frac{wT_{g1}+\mu(1-w)T_{g2}}{w+\mu(1-w)}$ (9)

T_{g1} and T_{g2} are glass transition temperatures of CO_2 and PMMA, respectively; k and µ are constants selected for a best fit. T_g of CO_2 is recently reported as -223 ℃ (50 K)[36] and T_g of PMMA is 103 ℃.

Predictions from these equations are shown in Figure 6.7. The Fox equation predicts the T_g very poorly. The best-fit constants selected are k=-175 and µ=0.62 for Jenckel & Heusche and Gordon & Taylor equation, respectively. Predictions from these two equations are very close to each other. Among various models selected, these two models can best fit our experimental data. However, they underestimate the T_g when below 24% equilibrium mass% of CO_2 and overestimate the T_g when above 24% equilibrium mass% of CO_2.

A model based on both classical and statistical thermodynamics predicting the T_g of diluent laden polymer was developed by Chow[37]. The model was successfully applied to predict the T_g of polystyrene with a variety of diluents and a range of mass% of diluents. The model is as follows:

$$\ln\left(\frac{T_g}{T_{g0}}\right) = \beta[(1-\theta)\ln(1-\theta) + \theta\ln\theta] \quad (10)$$

$$\beta = \frac{zR}{M_p\Delta C_{pp}} \quad (11)$$

$$\theta = \frac{M_p}{zM_d}\frac{w}{1-w} \quad (12)$$

where T_g and T_{g0} are the glass transition temperature for the polymer-diluent system and the neat polymer, respectively, M_p is the molar mass of the polymer repeat unit, M_d is the molar mass of diluent, R is the gas constant, w is the mass (or weight) fraction of the diluent, ΔC_{pp} is the excess transition isobaric specific heat of the polymer, and z is the lattice coordination number.

In the figure, we also show the T_g prediction based on Chow's model with z=2 and ΔC_{pp}=0.265 J K^{-1} g^{-1}, which were suggested[37]. The model can predict the general decreasing trend of T_g; however, it predicts the T_g values poorly with the prediction always lower than our experimental data.

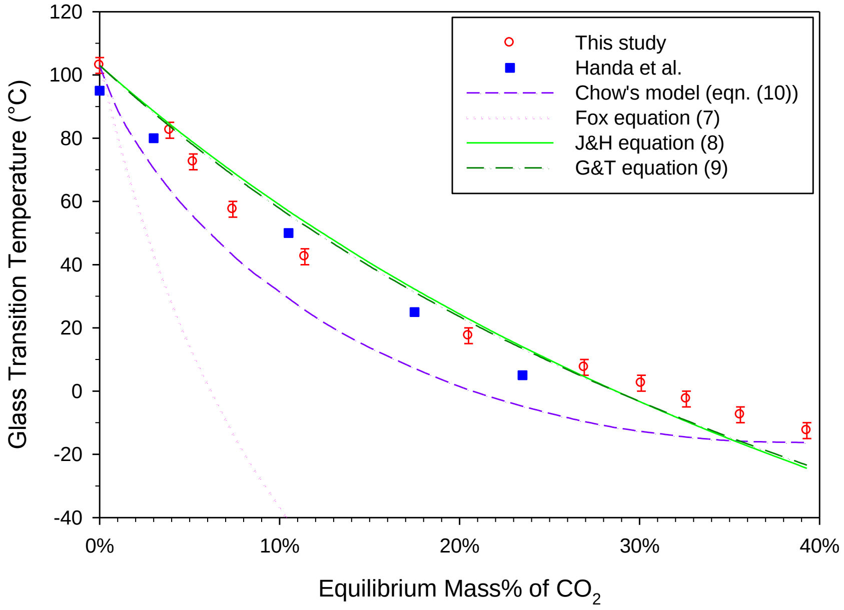

Figure 6.7 T_g of PMMA-CO_2 mixture as a function of equilibrium mass% of CO_2. Experimental data from this study and the study by Handa et al.[15], and predictions using Fox equation, Jenckel & Heusch (J&H) equation, Gordon & Taylor (G&T) equation and Chow's model with z=2 are shown.

Figure 6.8 shows a comparison between the T_g of PMMA-CO_2 mixture at each equilibrium mass% of CO_2 and the saturation temperature (T_{sat}) used to achieve the corresponding amount of CO_2. The same four regions mentioned previously are also labeled. The relative magnitude of T_g and T_{sat} determines whether the PMMA-CO_2 mixture is in a glassy or rubbery state. In region 1 and region 3, at the equilibrium mass% of CO_2, T_{sat} is greater than T_g so the PMMA-CO_2 system is in the rubbery state. In region 2 and region 4, T_{sat} is below the T_g so the PMMA-CO_2 system is in the glassy state. The transition points between different regions are between 50 ℃ and 60 ℃ for region 1 → region 2, between 20 ℃ and 30 ℃ for region 2 → region 3 and between 0 ℃ and 10 ℃ for region 3 → region 4. These transitions points match relatively well with the ones identified from diffusivity data (see Table 6.2). At very low T_{sat}

and thus high equilibrium mass% of CO_2, two lines are diverging from each other. The decrease in T_{sat} exceeds the reduction of T_g with the absorbed CO_2, so the system is in the glassy state.

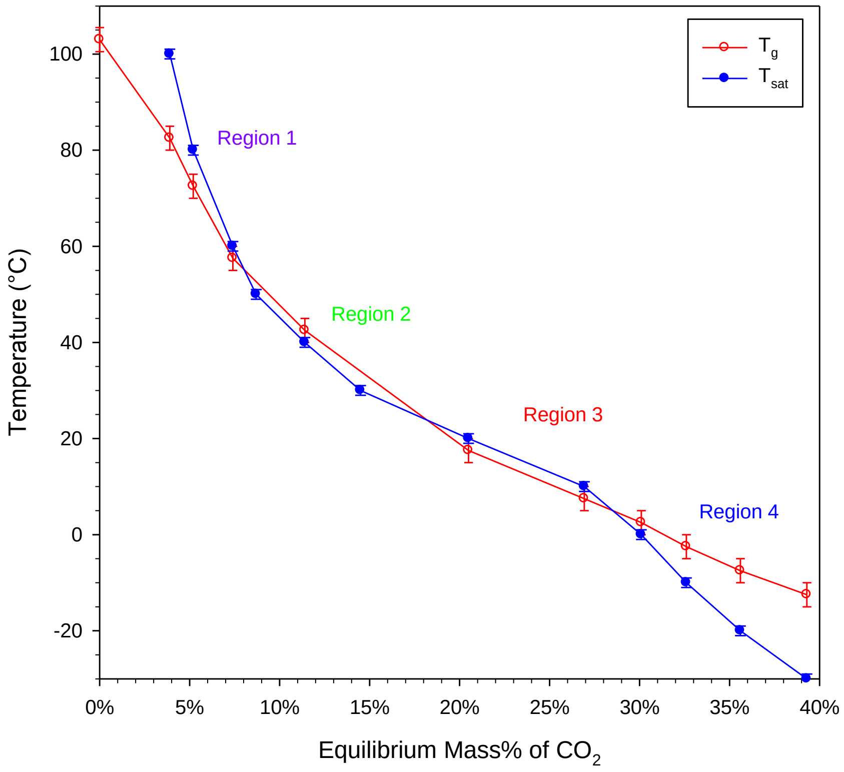

Figure 6.8 Comparison between the T_g of PMMA-CO_2 mixture at each equilibrium mass% of CO_2 and the T_{sat} used to achieve the corresponding amount of CO_2. The four regions are also labeled.

6.5 **Summary**

The effect of saturation temperature (T_{sat}) on sorption and diffusion of CO_2 in PMMA was investigated over the range -30 ℃ to 100 ℃. Saturation temperature has significant effects on both the solubility and diffusivity. Solubility increases with decreasing saturation temperature, a ten-fold increase from 3.9% at 100 ℃ to 39.3% at -30 ℃. A change in heat of sorption has been found to occur around 15 ℃, the vaporization temperature at 5 MPa for CO_2. The change in heat of sorption matches with heat of vaporization of CO_2. The effect of temperature on solubility can be described with an Arrhenius relationship.

For diffusivity, four distinct regions are identified, where diffusivity may increase or decrease with decreasing temperature, characterized by the different activation energies. As T_{sat} is lowered from 100 °C to -30 °C, a rubber-to-glass transition between 50-60 °C and a glass-to-rubber transition at 30 °C have been observed, which match with previously reported results. In addition, we observed a third transition from rubbery state to glassy state at 10 °C, in the vicinity of CO_2 vaporization temperature at 5MPa (15 °C).

Dissolution of CO_2 into PMMA plasticizes the polymer. Thus, at T_{sat} of -30 °C, incorporation of 39.3% CO_2 in PMMA decreases the T_g from 103 °C to -12.5 °C. The minimum foaming temperature, or equivalently the effective T_g of the polymer-gas mixture, shows a non-linear decreasing trend with the amount of CO_2 absorbed.

6.6 **Acknowledgment**

The authors would like to acknowledge the financial support from the University of Washington CGF fund and National Science Foundation Grant CMMI 1253072. Also, we would like to thank Mr. Andrei Nicholae from Mechanical Engineering Department at UW, and undergraduate research assistants Varun Gupta and Ankita Sharma from IIT-Gandhinagar, for their help in some of the experiments.

6.7 **References**

1. Kumar, V. *Colloid. Surface A* **2005**, 263, 336-340.
2. Kumar, V.; Weller, J. E. *J. Eng. Ind.* **1994**, 116, 413-420.
3. Crank, J.; Park, G. S. *Diffusion in Polymers*; Academic Press: London, 1968.
4. Martini, J.; Suh, N. P.; Waldman, F. A. Microcellular closed cell foams and their method of manufacture. Patent #4473665. USA: Massachusetts Institute of Technology; 1984.
5. Martini, J.; Waldman, F. A.; Suh, N. P. The production and analysis of microcellular thermoplastic foam. San Francisco, CA. In: SPE ANTEC, vol. 28; 1982. p. 674.
6. Wissinger, R. G.; Paulaitis, M. E. *J. Polym. Sci., Polym. Phys.* **1987**, 25, 2497-2510.
7. Wissinger, R. G.; Paulaitis, M. E. *Ind. Eng. Chem. Res.* **1991**, 30, 842-851.
8. Kamiya, Y.; Misoguchi, K.; Terada, K.; Fujiwara, Y.; Wang, J. S. *Macromolecules* **1998**, 31, 472-478.
9. Shieh, Y.; Liu, K. *J. Supercrit. Fluids* **2003**, 25, 261-268.
10. Rajendran, A.; Bonavoglia, B.; Forrer, N.; Storti, G.; Mazzotti, M.; Morbidelli, M. *Ind. Eng. Chem. Res.* **2005**, 44, 2549-2560.
11. Vogt, B. D.; RamachandraRao, V. S.; Gupta, R. R.; Lavery, K. A.; Francis, T. J.; Russell, T. P.; Watkins, J. J. *Macromolecules* **2003**, 36, 4029-4036.

12. Wissinger, R. G.; Paulaitis, M. E. *J. Polym. Sci., Polym. Phys.* **1991**, 29, 631-633.
13. Condo, P. D; Johnston, K. P. *Macromolecules* **1992**, 25, 6730-6732.
14. Condo, P.D.; Johnston, K. P. *J. Polym. Sci., Polym. Phys.* **1994**, 32, 523-533.
15. Handa, Y. P.; Zhang, Z.; Wong, B. *Cell. Polym.* **2001**, 20, 1-16.
16. Handa, Y. P.; Zhang, Z. *J. Polym. Sci., Polym. Phys.* **2000**, 38, 716-725.
17. Condo, P. D; Sanchez, I.C.; Panayiotou, C. G.; Johnston, K. P. *Macromolecules* **1992**, 25, 6119-6127.
18. Nawaby, A. V.; Handa, Y. P.; Liao, X.; Yoshitaka, Y.; Tomohiro, M. *Polym. Int.* **2007**, 56, 67-73.
19. Kumar, V.; Weller, J. E.; Montecillo, R. SPE ANTEC **1992**; p. 1452-1456.
20. Krause, B.; Mettinkhof R, Van Der Vegt, N. F. A.; Wessling M. *Macromolecules* **2001**, 34, 874-884.
21. Pantoula, M.; Panayiotou, C. *J. Supercritical Fluids* **2006**, 37, 254-262.
22. Guo, H.; Kumar, V. *Polymer* **2014**; DOI: 10.1016/j.polymer.2014.09.061
23. Kumar, V.; Weller, J. E. *Int. Polym. Proc.* **1993**, 8, 73-80.
24. Krause, B.; Sijbesma, H. J. P.; Munuklu, P.; Van Der Vegt, N. F. A; Wessling, M. *Macromolecules* **2001**, 34, 8792-8801.
25. Koros, W.J. *J. Polym. Sci., Polym. Phys.* **1985**, 23, 1611-1628.
26. Cengel, Y.; Boles, M. *Thermodynamics: An Engineering Approach*, 7th ed.; McGraw-Hill Higher Education, 2010.
27. Balik, C. M. *Macromolecules* **1996**, 29, 3025-3029.
28. Barrer, R. M. *Nature* **1937**, 140, 106-107.
29. Mozurkewich, M.; Benson, S. W. J. Phy. Chem. **1984**, 88, 6429-6435.
30. Mozurkewich, M.; Benson, S. W. J. Phy. Chem. **1984**, 88, 6435-6441.
31. Marton, D.; Fine, J.; Chambers, G. P. *Phys. Rev. Let.* **1998**, 61, 2697-2700.
32. Wilson, A. N.; Blenner, M.; Guiseppi-Elie A. *Polymers* **2014**, 6, 2451-2472.
33. Fox, T.G. *Bull. Am. Phys. Soc.* **1956**, 1, 123.
34. Jenckel, E.; Heusch, R. *Kolloidn. Zh.* **1958**, 130, 89.
35. Gordon, M.; Taylor, J. S. *J. Appl. Chem.* USSR, **1952**, 2, 493.
36. Souda, R. *J. Phys. Chem. B.* **2006**, 110, 17884-17888.
37. Chow, T. S. *Macromolecules* **1980**, 13, 362-364.

Chapter 7

Solid-state Poly(methyl methacrylate) (PMMA) Nanofoams. Part II: Low-temperature Solid-state Process Space Using CO_2 and the Resulting Morphologies

7.1 **Abstract**

In this paper, solid-state poly(methyl methacrylate) (PMMA) nanofoams are fabricated via a low-temperature CO_2 saturation process. Nanofoams with smallest cell size in 30-40 nm range and cell nucleation densities exceeding 10^{14} cells/cm^3 are achieved. We investigated the effect of saturation temperature on the solid-state foaming of PMMA and resulting morphologies of the foams in the range of -30 ℃ to 40 ℃. A range of equilibrium mass% of CO_2 are achieved via the different saturation temperatures, from 11.4% at 40 ℃ to 39.3% at -30 ℃. The amount of CO_2 absorbed greatly influences cellular structure of PMMA foams. We identify a critical mass% CO_2 between 30.1% and 32.6%, above which cell nucleation density rapidly increases and consequently foamed microstructure changes from microcellular to nanocellular. Nanofoams with void fraction as high as 86% are created. A transition from closed nanocellular structure to bicontinuous nanoporous structure, and also novel worm-like nanostructures have been observed.

7.2 **Introduction**

Nanofoams, or nanocellular foams, refer to thermoplastic foams with cells of order 10 nm. Nanofoams progressed from microcellular foams, which have cell sizes in the micrometer range. Polymer foams with micrometer cells were first discovered by McIntire [1] and Amos [2] around 1950 when processing polystyrene with gaseous alkyl halide (e.g. methyl chloride) and ammonia (added to regulate cell size). The cell size was close to 100 μm. In the early 1980's, Martini et al. [3, 4] developed a much cleaner and

---

This chapter has been published in Polymer, 2015, 70: 231-241.

controllable method to create microcellular foams with cells of order 10 μm, using inert gas such as nitrogen and carbon dioxide. They described a two-step process to create microcellular structure in high impact polystyrene (HIPS), that involved saturating the polymer with a non-reacting gas and then heating the gas laden polymer to near the glass transition temperature [3]. Since polymer foam is created near the T_g of the gas-polymer system, well below the melting point, this process is commonly termed as solid-state process. The solid-state process has been successfully used to create microcellular foams in many different polymers, such as PVC [5], ABS [6], PC [7], PET [8, 9], COC [10, 11] and PLA [12, 13].

Nanofoam is a novel class of material that may offer many properties that are superior to existing materials, and present a unique combination of properties not seen before. One example is the combination of high strength and high porosity. Biener et al. [14] showed that highly nanoporous gold can be as strong as bulk Au, and that the ligaments in nanoporous gold approach the theoretical yield strength of Au. Similar unique combination n of properties may also exist in the cellular polymeric materials. Recently, Miller and Kumar [15] showed improved mechanical properties in nanocellular polyetherimide (PEI) when compared to microcellular PEI foams. Zhou et al. [16] reported higher flexural modulus and strength in PEI nanofoams than the unfoamed material. Nanofoams were also shown to have lower conductivity than microcellular foams [17, 18]. In addition, when cell size is significantly smaller than the light wavelength, the scattering of the light becomes much less. This leads to the possibility of transparent foams if the cells are small enough. The transparent foams can be used as thermally insulative yet transparent windows, which can reduce heat loss and save the energy usage for buildings. Furthermore, if the nanosized cells can be interconnected and form open porous structure. These nanoporous structures may be used in filtration, gas separation, energy storage, and catalysis supports [19].

The first nanofoams reported were polyimide nanofoams. They were produced from block copolymers consisting of thermally stable and thermally labile blocks, where the thermally labile blocks underwent thermolysis upon thermal treatment and nanopores formed replacing these blocks [20]. Solid-state gas foaming process has been used to create polymeric nanofoams. Using this method, nanofoams were produced in polymers with relatively high glass transition temperature polymers, such as PEI and PES [21, 22], PI [23] PC [24] and PSU [25]. A variety of polymer blends, including PEEK/PEI [26], PP/rubber [27, 28], PMMA/MAM [29-33], and more recently in styrenic-acrylic blends PEMA/SAN and PMMA-co-EA/SAN [34] have been shown to produce nanofoams. For copolymer, nanofoams have been created mainly in PMMA and its copolymers, such as Poly(MMA-co-EMA) [35]. Polymer nanocomposites, which have some amount of nanoparticles dispersed in the polymer matrix, have been shown to generate nanofoams, such as in Poly(MMA-co-EA) with silica nanoparticles and Poly(MMA-co-EMA) with POSS [36]. A review on using the gas foaming process to create nanofoams can be found in a recent publication [37].

More specifically, solid-state gas foaming of PMMA, its relevant copolymers and blends have been studied by a few groups. Handa and Zhang [38] utilized the retrograde behavior of PMMA to obtain foams, with an average cell size of 350 nm, a cell density of 4.4×10^{13} cells/cm^3 and a relative density of about 10%, by saturating in CO_2 at -0.2 ℃ and 3.4 MPa. Reglero-Ruiz et al. [29] studied the PMMA/MAM blend, in which 10% MAM (triblock copolymer) was added to PMMA. Using one-step batch process with the saturation at 30 MPa and room temperature, they achieved foams with an average cell size of 200nm, a cell density of 4.5×10^{14} cells/cm^3 and a relative density of 40%. Costeux et al. [35] investigated a family of acrylic copolymers. With the high molecular weight copolymer Poly(MMA-co-EMA), they achieved foams with cell size about 80 nm, cell density exceeding 10^{16} cells/cm^3, and relative density less than 20%, by saturating the copolymer in supercritical CO_2 at 30 MPa and 35 ℃. Costeux and Zhu [36] found an enhanced cell nucleation by addition of nanoparticles with a particle size less than 30 nm. For Poly(MMA-co-EA) with 0.5%wt nanosilica, foams with an average cell size of 95 nm, a cell density 8.6×10^{15} cells/cm^3, and a relative density of 20.5% were achieved, by saturating in supercritical CO_2 at 30 MPa and 40 ℃. For Poly(MMA-co-EMA) with 0.25% wt POSS nanoparticles, foams with an average cell size of 100 nm, a cell density of 10^{16} cells/cm^3, and a relative density of 15% were achieved, by saturating in supercritical CO_2 at 33 MPa and 50 ℃.

Most studies described above used specially modified PMMA via additional synthesis or blending processes, one disadvantage of which might be a longer processing time and higher manufacturing cost. In this paper, we describe the creation of nanofoams in commercial PMMA with cell size as low as 30-40 nm. Our process involves using low temperature saturation, where the saturation temperature is as low as -30 ℃ and CO_2 is in the liquid state. In this paper, we firstly present the solubility of CO_2 in PMMA at various saturation temperatures in the range of -30 ℃ up to 40 ℃. Then, the solid-state batch foaming of samples initially saturated at various temperatures is conducted. Characterizations of density and microstructural morphology of the foams are presented.

7.3 **Experimental**

7.3.1 **Materials**

Acrylite FF PMMA sheets manufactured by CYRO Industries (New Jersey, USA) with a thickness of 1.48 mm were purchased. The PMMA has a M_w=134,000 g/mol, M_n=71,000 g/mol, and a density of 1.19 g/cm^3. Sheets were cut into 2.5 cm × 2.5 cm samples using a band saw. Glass transition temperature (T_g) was measured to be 103 ℃ in differential scanning calorimeter (TA Instruments Q20), with a heating rate of 10^{o}C/min. T_g was determined using the half-height method. Medical grade CO_2 (99.9% purity) was purchased from Praxair, Inc.

7.3.2 **Foaming**

Specimens used for foaming studies were first placed in a pressure vessel and the pressure was kept at 5 MPa with an accuracy of +/- 0.1 MPa. Samples were allowed to absorb CO_2 over a predetermined amount of time (based on sorption studies) to reach equilibrium saturation. Refer to part I of this paper for detailed setup and sorption results [39]. Saturation temperature (T_{sat}) varied over a range from -30 ℃ to 40 ℃. After full saturation, samples were removed from the pressure vessel, and immediately immersed in a silicone oil bath (Thermo Haake B5) set at a desired foaming temperature (T_f) in the range of 0 ℃ - 120 ℃. The foaming time was kept constant at 1 minute, which was found appropriate to achieve stable foam structure. After foaming, the sample was immediately quenched in an oil bath which was kept much colder than the foaming oil bath.

7.3.3 **Characterizations**

After foaming, samples were washed with general purpose detergent. The density of each sample was determined according to ASTM D792 using Mettler AE240 analytical scale. Samples were desorbed for at least one week before density measurement in order to eliminate the effect of residual CO_2. Solid skins on the surface of the foams were kept for density measurement. Relative density, *RD*, and void fraction (or equivalently porosity), V_f , are calculated as follows:

$$RD = \frac{\rho_f}{\rho_s} \qquad (1)$$

$$V_f = 1 - RD \qquad (2)$$

where ρ_f is the density of foamed sample and ρ_s the density of unfoamed solid sample.

FEI Sirion scanning electron microscope (SEM) was used to examine the microstructures of foams. Samples were first scored slightly with a razor blade and freeze fractured with liquid nitrogen to expose the cross section. They were then coated with Au/Pd. Micrographs were taken at the center of the cross section of the specimen and analyzed using software ImageJ (National Institute of Health, USA). Average cell size was calculated by taking average cell diameters of at least 50 cells in the SEM micrographs. Cell nucleation density (number of cells nucleated per cubic centimeter of the unfoamed sample) was calculated as follows [7]:

$$N_0 = \left(\frac{nM^2}{A}\right)^{3/2} * \frac{1}{1 - V_f} \qquad (3)$$

where V_f is the void fraction; *n*, the number of cells in the SEM micrograph; *M*, the magnification of the micrograph; *A*, the area of the micrograph (cm^2).

7.4 **Results and Discussions**

7.4.1 **CO_2 Solubility**

The amount of CO_2 absorbed in a polymer is commonly characterized by the mass percentage (or mass%) of CO_2, which is defined as mass of CO_2 absorbed divided by mass of original polymer. For example, if the mass% of CO_2 in a polymer is 10%, this means CO_2 with the amount equal to 10% of the mass of original polymer is now absorbed into the polymer matrix, i.e. 10 g of CO_2 is absorbed in 100 g of polymer. When a polymer-CO_2 system is in equilibrium at a specific pressure and temperature condition, the equilibrium mass% of CO_2 defines the CO_2 solubility in the polymer. CO_2 solubility and equilibrium mass% of CO_2 are used interchangeably in this paper.

Part I of this paper [39] describes an extensive study on CO_2 sorption in PMMA over the saturation temperature range of -30 ℃ to 100 ℃. Table 7.1 shows part of the solubility data that pertain to the foaming study in this paper. By varying the saturation temperature, we are able to achieve a range of solubilities from 11.4% at 40 ℃ to 39.3% at -30 ℃. As will be revealed later, the very high solubility at the low saturation temperature is critical for creating nanocells in the PMMA.

Table 7.1 Saturation temperature and corresponding CO_2 solubility in PMMA [39].

Saturation temperature (℃)	CO_2 solubility
40	11.4%
20	20.5%
0	30.1%
-10	32.6%
-20	35.6%
-30	39.3%

7.4.2 **Relative Density of Foams**

Samples were initially saturated at different saturation temperatures, ranging from -30 ℃ to 40 ℃, and then foamed in a range of temperatures. Figure 7.1 shows the relative density of foamed samples as a function of foaming temperatures. Table 7.2 summarizes the processing conditions and foam characteristics, including relative density. We can see that the density decreases with increasing foaming temperature. The rate of density reduction with foaming temperature is different. The reduction rate is higher for samples saturated at higher temperatures, which has lower equilibrium mass% of CO_2. For example, it only needs 40 ℃ increase in foaming temperature for samples saturated at 40 ℃ in order to reduce its relative density from 100% to about 18%; however, it needs at least 80 ℃ for -20 ℃ saturated samples to achieve roughly the same amount of density reduction. As will be mentioned later, -10 ℃, -20 ℃ and -30 ℃ saturated samples provide sufficient cell nucleation and thus generate nanofoams. From the figure, we can see that nanofoams with relative density as low as 14% (or 86% void fraction) can be achieved.

When investigating the effect of cell size on foams properties, such as mechanical, thermal, optical and acoustic properties, it’s desirable to compare samples of the same density. We are able to produce foams with similar densities but different cell sizes. For example, if we want to achieve 75% relative density (horizontal line in the figure), we can prepare the foam by saturating it at 40 ℃ and then foaming it at 70 ℃ (sample #2), or by saturating it at -30 ℃ and foaming it at 10 ℃ (sample #34). The cellular morphologies of these two samples are remarkably different (see Figure 7.2). Sample #2 has a cell size of 96 μm, but sample #34 has a cell size of 45 nm, over 2,000 times smaller.

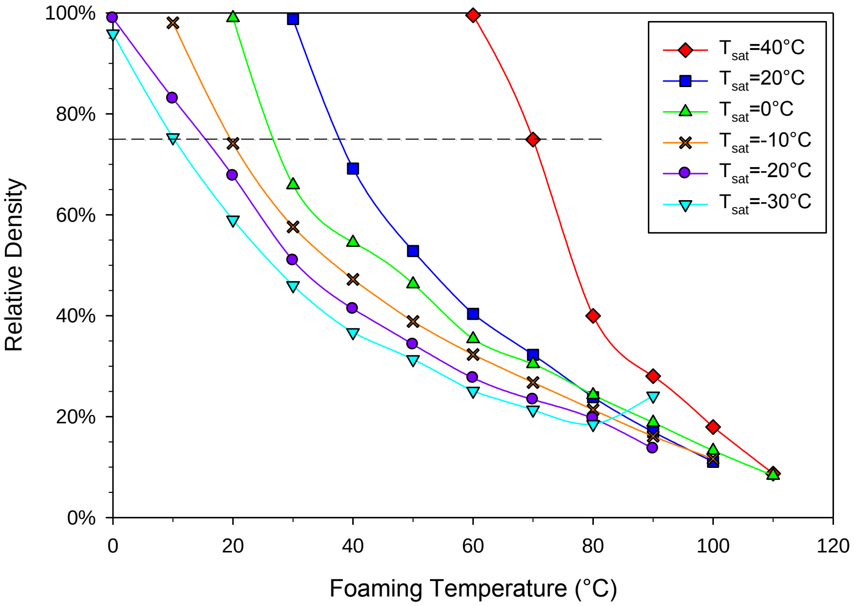

Figure 7.1 Relative density as a function of foaming temperature for samples initially saturated at various temperatures. Also, a 75% relative density line is drawn.

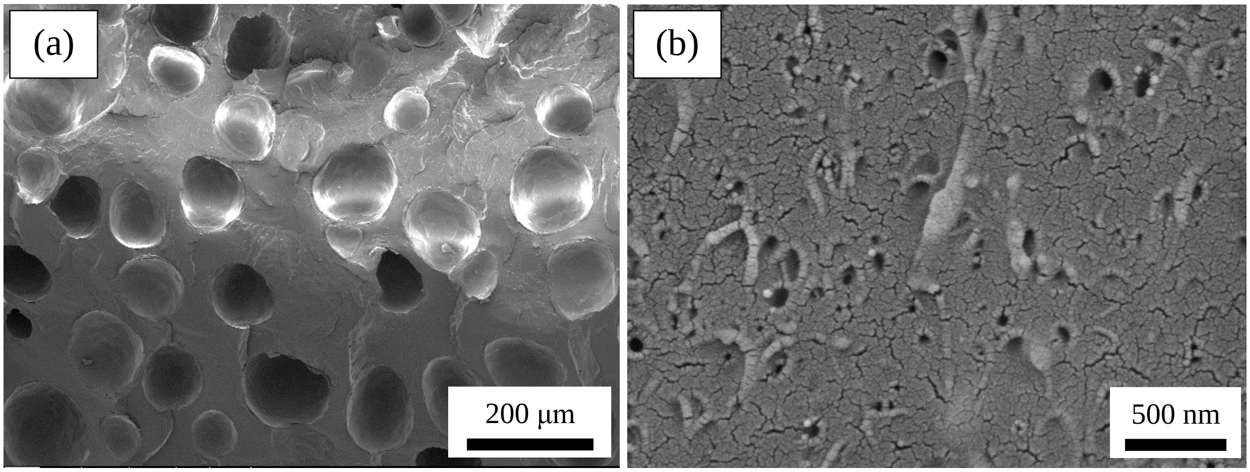

Figure 7.2 (a) sample #2 with cell size 96 µm and 74.9% relative density, (b) sample #34 with cell size 45 nm and 75.3% relative density. Notice the scale bar difference.

Table 7.2 Summary of processing conditions and foam characteristics. (--) indicates the sample didn't have regular cell structures and thus was not analyzed.

Sample #	T_{sat} (℃)	Equilibrium mass% of CO_2	T_f (℃)	Relative density	Void fraction	Nucleation density (cells/cm^3)	Average cell size (µm)
1	40	11.4%	60	99.5%	0.5%	9.18×10^{3}	42
2	40	11.4%	70	74.9%	25.1%	3.86×10^{5}	96
3	40	11.4%	80	40.0%	60.0%	6.49×10^{6}	61
4	40	11.4%	90	28.0%	72%	1.03×10^{7}	54
5	40	11.4%	100	17.9%	82.1%	1.45×10^{7}	57
6	40	11.4%	110	8.7%	91.3%	2.22×10^{7}	72
7	20	20.5%	30	98.8%	1.2%	9.49×10^{5}	14
8	20	20.5%	40	69.2%	30.8%	5.59×10^{7}	18
9	20	20.5%	50	52.8%	47.2%	1.26×10^{8}	18
10	20	20.5%	60	40.4%	59.6%	1.32×10^{8}	18
11	20	20.5%	70	32.2%	67.8%	1.46×10^{8}	23
12	20	20.5%	80	23.8%	76.2%	2.04×10^{8}	19
13	20	20.5%	90	17.0%	83.0%	2.04×10^{8}	24
14	20	20.5%	100	11.0%	89.0%	2.22×10^{8}	27
15	0	30.1%	20	99.0%	1.0%	2.50×10^{8}	1.8
16	0	30.1%	30	65.9%	34.1%	3.73×10^{10}	2.2
17	0	30.1%	50	46.3%	53.7%	1.05×10^{10}	4.8
18	0	30.1%	70	36.2%	63.8%	5.60×10^{9}	6.7
19	0	30.1%	90	22.4%	77.6%	5.55×10^{9}	8.4
20	0	30.1%	110	8.3%	91.7%	2.53×10^{9}	13.3
21	-10	32.6%	10	98.0%	2.0%	8.74×10^{11}	0.509
22	-10	32.6%	20	74.1%	25.9%	2.52×10^{13}	0.173
23	-10	32.6%	30	57.6%	42.4%	2.91×10^{13}	0.185
24	-10	32.6%	50	38.8%	61.2%	2.71×10^{13}	0.273
25	-10	32.6%	70	26.7%	73.3%	1.42×10^{12}	1.1
26	-10	32.6%	90	16.1%	83.9%	6.89×10^{10}	4.3
27	-20	35.6%	0	98.9%	1.1%	8.91×10^{12}	0.053
28	-20	35.6%	10	83.0%	17.0%	5.50×10^{13}	0.039
29	-20	35.6%	30	50.9%	49.1%	2.07×10^{14}	0.056
30	-20	35.6%	50	34.3%	65.7%	5.56×10^{14}	0.055
31	-20	35.6%	70	23.4%	76.6%	1.54×10^{14}	0.120
32	-20	35.6%	90	13.65%	86.4%	6.57×10^{13}	0.235
33	-30	39.3%	0	95.9%	4.1%	3.56×10^{13}	0.054
34	-30	39.3%	10	75.3%	24.7%	5.72×10^{13}	0.045
35	-30	39.3%	30	46.0%	54.0%	3.01×10^{14}	0.035
36	-30	39.3%	50	31.3%	68.7%	3.09×10^{14}	0.049
37	-30	39.3%	70	21.3%	78.7%	--	--
38	-30	39.3%	90	24.1%	75.9%	--	--

7.4.3 **Cellular Morphology**

7.4.3.1 Cell Nucleation Density and Average Cell Size

Table 7.2 summarizes the cell nucleation density and average cell size of the foams selected for cellular morphology investigation. Figure 7.3 shows cell nucleation density as a function of foaming temperature for foams initially saturated at different temperatures (T_{sat}). We can see that a lower saturation temperature (thus higher equilibrium mass% of CO_2 from Table 7.1) results in a higher cell nucleation density. For example, the cell nucleation densities have 7 orders of magnitude increase from about 10^7 cells/cm^3 for T_{sat}= 40 ℃ samples to around 10^{14} cells/cm^3 for T_{sat}= -30 ℃ samples.

Figure 7.4 shows average cell size as a function of foaming temperature for foams initially saturated at different temperatures (T_{sat}). A higher equilibrium mass% of CO_2 at the lower T_{sat} leads to a smaller cell size. The largest cell is 96 μm for T_{sat} =40 ℃ foams and the smallest cell is 35 nm for T_{sat} =-30 ℃ foams. For T_{sat} =40 °C, 20 °C and 0 °C samples, cell sizes are all above 1 μm. These are typical microcellular foams. For T_{sat} =-10 ℃ sample, cell sizes span a wide range, from 173 nm up to 4.3 μm, about 25 times difference. At this T_{sat} and corresponding 32.6% equilibrium mass% of CO_2, cell nucleation and cell size are very sensitive to the foaming temperature, resulting in a wide range of both cell nucleation density (see Figure 7.3) and cell size. In contrast, at other T_{sat}, cell sizes remain relatively constant with foaming temperature. For -20 ℃ and -30 ℃ saturated samples, cell sizes fall well below 100 nm, mostly in the 30-60 nm range.

Figure 7.5 and Figure 7.6 show SEM images of samples saturated at different, and then foamed at the same temperature, 50 ℃ and 90 ℃, respectively. Note that T_{sat} = 40 °C samples didn't foam under 50 °C, and T_{sat} = -30 °C samples didn't have regular cellular structure when foaming at 90 °C, and thus the no SEMs are shown here in the figures.

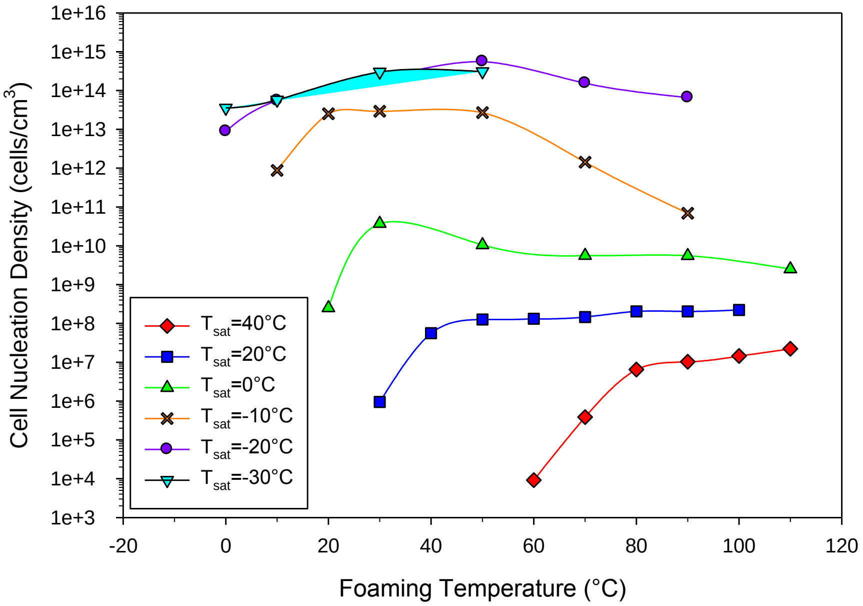

Figure 7.3 Cell nucleation density as a function of foaming temperature for foamed samples saturated at different temperatures.

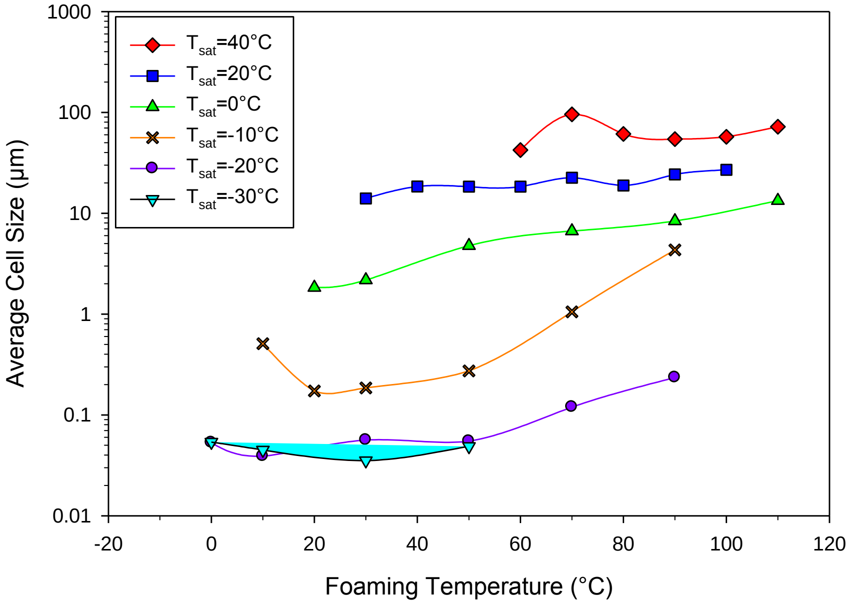

Figure 7.4 Average cell size as a function of foaming temperature for foamed samples saturated at different temperatures.

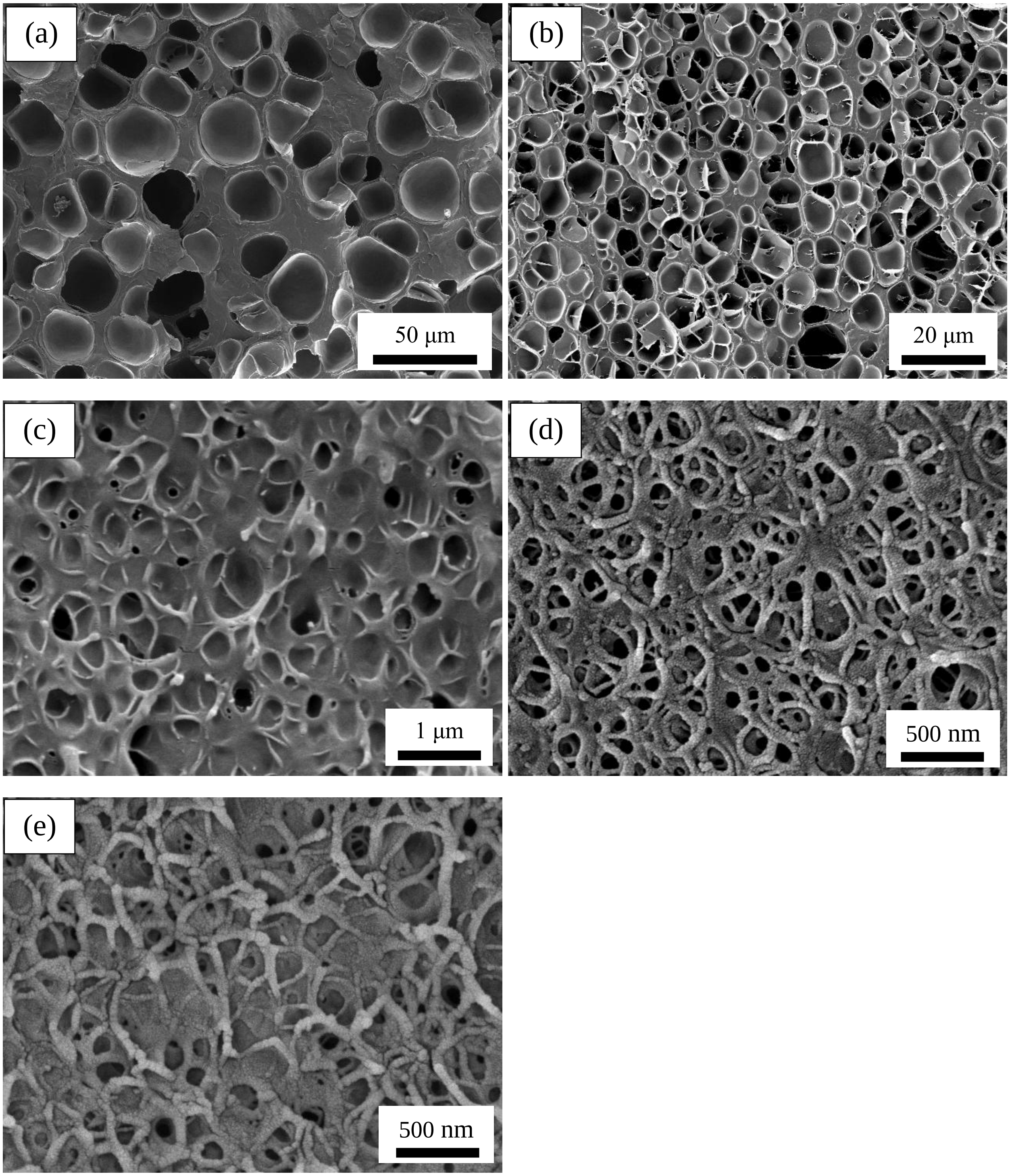

Figure 7.5 SEM images of (a) sample #9, cell size 18 μm, (b) sample #17, cell size 4.8 μm, (c) sample #24, cell size 273 nm, (d) sample #30, cell size 55 nm, and (e) sample #36, cell size 49 nm. All samples were foamed at 50 ℃. Notice the scale bars of the image are different.

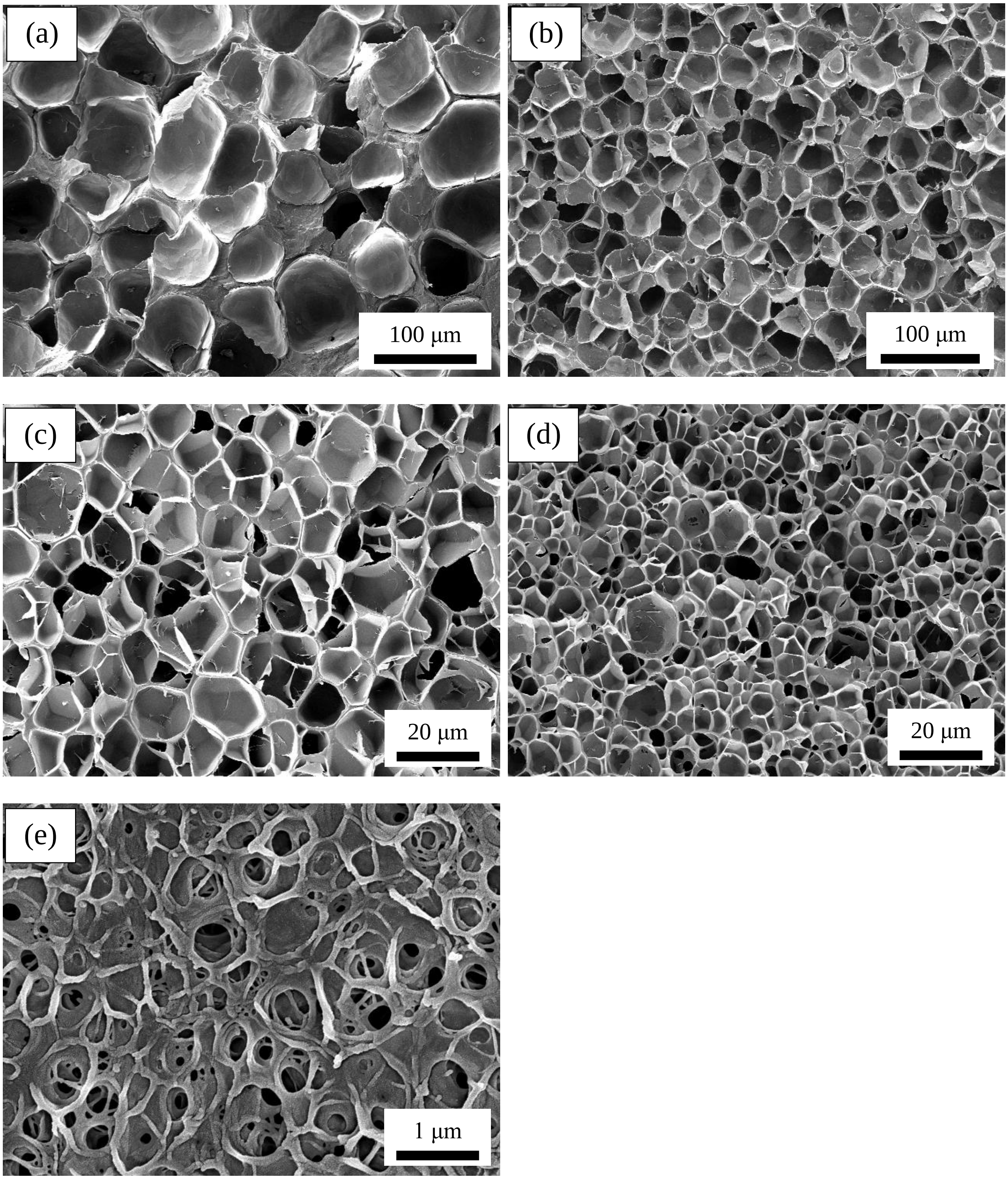

Figure 7.6 SEM images of (a) sample #4, cell size 57 μm (b) sample #13, cell size 24 μm, (c) sample #19, cell size 8.4 μm, (d) sample #26, cell size 4.3 μm, and (e) sample #32, cell size 235 nm. All samples were foamed at 90 °C. Notice the scale bars of the images are different.

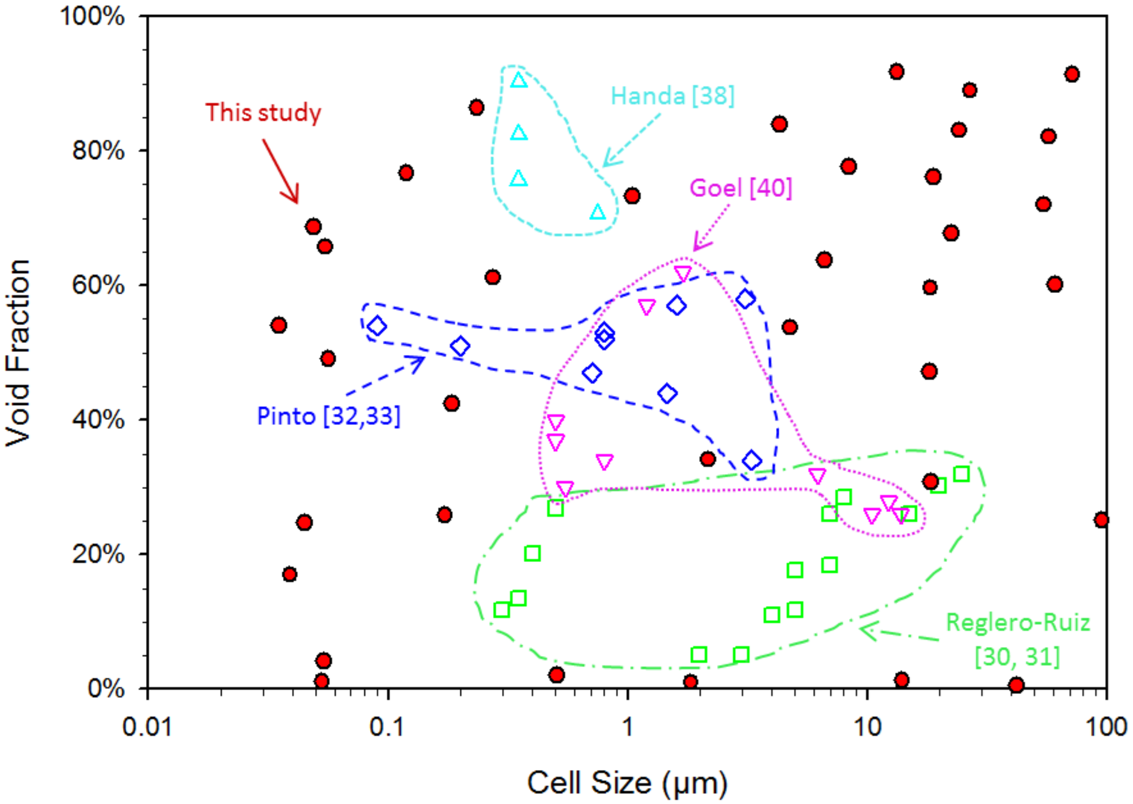

Figure 7.7 Void fraction as a function of cell size. Results from this study as well as other studies on PMMA foams are shown.

In Figure 7.7, we plot the void fraction as a function of cell size (data from Table 2). To give a better perspective of the capability of our method, literature data from other studies on PMMA foams are also shown. Handa and Zhang [38] used 3.4 MPa and -0.2 ℃ as the saturation condition, and other studies [30-33, 40] used supercritical CO_2 to saturate PMMA. In our study, by varying the saturation temperatures and foaming temperature, a very wide range of void fraction and cell size are achievable. Void fraction ranges from 0.5% to 91.7%, and cell size spans three orders of magnitude, from 35 nm to 96 μm. Using our low temperature saturation method, we are able to achieve cell size in the 30-40 nm range, which is the smallest ever reported for PMMA nanofoams. Also, for cell size below 100 nm, a range of void fraction (up to 68.7%) can be obtained in our process. Foams with high void fraction and small cell size are most desirable for thermal insulation applications.

7.4.3.2 Critical Concentration for Creating Nanofoams

From the above section, we see that the amount of CO_2 in PMMA significantly affects the nucleation density and cell size. How does the mass% of CO_2 affect the nucleation density and cell size quantitatively? To answer this question, in Figure 7.8 and Figure 7.9, we plot the cell nucleation densities and cell sizes at various saturation temperatures (T_{sat}) as a function of equilibrium mass% of CO_2. At each saturation temperature, data from different foaming temperatures are plotted together.

For 11.4% - 30.1% range, cell nucleation density exponentially increases with equilibrium mass% of CO_2. However, above 30.1% and up to 35.6%, the exponential increase of cell nucleation density is more significant (as can be seen from the much larger slope of the straight line). In this range, a 5.5% increase in the amount of CO_2 brings about four orders of magnitude increase in cell nucleation density, compared to only three order of magnitude increase in cell nucleation density for a 18.7% increase in the amount of CO_2 when equilibrium mass% of CO_2 is below 30.1%. Correspondingly, there is a sudden change in the slope of the cell size vs equilibrium mass% of CO_2 in the region 30.1%-32.6%, where a much more rapid decrease of cell size occurs and the cell size falls to below 100 nm. Therefore, there exists a critical concentration between 30.1% and 32.6%, where a significantly more rapid increase of nucleation density and decrease of cell size occurs. The critical CO_2 mass% phenomenon for creating nanofoams was reported in a few studies. The critical CO_2 mass% is 9.4%-11% for polyetherimide [22], 15.9%-18.9% for polycarbonate [24], and 10.7%-12.3% for polysulfone [25].

If we further increase the mass% of CO_2, can we achieve higher nucleation density and even smaller cell size? Our results provide some insights to this question. We can see that above 35.6%, a further increase in equilibrium mass% of CO_2 doesn’t result in an increase of cell nucleation density or a decrease of cell size. Instead, a relatively constant nucleation density and cell size is observed. This suggests that the additional amount of CO_2 does not enhance the cell nucleation and growth, and might simply diffuse out of the PMMA matrix during foaming process.

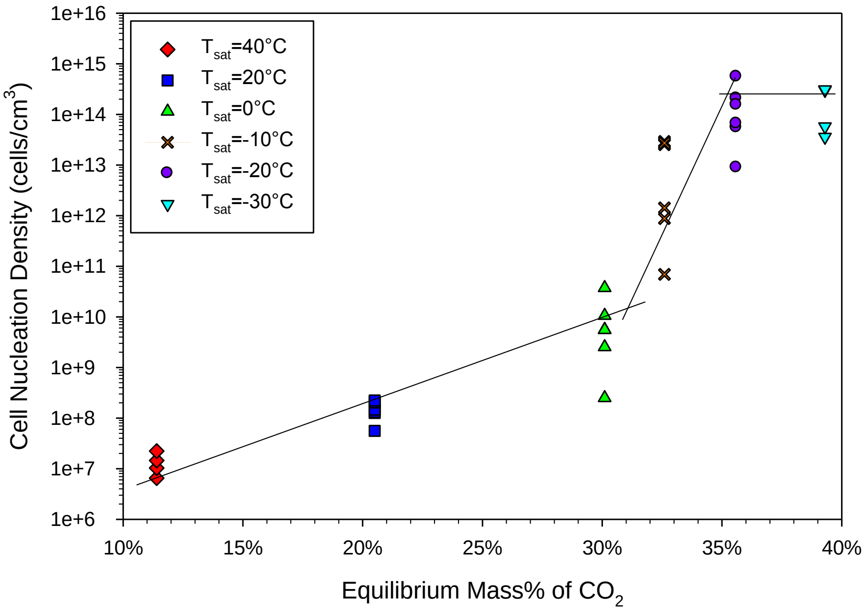

Figure 7.8 Cell nucleation density as a function of equilibrium mass% of CO_2. Cell nucleation densities obtained at different foaming temperatures are included. Lines are drawn to show the trend.

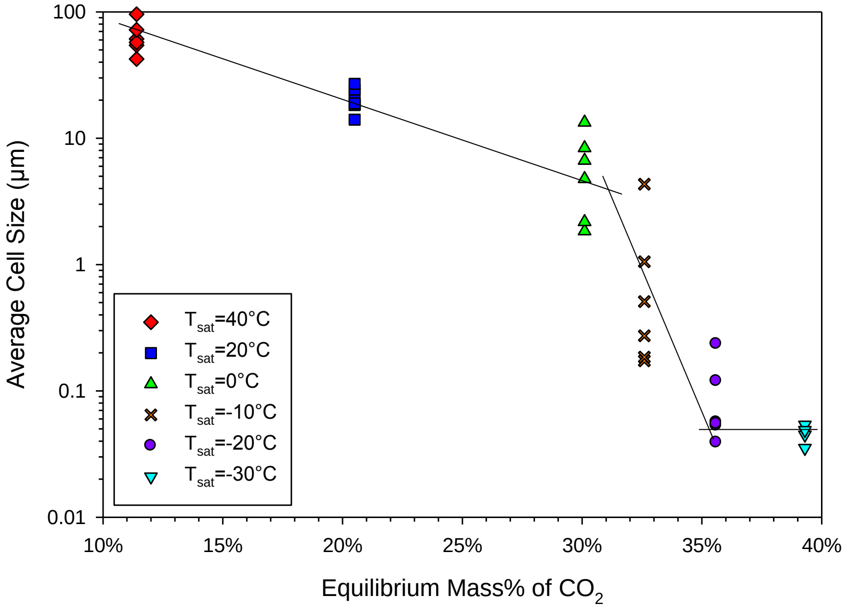

Figure 7.9 Average cell size as a function of equilibrium mass% CO_2. Lines are drawn to show the trend. Note the more rapid decrease of cell size beyond 30.1% equilibrium mass% CO_2 and the cell size transitions from microscale to nanoscale.

To understand the relationship between the nucleation density and mass% of CO_2, we resort to two available nucleation theories for some insights. Colton and Suh [41] developed a model based on classical nucleation theory, to predict the rate of nucleation of gas bubbles in microcellular foam made from amorphous thermoplastics. Two nucleation regimes were proposed: homogeneous nucleation and heterogeneous nucleation. Homogeneous nucleation occurs when a sufficient number of gas molecules come together to produce stable nuclei. Heterogeneous nucleation occurs when a second phase, such as additive or nucleating agent, is present, where the interfaces between the polymer matrix and the additives or nucleation agents act as nucleation sites. In our study, there were no nucleating agents used, so the expected nucleation mechanism is homogeneous nucleation. The rate of nucleation via homogeneous nucleation mechanism is given by Colton and Suh [41] as

$$N_{hom} = C_0 f_0 \exp\left(-\frac{\Delta G_{hom}}{kT}\right) \tag{4}$$

$$\Delta G_{hom} = \frac{16\pi\gamma^3}{3(p_s - p_0)^2} \tag{5}$$

where

N_{hom} = number of bubbles nucleating per cm^3 per second

C_0 = concentration of gas molecules, molecules/cm^3

f_0 = frequency factor of gas molecules joining the nucleus, sec^{-1}

ΔG_{hom} = Gibbs free energy (or activation energy barrier) for homogeneous nucleation, J

k = Boltzmann constant, 1.38×10^{-23} J/K

T = foaming temperature, K

γ = surface energy of the polymer-bubble interface, J/m^2

p_s = gas saturation pressure, Pa

p_0 = environmental pressure, Pa

f_0 is on the order of 10^{-5} sec^{-1} given by Colton and Suh [41]. Pressure drop (p_s - p_0) is 5 MPa or 5×10^6 J/m^3. γ ranges from 4.5 - 34 mN m^{-1} (or 0.0045 - 0.034 J/m^2) for 0%-30% CO_2 solubility at 90 ℃ []. Assume that the temperature dependency of γ is the same as that of pure PMMA, $\partial\gamma / \partial T$ = - 0.076 mN m^{-1} ℃$^{-1}$

[42]. Figure 7.10 shows the comparison of experimental and predicted nucleation density as a function of equilibrium mass% of CO_2. The theory predicts neither the absolute values nor the trend of nucleation density. At very low equilibrium mass% of CO_2, e.g. 10-15%, the predicted nucleation density is close to zero, which apparently contradicts to the fact that a substantial bubble nucleation (10^5-10^7 cells/cm^3) has occurred in our experiments. Also, the rate of increase of nucleation density decreases with the equilibrium mass% of CO_2. This is in contrast to our observation that there is a more rapid increase in nucleation density above a certain mass% of CO_2. In addition, foaming temperature seems to affect the nucleation density significantly, spanning many orders of magnitude for T_f between 70 ℃ and110 ℃. However, our experimental data shows a maximum difference of two orders of magnitude for this range of foaming temperatures. We conclude that the homogenous nucleation theory is not able to predict the nucleation density results observed in our study. The failure of using homogeneous nucleation theory to predict cell nucleation in polymer-gas systems was also reported in previous studies [7, 43], especially at low pressure conditions (up to 21 MPa).

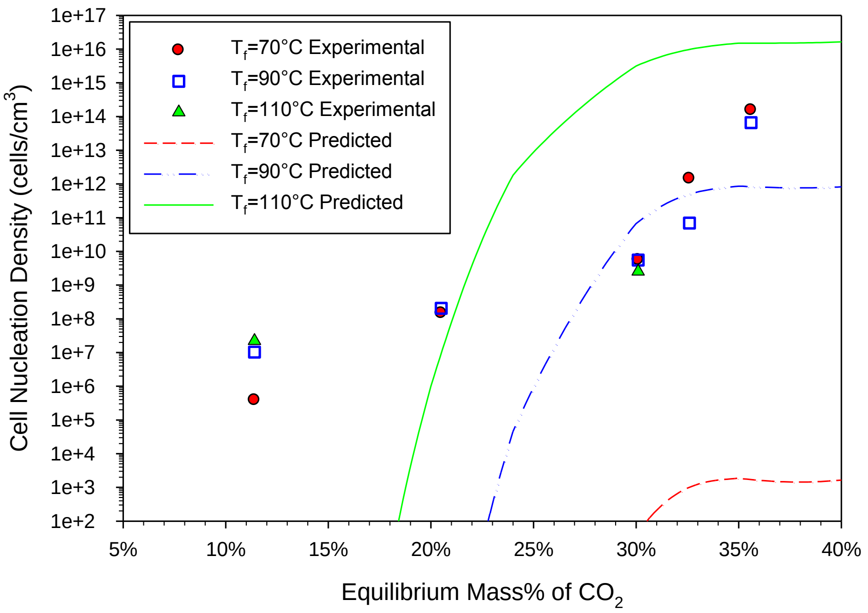

Figure 7.10 Comparison of experimental and predicted nucleation density as a function of equilibrium mass% of CO_2 for different foaming temperatures. The prediction is based on the homogeneous nucleation theory.

Another nucleation mechanism of gas bubbles in polymers proposed by Kweeder et al. [44] doesn't rely on classical nucleation theory. The model assumes a log-normal distribution of extremely small microvoids, resulting from the thermal processing history of the polymer. Bubbles formation relies on the survival of these voids to grow rather than the formation of a new phase as modeled by classical nucleation theory. The nucleation density is calculated by determining which microvoids within the distribution are large enough to survive as stable nuclei. This model predicts substantial bubble nucleation in the low pressure range, such as 1-5 MPa. However, the assumed size distribution of microvoids has yet to be confirmed.

The nucleation mechanism for cell nucleation polymer-gas system in the solid state is not well understood at present and is a subject of continuing investigation. Further investigations are undertaken to look into the nucleation mechanism and critical CO_2% for creating nanofams reported in this study. Nevertheless, our results show that cellular characteristics, i.e. nucleation density and cell size, can be highly tunable by adjusting the saturation and foaming conditions.

7.4.3.3 Bicontinuous Nanoporous Structures

For samples with sufficiently high CO_2 mass% (35.6% at -20 ℃ T_{sat} and 39.3% at -30 ℃ T_{sat}), foaming at higher temperatures (≥ 30°C) result in porous structures. Samples #29, #30, #31, #32, #35, #36 all show bicontinuous nanoporous structures. Figure 7.11 shows an example sample which was prepared by saturating at -20 ℃ and then foamed at 70 ℃. The relative density is 23.4%. The visible underlying struts indicate some interconnectivity in the structure. The open nanoporous structure can potentially be used for filtration, gas separation, and battery separator applications.

As can be noticed, a combination of sufficiently high CO_2 mass% and sufficiently high foaming temperature is needed to generate bicontinous nanoporous structures. A CO_2 mass% larger than 35.6% and a foaming temperature higher than 30 ℃ is found to be needed for generating nanoporous structures in PMMA. Krause et al. [21] also reported the open nanoporous structure in PEI and PES when processed with higher CO_2 mass% and at high foaming temperatures.

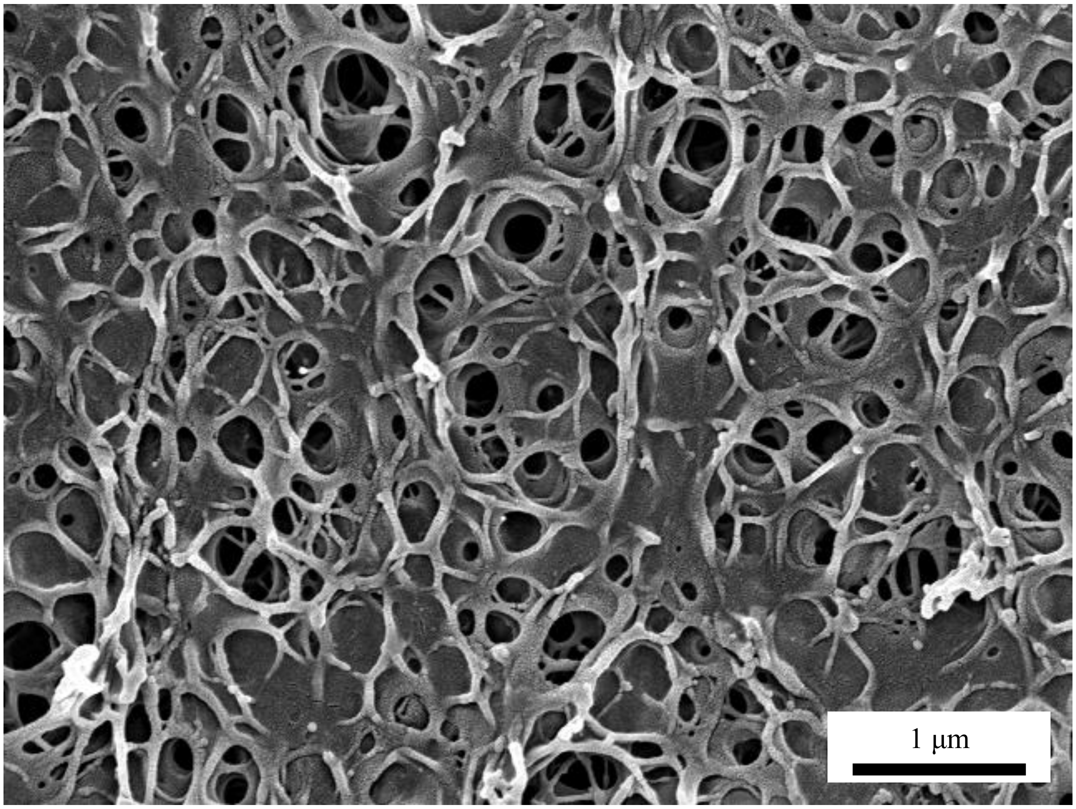

Figure 7.11 SEM of sample #31, 23.4% relative density and 120 nm cell size. Note that pores are interconnected, indicating porous nature of the structure.

Two major mechanisms are known to occur in new phase formation [45-49]. The separation of gas phase (e.g. CO_2) from the polymer phase (e.g. PMMA) may take either of the two mechanisms. One is nucleation and growth in which discrete nuclei form and grow over time. The other is spinodal decomposition, in which a wavelike concentration fluctuation with periodic wavelength increasing over time by uphill diffusion, producing an interconnected bicontinuous structure [46]. One might argue that rapid cell wall rupture of closed cells (created via nucleation and growth) at higher temperatures might result in the nanoporous structures. Cell wall rupture is an unpredictable phenomenon and typically generates non-uniform structures. However, the nanoporous structures we obtained are very uniform, which suggests that cell wall rupture does not occur. Therefore, we believe the spontaneous spinodal decomposition mechanism is more likely to be responsible for creating the bicontinuous nanoporous structures.

Figure 7.12 shows a general schematic of low critical solution temperature (LCST) phase diagram of polymer-solvent mixture, determined by a combination of temperature and solvent concentration values. LCST will be explained later. Below a certain temperature the polymer and solvent form a homogenous solution at all compositions. But at other higher temperature, the system is not stable at certain compositions and will separate into two phases. If the temperature increase results in a metastable state, nucleation will be the dominant mechanism; in the unstable region, the spinodal decomposition will be the dominant mechanism [46, 50, 51]. Binodal and spinodal lines define the boundaries between different regions.

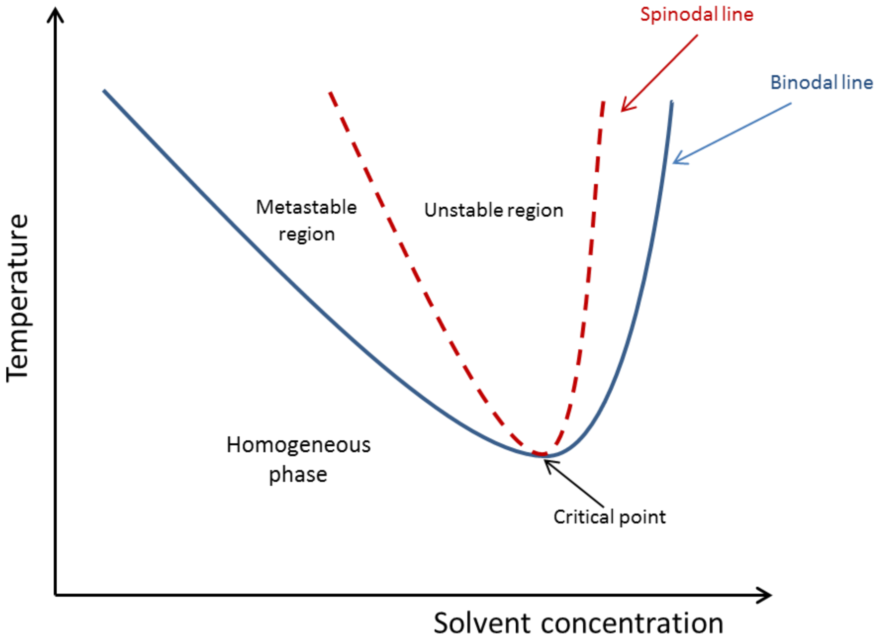

Figure 7.12 General schematic of LCST phase diagram for polymer-solvent mixture.

An established theory to understand the thermodynamics of polymer-solvent mixture is the Flory-Huggins theory. It is commonly used to analyze the phase behavior of polymer-solvent mixture. The binodal and spinodal decomposition lines are attained by solving the following equations [46, 47]:

Gibbs free energy of mixing: $$\Delta G_{mixing} = kT(N_1 \ln \emptyset_1 + N_2 \ln \emptyset_2 + \chi N_1 \emptyset_2) \quad (6)$$

Binodal line: $$\frac{\partial \Delta G_{mixing}}{\partial \emptyset_1} = 0 \quad (7)$$

Spinodal decomposition line: $$\frac{\partial^2 \Delta G_{mixing}}{\partial {\emptyset_1}^2} = 0 \quad (8)$$

where

N_1 = number of solvent molecules

N_2 = number of polymer molecules

$\emptyset_1$ = volume fraction of solvent

$\emptyset_2$ = volume fraction of polymer

χ = Flory-Huggins interaction parameter (generally a function of T)

k = Boltzmann constant

T = temperature in K

We use the Flory-Huggins theory to estimate the phase diagram of the PMMA-CO_2 when the mixture is in the solid state. Since little information regarding to the interaction parameter χ (T) for solid-state polymer-gas mixture (including PMMA-CO_2) is available, we need to obtain χ (T) via experiments. Experimentally, the binodal curve of a solution is often approximated by a cloud-point curve [52]. The cloud point is the temperature at which dissolved solids are no longer completely soluble, precipitating as a second phase giving a cloudy appearance. In our study, we obtained the minimum foaming temperature by raising the foaming temperature incrementally until the foaming started to occur [39]. The minimum foaming temperature line is similar to the cloud-point for solution, and thus can be considered as binodal line for PMMA-CO_2 system.

From this binodal line, we are able to find the interaction parameter χ(T) at different T. For most of the polymer-solvent systems, the χ(T) decreases with increasing temperature, showing an upper critical solution temperature (UCST) and phase separation occurs at some lower temperature. However, in our system, χ(T) actually increases with increasing temperature, from $\chi = 0.882$ at 42.5°C to $\chi = 1.702$ at 82.5 ℃. This results in lower critical solution temperature (LCST), phase separation occurring at some higher temperature. In Figure 7.14, we plot the estimated spinodal decomposition line (dashed line). We can see that the theory can provide an estimate of the closed-cell to open-cell transition in the nanocells region (i.e. closed nanocellular to bicontinuous nanoporous). The predicted transition temperatures are about 20 ℃ higher than our experimental values. The theory also predicts a closed-cell to open-cell transition in the microcells region, which is not observed in our experiments. Although discrepancies exist between the predicted and experimental data, our results suggest the possibility that at least in the nanocells region the close-cell to open-cell transition could be due to spinodal decomposition.

The discrepancies between the predicted and experimental data could be due to various reasons. There are limitations to the theory itself. Volume change upon mixing the polymer and solvent, the contribution of polymer chain flexibility to the entropic term, and specific polymer-solvent interactions are all neglected in the theory. Also, the minimum foaming temperature line is an approximation of the binodal line of the system. The $\chi(T)$ obtained from equating these two lines might not be very accurate. In addition, the loss of CO_2 upon heating before or during cell nucleation is neglected in the theory. Unlike liquid polymer-solvent solution case where mass loss of either polymer or solvent is negligible, the diffusion of CO_2 to the outside of the PMMA-CO_2 mixture reduces the amount of CO_2 participating in the phase separation, which is not accounted for in the theory. An improved model needs to be developed in the future.

7.4.3.4 Worm-like Nanostructures

When foamed at 70 ℃ and above, -30 ℃ saturated samples (sample #37 and #38) showed uniform worm-like nanostructures, which have not been reported before. These structures seem very different from the regular foams structures (see Figure 7.5 and Figure 7.6). Figure 7.13 shows these interesting structures. The diameter of the “worms” is about 100 nm. The “worms” seem to be tightly packed together, with some spacing between. However, the relative density is very low, about 21.3%. This lower relative density is unlikely to be justified by the volume of the spacing between “worms” shown in the micrographs. This leads us to suspect that the “worms” have pores in themselves. One possibility is that there are pores throughout the “worms”, but they are too small to be detected by SEM. The other possibility is that pores only exist inside the “worms”, and there is a solid skin on the surface. SEM cannot detect the pores under the solid skin. Other tools, such as TEM and FIB-SEM, might be used to substantiate the existence of these pores. One hypothesis for the formation of these hollow “worms” is that upon heating, the initially homogeneous PMMA-CO_2 solution form many individual nanosized domains, and within each domain polymer/gas phase separation occurs locally. These domains become the “worms”, and localized phase separation creates the pores inside the “worms”. Further investigation on the formation mechanism and potential applications of the worm-like nanostructures are needed.

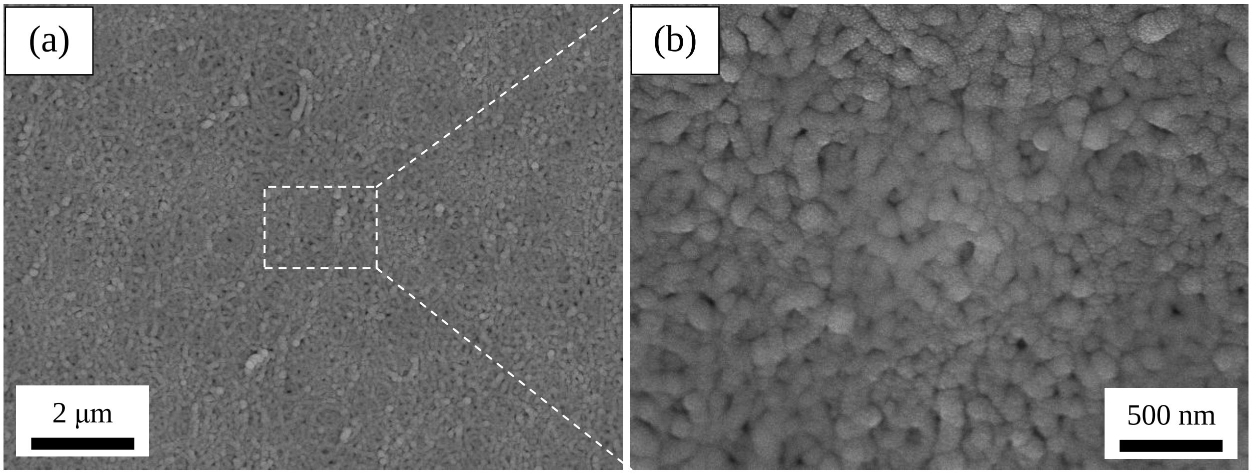

Figure 7.13 Sample #37, 21.3% relative density, showing uniform worm-like nanostructures. The diameter of the “worms” is about 100 nm. (b) is a zoom-in image of (a) in center area.

7.4.4 **Equilibrium mass percentage of CO_2 - foaming temperature-structure Diagram**

Figure 7.14 summarizes our results with a diagram that correlates foam structures with the equilibrium mass% of CO_2 and foaming temperature (T_f). Experimental data points from this study are shown. The typical way of generating phase diagram for polymer/solvent is to plot the temperature against solvent concentration and identity the corresponding structures. Our diagram is created the same way and thus it should be part of the PMMA-CO_2 phase diagram. In our diagram, we have identified five different regions:

1) Below the effective T_g line of PMMA-CO_2 mixture (see part I of this paper), no cellular structure is observed and samples remain solid. Phase separation does not occur and CO_2 simply diffuses out of the PMMA matrix.
2) Above the effective T_g line and when mass% $CO_2 \leq 30.1\%$, microcellular foams with cell size in the range of 1 – 100 µm are obtained. Also, when mass% $CO_2 = 32.6\%$ and $T_f \geq 70$ °C, the cell sizes are also in the microcellular range.
3) When mass% $CO_2 = 32.6\%$ and $T_f \leq 50$ °C, or mass% $CO_2 = 35.6\%$ or 39.3% and $T_f \leq 10$ °C, nanocellular foams with cell size in the range of 40 nm - 500 nm are achieved. The cells are closed cells. The formation mechanism of closed cellular structures (including the microcellular region mentioned above) is the typical cell nucleation and growth.
4) When mass% $CO_2 = 35.6\%$ and $T_f \geq 30$ °C, or mass% $CO_2 = 39.3\%$ and 30 °C $\leq T_f \leq$ 50 °C, bicontinuous nanoporous structures are created, where pores are interconnected. Spinodal decomposition is shown to be responsible for this open porous structure.
5) When mass% $CO_2 = 39.3\%$ and $T_f \geq 70$ °C, novel worm-like nanosturcures are obtained. These nanoworms probably have pores inside, as can be deduced from its low relative density. The novel structure is hypothesized due to localized phase separation within nanosized domains of polymer/gas mixture.

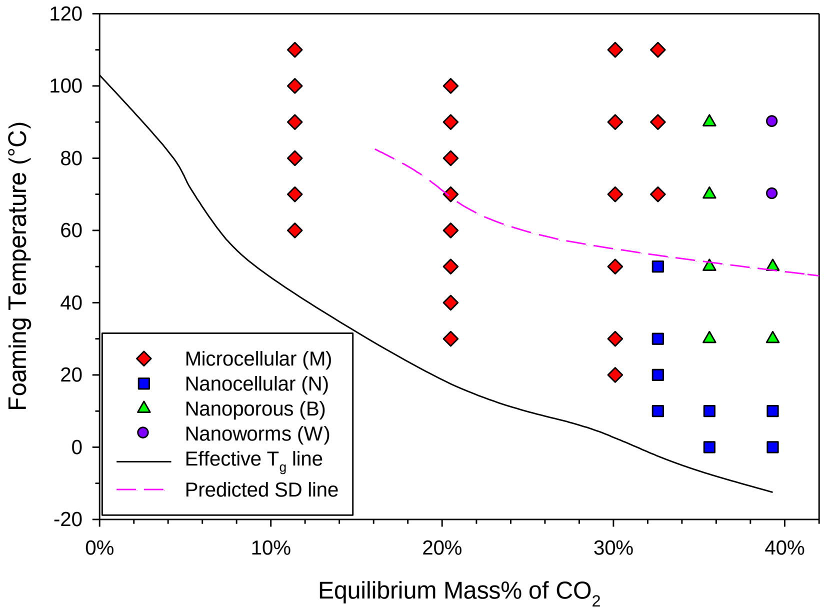

Figure 7.14 Equilibrium mass% of CO_2 - foaming temperature – structure diagram, for creating PMMA with solid (S) or non-cellular structure, microcellular structure (M), nanocellular structure (N), bicontinuous nanoporous structure (B), and worm-like nanostructure (W). The effective T_g line and estimated spinodal decomposition (SD) line are also included.

7.5 **Summary**

A low-temperature saturation pathway to create PMMA nanofoams was discovered in this study. Uniform PMMA nanofoams with average cell sizes in 30-40 nm range and cell nucleation densities over 10^{14} cells/cm^3 have been achieved. Nanofoams with void fraction as high as 86% are created.

A range of solubility, from 11.4% to 39.3%, was achieved by varying the saturation temperature (T_{sat}) over the range of -30 ℃ to 40 ℃. The amount of CO_2 absorbed greatly influences cellular structure. As CO_2 mass% increases, cell nucleation densities increase and cell sizes reduce across the mass% range investigated. More importantly, we have identified a critical CO_2 mass% between 30.1% and 32.6%. Above this critical mass%, cell nucleation density increases much more rapidly with a small increase in CO_2 mass%, and consequently microcellular foams turn into nanocellular foams. Compared to previous studies, our low temperature saturation method expands the processing space of PMMA foams, especially in generating nanofoams with high void fraction and very small cell size.

In addition, a transition from closed nanocellular to bicontinuous nanoporous structure has been observed when PMMA saturated with very high CO_2 mass% (35.6% - 39.3%) were foamed at temperatures ≥ 30 ℃. The nanoporous structure is shown to be due to spinodal decomposition. Moreover, a novel worm-like nanostructure have been discovered when PMMA saturated with 39.3% CO_2 mass% and then foamed at ≥ 70 °C.

7.6 Acknowledgment

The authors would like to acknowledge the financial support from the University of Washington CGF fund and National Science Foundation Grant CMMI 1253072. We would like to thank undergraduate research assistants Varun Gupta and Ankita Sharma from IIT-Gandhinagar, for their help in some of the experiments. Also, we acknowledge Evonik Cyro LLC for providing relevant material property information.

7.7 References

1. McIntire OR. Manufacture of cellular thermoplastic products. The Dow Chemical Company. US Patent 2,450,436, 1948.
2. Amos JL. Method of making cellular thermoplastic products. The Dow Chemical Company. US Patent 2,576,911, 1951.
3. Martini JE, Waldman FA, and Suh NP. The production and analysis of microcellular thermoplastic foam. SPE ANTEC. San Francisco, CA, 1982. Vol. 28, pp 674.
4. Martini JE, Suh NP, and Waldman FA. Microcellular closed cell foams and their method of manufacture. Massachusetts Institute of Technology. US Patent 4,473,665, 1984.
5. Kumar V and Weller JE. International Polymer Processing 1993;8(1):73-80.
6. Murray RE, Weller JE, and Kumar V. Cellular Polymers 2000;19(6):413-425.
7. Kumar V and Weller J. Journal of Manufacturing Science and Engineering 1994;116(4):413-420.
8. Shimbo M, Higashitani I, and Miyano Y. Journal of Cellular Plastics 2007;43(2):157-167.
9. Guo H, Nadella K, and Kumar V. Journal of Materials Research 2013;28(17):2374-2379.
10. Guo H and Kumar V. Solid-state Microcellular Foaming of Low- and High- Tg Cyclic Olefin Copolymer (COC). SPE FOAMS Conference. Iselin, NJ, 2014.
11. Guo H and Kumar V. Journal of Applied Polymer Science 2015;132(28):42226.
12. Richards E, Rizvi R, Chow A, and Naguib H. Journal of Polymers and the Environment 2008;16(4):258-266.
13. Wang X, Kumar V, and Wei L. Cellular Polymers 2007;26(1):1-25.
14. Biener J, Hodge AM, Hayes JR, Volkert CA, Zepeda-Ruiz LA, Hamza AV, and Abraham FF. Nano Letters 2006;6(10):2379-2382.
15. Miller D and Kumar V. Polymer 2011;52(13):2910-2919.
16. Zhou C, Vaccaro N, Sundarram SS, and Li W. Journal of Cellular Plastics 2012;48(3):239-255.

17. Pinto J, Solorzano E, Rodríguez-Pérez MA, de Saja JA, and Dumon M. Thermal conductivity transition between microcellular and nanocellular polymeric foams: experimental validation of the Knudsen effect. SPE FOAMS Conference. Barcelona, Spain, 2012.
18. Notario B, Pinto J, Solorzano E, de Saja JA, Dumon M, and Rodríguez-Pérez MA. Polymer 2015;56:57-67.
19. Lu GQ and Zhao XS. Nanoporous materials: science and engineering. London: Imperial College Press, 2004; Chapter 1, pp 1-13.
20. Hedrick JL, Carter KR, Cha HJ, Hawker CJ, DiPietro RA, Labadie JW, Miller RD, Russell TP, Sanchez MI, Volksen W, Yoon DY, Mecerreyes D, Jerome R, and McGrath JE. Reactive and Functional Polymers 1996;30(1–3):43-53.
21. Krause B, Sijbesma HJP, Münüklü P, van der Vegt NFA, and Wessling M. Macromolecules 2001;34(25):8792-8801.
22. Miller D, Chatchaisucha P, and Kumar V. Polymer 2009;50(23):5576-5584.
23. Krause B, Diekmann K, van der Vegt NFA, and Wessling M. Macromolecules 2002;35(5):1738-1745.
24. Guo H and Kumar V. Polymer 2015;56:46-56.
25. Guo H, Nicolae A, and Kumar V. Journal of Polymer Science Part B: Polymer Physics 2015;53(14):975-985.
26. Nemoto T, Takagi J, and Ohshima M. Polymer Engineering & Science 2010;50(12):2408-2416.
27. Nemoto T, Takagi J, and Ohshima M. Macromolecular Materials and Engineering 2008;293(7):574-580.
28. Nemoto T, Takagi J, and Ohshima M. Macromolecular Materials and Engineering 2008;293(12):991-998.
29. Reglero Ruiz JA, Dumon M, Pinto J, and Rodriguez-Pérez MA. Macromolecular Materials and Engineering 2011;296(8):752-759.
30. Reglero Ruiz JA, Pedros M, Tallon JM, and Dumon M. The Journal of Supercritical Fluids 2011;58(1):168-176.
31. Reglero Ruiz JA, Tallon JM, Pedros M, and Dumon M. The Journal of Supercritical Fluids 2011;57(1):87-94.
32. Pinto J, Dumon M, Pedros M, Reglero Ruiz JA, and Rodriguez- Pérez MA. Chemical Engineering Journal 2014;243:428-435.
33. Pinto J, Reglero Ruiz JA, Dumon M, and Rodriguez- Pérez MA. The Journal of Supercritical Fluids 2014;94:198-205.
34. Costeux S, Khan I, Bunker SP, and Jeon HK. Journal of Cellular Plastics 2015;51(2):197-221.
35. Costeux S, Khan I, Bunker SP, and Jeon HK. Journal of Cellular Plastics 2014.
36. Costeux S and Zhu L. Polymer 2013;54(11):2785-2795.
37. Costeux S. Journal of Applied Polymer Science 2014;131(23):41293.
38. Handa YP and Zhang Z. Journal of Polymer Science Part B: Polymer Physics 2000;38(5):716-725.
39. Guo H and Kumar V. Polymer 2015;57:157-163.
40. Goel SK and Beckman EJ. Polymer Engineering & Science 1994;34(14):1148-1156.
41. Colton JS and Suh NP. Polymer Engineering & Science 1987;27(7):485-492.
42. Cherry BW. Polymer Surfaces: Cambridge University Press, 1981; Chapter 1, pp 9.
43. Goel SK and Beckman EJ. Polymer Engineering & Science 1994;34(14):1137-1147.
44. Kweeder JA, Ramesh NS, Campbell GA, and Rasmussen DH. The nucleation of microcellular polystyrene foam. SPE ANTEC. Montreal, Canada, 1991. Vol. 37, pp 1398-1400.
45. Olabisi O, Robeson LM, and Shaw MT. Polymer-Polymer Miscibility. New York: Academic Press, 1979; Chapter 2, pp 31-47.
46. Sperling LH. Introduction to Physical Polymer Science, 4th ed. Hoboken, NJ: John Wiley & Sons, Inc., 2006; Chapter 4, pp 153-162.
47. Hamley IW. Introduction to Soft Matter. Chichester: John Wiley & Sons, Ltd., 2000; Chapter 2, pp 74-90.

48. Strobl G. The Physics of Polymers: Concepts for Understanding Their Structures and Behavior, 3rd ed. Berlin: Springer, 2007; Chapter 4, pp 122-129.
49. Fukasawa Y, Saito H, Kato M, Chiba T, and Inoue T. Polym. J 2008;40(4):339-342.
50. Jacobs LJM, Kemmere MF, and Keurentjes JTF. Green Chemistry 2008;10(7):731-738.
51. Strathmann H. Introduction to Membrane Science and Technology. Weinheim, Germany: Wiley-VCH, 2011; Chapter 3, pp 126-133.
52. Chen JS, Tu SL, and Tsay RY. Journal of the Taiwan Institute of Chemical Engineers 2010;41(2):229-238.

Chapter 8

Solid-state Microcellular and Nanocellular Polysulfone (PSU) Foams

8.1 **Abstract**

In this paper, we report on the process for creating microcellular and nanocellular polysulfone (PSU) foams. Microcellular foams with cell size up to 8 μm and nanocellular foams with cell size in the range of 20-30 nm were created. A range of CO_2 concentration was achieved by varying saturation temperature, from 5% at 60 ℃ to 14.7% at -10 ℃. The CO_2 concentration has a strong influence on the cellular structure. There exists a critical concentration, between 10.7% and 12.3%, above which cell nucleation densities increase rapidly and cell sizes drop from micrometer range to below 1 μm into the nanometer range. Nanofoams with cell nucleation densities exceeding 10^{15} cells/cm^3 and void fraction of up to 48% are achieved. At the high CO_2 concentration region, the change from closed nanocellular structure to bicontinuous nanoporous structure is observed. Also, nanostructures on the cell wall of microcells are observed and believed to be formed via stress-induced nucleation/spinodal decomposition. The PSU nanofoams produced in this study present an opportunity to produce polymer nanofoams with a relatively high service temperature. The ability to create cells of different length scales provides an opportunity to study the effect of cell size on the foams properties.

Keywords: microcellular; nanocellular; nanofoams; nanoporous; solid-state

8.2 **Introduction**

Nanocellular polymer foams (or polymer nanofoams), are thermoplastic foams with cell size in the range of nanometers. During the past decade, they have drawn tremendous attention from researchers in academia and various industries, such as the aerospace, building, insulation, electronics and membrane

---

This chapter has been published in Journal of Polymer Science, Part B: Polymer Physics, 2015, 53: 975-985 (featured in journal cover).

industries. Nanofoams can be regarded in concept as an extension of microcellular foams with cells on the order of 10 μm, that was conceived at MIT three decades ago [1, 2]. The rationale of introducing microsized bubbles was that if the cell size is smaller than the critical flaws, already existing in the polymer matrix and could be introduced in larger numbers, then the density could be reduced while maintaining the essential mechanical properties. Later studies verified the much improved properties in microcellular foams [3-9].

Now nanofoams have cell size that is 1,000 times smaller than that of the microcellular foams. The cell size is close to the length scale of polymer molecules. It has been widely hypothesized that nanofoams would become a new class of materials that offer many properties that are superior to existing materials. Recent studies have shown some of the promising properties. Improved mechanical properties were reported in PEI nanofoams when compared to microcellular PEI foams [10, 11]. Thermal conductivity in nanofoams was reduced due to the gas phase heat conduction, when cell size is close to the mean free path of air molecules (about 70 nm at ambient temperature and pressure). This effect was known as the Knudsen effect. Experimental evidence of the Knudsen effect in polymer nanofoams were recently reported [12, 13]. A higher glass transition temperature was reported in PMMA nanofoams compared to the unfoamed polymer, possibly due to the nanoscale confinement effect of the cell wall [14]. Also, nanofoams possessing interconnected nanoporous structures were created and they can be potentially used as a new class of membranes for filtration and gas separation applications [15, 16].

Although the idea of creating nanofoams is exciting, the methods of making nanofoams have been very limited, and only a few polymers with uniform nanocells have been discovered. Polymer nanofoams were first fabricated using a template method developed by Hedrick [17]. In order to make thin film dielectric layers with very low dielectric constant for use in microelectronic devices, polyimide nanofoams were produced, from block copolymers consisting of thermally stable and thermally labile blocks, where the thermally labile blocks underwent thermolysis upon thermal treatment, leaving nanopores inside.

Solid-state gas foaming has shown a great utility in creating nanofoams. The solid-state gas foaming process was first reported in a pioneering paper by Martini et al. [2]. A two-step process was described to create microcellular structure in high impact polystyrene (HIPS), that involved saturating the polymer with a non-reacting gas and then heating the gas laden polymer to near the glass transition temperature. This process later became known as the solid-state process, as the polymer foam is created near the T_g of the gas-polymer system, well below the melting point. Using this method, nanofoams were first fabricated in LDPE [18], HDPE [18], PVC [18], PMMA [19, 20], and ABS [21, 22] with cell size between 100 nm – 1 μm. Later, PEI, PES, and PI Nanofoams with a much smaller cell size (below 100 nm) were produced [15, 16, 23].

Surrounding the solid-state foaming method, many of current research efforts on nanofoams lie in the innovation of the materials, such as copolymerization, blending one polymer with another polymer, and adding nanoparticles to polymer matrix. A review on the fabrication of nanofoams was recently published [24]. A variety of polymer blends, including PI/PSU [16], PEEK/PEI blends [25], PP/rubber blends [26, 27], PMMA/MAM blends [28, 29], and more recently in styrenic-acrylic blends PEMA/SAN and PMMA-co-EA/SAN [30] have been shown to produce nanofoams. The concept for these polymer blends nanofoams was similar: one phase acted as the matrix and the other dispersed phase served as a template for bubble nucleation and growth. For copolymers, nanofoams have been created mainly in PMMA based copolymers, such as Poly(MMA-co-EMA) and Poly(MMA-co-tBMA) [31]. Polymer nanocomposites, which have some amount of nanoparticles dispersed in the polymer matrix, have been shown to generate nanofoams, such as in Poly(MMA-co-EA) with silica nanoparticles and Poly(MMA-co-EMA) with POSS [32]. In the nanocomposites, the added nanoparticles serve as nucleation sites and greatly enhanced cell nucleation. To overcome some of the issues associated with modification of polymers, such as tedious synthesis and blending process and non-uniformity of blending and dispersion of nanoparticles, Guo and Kumar [33] recently developed a low-temperature pathway to create nanofoams in neat polycarbonate.

In this study, we report on the fabrication of PSU microcellular and nanocellular foams using solid-state foaming process. We successfully fabricated PSU nanofoams with cell size in the range of 20-30 nm and cell nucleation density exceeding 10^{15} cells/cm^3. PSU is a high-temperature commercial polymer. One application of high-temperature polymer foams is to be used as the core material for high performance lightweight sandwich structures, which are widely used in automotive, transport, and aeronautic industries. Conventional polymeric core foams have rather low temperature capabilities, and they, with cell size in the millimeter range, have much weaker mechanical properties especially at elevated temperatures, which greatly comprises structural integrity of the sandwich structure. Microcellular PSU foams were investigated in a few studies [34, 35]. Until now, PSU nanofoams have not been reported and neither has the potential property enhancement that can be realized by reducing cell size to nanometer range.

In this paper, we first show the processing space of PSU microcellular foams and nanocellular foams, including both sorption and foaming conditions in the solid-state foaming process. Characterizations of the foams properties and cellular morphologies are then presented. Microcellular structures, closed nanocellular and bicontinuous nanoporous structures, and nanostructures on the cell wall of microcells are shown.

8.3 **Experimental**

8.3.1 **Materials**

Material used in this study was TECASON^{TM}S polysulfone (PSU). 0.6 mm thick circular disc samples with 1 inch diameter were machined from a long rod. Glass transition temperature (T_g) of the materials was measured using a differential scanning calorimeter (DSC) TA Instruments Q20, with a heating rate of 10 °C/min. T_g was determined to be 185 °C using the half-height method. Density was 1.24 g/ cm^3. The molecular structure of PSU is shown in Figure 8.1. Medical grade CO_2 (99.9% purity) was purchased from Praxair, Inc.

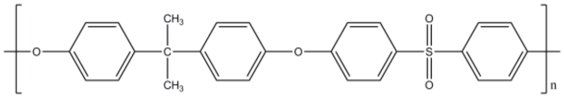

Figure 8.1 Molecular structure of PSU.

8.3.2 **Sorption**

Sorption experiments were conducted by placing samples in a pressure vessel, with the CO_2 pressure inside maintained at 5 MPa with an accuracy of +/- 0.1 MPa. In order to maximize CO_2 sorption in polymer and eliminate the need of a pressure boosting device, we chose 5 MPa as the saturation pressure, which was slightly below the pressure of a fresh CO_2 gas cylinder. Saturation temperatures (T_{sat}) were carefully controlled. For the temperatures above room temperature, a heating jacket was wrapped around the pressure vessel and a temperature controller was used to maintain the pressure vessel at a desired temperature. For the temperatures between room temperature and 0 ℃, a Peltier cooling module was used. For temperatures below 0 ℃, the pressure vessel was placed in a freezer capable of achieving -30 ℃ to 0 ℃. During saturation, samples were periodically taken out from the pressure vessel, and immediately weighed on a Mettler AE240 analytical scale accurate to +/- 10 μg. Samples were then promptly put back to the pressure vessel and repressurized. The sorption experiment continued until no further weight increase was observed in the specimen.

8.3.3 **Foaming**

Specimens used for foaming studies were first wrapped in porous paper towel, and then placed in a pressure vessel which was maintained at 5 MPa. A range of saturation temperatures were used. Samples were allowed to absorb CO_2 over a predetermined amount of time (based on sorption studies). After full saturation, samples were removed from the pressure vessel, and immediately immersed in a silicone oil bath (Thermo Haake B5) set at a desired foaming temperature (T_f). The foaming time used for all samples was 1 minute, which was sufficient to ensure the completion of foaming. After foaming, the sample was immediately quenched in an oil bath which was kept much colder than the foaming oil bath, to stop further foaming.

8.3.4 Characterizations

The excess silicone oil was removed from the surface of the sample before any characterization. The density of each sample was determined according to ASTM D792 using Mettler AE240 analytical scale. Samples were allowed to desorb for at least one week before density measurement was performed in order to eliminate the effect of residual CO_2. Three measurements were performed for each sample, with a typical standard deviation of relative density about 0.2%. Solid skin on the edge of the foam was kept for the density measurement. As will be elaborated later, the skin thickness is typically very small due to the very short desorption time. The effect of skin on the density measurement is thus negligible.

A representative set of samples were imaged with a scanning electron microscope (SEM) to examine the microstructures produced. All images were taken on a FEI Sirion SEM. Samples were first scored with a razor blade and freeze fractured with liquid nitrogen to expose the cross section. They were then coated with Au/Pd for 90 s at a current of 18 mA. Micrographs were taken at the center of the cross section of the specimen and analyzed using software ImageJ (National Institute of Health, USA). Average cell size was calculated by taking average cell diameters of at least 50 cells in the SEM micrographs. The cell nucleation density N_0 (number of cells nucleated per cubic centimeter of the original unfoamed sample) was calculated using a procedure described by Kumar and Weller [36]:

$$N_0 = (\frac{nM^2}{A})^{3/2} * \frac{1}{1-V_f} \qquad (1)$$

where V_f is the void fraction; n, the number of cells in the SEM micrograph; M, the magnification of the micrograph; A, the area of the micrograph (cm^2).

8.4 **Results and Discussions**

8.4.1 **CO_2 Solubility in PSU**

CO_2 solubility is defined as the equilibrium CO_2 concentration at a specified condition. CO_2 concentration is usually expressed as the percentage of the mass of the original polymer, e.g. 10% CO_2 concentration means CO_2 with the amount equal to 10% of the mass of original polymer is now absorbed into the polymer matrix. Note that there was a short interval between the pressure release and weight measurement in the sorption experiment. To account for the gas lost during this interval, the solubility of CO_2 in the samples was obtained by extrapolating the desorption curve to zero desorption time. Detailed procedures can be found in literature [33, 37]. Figure 8.2 shows the CO_2 solubility as a function of temperature. Solubility decreases with increasing temperature. At low temperatures, the solubility is much higher, 14.7% at -10 ℃ compared to 5% at 60 ℃. Sun and Mark [35] found that CO_2 solubility in PSU was 10% at 830 psi (or 5.7 MPa) and 22-23 ℃. Our solubility result at a similar condition (10.7% at 5 MPa and 20 ℃) is comparable with their data. Solubility is known to significantly influence cell nucleation and resulting microstructures [36, 38]. The very high solubilities at low temperatures are critical for creating nanocells in the PSU, which will be presented later.

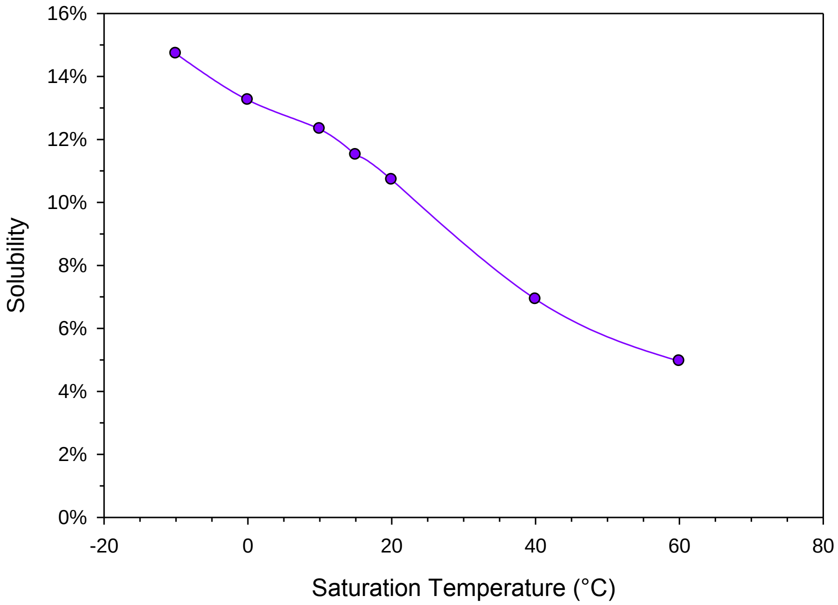

Figure 8.2 Solubility of CO_2 in PSU as a function of saturation temperature.

The temperature dependence of solubility can be described by Arrhenius equation [20, 39],

$$S = S_0 \exp\left(-\frac{\Delta H_S}{RT}\right) \qquad (2)$$

where S_0 is the pre-exponential factor, ΔH_S is the heat of sorption or enthalpy change upon solution of gas in the polymer, T is temperature in Kelvin, and R is gas constant, 8.314 J K^{-1} mol^{-1}.

Figure 8.3 shows the natural logarithm of solubility as a function of 1000/T. Two best-fit lines were drawn: one for data below 15 °C and the other above 15 °C. 15 °C is the vaporization temperature of CO_2 at 5 MPa pressure. ΔH_S can be calculated from the slope of the best-fit line. Below 15 °C, ΔH_S is calculated to be -6 kJ/mol; above 15 °C, ΔH_S is -15.3 kJ/mol. Negative values indicate the exothermic nature of the CO_2 sorption in PSU. The change of ΔH_S, is due to the phase change of CO_2 from gas to liquid when the temperature decreases passing through the 15 °C point, or vice versa. The difference between these two ΔH_S is 9.3 kJ/mol. This value is about 18% smaller than the heat of vaporization of CO_2, which is about 11.3 kJ/mol [40]. The change of ΔH_S at the vaporization temperature of CO_2 was reported in polycarbonate [33] and poly(methyl methacrylate) [41].

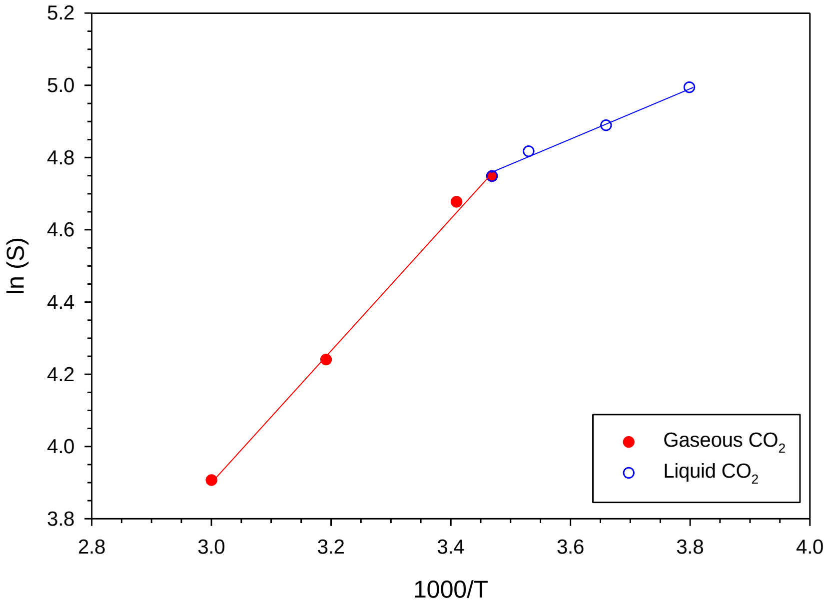

Figure 8.3 Natural logarithm of solubility as a function of 1000/T with two best-fit lines. Note the change in slope when CO_2 changes from gas to liquid at 15 ℃.

8.4.2 **Foam Morphology and Relative Density**

After foaming, the originally transparent PSU sample became opaque because the light is diffused by the cells (or voids) in the foamed sample. Figure 8.4 (a) shows an example of the comparison between unfoamed and foamed sample. Also, in Figure 8.4 (b), we show the cross section of the foamed sample. The cross section of the foamed sample is composed of 740 μm foam core and 50 μm solid skin layers (25 μm on either side). The formation of solid skin layers is due to the loss of gas during the interval after removing sample from pressure vessel and before foaming in the oil bath [42]. Skin thickness accounts for only 6% of the overall thickness, thus its effect on density measurement is negligible.

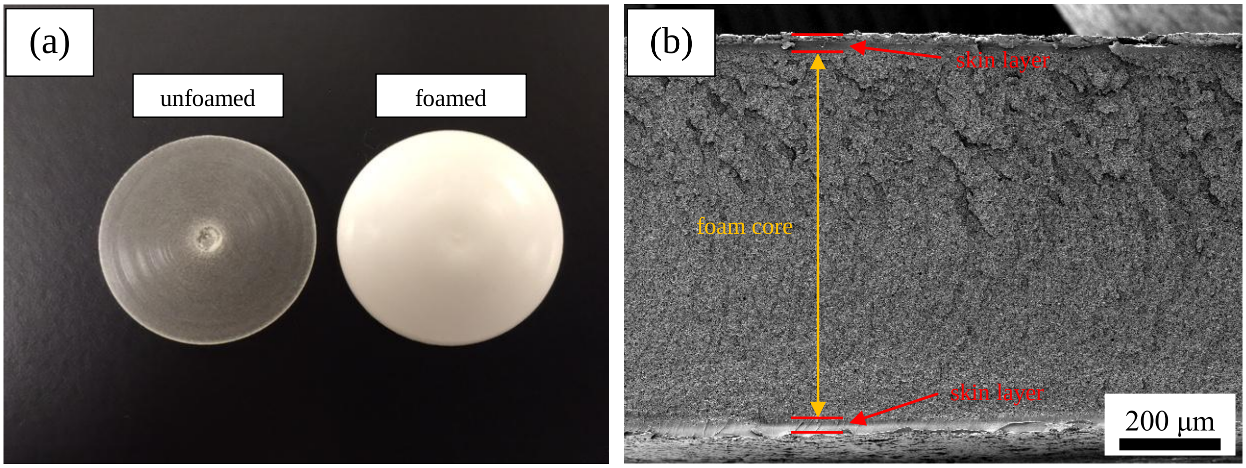

Figure 8.4 Images showing (a) unfoamed PSU and foamed sample (sample#12); (b) cross section of the foamed sample. Notice the large foam core region and a very thin skin layer on either side.

Density is one of the most important characteristics of foams. Relative density is defined as density of foam divided by density of unsaturated polymer. Figure 8.5 shows the relative density as a function of foaming temperatures. Samples were initially saturated at different temperatures and then foamed in a range of temperatures. The foaming temperature was varied to achieve a range of foam densities.

The general decreasing trend of relative density with increasing foaming temperature is observed. Beyond a certain higher foaming temperature, density increases due to the collapse of the cellular structures. At lower saturation temperatures, where the solubilities are higher, a lower foaming temperature is needed to initiate the foaming. For example, 50 ℃ is needed to foam the samples that are saturated at 0 ℃, whereas 110 ℃ is needed for 60 ℃ saturated samples. Absorption of CO_2 into a polymer plasticizes the polymer, depressing its T_g. The larger amount of CO_2 there is in the polymer, the lower T_g the polymer-CO_2 mixture has. Since solid-state foaming initiates near the T_g of the polymer-CO_2 mixture [34, 43], foaming temperature to initiate foaming is lower for samples absorbed with a larger amount of CO_2 (higher CO_2 solubility).

As will be discussed later, foams created by saturating at 0 ℃ and -10 ℃ are nanofoams with cell size below 100 nm. From the density plots, we can see that nanofoams (cells size < 100 nm) with the relative density as low as 52.3% can be created.

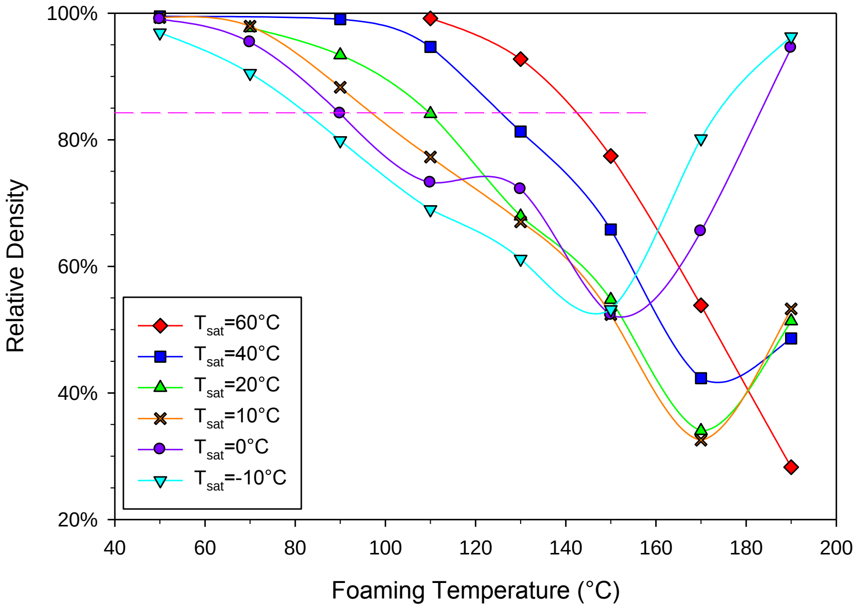

Figure 8.5 Relative density as a function of foaming temperature for samples initially saturated at various T_{sat}. A constant 84.1% relative density line is also drawn.

In addition, different foam samples with similar relative densities can be prepared by the proper choice of processing conditions, based on the density plots. However, the cellular morphology of the samples may be quite different. For example, a line indicating 84.1% relative density was drawn in the density plots. Two sets of conditions can be used to generate foams with this relative density. The sample can be saturated at 20 ℃ and then foamed at 110 ℃, or it can be saturated at 0 ℃ and then foamed at 90 ℃. The former condition resulted in microcellular foams with an average cell size of 1.4 μm, whereas the latter condition created nanofoams with an average cell size of 22 nm. The cell size is about 60 times smaller. Figure 8.6 shows the cellular morphology of these two samples. The ability to produce foams with similar relative densities but vastly different cell sizes provides an opportunity for investigating the effect of cell size on foams properties. A particularly interesting study is to compare properties of microfoams and nanofoams.

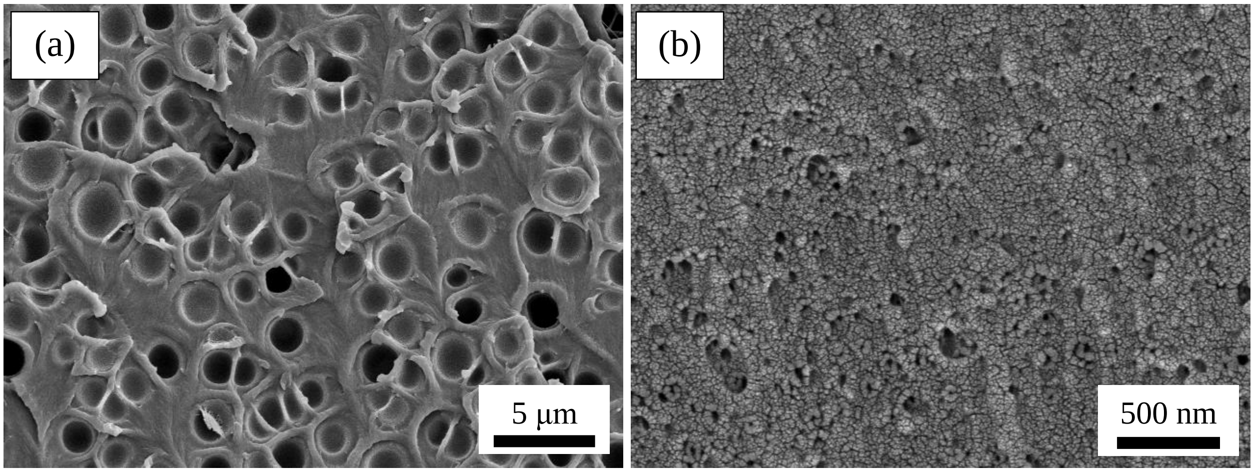

Figure 8.6 Example of microcellular and nanocellular foams: (a) sample #11, cell size 1.4 μm and (b) sample #21, cell size 22 nm. Both have 84.1% relative density.

Table 8.1 Summary of processing conditions, foam densities, cell nucleation densities and average cell sizes.

Sample #	T_{sat} (°C)	CO_2 Concentration	T_f (°C)	Foam Density (g/cm^3)	Rel. Density	Cell Nucleation density ($cell/cm^3$)	Average Cell size (μm)
1	60	5.0%	130	1.15	92.7%	5.02×10^{9}	2.2
2	60	5.0%	150	0.96	77.4%	5.01×10^{9}	4.3
3	60	5.0%	170	0.67	53.8%	6.30×10^{9}	5.9
4	60	5.0%	190	0.35	28.3%	8.29×10^{9}	7.5
5	40	6.9%	110	1.17	94.7%	1.69×10^{10}	1.4
6	40	6.9%	130	1.01	81.3%	2.07×10^{10}	2.1
7	40	6.9%	150	0.82	65.8%	2.49×10^{10}	3.0
8	40	6.9%	170	0.52	42.3%	2.59×10^{10}	3.8
9	40	6.9%	190	0.60	48.6%	3.52×10^{10}	3.2
10	20	10.7%	90	1.16	93.4%	6.01×10^{10}	0.739
11	20	10.7%	110	1.04	84.1%	7.25×10^{10}	1.4
12	20	10.7%	130	0.89	71.7%	1.13×10^{11}	1.6
13	20	10.7%	150	0.69	55.5%	9.68×10^{10}	2.2
14	20	10.7%	170	0.42	34.0%	7.13×10^{10}	3.0
15	20	10.7%	190	0.64	51.3%	1.03×10^{11}	2.0
16	10	12.3%	90	1.09	88.3%	5.79×10^{12}	0.081
17	10	12.3%	110	0.96	77.3%	2.46×10^{12}	0.351
18	10	12.3%	130	0.83	67.0%	1.60×10^{12}	0.516
19	10	12.3%	150	0.65	52.4%	2.40×10^{11}	1.4
20	10	12.3%	170	0.40	32.5%	1.10×10^{12}	1.0
21	0	13.3%	90	1.04	84.1%	2.75×10^{14}	0.022
22	0	13.3%	110	0.91	73.2%	2.17×10^{14}	0.036
23	0	13.3%	150	0.65	52.3%	9.14×10^{14}	0.031
24	-10	14.7%	70	1.12	90.5%	1.50×10^{14}	0.029
25	-10	14.7%	90	0.99	79.9%	1.45×10^{14}	0.026
26	-10	14.7%	110	0.86	69.0%	2.57×10^{14}	0.028
27	-10	14.7%	130	0.76	61.2%	3.58×10^{14}	0.027
28	-10	14.7%	150	0.66	53.2%	1.71×10^{15}	0.027

8.4.3 **Cellular Morphology of Foams**

8.4.3.1 Effect of Foaming Temperature on Cell Nucleation Density and Average Cell Size

Representative samples were imaged by SEM to characterize the cellular morphologies of foams. Table 8.1 summarizes the processing conditions and cellular characteristics of the resulting foams. Figure 8.7 shows cell nucleation density as a function of foaming temperature for foamed samples that were initially saturated at different T_{sat}. The lower T_{sat} (higher CO_2 concentration from Figure 8.2) results in a higher cell nucleation density. For example, cell nucleation densities of -10 ℃ saturated sample (14.7% CO_2 concentration) are on the order of 10^{14} cells/cm^3, whereas 60℃ saturated samples sample (5% CO_2 concentration) on the order of 10^9 cells/cm^3, five orders of magnitude lower. Sun and Mark [35] found that the cell nucleation density was on the order of 10^{11} cells/cm^3, when PSU was saturated with 9% CO_2 and foamed between 130 ℃ and 190 ℃. Our results at similar conditions (T_{sat}=20 ℃ case) match well with their data.

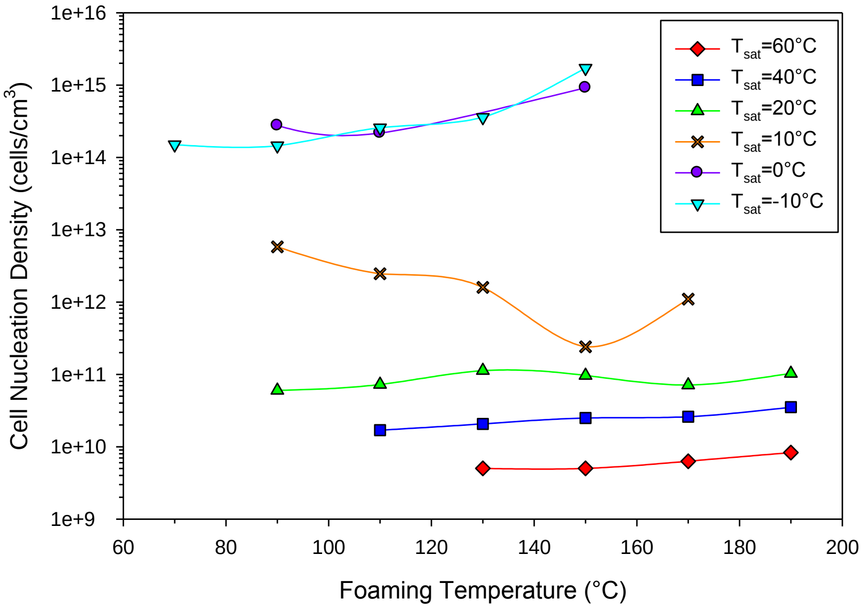

Figure 8.7 Cell nucleation density as a function of foaming temperature for samples initially saturated at different T_{sat}.

Figure 8.8 shows the average cell size as a function of foaming temperature for foamed samples. A higher CO_2 concentration at lower saturation temperature leads to a smaller cell size. For T_{sat} at 20 ℃ and above (CO_2 concentration below 10.7%, cell sizes are above 1 μm. These are microcellular foams. For T_{sat} at 10 ℃ (CO_2 concentration of 12.3%), cell sizes lie mostly in the 100 nm to 1 μm region. For T_{sat} at 0 ℃ and -10 ℃ (CO_2 concentration of 13.3% and 14.7%), cell sizes fall below 100 nm. The latter two cases are nanofoams. Figure 8.9 shows cellular morphologies of samples initially saturated at different temperatures and subsequently foamed 130 ℃. (a) (b) are microcellular foams, and (c) (d) are nanofoams. All the cellular structures are quite uniform.

Cellular structures are more sensitive to the foaming temperatures, for 10 ℃ saturated samples. The cell nucleation densities span two orders of magnitude and cell sizes cover the whole 100 nm – 1 μm range. For all other T_{sat}, cell nucleation densities and cell sizes vary in a much smaller range.

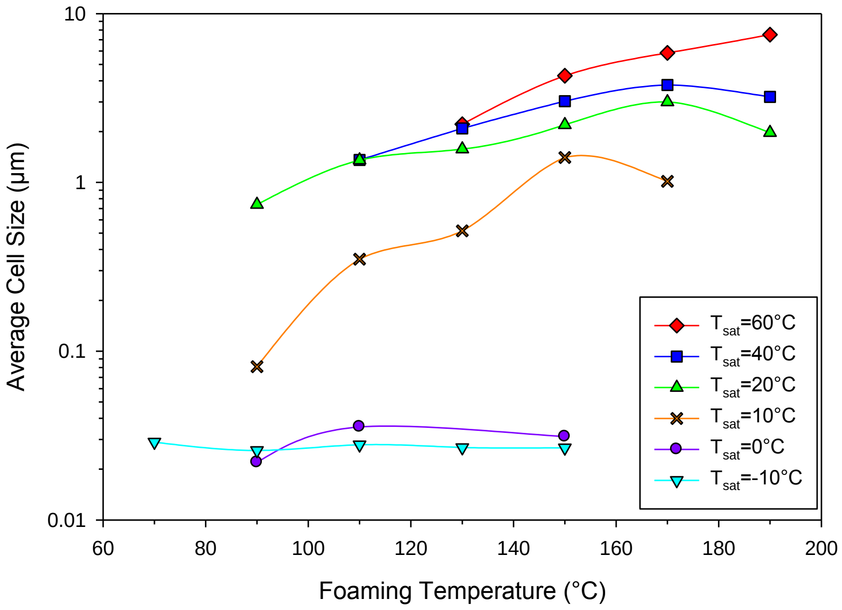

Figure 8.8 Average cell size as a function of foaming temperature for samples initially saturated at different T_{sat}.

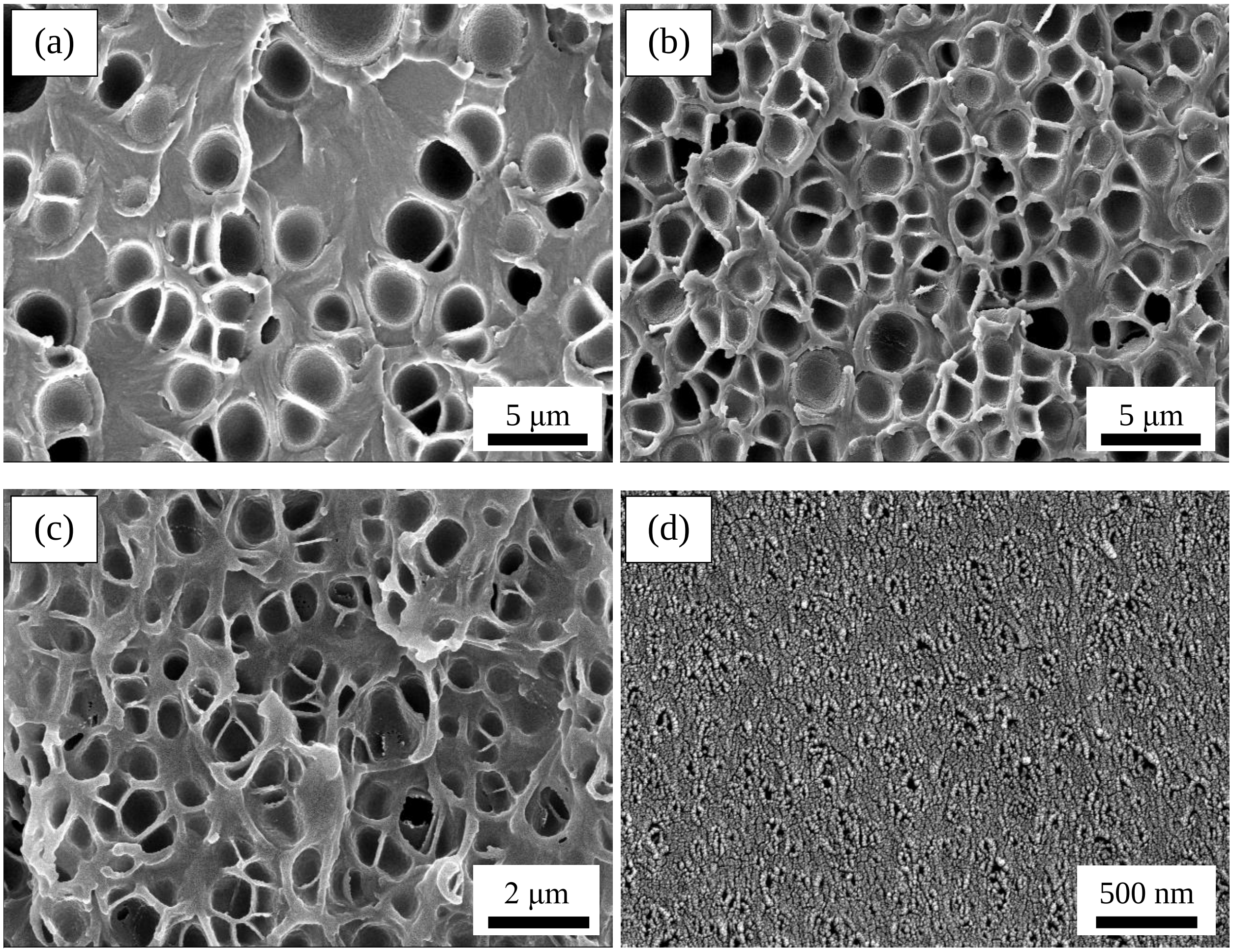

Figure 8.9 Cellular structures of (a) sample #6, (b) sample #12, (c) sample #18, (d) sample #27. All samples were foamed at 130 ℃. Notice the different scale bars. Magnifications are (a,b) 4,000X, (c) 10,000X and (d) 40,000X.

8.4.3.2 Processing Window for Nanofoams

To better visualize the effect of CO_2 concentration on cell nucleation density and cell size, we have plotted the cell nucleation densities and average cell sizes as a function of CO_2 concentration, in Figure 8.10 and Figure 8.11, respectively. At each concentration, cell nucleation densities and average cell sizes from a range of foaming temperature were plotted together. Lines were drawn to show the trends.

For CO_2 concentration between 5% and 10.7%, cell nucleation densities increase exponentially with CO_2 concentration. For CO_2 concentration above 10.7%, there is a much more rapid increase in nucleation density. There are two orders of magnitude increase in nucleation density when CO_2 concentration increases from 12.3% to 13.3%, as opposed to only one order of magnitude increase when CO2 concentration increases from 5% - 10.7%.

Similarly, for cell sizes, when CO_2 concentration is between 5% and 10.7%, they decrease exponentially but all the cell sizes are still within in the range of 1 – 10 μm. For CO_2 concentration above 10.7%, cell sizes drop rapidly. There is one order of magnitude decrease in cell size when CO_2 concentration increases from 12.3% to 13.3%.

It's evident from the figures that there exists a critical concentration, between 10.7% and 12.3%, where there is change in the rate of the nucleation density increase, or the rate of cell size decrease, with increasing CO_2 concentration. Above the critical concentration, cell nucleation densities increase rapidly and cell sizes drop from micrometer range to below 1 μm into the nanometer range.

One interesting observation from these two figures is that when the CO_2 concentration is sufficiently high to create nanocells, further increase in concentration doesn't result in a higher nucleation density or smaller cell size. This may suggest that there exists a limit for the maximum number of nuclei and for the smallest size for stable cells. The underlying mechanism needs further investigation.

The critical concentration for creating nanofoams has also been reported previously in other amorphous polymers. Krause et al. [15] reported a critical CO_2 concentration between 47-49 cm^3 CO_2 / cm^3 polymer (or equivalently 7.2-7.5%) for both polyetherimide (PEI) and poly(ether sulfone) (PES) thin films. Miller et al. [23] found the critical CO_2 concentration between 9.4%-11% for PEI sheets. Guo and Kumar [33] recently reported the critical CO_2 concentration between 15.9%-18.9% for polycarbonate (PC). The different critical CO_2 concentration in PEI, PES, PC, and PSU indicate that the critical CO_2 concentration is polymer dependent. This polymer-dependence is probably due to the differences in molecular structures and properties between these polymers.

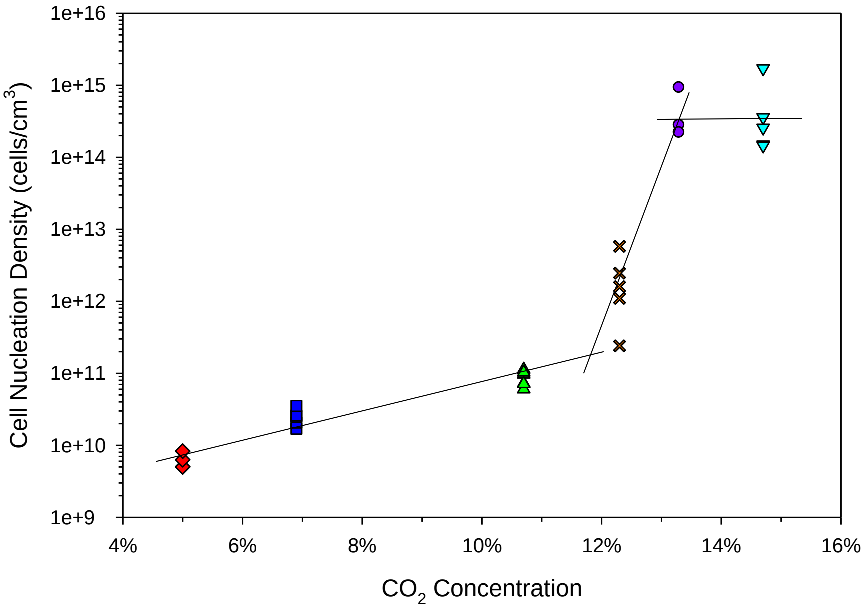

Figure 8.10 Cell nucleation density as a function of CO_2 concentration. Lines are drawn to show the trends.

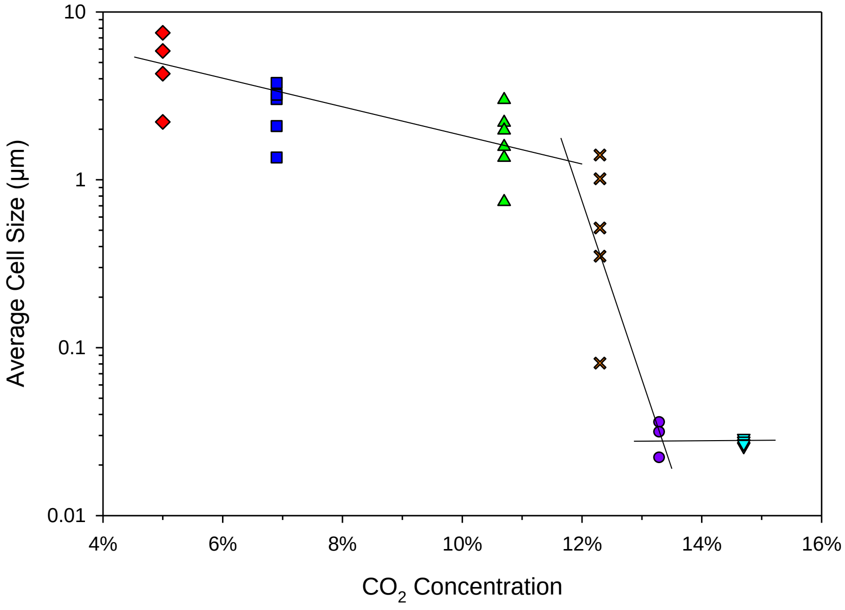

Figure 8.11 Average cell size as a function of CO_2 concentration. Lines are drawn to show the trends.

8.4.3.3 Bicontinuous Nanoporous Structures

The SEM images of sample #23 and #28 are shown in Figure 8.12. The cellular structures show some interconnectivity, indicated by the visibility of the structures below the fracture plane. For typically closed-cell structures, e.g. Figure 8.9, cells have well-defined cell walls and the structures below the fracture plane are not visible. However, the cellular structures shown here allow us to see the underlying structures through the cells. Therefore, the cells are interconnected. This type of structure is called as bicontinuous nanoporous structure: two continuous phases are the polymer matrix and air pores. Similar bicontinuous nanoporous structures were reported in PEI [11], PES [15], PI/PSU blend [16], and PC [33].

The phenomenon of the change of foam morphology from closed nanocellular to bicontinuous nanoporous at a higher foaming temperature is not yet understood at present. Certainly, the higher thermal instability at a higher foaming temperature plays a critical role. The structural transition is likely due to the spinodal decomposition triggered by the higher foaming temperature. In the spinodal decomposition, a wavelike concentration fluctuation with periodic wavelength increasing over time by uphill diffusion producing an interconnected bicontinuous structure [44]. In our case, originally homogeneous PSU-CO_2 mixture separates into two continuous phases: PSU-rich phase (i.e. polymer matrix) and CO_2-rich phase (i.e. voids).

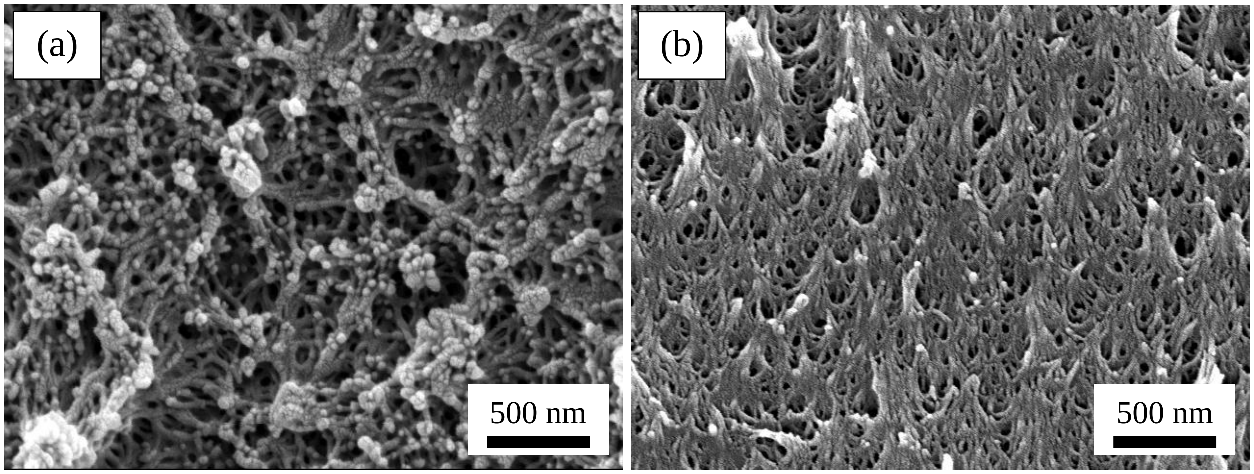

Figure 8.12 Bicontinuous nanoporous structures in (a) sample #23, cell size 31 nm and (b) sample #28, cell size 27 nm. Magnifications are 40,000X.

Although both cellular structures are bicontinuous nanoporous, and cell size and relative density are also similar, they seem to have different morphologies. The left-side sample shows a more open porous and three-dimensional structure, where cells are very randomly distributed. The right-side sample shows a layered structure, where there seem to be many layers and cells distribute on each layer. The only difference in these two samples is the CO_2 concentration. The different CO_2 concentration can result in different levels of thermal instability, which may cause the formation of different morphologies. Zhou et al. [11] reported two similar types of morphologies in PEI nanofoams when processed with a different combination of CO_2 concentration and foaming temperature.

8.4.4 Nanostructures on the Cell Wall of Microcells in Microcellular Foams

Interesting structures were observed while imaging the cellular structures of microcellular foams. These foams were initially saturated at 60 ℃, 40 ℃, and 20 ℃, and had CO_2 concentration between 5% and 10.7%. These samples exhibit the normal microcellular structure, but upon close inspection, the inner cell walls of the microcells show many nanoscale features. Figure 8.13 (a) shows such an example. This sample was saturated at 40 ℃ and foamed at 110 ℃. (b) is the close-up image of (a). On the cell wall, nanosized cells, with the cell size about 20 nm, can be seen. One thing worth mentioning is that the nanoscale features seem to only exist on or close to the surface of the cell wall.

In order to see the evolution of the nanostructures on the cell wall, we foamed samples in a range of temperatures. Figure 8.13 (c), (d) and (e) show the nanostructures on the cell wall of microcells in samples that were foamed 130 ℃, 150 ℃, and 170 ℃, respectively. From (b) to (e), average cell size of the cells on the cell wall increases with foaming temperature, from 20 nm for (b) to 36 nm for (e). Also, from (b) to (e), more cells in a unit area are present. Compared to (b), (c) and (d) have significantly more cells. The cells are still closed cells and discretely distributed. However, (e) shows the bicontinuous nanoporous structures. The evolution of nanostructures on cell wall with foaming temperature is very similar to the cell structure change when PSU is saturated with 13.3% and 14.7% CO_2 concentration and then foamed at increasingly higher temperatures. As the temperature increases, more cells are nucleated, and at 150 ℃ closed nanocellular structure changes into bicontinuous nanoporous structure.

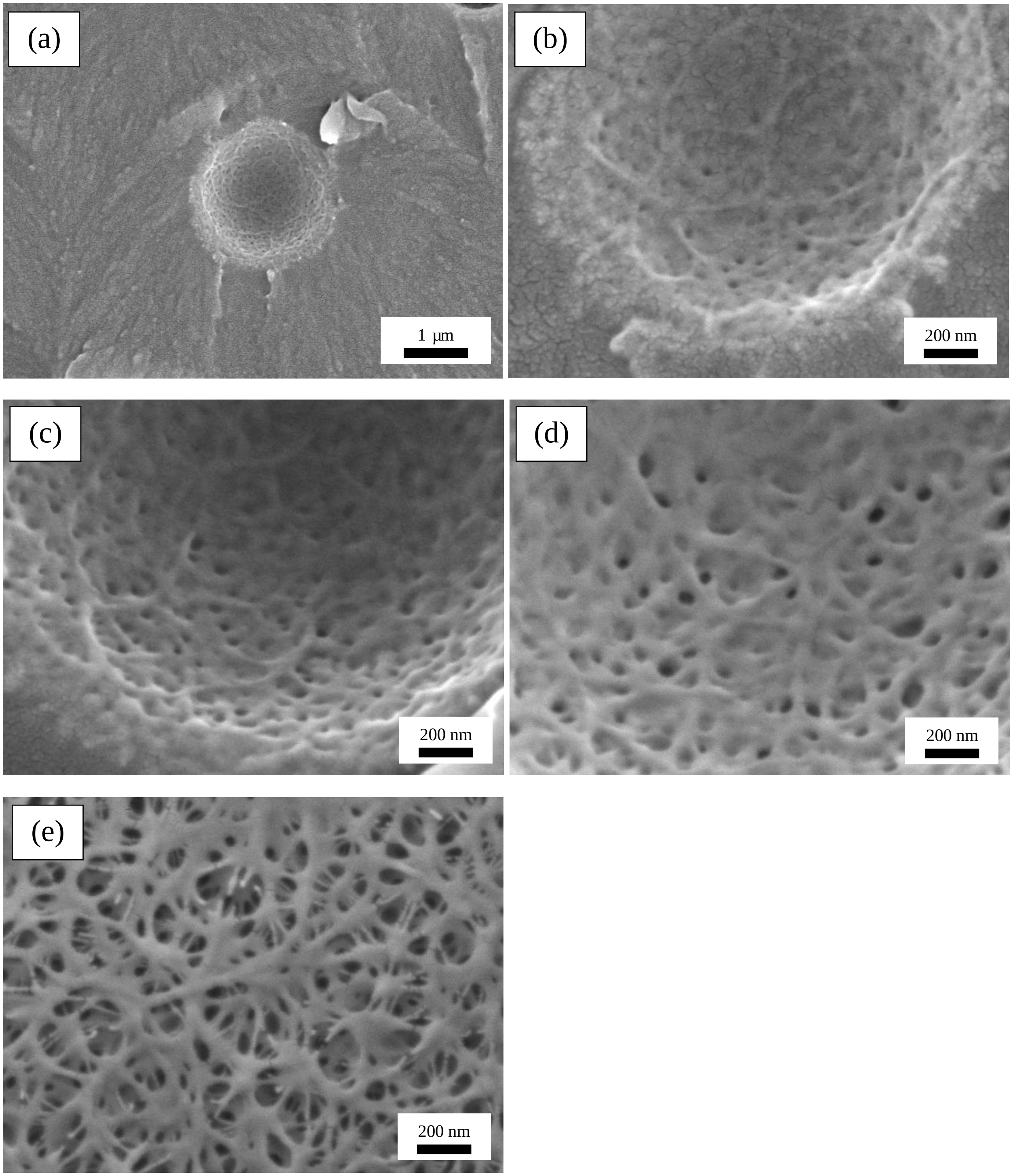

Figure 8.13 Nanostructures on the cell walls of microcells in microcellular foams: (a) sample #5; (b) close-up of (a), cell size 20 nm; (c) sample #6, cell size 26 nm; (d) sample #7, cell size 35 nm; and (e) sample #8, cell size 36 nm.

Nanostructures on the cell wall were observed previously in PEI [11, 23], PES [45], and PC [46, 47]. Different formation mechanisms for the nanostructures on the cell wall were proposed, such as orientation-induced crystallization [46], crazing [47], and stress-induced nucleation or spinodal decomposition [23]. However, evolution of the nanostructures on cell wall and its similarity to that of bulk nanofoams were not reported. In fact, in most of these studies, only bicontinuous nanoporous structures were reported. Here we show that besides the bicontinuous nanoporous structure, there exist closed nanocellular structures at lower foaming temperatures.

The remarkable similarity between the nanostructures on the cell wall of microcells in microcellular foams and the nanostructures of bulk nanofoams, leads us to believe that the formation mechanism might be stress-induced nucleation/spinodal decomposition. Stress-induced foaming phenomenon was studied previously [48-52]. In the solid state, two studies were carried out by directly applying external stresses to CO_2-saturated polymers. Handa and Zhang [48] found that under compressive stresses CO_2-saturated PMMA, PETG, PEMA, and PC showed foaming with mostly closed cells, whereas no or less foaming occurred when without the compressive stresses. Hu and Lesser [49] investigated the drawing of PC thin film in the presence of supercritical CO_2, and found that the uniaxial drawing led to creation of open microporous structures with pore size less than 1 μm and porosity of 20-70%. These studies indicate that both compressive and tensile stresses can introduce thermodynamic instability and result in the phase separation of polymer-gas mixture.

Figure 8.14 shows the proposed formation mechanism of nanostructures on the cell wall of microcells. The growth of the microcells stretches its cell wall and results in biaxial tensile stresses, which induce the nanostructures. The specific nanostructure formed depends on the foaming temperature. At low T_f, closed nanocells are formed, whereas at high T_f, bicontinuous nanoporous structures are formed. High T_f brings in two effects: one is the higher tensile stresses due to a larger degree of stretching (indicated by the larger cell size of the microcells) and the other is a higher thermal energy input. These two effects combined could trigger the spinodal decomposition mechanism and result in bicontinuous nanoporous structures on the cell wall.

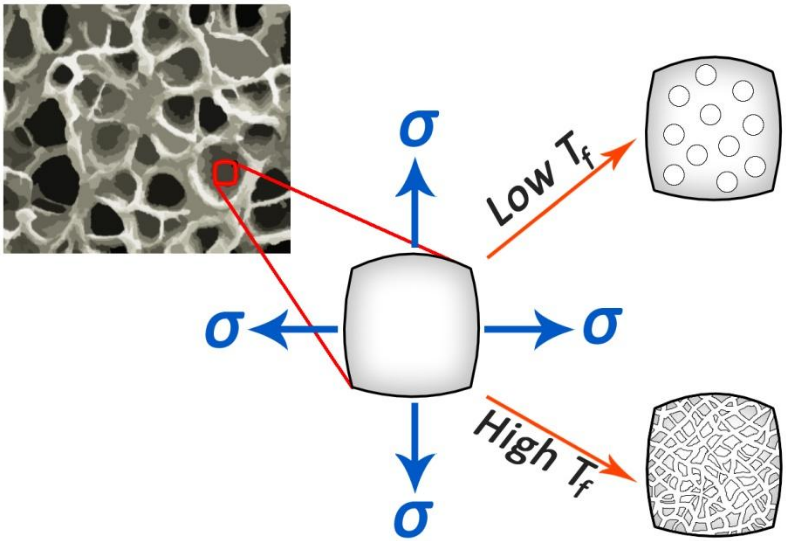

Figure 8.14 Formation of closed nanocellular and bicontinuous nanopourous structures on the cell wall of microcells, via the biaxial tensile stress-induced 1) nucleation (low T_f) and 2) spinodal decomposition (high T_f).

8.5 **Summary**

This research presents processing space where PSU foams with a range of densities and with various cellular structures, such as microcellular, closed nanocellular, and bicontinuous nanoporous structures, can be created. Microcellular foams with cell size up to 8 μm and nanocellular foams with cell size down to the range of 20-30 nm were successfully fabricated. In the nanofoams, cell nucleation densities exceeding 10^{15} cells/cm^3 were achieved. The PSU foams produced present an opportunity to achieve high-temperature polymer nanofoams.

The effect of saturation temperature on the solid-state foaming of PSU was investigated over the range of -10 ℃ to 60 ℃, and the resulting morphologies were characterized. Solubility is found to increase significantly with decreasing saturation temperature, from 5% at 60 ℃ to 14.7% at -10 ℃. A change of heat of sorption, about 9.3 kJ/mol, due to CO_2 phase change, has been found at the vaporization temperature of CO_2.

The CO_2 concentration has a strong influence on the cellular structure. There exists a critical concentration, between 10.7% and 12.3%, that leads to nanocells. At low concentrations (10.7% and below), microcellular foams are formed. At high concentrations (12.3% and above), cell nucleation densities increase and cell sizes decrease much more rapidly with CO_2 concentration. In this region, nanofoams are formed.

At the high concentration region, the change from closed nanocellular structure to bicontinuous nanoporous structure is observed when the sample was foamed at a higher temperature. Two types of bicontinuous nanoporous morphologies are obtained depending on the CO_2 concentration level: one is more open porous and three-dimensional, and the other is a layered structure.

Nanostructures are observed on the cell walls of microcells in microcellular foams. Evolution of the nanostructures on the cell wall with foaming temperature resembles that of nanofoams. We believe the formation mechanism of these nanostructures is stress-induced nucleation/spinodal decomposition, where the stress is a biaxial tensile stress caused by the expansion growth of microcells.

8.6 Acknowledgment

The authors would like to acknowledge the financial support from the University of Washington CGF fund, National Science Foundation Grant CMMI 1253072, and MicroGREEN Polymers, Inc.

8.7 References

1. Martini JE, Suh NP, and Waldman FA. Microcellular closed cell foams and their method of manufacture. Massachusetts Institute of Technology, 1984.
2. Martini JE, Waldman FA, and Suh NP. The production and analysis of microcellular thermoplastic foam. SPE ANTEC, vol. 28. San Francisco, CA, 1982. pp. 674.
3. Shimbo M, Higashitani I, and Miyano Y. Journal of Cellular Plastics 2007;43(2):157-167.
4. Kumar V, VanderWel M, Weller J, and Seeler KA. Journal of Engineering Materials and Technology 1994;116(4):439-445.
5. Kumar V, Weller JE, Ma M, Montecillo R, and Kwapisz R. Cellular Polymers 1998;17(5):350-361.
6. Bureau MN and Kumar V. Journal of Cellular Plastics 2006;42(3):229-240.
7. Barlow C, Kumar V, Flinn B, Bordia RK, and Weller J. Journal of Engineering Materials and Technology 2000;123(2):229-233.
8. Kumar V, Juntunen RP, and Barlow C. Cellular Polymers 2000;19(1):25-37.

9. Juntunen RP, Kumar V, Weller JE, and Bezubic WP. Journal of Vinyl and Additive Technology 2000;6(2):93-99.
10. Miller D and Kumar V. Polymer 2011;52(13):2910-2919.
11. Zhou C, Vaccaro N, Sundarram SS, and Li W. Journal of Cellular Plastics 2012;48(3):239-255.
12. Pinto J, Solorzano E, Rodriguez-Perez MA, de Saja JA, Dumon M.. Thermal conductivity transition between microcellular and nanocellular polymeric foams: experimental validation of the Knudsen effect. SPE FOAMS. Barcelona, Spain, 2012.
13. Notario B, Pinto J, Solorzano E, de Saja JA, Dumon M, and Rodríguez-Pérez MA. Polymer 2015;56:57-67.
14. Reglero Ruiz JA, Dumon M, Pinto J, and Rodriguez-Pérez MA. Macromolecular Materials and Engineering 2011;296(8):752-759.
15. Krause B, Sijbesma HJP, Münüklü P, van der Vegt NFA, and Wessling M. Macromolecules 2001;34(25):8792-8801.
16. Krause B, Diekmann K, van der Vegt NFA, and Wessling M. Macromolecules 2002;35(5):1738-1745.
17. Hedrick JL, Carter KR, Cha HJ, Hawker CJ, DiPietro RA, Labadie JW, Miller RD, Russell TP, Sanchez MI, Volksen W, Yoon DY, Mecerreyes D, Jerome R, and McGrath JE. Reactive and Functional Polymers 1996;30(1–3):43-53.
18. Baldwin DF, Suh NP, Park CB, and Cha SW. Supermicrocellular foamed materials. Massachusetts Institute of Technology, 1994.
19. Handa YP and Zhang Z. Journal of Polymer Science Part B: Polymer Physics 2000;38(5):716-725.
20. Handa YP, Zhang Z, and Wong B. Cellular Polymers 2001;20(1):1-16.
21. Murray RE, Weller JE, and Kumar V. Cellular Polymers 2000;19(6):413-425.
22. Nawaby AV, Handa YP, Liao X, Yoshitaka Y, and Tomohiro M. Polymer International 2007;56(1):67-73.
23. Miller D, Chatchaisucha P, and Kumar V. Polymer 2009;50(23):5576-5584.
24. Costeux S. Journal of Applied Polymer Science 2014;131(23):n/a-n/a.
25. Nemoto T, Takagi J, and Ohshima M. Polymer Engineering & Science 2010;50(12):2408-2416.
26. Nemoto T, Takagi J, and Ohshima M. Macromolecular Materials and Engineering 2008;293(7):574-580.
27. Nemoto T, Takagi J, and Ohshima M. Macromolecular Materials and Engineering 2008;293(12):991-998.
28. Ruiz JAR, Pedros M, Tallon J-M, and Dumon M. The Journal of Supercritical Fluids 2011;58(1):168-176.
29. Ruiz JAR, Marc-Tallon J, Pedros M, and Dumon M. The Journal of Supercritical Fluids 2011;57(1):87-94.
30. Costeux S, Bunker SP, and Jeon HK. Journal of Materials Research 2013;28(17):2351-2365.
31. Costeux S, Khan I, Bunker SP, and Jeon HK. Journal of Cellular Plastics 2014.
32. Costeux S and Zhu L. Polymer 2013;54(11):2785-2795.
33. Guo H and Kumar V. Polymer 2015;56:46-56.
34. Krause B, Mettinkhof R, van der Vegt NFA, and Wessling M. Macromolecules 2001;34(4):874-884.
35. Sun H and Mark JE. Journal of Applied Polymer Science 2002;86(7):1692-1701.
36. Kumar V and Weller J. Journal of Manufacturing Science and Engineering 1994;116(4):413-420.
37. Chen Z, Zeng C, Yao Z, and Cao K. Industrial & Engineering Chemistry Research 2013;52(27):9381-9396.
38. Kumar V. Colloids and Surfaces A: Physicochemical and Engineering Aspects 2005;263(1-3):336-340.
39. Crank J and Park GS. Diffusion in polymers. London: Academic Press, 1968.
40. Cengel Y and Boles M. Thermodynamics: an engineering approach, 7th ed.: McGraw-Hill Science/Engineering/Math, 2011.
41. Guo H and Kumar V. Polymer 2015;57:157-163.
42. Kumar V and Weller JE. Polymer Engineering & Science 1994;34(3):169-173.

43. Kumar V, Weller JE, and Montecillo R. Journal of Vinyl Technology 1992;14(4):191-197.
44. Sperling LH. Introduction to Physical Polymer Science, 4th ed. Hoboken, NJ: John Wiley & Sons, Inc., 2006.
45. Sorrentino L, Aurilia M, and Iannace S. Advances in Polymer Technology 2011;30(3):234-243.
46. Fukasawa Y, Chen J, and Saito H. Journal of Polymer Science Part B: Polymer Physics 2008;46(8):843-846.
47. Gong P, Taniguchi T, and Ohshima M. Journal of Materials Science 2014;49(6):2605-2617.
48. Handa YP and Zhang Z. Cellular polymers 2000;19(2):77-91.
49. Hu X and Lesser AJ. Journal of Cellular Plastics 2006;42(6):517-527.
50. Lee S-T. Polymer Engineering & Science 1993;33(7):418-422.
51. Wong A, Chu RKM, Leung SN, Park CB, and Zong JH. Chemical Engineering Science 2011;66(1):55-63.
52. Chen L, Sheth H, and Wang X. Journal of Cellular Plastics 2001;37(4):353-363.

Chapter 9

Fabrication of High Temperature Polyphenylsulfone Nanofoams Using High Pressure Liquid Carbon Dioxide

9.1 **Abstract**

In this paper, we describe fabrication of micro- and nano-structured foams in high temperature polyphenylsulfone (PPSU) with a T_g of 219 °C using a solid-state carbon dioxide (CO_2) foaming process. We have fabricated microcellular foams with cell size in 1-10 μm range, and for the first time, nanocellular foams with cell size in 20-40 nm range. We discovered a critical CO_2 concentration between 10.5%-11.8%, where a rapid 2-3 orders of increase in cell nucleation density is observed and cell size drops to below 100 nm. Two approaches are demonstrated to create PPSU nanofoams with a cell size of 20-40 nm: increasing saturation pressure to 7 MPa or decreasing saturation temperature to 10 °C. Both approaches use high pressure liquid CO_2 and the CO_2 concentration in the polymer are above the critical concentration, which result in the formation of nanocells. At high CO_2 concentration of 11.8% and 13%, as foaming temperature increases, the nanostructures transition from closed structure to an open porous structure.

Keywords: foams; nanofoams; microcellular; nanocellular; nanoporous

9.2 **Introduction**

Microcellular foams are thermoplastic foams with cell size on the order of 10 μm. In the 1980s, to meet the demand of material savings on thin wall packaging, Martini et al. [1, 2] developed a solid-state gas foaming process to create the microcellular foams. The bubbles introduced were sufficiently small so that the thin wall packaging still maintained its mechanical integrity. The solid-state gas foaming process involves two steps: in the first step, polymer sample is placed in a pressure vessel filled with high

---

This chapter has been accepted by Cellular Polymer and will appear in the issue in 2016.

pressure gas, such as carbon dioxide or nitrogen; in the second step, the saturated polymer sample is heated to near the T_g of the polymer-gas system to introduce cell nucleation and cell growth. Throughout the whole process, polymer sample is in the solid state. Compared to traditional foaming method, this process has much better control of density and cell size, and is also environmentally friendly since a benign gas is used as the blowing agent. Over the years, this process has been used to create microcellular foams in many polymers, including polyvinyl chloride (PVC) [3], acrylonitrile butadiene styrene (ABS) [4], polyethylene terephthalate (PET) [5, 6] , polycarbonate (PC) [7], cyclic olefin copolymer (COC) [8, 9] and polylactic acid (PLA) [10, 11], to name a few. In a variation of this process, microcellular foams have also been created by a sudden drop in gas pressure that causes a solubility drop resulting in a cell nucleation [12].

Nanocellular polymer foams (or polymer nanofoams), are thermoplastic foams with cell size in the range of nanometers. They can be regarded in concept as an extension of microcellular foams. During the past decade, they have drawn much attention due to their potential as a new class of materials having superior properties compared to existing materials, or even new properties never seen before. For example, improved mechanical properties were reported in nanofoams when compared to microcellular foams in polyetherimide (PEI) [13, 14] and polymethyl methacrylate (PMMA) [15]. A lower thermal conductivity was recently found in PMMA based nanofoams due to the Knudsen effect [16]. Among the few methods for making nanofoams, solid-state gas foaming has been proven to be the most successful process. Using this method, nanofoams were first fabricated in low-density polyethylene (LDPE) [17], high-density polyethylene (HDPE) [17], PVC [17], PMMA [18, 19], and ABS [4, 20] with cell size between 100 nm – 1 μm. Later, nanofoams with a much smaller cell size (below 100 nm) in PEI [21-23], polyethersulfone (PES) [22], polyimide (PI) [24], and recently, PC [25], PMMA [26], polysulfone (PSU) [27, 28] were produced. Nanofoams have also been created in polymer blends, such as PI/PSU [24], polyether ether ketone (PEEK)/PEI blends [29], polypropylene (PP)/rubber blends [30, 31], PMMA/MAM (methylmethacrylate-co-butylacrylate-co-methylmethacrylate) blends [32, 33], PEMA (polyethyl methacrylate)/SAN (styrene acrylonitrile) [34], and copolymers, such as Poly(MMA-co-EMA) and Poly(MMA-co-tBMA) [35], and nanocomposites, such as Poly(MMA-co-EA) with silica nanoparticles and Poly(MMA-co-EMA) with methacryl-substituted polyhedral oligomeric silsesquioxane (POSS) [36]. More details regarding to the fabrication of nanofoams using solid-state gas foaming process can be found in a recently published review paper [37].

Polyphenylsulfone (PPSU) has many applications due to its superior properties, such as high service temperature, excellent chemical resistance, exceptional hydrolytic stability, high toughens and impact strength. Microcellular and nanocellular PPSU foams have potential for applications in aircraft interiors and high performance lightweight sandwich structures. PPSU is currently used in aircraft interiors because it is intrinsically flame retardant, and meets the stringent Federal Aviation Administration requirements for smoke, heat release, and toxic gas emission requirements. Reducing the weight of the interior materials means reducing fuel consumption and carbon footprint. Further, microcellular and nanocellular PPSU foams can be used as high temperature foam core for high performance lightweight sandwich structures, which are widely used in automotive, transport, and aeronautic industries. Conventional polymeric core foams have rather low temperature capabilities, and they, with cell size in the millimeter range, have much weaker mechanical properties especially at elevated temperatures, which compromises structural integrity of the sandwich structure.

Microcellular foaming of the PPSU has been rarely explored. So far, only two studies on this topic were reported. Sun et al. [38] saturated PPSU in CO_2 at 810-820 psi (5.59-5.65 MPa) and at room temperature (21-22 °C), and fabricated microcellular PPSU foams of cell size between 1.3 and 7.2 µm, cell nucleation density 10^{11} cells/cm^3, and relative density 40%. In their study, only one saturation condition was explored. Sorrentino et al. [39] first saturated PPSU in CO_2 at 6.5 MPa and 50 °C, then in the second step, they either removed the sample from pressure vessel and then heated it to a temperature of 160-240 °C, or heated the sample to 140-260 °C with the pressure maintained and then suddenly dropped the pressure to atmospheric pressure. They fabricated microcellular PPSU foams of cell size between 1 and 10 μm, cell nucleation density 10^{11}-10^{12} cells/cm^3, and lowest relative density around 40%.

Above studies only showed a very narrow range of processing conditions, especially the saturation conditions. To tailor the microcellular PPSU foams for a given application, certain density and cell size needs to be achieved. Thus, a much more complete processing space for microcellular foaming of PPSU needs to be established, which correlates the density and cell size with processing conditions. This is the first objective of this study. A second objective is to explore the possibility of using the solid-state gas foaming process to create PPSU nanofoams. To the best of authors' knowledge, PPSU nanofoams have not been reported previously.

In this study, we conduct a series of experiments to address these two objectives. We present expanded processing conditions (saturation pressure, saturation temperature and foaming temperature) to achieve a much wider range of foam structures. We map out a detailed processing space, which correlates the processing conditions with the density and cell size of PPSU foams. We discovered two approaches to fabricate PPSU nanofoams with cell size below 100 nm: by increasing saturating pressure to sufficiently high, or by lowering the saturation temperature to below room temperature.

9.3 **Experimental**

9.3.1 **Materials**

Radel R-5000 polyphenylsulfone (PPSU) was used in this study. A one-foot long rod with diameter of 19 mm (or 0.75 inch) was purchased and machined into 0.6 mm thick circular disks. The molecular structure of PPSU is shown in Figure 9.1. The PPSU has a density of 1.29 g/cm^3 and glass transition temperature of 219 °C. T_g was measured with a TA Q20 DSC using a heating rate of 10 °C/min. Medical grade CO_2 with >99.9% purity from Praxair, Inc. was used as the physical blowing agent.

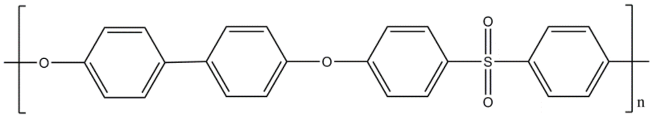

Figure 9.1 Molecular structure of PPSU.

9.3.2 **Solubility Measurement**

Samples were first placed in a homemade stainless-steel pressure vessel. The pressure and temperature of the pressure vessel was set to desired values in the range of 0.5-7 MPa and 10-60 ℃, respectively. The accuracy of pressure and temperature was controlled to be +/- 0.1 MPa and +/- 1 ℃. Two sets of sorption experiments were conducted where either saturation pressure (P_{sat}) or saturation temperature (T_{sat}) was varied. In first set of sorption experiments, P_{sat} was varied from 0.5 to 7 MPa and T_{sat} was kept at room temperature (20 ℃). In the second set of sorption experiments, T_{sat} was varied from 10 to 60 ℃ and P_{sat} was kept at 5 MPa constant pressure. For temperatures above room temperature, a flexible heating jacket was wrapped around the pressure vessel. The heating jacket input heat to the vessel until it reached the set temperature. For 10 ℃, a Peltier cooling module (TE Technology Inc.) was used. During the sorption, samples were periodically removed from the pressure vessel and quickly weighed on a Mettler AE240 analytical scale with an accuracy of +/-10 μg. Since the amount of CO_2 absorbed is typically of microgram order, the scale can accurately detect CO_2 sorption in the polymer. CO_2 concentration in the polymer was determined from the mass increase of the samples. After weighing, samples were then immediately put back to the pressure vessel. Above procedures continued until no further mass increase was observed.

9.3.3 **Saturation and Foaming**

Samples were first saturated in the pressure vessel under a set pressure and temperature. Samples were allowed to absorb CO_2 in the vessel for two days in order to achieve full saturation. The full saturation is important in order to achieve a uniform microstructure in the foamed sample. After full saturation, samples were removed and quickly transferred to a hot oil bath (ThermoHaake B5). The oil bath was controlled to a desired temperature with +/- 1 ℃ accuracy. Samples were immersed in the bath for 1 min, which was found to be sufficient to achieve a stable structure. Further heating didn’t result in any change in foam structures.

9.3.4 **Characterization Techniques**

After foaming, samples were cleaned with detergent. After cleaning, samples were dried and left in the ambient environment for a week in order to let the residue CO_2 completely diffuse out of the samples. This ensured a more accurate measurement of foam density. Density of samples was measured using a water displacement method according to ASTM D792. Solid skin on the edge of the foamed samples was kept for the density measurement. In our experiments, the skin thickness was typically very small compared the sample thickness, due to the very short desorption time. The effect of skin on the density measurement is thus negligible.

To image the microstructures of the foamed samples, a FEI Sirion SEM was used. Samples were first freeze fractured in liquid nitrogen to expose the cross section. Samples were then mounted and coated with a thin layer of Au/Pd in a sputter coater. After coating, samples were transferred to SEM and images were taken in the center of the cross section of the samples. Images were then analyzed using an open source software ImageJ. Cell size was determined by averaging the diameter of the cells (over 50 cells) in the image. The cell nucleation density N_0 (number of cells nucleated per cubic centimeter of the original unfoamed sample) was calculated using a procedure described in previous literature [40].

To test whether the microstructure of a foamed sample is interconnected (i.e. open porous), dye test was conducted. Closed cellular structure will block the penetration of the dye, whereas open porous structure will allow dye to penetrate into the sample. Liquid food colorant containing blue # 1 dye (from LorAnn Oils, Inc.) was mixed with isopropyl alcohol. Sample was first freeze fracture in liquid nitrogen to expose a clean cross section. Then a few drops of the dye/IPA solution were applied to this cross section. The dye solution was allowed to penetrate the sample for about 5 minutes. Then, the sample was freeze fractured again perpendicular to the previous cross section, in order to see the penetration depth of the dye.

Olympus microscope was used to image this depth direction. The penetration depth of the dye was also measured.

9.4 **Results and Discussions**

9.4.1 **Effect of Saturation Pressure**

9.4.1.1 CO_2 Solubility

Gas concentration in polymer is defined as the mass of gas absorbed in the polymer divided by the mass of the original, unsaturated polymer, and typically expressed as the percentage of the original polymer mass. Gas solubility is the equilibrium gas concentration (at an infinite long time) in the polymer. There was a short duration between removal of the sample from the pressure vessel and weighing of the sample on the scale. During this interval, CO_2 molecules on the edge of the sample diffused to the ambient, which caused the measured solubility to be slightly below the actual solubility. A correction procedure [25] was performed to obtain a more accurate solubility, which extrapolated the gas concentration to zero desorption time.

CO_2 solubility in PPSU at various saturation pressures (while keeping temperature at 20 ℃) are listed in Table 9.1. To better visualize the trend, we also plot the CO_2 solubility as a function of saturation pressure in Figure 9.2. We can see that a higher pressure results in a higher CO_2 solubility and CO_2 solubility at 7 MPa is over 4 times as that of 0.5 MPa case. Literature data [41] is also included for comparison. The slightly lower value reported previously was probably due to the higher saturation temperature used in their experiment. The trend can be predicted using the dual-mode model (Henry’s mode combined with Langmuir’s mode). This model was widely used to predict gas solubility in amorphous polymers [42, 43]. The dual-mode model is given by

$$C = k_D P_{sat} + \frac{C'_H b P_{sat}}{1 + b P_{sat}} \quad (1)$$

where C is the equilibrium gas concentration (or solubility), k_D is Henry's Law dissolution constant, C'_H is the capacity constant for Langmuir mode adsorption, b is the affinity constant of the Langmuir mode sites, and P_{sat} is the applied saturation pressure.

The fitting parameters for our data are as follows: k_D=0.0069/MPa, C_H'=0.089, b=0.598/MPa. The fitting curve is also included in the figure.

Table 9.1 CO_2 solubility in PPSU at various saturation pressures (P_{sat}) and saturation temperatures (T_{sat}).

P_{sat} (MPa)	T_{sat} (℃)	CO_2 Solubility
0.5	20	2.7%
1	20	3.9%
2	20	5.9%
3	20	7.8%
5	20	10.5%
7	20	11.8%
5	60	5%
5	40	6.8%
5	20	10.5%
5	10	13%

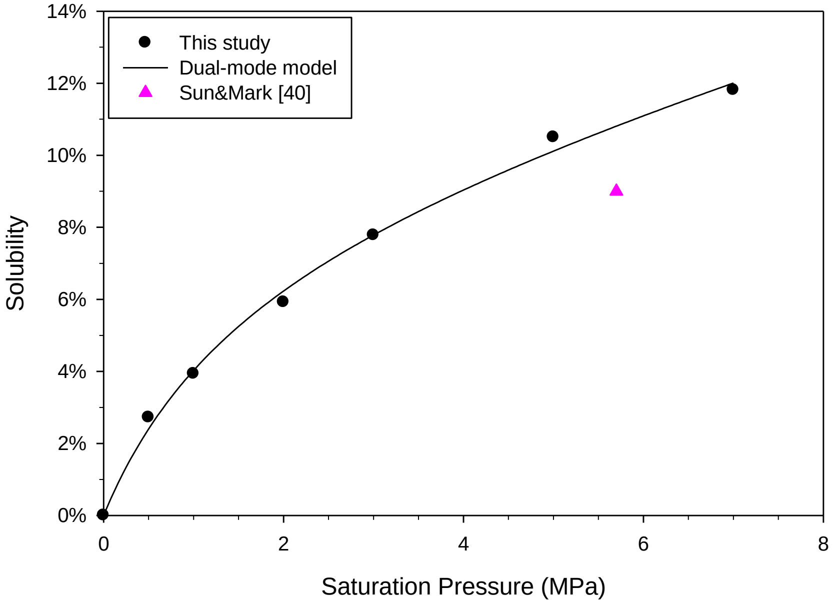

Figure 9.2 CO_2 solubility in PPSU as a function of saturation pressure.

9.4.1.2 Relative Density

For the foaming study, samples were initially saturated at four different pressures (1, 3, 5, 7 MPa), and in all these cases 20 ℃ saturation temperature was used. After samples were fully saturated with CO_2, they were foamed at different temperatures in the range of 90-230 ℃, in order to see the effect of foaming temperature on the properties and cellular structures of resultant foams. Relative density, cell nucleation density and cell size of these foamed samples were characterized. All the data are included in Table 9.2.

Figure 9.3 shows the relative density as a function of foaming temperatures. Relative density is defined as the density of foams over the density of original, unfoamed polymer. We can see that the relative density decreases with increasing foaming temperatures. For example, relative density decreases from 93.1% at 170 ℃ to 24% at 230 ℃ for 1 MPa case. Notice that for 3, 5 and 7 MPa cases, above a certain foaming temperature, foam density decreases as the foaming temperature increases further. This phenomenon is due to cell collapse and fast gas diffusion at the higher temperatures [3, 4, 44].

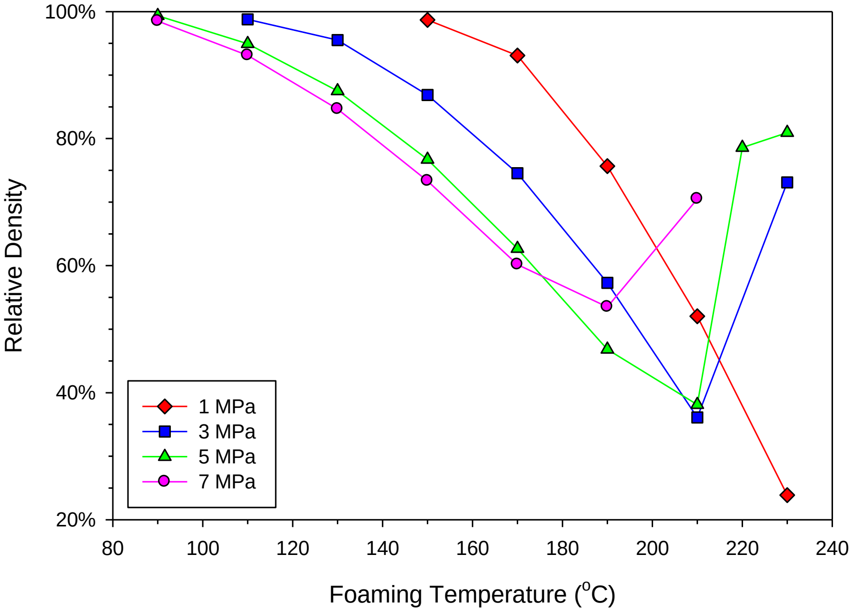

Figure 9.3 Plot of relative density as a function of foaming temperature. Samples were initially saturated at four different pressures and the same saturation temperature of 20 ℃.

Table 9.2 Summary of processing conditions and foam characteristics for varying saturation pressures.

Sample #	**P_{sat} (MPa)**	**T_{sat} (°C)**	**CO_2 Concentration**	**T_f (°C)**	**Foam Density (g/cm^3)**	**Rel. Density**	**Cell Nucleation density ($cell/cm^3$)**	**Cell size (μm)**
1	1	20	3.9%	170	1.20	93.1%	3.56×10^{9}	2.3
2	1	20	3.9%	190	0.98	75.7%	9.42×10^{9}	3.3
3	1	20	3.9%	210	0.67	52%	2.16×10^{10}	3.5
4	1	20	3.9%	230	0.31	23.9%	8.66×10^{9}	7.7
5	3	20	7.8%	150	1.12	86.9%	1.38×10^{11}	0.76
6	3	20	7.8%	170	0.96	74.5%	3.23×10^{11}	0.776
7	3	20	7.8%	190	0.74	57.3%	2.79×10^{11}	1.3
8	3	20	7.8%	210	0.47	36.1%	3.23×10^{11}	1.5
9	5	20	10.5%	130	1.13	87.5%	2.81×10^{11}	0.413
10	5	20	10.5%	150	0.99	76.7%	5.61×10^{11}	0.516
11	5	20	10.5%	170	0.81	62.7%	8.74×10^{11}	0.673
12	5	20	10.5%	190	0.61	46.8%	1.50×10^{12}	0.761
13	5	20	10.5%	210	0.49	38.1%	1.38×10^{12}	0.861
14	7	20	11.8%	150	0.95	73.3%	2.81×10^{14}	0.022
15	7	20	11.8%	170	0.78	60.2%	4.05×10^{14}	0.027
16	7	20	11.8%	190	0.69	53.5%	4.66×10^{14}	0.037

9.4.1.3 Cellular Morphology

Higher pressure typically results in a higher cell nucleation density and smaller cell size. Figure 9.4 shows an example of the effect of saturation pressure on cell size. Samples were saturated at various pressures between 1 and 7 MPa, and then foamed at the same temperature 190 °C. With an increase of pressure, the cell size reduces from 3.3 μm (sample #2, P_{sat} = 1 MPa) to 37 nm (sample #16, P_{sat} = 7 MPa).

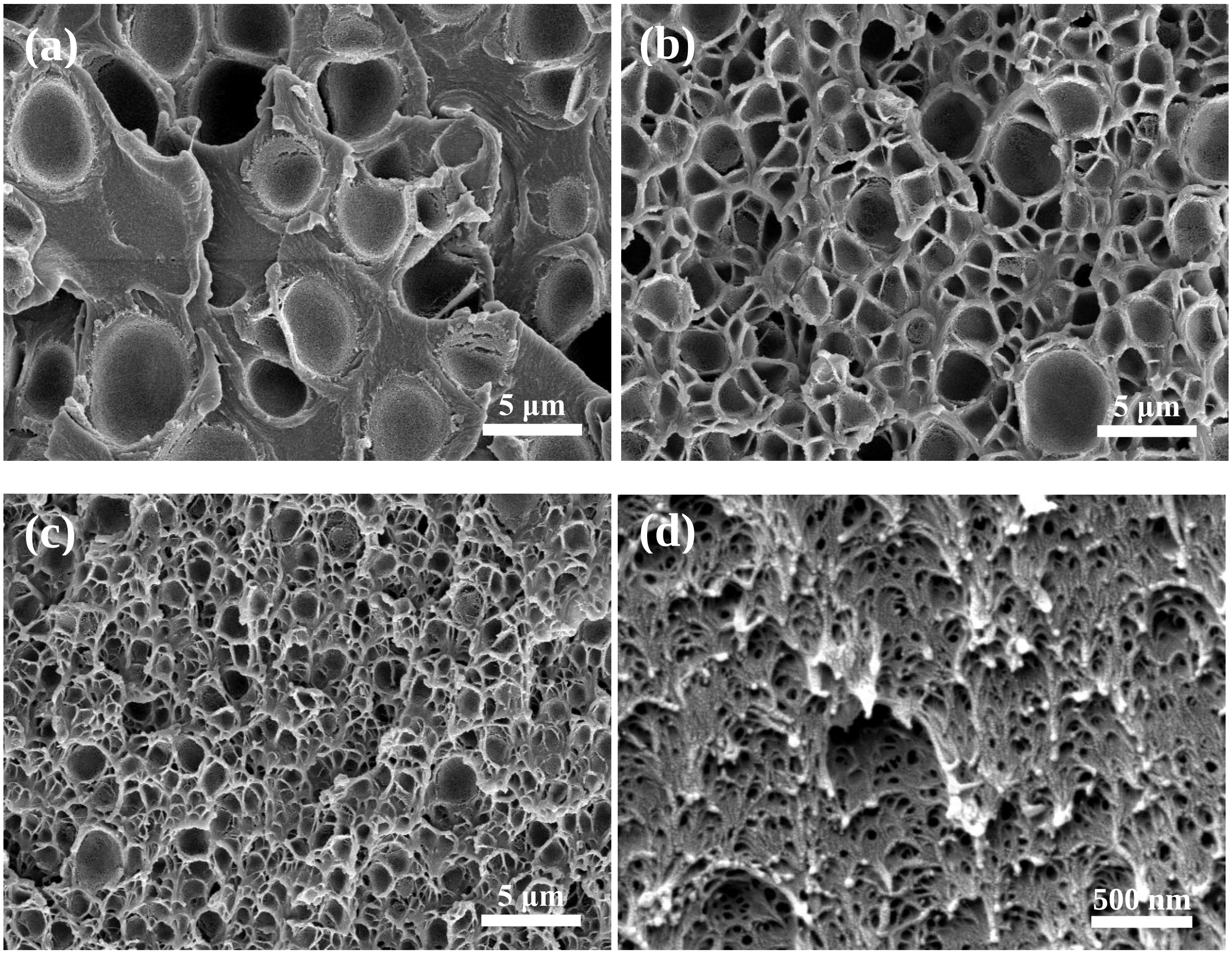

Figure 9.4 Cellular structures of PPSU saturated at 20 ℃ and various pressures, and subsequently foamed at 190 ℃: (a) sample #2, P_{sat} = 1 MPa, cell size 3.3 µm, (b) sample #7, P_{sat} = 3 MPa, cell size 1.3 µm, (c) sample #12, P_{sat} = 5 MPa, cell size 761 nm, (d) sample #16, P_{sat} = 7 MPa, cell size 37 nm.

Figure 9.5 and Figure 9.6 shows cell nucleation density and cell size as a function of CO_2 concentration, respectively. At each concentration, a few different foaming temperatures were used, and the nucleation density & cell size data were shown together under the same concentration. The cell nucleation density increases from 10^{10} cells/cm^3 at 1 MPa, to 10^{11} - 10^{12} cells/cm^3 for 3 and 5 MPa, and 10^{14} cells/cm^3 at 7 MPa. In terms of cell size, at 1 MPa, the cell sizes are 1-10 µm. These are the typical microcellular foams. At 3 and 5 MPa, cell sizes are mostly 400 nm - 1 µm. These can be considered as upper range of nanofoams (these are also sometimes called ultramicrocellular foams [18] or supermicrocellular foams [17]). At 7 MPa, cell sizes are 20-40 nm. PPSU nanofoams in 20-40 nm range are the smallest cell size ever reported. Apparently, the cell nucleation density increases and cell size reduces much more rapidly between 5 and 7 MPa (or equivalently, 10.5% and 11.8% CO_2 concentration).

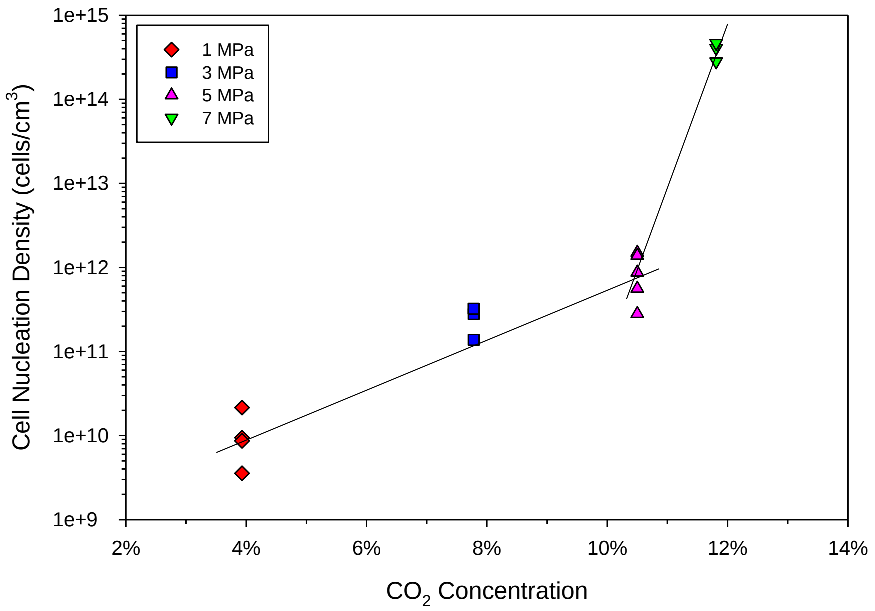

Figure 9.5 Cell nucleation density as a function of CO_2 concentration prepared via different saturation pressures. Lines are drawn to aid the eyes. Notice the much more rapid increase of nucleation density between 10.5% and 11.8%.

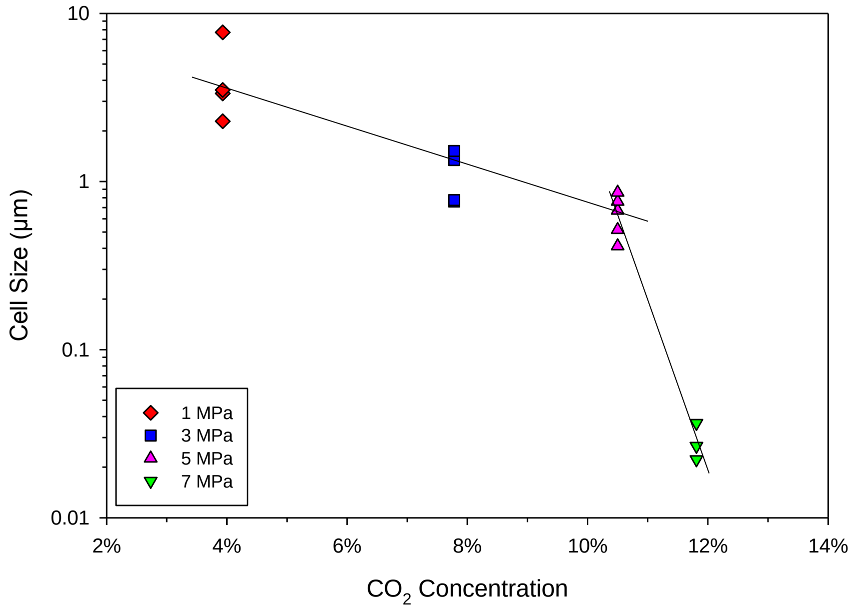

Figure 9.6 Cell size as a function of CO_2 concentration prepared via different saturation pressures. Notice the much more rapid decrease of cell size between 10.5% and 11.8%.

9.4.2 **Effect of Saturation Temperature**

9.4.2.1 CO_2 Solubility

CO_2 solubility in PPSU at various saturation temperatures (while keeping saturation pressure constant at 5 MPa) are also listed in Table 9.1 and plotted in Figure 9.7 (a). From the data, we see that as the saturation temperature decreases the CO_2 solubility increases. The solubility at 10 ℃ is almost 3 times as that at 60 ℃. As in by previous studies [45, 46], temperature dependence of gas solubility can be described by Arrhenius equation given as follows:

$$S = S_0 \exp(-\frac{\Delta H_s}{RT}) \quad (2)$$

where S_0 is the pre-exponential factor, ΔH_S is the heat of sorption or enthalpy change upon solution of gas in the polymer, R is the gas constant, and T is the saturation temperature in K.

If we take natural logarithm on both sides of the equation, we should get a linear relationship between ln(S) and 1/T. In Figure 9.7 (b), we plot the natural logarithm of the solubility as function of 1000/T (instead of 1/T for scaling purpose). A straight line can best fit all the data points. From the slope, the ΔH_S is calculated to be -15.2 kJ/mol.

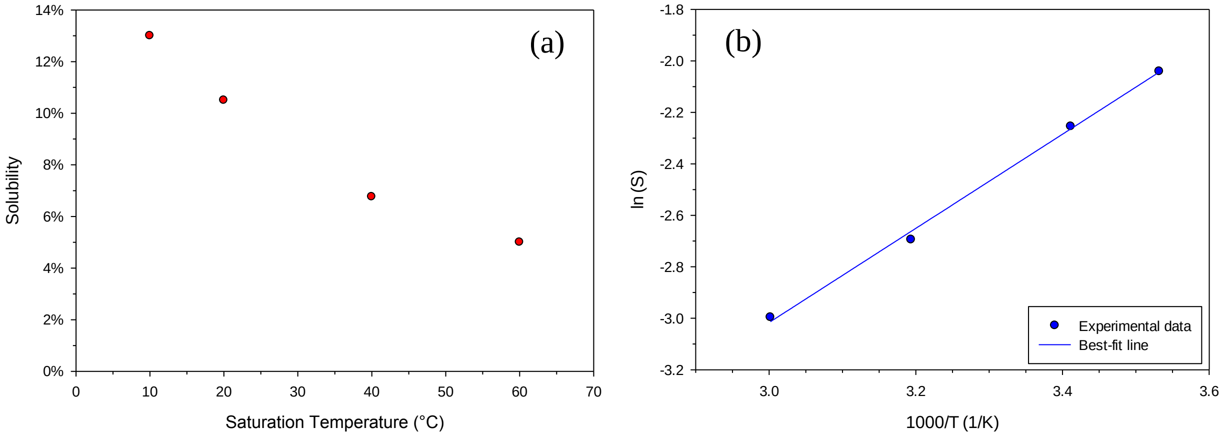

Figure 9.7 Plot of (a) CO_2 solubility as a function of saturation temperature, keeping P_{sat} = 5 MPa; (b) natural logarithm of solubility as a function of 1000/T and a best-fit line using Arrhenius equation.

9.4.2.2 Relative Density

For the foaming study, samples were initially saturated at four different temperatures (60 ℃, 40 ℃, 20 ℃, 10 ℃), and in all these cases 5 MPa saturation pressure was used. After samples were fully saturated with CO_2, they were foamed at different temperatures in the range of 90-230 ℃. Relative density, cell nucleation density, and cell size of the foamed samples were characterized, and data are included in Table 9.3. Figure 9.8 shows the relative density as a function of foaming temperatures. We can see that the relative density decreases with increasing foaming temperatures. For example, relative density decreases from 98.5% at 130 ℃ to 36.4% at 210 ℃ for T_{sat} = 40 ℃ case.

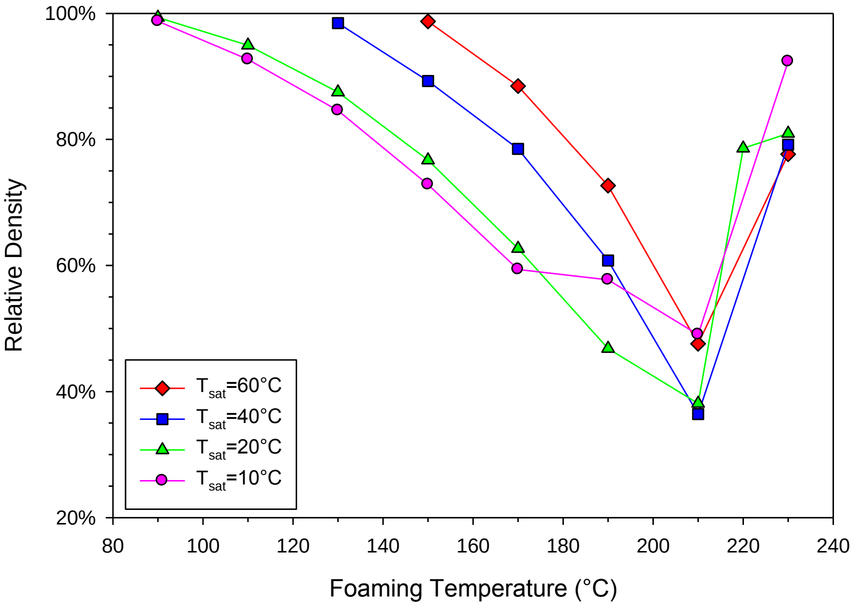

Figure 9.8 Plot of relative density as a function of foaming temperature. Samples were initially saturated at four different temperatures and the same saturation pressure of 5 MPa.

Table 9.3 Summary of processing conditions and foam characteristics for varying saturation temperatures.

Sample #	**P_{sat} (MPa)**	**T_{sat} (℃)**	**CO_2 Concentration**	**T_f (℃)**	**Foam Density (g/cm^3)**	**Rel. Density**	**Nucleation Density (cell/cm^3)**	**Cell size (μm)**
17	5	60	5%	170	1.20	88.5%	2.29×10^{11}	0.626
18	5	60	5%	190	0.98	72.7%	4.50×10^{11}	0.86
19	5	60	5%	210	0.67	47.6%	5.33×10^{11}	1.2
20	5	40	6.8%	150	1.16	89.3%	2.76×10^{11}	0.471
21	5	40	6.8%	170	1.02	78.5%	5.40×10^{11}	0.574
22	5	40	6.8%	190	0.79	60.8%	5.31×10^{11}	0.862
23	5	40	6.8%	210	0.47	36.4%	1.01×10^{12}	0.884
9	5	20	10.5%	130	1.13	87.5%	2.81×10^{11}	0.413
10	5	20	10.5%	150	0.99	76.7%	5.61×10^{11}	0.516
11	5	20	10.5%	170	0.81	62.7%	8.74×10^{11}	0.673
12	5	20	10.5%	190	0.61	46.8%	1.50×10^{12}	0.761
13	5	20	10.5%	210	0.49	38.1%	1.38×10^{12}	0.861
24	5	10	13%	150	0.94	72.8%	2.66×10^{14}	0.028
25	5	10	13%	170	0.77	59.4%	4.96×10^{14}	0.026
26	5	10	13%	190	0.75	57.7%	6.91×10^{14}	0.027

Note: data for P_{sat} = 5 MPa and T_{sat} = 20 ℃ condition are also included in this table for direct comparison.

9.4.2.3 Cellular Morphology

A lower saturation temperature results in a higher CO_2 concentration, which will enhance the cell nucleation and reduce cell size. Figure 9.9 shows an example of the effect of saturation temperature on cell size. Samples were saturated at various temperatures from 10-60 ℃ and all at 5 MPa, and then foamed at the same temperature 170 ℃. With a decrease of T_{sat}, the cell size reduces from 626 nm (sample #17, T_{sat} = 60 ℃) to 26 nm (sample #25, T_{sat} = 10 ℃).

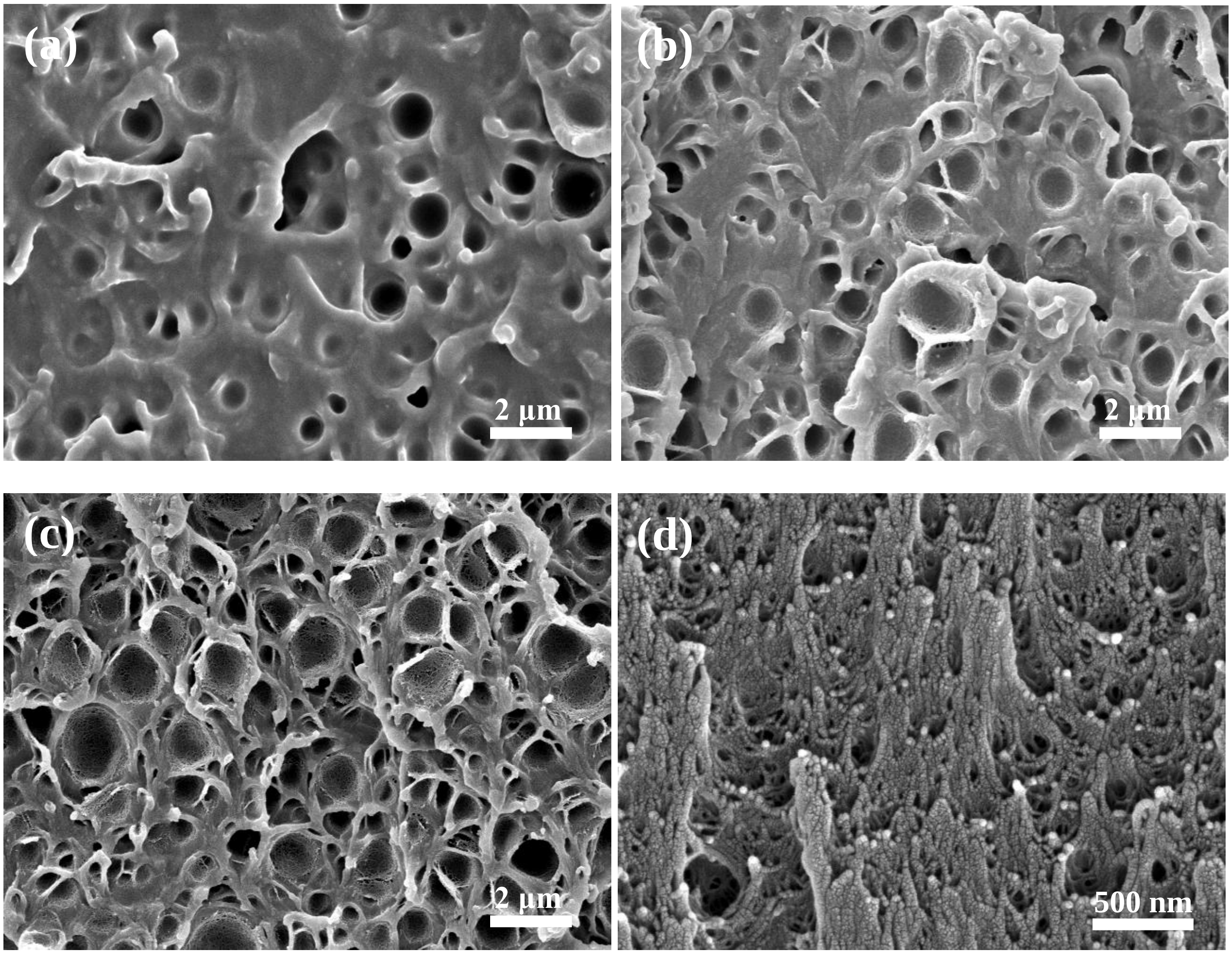

Figure 9.9 Cellular structures of PPSU saturated at 5 MPa and various temperatures, and subsequently foamed at 170 ℃: (a) sample #17, T_{sat} = 60 ℃, cell size 626 nm, (b) sample #21, T_{sat} = 40 ℃, cell size 574 nm, (c) sample #11, T_{sat} = 20 ℃, cell size 673 nm, (d) sample #25, T_{sat} = 10 ℃, cell size 26 nm.

Figure 9.10 and Figure 9.11 shows cell nucleation density and cell size as a function of CO_2 concentration, respectively. At each CO_2 concentration, cell nucleation density and cell size data from samples that were foamed at different temperatures are included. For T_{sat} = 20-60 ℃, a slight increase in cell nucleation density and cell size is observed; however, when T_{sat} decreases from 20 ℃ to 10 ℃, there is a very significant increase in cell nucleation density and reduction in cell size.

The rapid increase of nucleation density (or reduction in cell size) occurs between 10.5% and 13%. This is consistent with our previous results on the saturation pressure, where it occurs between 10.5% and 11.8%. The rapid increase of cell nucleation density and rapid decrease of cell size within a narrow range of CO_2 concentration have been observed in other polymers, including PEI [21, 22], PES [22], PC [25], PMMA [26, 27], and PSU [27, 28]. In these systems, a critical concentration was identified above which a rapid increase of cell nucleation density or a rapid decrease of cell size occurred. In PPSU, we can see the critical concentration exists between 10.5% and 11.8%.

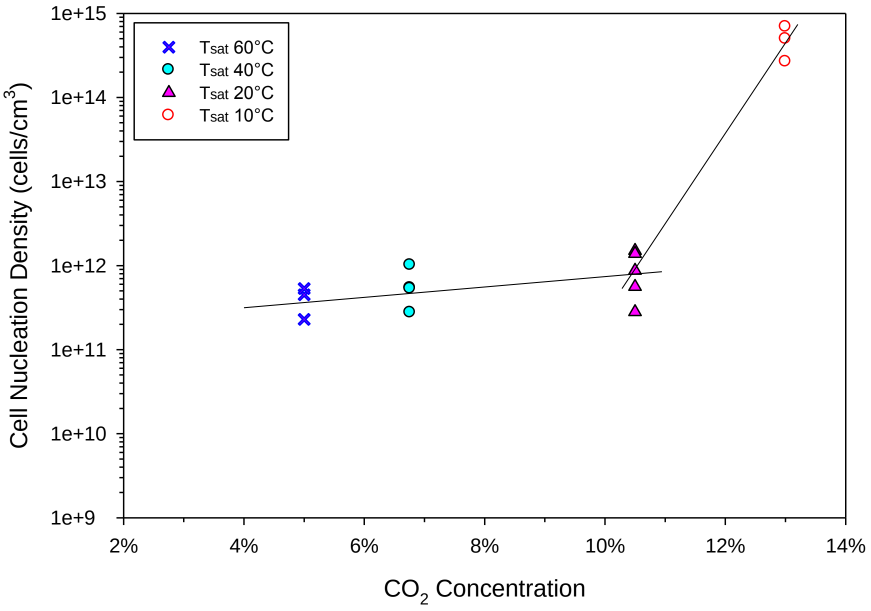

Figure 9.10 Cell nucleation density as a function of CO_2 concentration prepared via different saturation temperatures. Lines are drawn to aid the eyes. Notice the much more rapid increase of nucleation density between 10.5% and 13%.

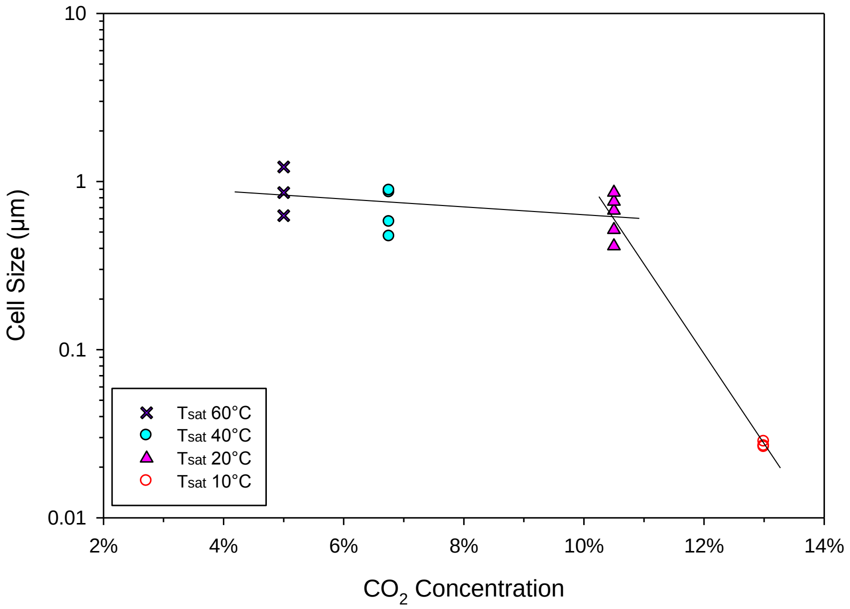

Figure 9.11 Cell size as a function of CO_2 concentration prepared via different saturation temperatures. Notice the much more rapid decrease of cell size between 10.5% and 13%.

For CO_2 concentration of 11.8% (P_{sat} = 7 MPa, T_{sat} = 20 ℃) and 13% (P_{sat} = 5 MPa, T_{sat} = 10 ℃), the cell nucleation densities are both on the order of 10^{14} cells/cm^3 and the cell sizes around 20-40 nm. An increase in CO_2 concentration in this range doesn't result in further increase in cell nucleation density, We observed a similar leveling off phenomenon in PMMA [26] and PSU [28]. The additional amount of CO_2 might not participate in the nucleation process and might simply diffuse out of the polymer.

The two CO_2 concentration that result in nanofoams with cell size below 100 nm are 11.8% and 13%, which corresponds to the saturation condition of P_{sat} = 7 MPa & T_{sat} = 20 ℃ and P_{sat} = 5 MPa & T_{sat} = 10 ℃, respectively. Both approaches are able to achieve sufficiently high concentration above the critical concentration. These two conditions can be approached from a typical pressure and temperature condition, such as 5 MPa and 20 ℃, using two different paths (see Figure 9.12). Interestingly, in both conditions the CO_2 is in liquid state. Traditional solid-state foaming process uses mostly gaseous CO_2 and supercritical CO_2 and typically microcellular foams are generated. From our study, we can see that using high pressure liquid CO_2 in the solid-state foaming process is an effective way to further reduce cell size and create nanofoams.

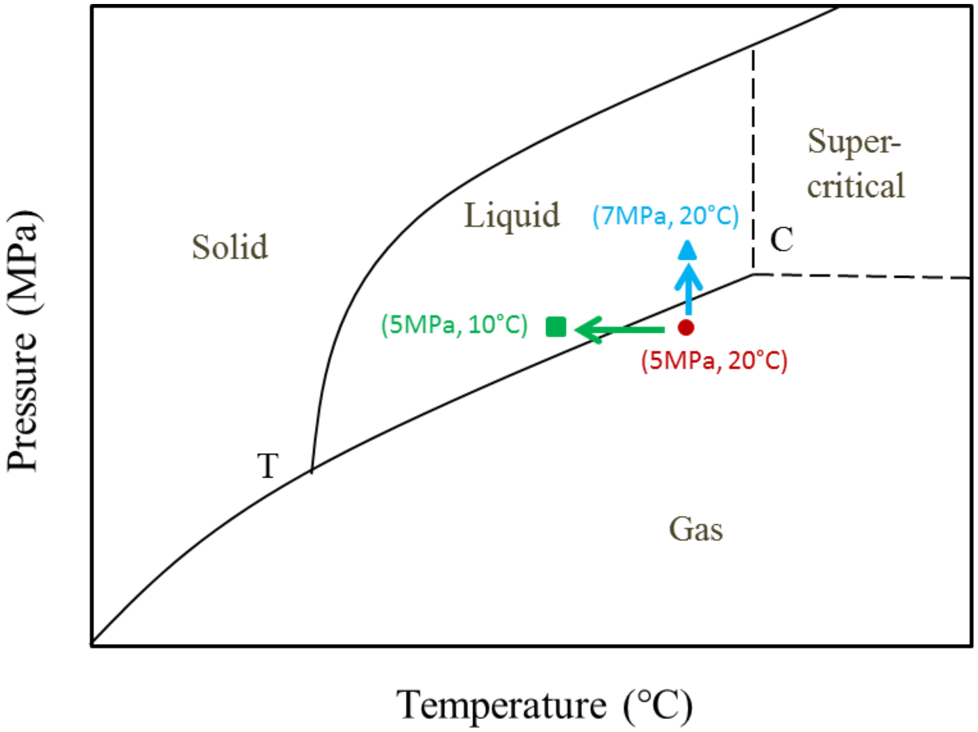

Figure 9.12 CO_2 phase diagram containing two sets of conditions (7 MPa, 20 ℃) and (5 MPa, 10 ℃) for creating PPSU nanofoams with the cell size below 100 nm. The two sets of conditions can be approached from a typical pressure and temperature condition using two different paths.

9.4.3 **Transition from Closed Cellular to Open Porous Structures**

In the nanofoams we created, using both saturation conditions (P_{sat} = 7 MPa, T_{sat} = 20 ℃) and (P_{sat} = 5 MPa, T_{sat} = 10 ℃), we observed differences in the cellular morphology. Some of the samples had closed cells distributed discretely, while some have cell interconnected (absence of cell walls). Figure 9.13 shows the microstructure of the nanofoams that were initially saturated at 7 MPa and 20 ℃, and then foamed between 130 ℃ and 190 ℃. At 130 ℃, nanosized cells with a cell size of 18 nm are sparsely distributed. At 150 ℃, the cellular structure seem to be slightly open (or bicontinuous) porous with cell size around 22 nm. At 170 ℃ and 190 ℃, many interconnectivities between the cells can be observed and cell size were 27 nm and 37 nm, respectively.

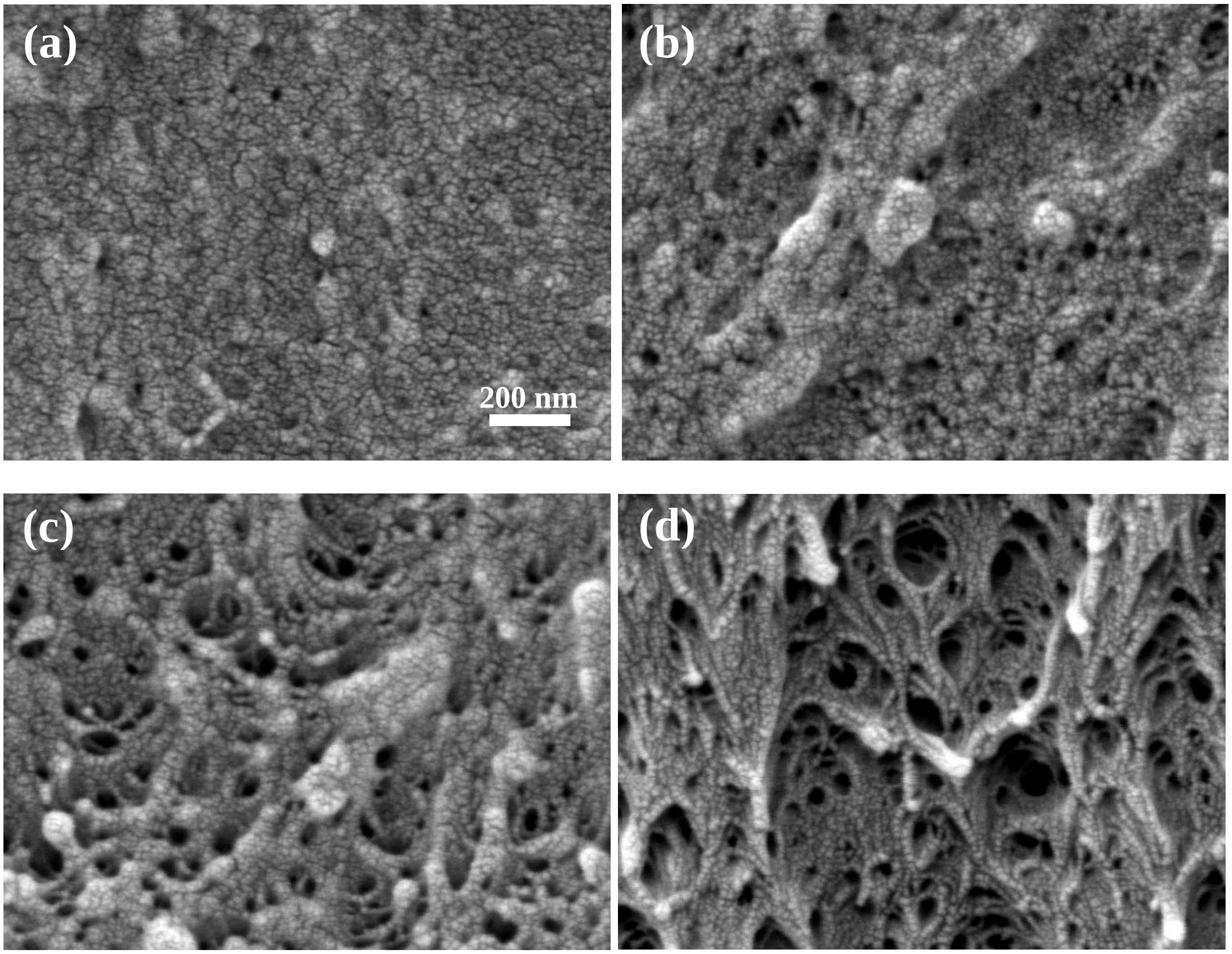

Figure 9.13 Cellular structures of nanofoams prepared at different foaming temperatures: (a) 130 ℃, (b) 150 ℃, (c) 170 ℃, (d) 190 ℃. All samples were initially saturated at 7 MP and 20 ℃. All images have the same scale bar.

To substantiate whether these samples were open porous, dye test was performed. Figure 9.14 shows the dye penetration results on these four samples. The dye was applied on the top and it penetrated into the depth direction. We can see that sample in (a) doesn't have any dye penetration and sample in (b) has little dye penetration. In (c) and (d), dye penetrates a significant distance in the depth direction. It seems that as the foaming temperature increases the dye penetrates deeper into the sample. A similar trend was found in nanofoams that were prepared at 5 MPa and 10 ℃.

The open porous structure in high temperature PPSU provides great opportunities to create materials for high performance filtration or gas separation applications, where, for example, the working temperature is relatively high. The transition from closed-nanocellular to open-nanoporous was reported previously in PEI [22], PES [22], PC [25], PSU [28] and recently PMMA [26]. The transition was believed to be due to spinodal decomposition mechanism [26], where homogenous binary mixture separated into two uniform and interconnected phases: polymer rich phase and CO_2 rich phase.

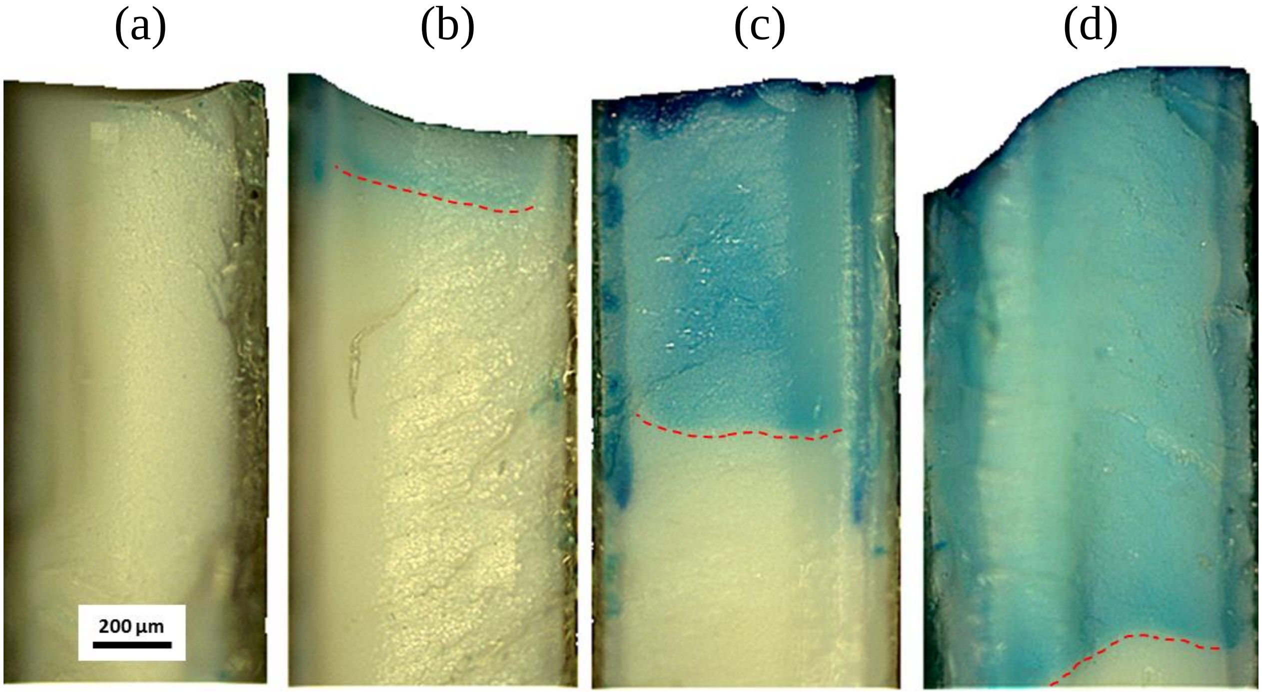

Figure 9.14 Dye penetration in nanofoams that were prepared at (a) 130 ℃, (b) 150 ℃, (c) 170 ℃, (d) 190 ℃. All samples were initially saturated at 7 MP and 20 ℃. Dashed lines that indicate where the dye penetration stopped are drawn to aid the eyes.

9.4.4 **Nanostructures on the Cell Wall**

On the cell wall of foams that are processed under certain conditions, nanostructures were observed. Figure 9.15 shows such nanostructures in sample #22. The big cell in (a), of which the cell wall is imaged is around 2 µm, and its cell wall thickness is about 300 nm. Open porous nanostructures in (b) appear on the cell wall, with cell sizes of the nanostructures around 10-70 nm and cellular struts around 20 nm. The nanostructures on the cell wall are a network of stretched struts (which are essentially nanosized fibers) and these stretched nanofibers might greatly reinforce the cell wall. As a result, the foams with these nanostructures on the cell wall might exhibit enhanced strength, toughness, and impact absorption properties.

Several polymers have shown similar nanostructures on the cell wall. These include PEI [14, 21], PES [39] , PC [47, 48] and recently PSU [28]. A detailed discussion regarding to nanostructures on the cell wall be found in our recent study [28]. One interesting observation in this study is that the cells have to be sufficiently large enough to accommodate these nanostructures on their cell wall. No nanostructures were observed on the cell wall of nanocells with cell size below 100 nm. This makes sense if we consider the fact that the size of the nanostructures on the cell wall are on the same order as the nanocells.

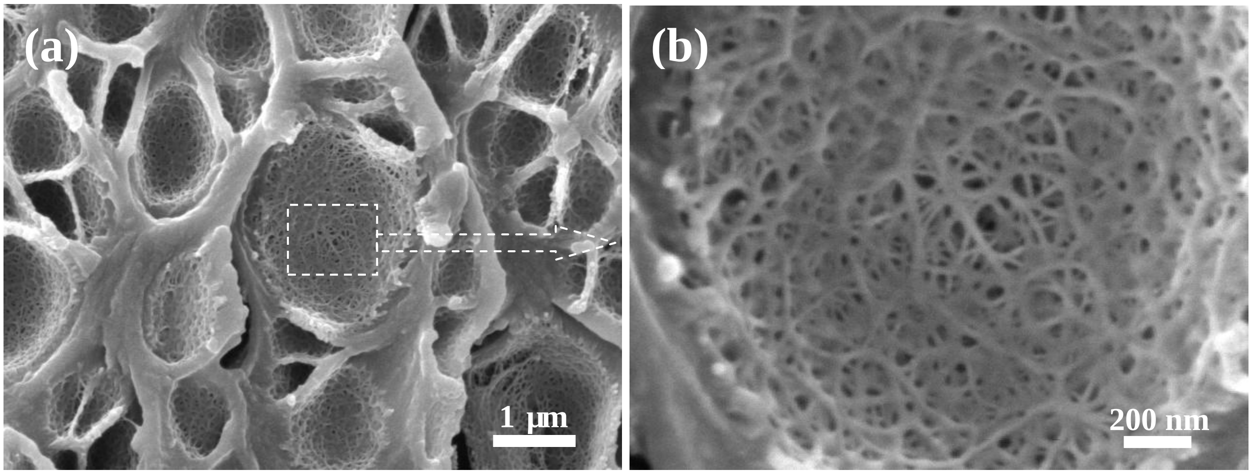

Figure 9.15 Nanostructures on the cell wall. (b) is a close-up view of (a). This sample (sample#22) was saturated at 5 MPa and 40 ℃, and then foamed at 190 ℃.

9.4.5 **Void Fraction-Cell Size Map of PPSU Foams**

Void fraction (1-relative density) and cell size are the two most important characteristics of foams. In Figure 9.16 we show the void fraction - cell size map for samples created in this study. Literature data from previous studies by Sun et al. [38] and Sorrentino et al. [39]are also included for comparison. Our study expands the processing space of PPSU foams. The previous studies have cell size limited in the range of 1-10 µm. Via the two approaches we demonstrated, we are able to create cells between 100 nm - 1 µm, and more significantly below 100 nm. At the meantime, a range of void fraction for these cell sizes are achievable. The expanded processing space provided us a greater number of choices in tailoring foams structure to specific applications.

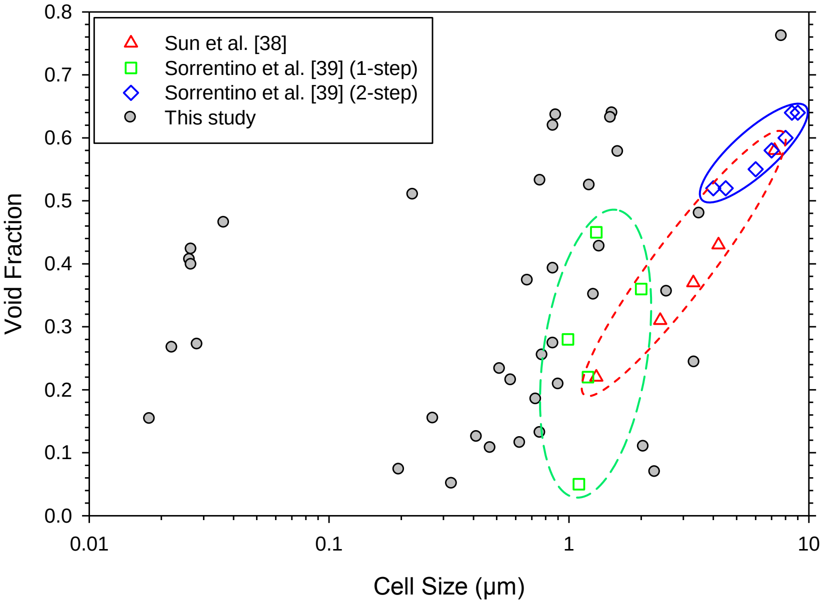

Figure 9.16 Void fraction-cell size map of PPSU foams created in this study. Literature data are also included for comparison.

9.5 **Summary**

This research presents a detailed investigation of the PPSU-CO_2 system where high temperature PPSU foams with a range of densities and various microstructures can be created. Microcellular foams with cell size up to 10 μm and nanocellular foams with cell size down to the range of 20-40 nm are successfully fabricated. The processing space of PPSU foams have been significantly expanded through this study.

The effects of the saturation pressure (1-7 MPa) and saturation temperature (10-60 ℃) on PPSU foaming are systematically investigated. Increasing saturation pressure results in an increase of CO_2 solubility in PPSU, an increase of cell nucleation density and a decrease of cell size. Similarly, decreasing saturation temperature leads to an increase of CO_2 solubility in PPSU, an increase of cell nucleation density and a decrease of cell size.

We discovered a critical concentration between 10.5% and 11.8%, above which the cell nucleation density increases and cell size drops much more rapidly, resulting in a small cell size below 100 nm. Two different sets of saturation conditions were used to create nanofoams with a cell size of 20-40 nm: 7 MPa & 20 °C and 5 MPa & 10 °C. Both cases use high pressure liquid CO_2.

Nanofoams exhibit different microstructures depending on the foaming temperature used. At high CO_2 concentration of 11.8% and 13%, microstructures of nanofoams transition from closed nanocellular structure to open nanoporous structure. The open porous nature was verified by dye test.

9.6 **Acknowledgment**

The authors would like to acknowledge the financial support from the University of Washington CGF fund, National Science Foundation Grant CMMI 1253072, and MicroGREEN Polymers, Inc.

9.7 **References**

1. Martini JE, Waldman FA, and Suh NP. The production and analysis of microcellular thermoplastic foam. SPE ANTEC, vol. 28. San Francisco, CA, 1982. pp. 674.
2. Martini JE, Suh NP, and Waldman FA. Microcellular closed cell foams and their method of manufacture. Patent No. US 4,473,665: Massachusetts Institute of Technology, 1984.
3. Kumar V and Weller JE. International Polymer Processing 1993;8(1):73-80.
4. Murray RE, Weller JE, and Kumar V. Cellular Polymers 2000;19(6):413-425.
5. Guo H, Nadella K, and Kumar V. Journal of Materials Research 2013;28(17):2374-2379.
6. Shimbo M, Higashitani I, and Miyano Y. Journal of Cellular Plastics 2007;43(2):157-167.
7. Kumar V and Weller J. Journal of Manufacturing Science and Engineering 1994;116(4):413-420.
8. Guo H and Kumar V. Solid-state Microcellular Foaming of Low- and High- Tg Cyclic Olefin Copolymer (COC). SPE FOAMS Conference. Iselin, NJ, 2014.
9. Guo H and Kumar V. Journal of Applied Polymer Science 2015;132(28):42226.
10. Wang X, Kumar V, and Wei L. Cellular Polymers 2007;26(1):1-25.
11. Richards E, Rizvi R, Chow A, and Naguib H. Journal of Polymers and the Environment 2008;16(4):258-266.
12. Goel SK and Beckman EJ. Cellular Polymers 1993;12(4):251-274.
13. Miller D and Kumar V. Polymer 2011;52(13):2910-2919.
14. Zhou C, Vaccaro N, Sundarram SS, and Li W. Journal of Cellular Plastics 2012;48(3):239-255.
15. Notario B, Pinto J, and Rodríguez-Pérez MA. Polymer 2015;63:116-126.
16. Notario B, Pinto J, Solorzano E, de Saja JA, Dumon M, and Rodríguez-Pérez MA. Polymer 2015;56(0):57-67.
17. Baldwin DF, Suh NP, Park CB, and Cha SW. Supermicrocellular foamed materials. Patent No. US 5,334,356: Massachusetts Institute of Technology, 1994.
18. Handa YP and Zhang Z. Journal of Polymer Science Part B: Polymer Physics 2000;38(5):716-725.
19. Handa YP, Zhang Z, and Wong B. Cellular Polymers 2001;20(1):1-16.
20. Nawaby AV, Handa YP, Liao X, Yoshitaka Y, and Tomohiro M. Polymer International 2007;56(1):67-73.
21. Miller D, Chatchaisucha P, and Kumar V. Polymer 2009;50(23):5576-5584.

22. Krause B, Sijbesma HJP, Münüklü P, van der Vegt NFA, and Wessling M. Macromolecules 2001;34(25):8792-8801.
23. Aher B, Olson NM, and Kumar V. Journal of Materials Research 2013;28(17):2366-2373.
24. Krause B, Diekmann K, van der Vegt NFA, and Wessling M. Macromolecules 2002;35(5):1738-1745.
25. Guo H and Kumar V. Polymer 2015;56:46-56.
26. Guo H, Nicolae A, and Kumar V. Polymer 2015;70:231-241.
27. Guo H and Kumar V. Solid-state thermoplastic nanofoams via a novel low-temperature saturation pathway. SPE ANTEC. Orlando, FL, 2015. pp. 2834-2840.
28. Guo H, Nicolae A, and Kumar V. Journal of Polymer Science Part B: Polymer Physics 2015;53(14):975-985.
29. Nemoto T, Takagi J, and Ohshima M. Polymer Engineering & Science 2010;50(12):2408-2416.
30. Nemoto T, Takagi J, and Ohshima M. Macromolecular Materials and Engineering 2008;293(7):574-580.
31. Nemoto T, Takagi J, and Ohshima M. Macromolecular Materials and Engineering 2008;293(12):991-998.
32. Pinto J, Dumon M, Pedros M, Reglero J, and Rodriguez-Perez MA. Chemical Engineering Journal 2014;243:428-435.
33. Pinto J, Dumon M, Rodriguez-Perez MA, Garcia R, and Dietz C. The Journal of Physical Chemistry C 2014;118(9):4656-4663.
34. Costeux S, Bunker SP, and Jeon HK. Journal of Materials Research 2013;28(17):2351-2365.
35. Costeux S, Khan I, Bunker SP, and Jeon HK. Journal of Cellular Plastics 2015;51(2):197-221.
36. Costeux S and Zhu L. Polymer 2013;54(11):2785-2795.
37. Costeux S. Journal of Applied Polymer Science 2014;131(23):41293.
38. Sun H, Sur GS, and Mark JE. European Polymer Journal 2002;38(12):2373-2381.
39. Sorrentino L, Aurilia M, and Iannace S. Advances in Polymer Technology 2011;30(3):234-243.
40. Kumar V and Weller JE. Journal of Manufacturing Science and Engineering 1994;116(4):413-420.
41. Sun H and Mark JE. Journal of Applied Polymer Science 2002;86(7):1692-1701.
42. Koros WJ, Paul DR, and Rocha AA. Journal of Polymer Science Part B: Polymer Physics 1976;14(4):687-702.
43. Kamiya Y, Hirose T, Mizoguchi K, and Naito Y. Journal of Polymer Science Part B: Polymer Physics 1986;24(7):1525-1539.
44. Handa YP, Wong B, Zhang Z, Kumar V, Eddy S, and Kehmani K. Polymer Engineering and Science 1999;39(1):55-61.
45. Crank J and Park GS. Diffusion in Polymers. London: Academic Press, 1968.
46. Guo H and Kumar V. Polymer 2015;57:157-163.
47. Gong P, Taniguchi T, and Ohshima M. Journal of Materials Science 2014;49(6):2605-2617.
48. Fukasawa Y, Chen J, and Saito H. Journal of Polymer Science Part B: Polymer Physics 2008;46(8):843-846.

Chapter 10

Some Properties of Polymer Nanofoams

10.1 **Introduction**

Polymer nanofoams have drawn tremendous interest in the past decade. They are believed to exhibit superior properties than existing cellular polymers and may even show some novel properties. However, only few studies [1-4] reported the properties of nanofoams and compared the properties of microcellular and nanocellular foams. More studies on the properties of nanofoams need to be conducted.

Miller and Kumar [1] compared the properties of microcellular and nanocellular PEI at similar densities. They showed that at a similar density PEI nanofoams had a significantly higher strain to failure, resulting in an improvement in the tensile toughness by 350% compared to microcellular foams. They also found a brittle-to-ductile transition in PEI nanofoams resulting in impact energies that are up to 600% higher compared to microcellular foams. However, no difference was observed in the elastic modulus between microcellular and nanocellular PEI. Zhou et al. [2] conducted three-point bending test on microcellular and nanocellular PEI, and showed that PEI nanofoams had higher specific flexural strength and specific flexural modulus. Notario et al. [3] studied the thermal conductivity of microcellular and nanocellular PMMA/MAM. They found a lower thermal conductivity in the nanofoams which was believed due to the reduced gas phase heat conduct and increased tortuosity of the matrix materials. Notario et al. [4] also compared the various properties of microcellular and nanocellular PMMA, with cell size ranging from 200 nm to 11 μm. Nanocellular foams presented a significant improvement in several physical properties, including storage modulus, elastic modulus, impact resistance, and shore hardness.

In this study, we investigate the tensile, impact, thermal conductivity, glass transition temperature, and light transmittance properties of nanocellular PC. Microcellular PC with similar densities are also added for comparison. We utilize the hot press foaming technique to make large and flat samples with a range of densities. Microstructures of these foams are first characterized. Subsequently, aforementioned tests and measurements are performed.

10.2 **Experimental**

10.2.1 **Hot Press Foaming**

All the material used in this study was MAKROLON PC. 0.8 mm thick sheets were used to prepare samples for all the tests except for the light transmittance. Two types of samples were first cut from the large sheets: 75 mm x 75 mm squares for impact, thermal conductivity, and glass transition temperature measurement, and 32 mm x 108 mm rectangles for tensile test. These samples were then placed in a pressure vessel. For making microcellular foams samples were saturated at 4 MPa and room temperature (~23 ℃). For making nanocellular foams, samples were saturated at 5 MPa and -30 ℃. After full saturation, samples were then removed from the pressure vessel and quickly transferred to the hot press, which was preheated to a desired temperature. Samples were then placed between two heated platen, and 6 psi clamping pressure was applied to ensure that foamed samples were flat. After 10 minute foaming, samples were kept between platens with the pressure still on and the heated platen were cooled down to room temperature via air and water cooling. Samples were then removed once the hot press reached the room temperature. The transfer time between the pressure vessel and hot press was kept short to ensure that all the samples were created with a negligible skin thickness.

10.2.2 **Tensile Test**

Tensile test was performed according to the ASTM D638. Type IV dogbone shaped specimens were first die cut from the rectangular shaped samples. Die cutting was performed after the foaming was completed. Tensile test was conducted using Instron 5585H with a constant crosshead speed of 10 mm/min. A non-contacting video extensometer was used to record the strain. At least five specimens were tested for each processing condition.

10.2.3 **Impact Test**

Impact test was conducted using Dynatup impact tester following the ISO 6603-2 Standard. The square shaped samples were used. A 7.4 kg drop weight was used for all the tests and the drop height was fixed at 0.6 m. At least five specimens were tested for each processing condition.

10.2.4 **Thermal Conductivity Measurement**

Thermal conductivity of the specimen was measured using the guarded hot plate method, following ASTM C177-10. A home-made apparatus was used. Two specimens were required. Each specimen was sandwiched between one hot plate and one cold plate. A known amount of energy was supplied to hot plate and the steady-state temperature drop across the specimen was measured using thermocouples.

10.2.5 **Glass Transition Temperature Measurement**

Glass transition temperature of the specimen was measured using TA Auto Q20 with a heating rate of 10 ℃/min. Specimen weighing about 5 mg was placed in a Tzero aluminum pan and then sealed with an aluminum lid. Specimen was heated up to 200 ℃. At least three specimens were measured for each processing condition.

10.2.6 **Light Transmittance Measurement**

Light transmittance of the specimens was measured using Cary 5000 UV-Vis-NIR spectrophotometer with a maximum range of 175 nm – 3000 nm. The scanning range used in this study was 200 – 1600 nm. Specimen was placed behind a metal blank with a 5 mm diameter hole in the center. Light from one end passed through the hole, the specimen, and then was detected by the sensor on the other end. At least five specimens were measured for each processing condition.

10.3 **Results and Discussions**

10.3.1 **Microstructure**

Table 10.1 shows the processing conditions and corresponding relative density and cell size of the specimens. The relative density spans 0.5-0.9 for microcellular and nanocellular PC. Cell size ranges from 5 – 8 μm for microcellular PC and 17-25 nm for nanocellular PC. Figure 10.1 and Figure 10.2 show the cellular structure of the microcellular and nanocellular PC, respectively. From the micrographs, we can see that the cell structures are very uniform, which is essential for property tests.

Table 10.1 Processing conditions, relative density, and cell size of microcellular and nanocellular PC.

Sample	Sat. Pressure (MPa)	Sat. Temperature (℃)	Foaming Temperature (℃)	Relative Density	Cell Size
Unprocessed PC	--	--	--	1	--
Microcellular PC - 1	4	23	78	0.875	5 μm
Microcellular PC - 2	4	23	91	0.758	6 μm
Microcellular PC - 3	4	23	103	0.647	7 μm
Microcellular PC - 4	4	23	115	0.553	8 μm
Nanocellular PC - 1	5	-30	35	0.865	17 nm
Nanocellular PC - 2	5	-30	45	0.783	20 nm
Nanocellular PC - 3	5	-30	55	0.69	24 nm
Nanocellular PC - 4	5	-30	70	0.608	25 nm

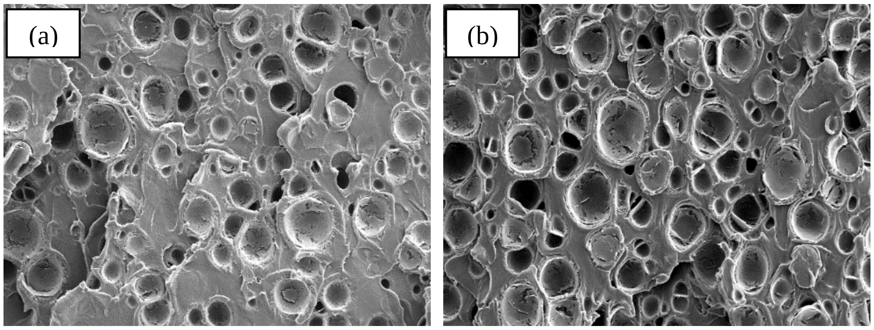

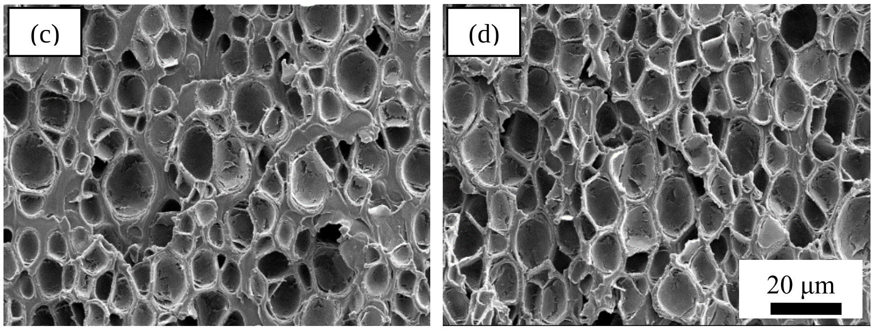

Figure 10.1 SEM images of microcellular PC with a relative density of (a) 0.875, (b) 0.758, (c) 0.647, (d) 0.553. All images have the same magnification and scale bar.

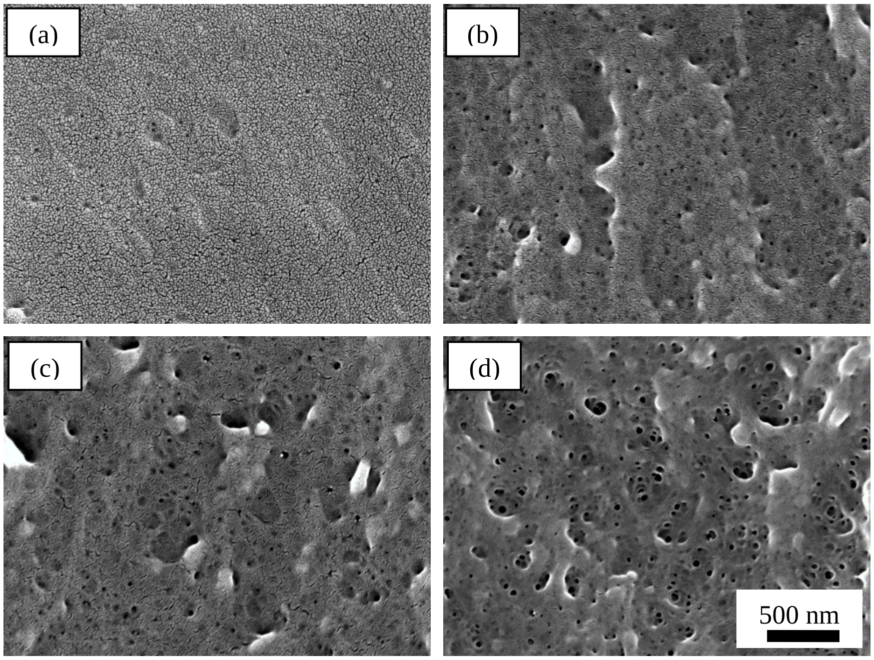

Figure 10.2 SEM images of nanocellular PC with a relative density of (a) 0.865, (e) 0.783, (f) 0.69, (d) 0.608. All images have the same magnification and scale bar.

10.3.2 **Tensile Property**

The stress-strain curves for unprocessed, microcellular, and nanocellular PC are shown in Figure 10.3. Gas sorption and desorption can affect the properties of polymers. In order to see this effect, samples that were saturated first and then desorbed slowly overtime without foaming were also tested. They are termed as "*saturation annealed*" samples. Materials properties that can be derived from the stress-strain curves will be presented later in this section.

Generally, all the curves show a similar behavior, with elastic region at the beginning and then large plastic region before the break. Some samples (microcellular PC RD=0.55 and nanocellular PC, RD=0.61, 0.69, 0.78) show different behaviors in the yield region. In these samples, no reduction in stress can be observed. This is in contrast to typical plastic materials, where a reduction in stress occurs in the yield region due to necking phenomenon.

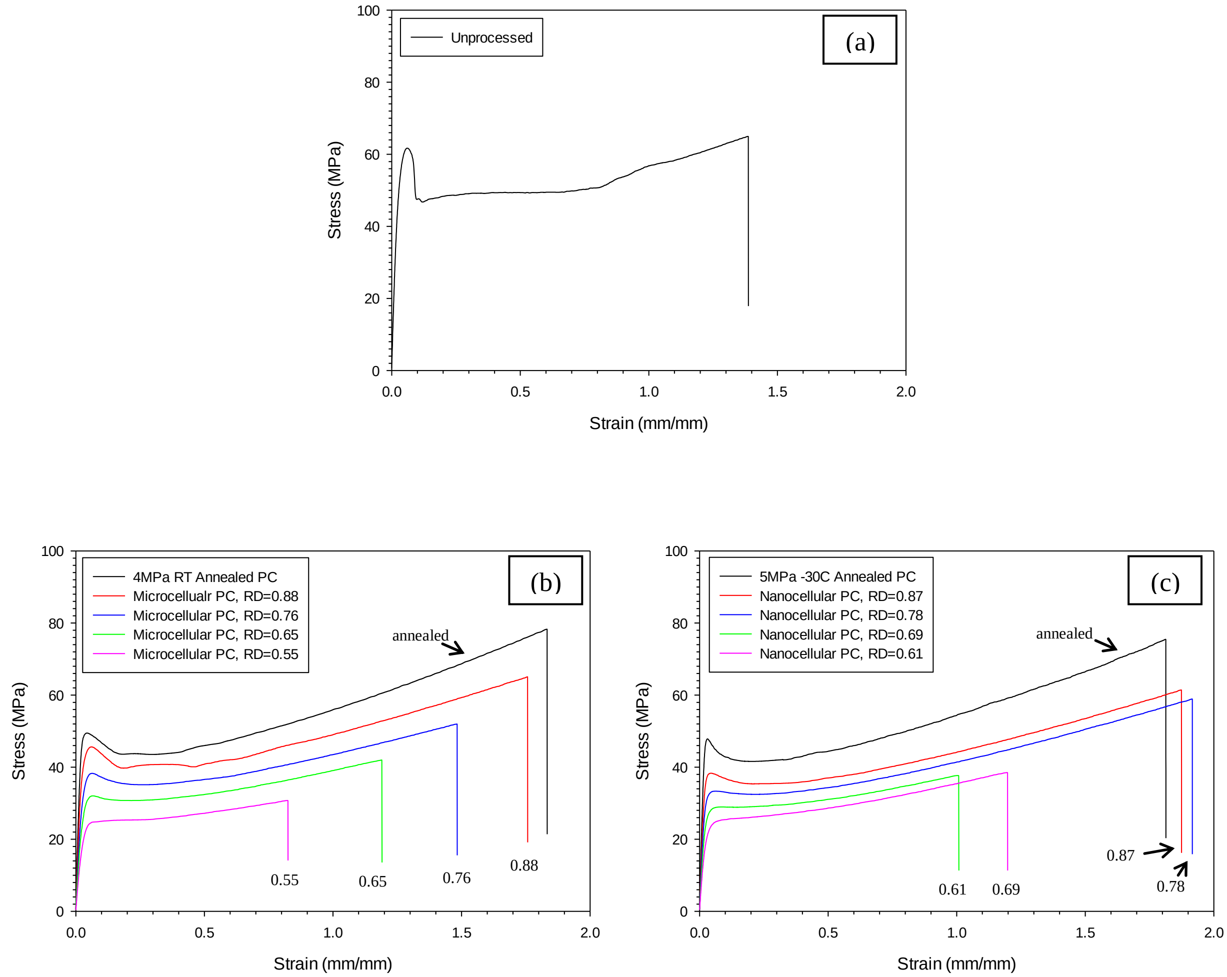

Figure 10.3 Stress-strain curve of unprocessed, microcellular, and nanocellular PC. For the microcellular and nanocellular PC, saturation annealed samples are also tested.

Elastic modulus, or Young’s modulus as a function of relative density is shown in Figure 10.4 (a). Notice that at relative density of 1, the data of saturation annealed samples are also included. Young’s modulus of microcellular and nanocellular PC decreases as the relative density decreases, following the same trend.

Relative modulus of cellular materials is defined as modulus of foams, E_f, divided by modulus of matrix material, E_m. Relative modulus is closely related to relative density of the foams. One of the commonly used models is Gibson-Ashby model [5], described as follows:

$$\frac{E_f}{E_m} = (\frac{\rho_f}{\rho_m})^2 \tag{1}$$

where E_f is the Young's modulus of the foam, E_m the Young's modulus of matrix material, ρ_f the foam density, and ρ_m the density of matrix material.

Figure 10.4 (b) plots the relative modulus as a function of relative density. Note that for microcellular and nanocellular foams, the relative modulus was calculated by dividing the modulus of foams by the modulus of saturation annealed sample, as the property of saturation annealed sample can better represent the property of matrix material in the foams. Microcellular and nanocellular PEI data reported by Miller and Kumar [1] are also included. Also, it can be seen that the Gibson-Ashby model can predict the data very well. This also suggests that modulus of foams is a strong function of foam density but independent of cell size for the range of density and cell size studied.

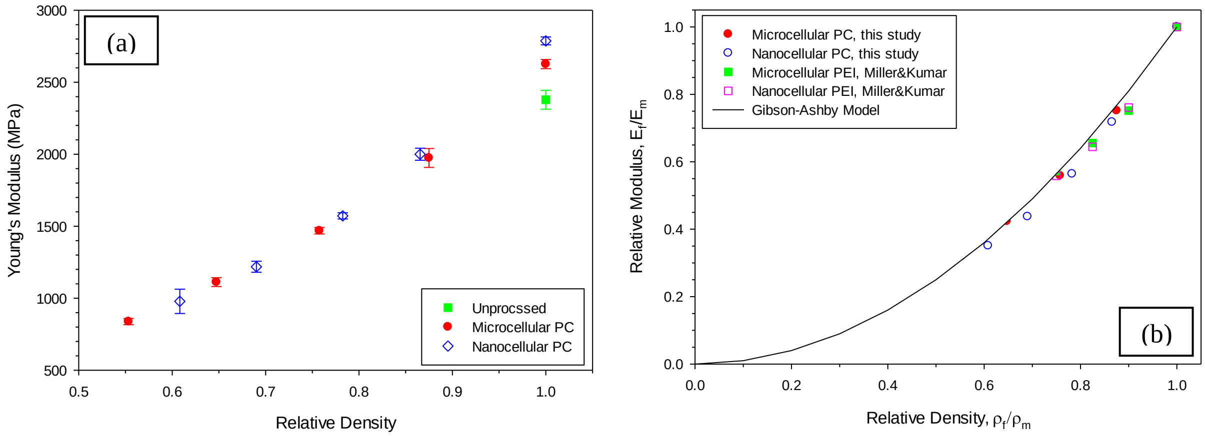

Figure 10.4 (a) Young's modulus of unprocessed, microcellular, and nanocellular PC, as a function of relative density. (b) Comparison of experimental data with Gibson-Ashby model prediction. Data of microcellular and nanocellular PEI reported by Miller and Kumar [1] are also included.

Yield strength is defined as the stress at the first point where slope becomes zero. Yields strength data are shown in Figure 10.5 (a). Saturation annealed samples have a lower yield strength than unprocessed PC, indicating the effect of the gas saturation & desorption on material properties. For microcellular and nanocellular PC, yield strength is linear function of relative density, decreasing linearly from the value for corresponding saturation annealed samples at the relative density of 1.

Figure 10.5 (b) and (c) show the stress at break and strain at break as a function of relative density, respectively. Saturation annealed samples have higher stress at break and strain at break than unprocessed PC. Stress at break for microcellular and nanocellular PC seems to follow a linear trend. No clear trend can be seen for strain at break, but it generally decreases with relative density.

Figure 10.5 (d) plots the toughness as a function of relative density. Toughness is defined as the area under stress-strain curve. Saturation annealed samples have a higher toughness than unprocessed PC. Toughness of microcellular and nanocellular PC decreases linearly with relative density. Also, from the figure, we can see that microcellular PC with RD=0.875 and nanocellular PC with RD=0.865 & 0.783, have higher toughness than unprocessed PC. This provides an exciting opportunity to reduce material weight without sacrificing its toughness.

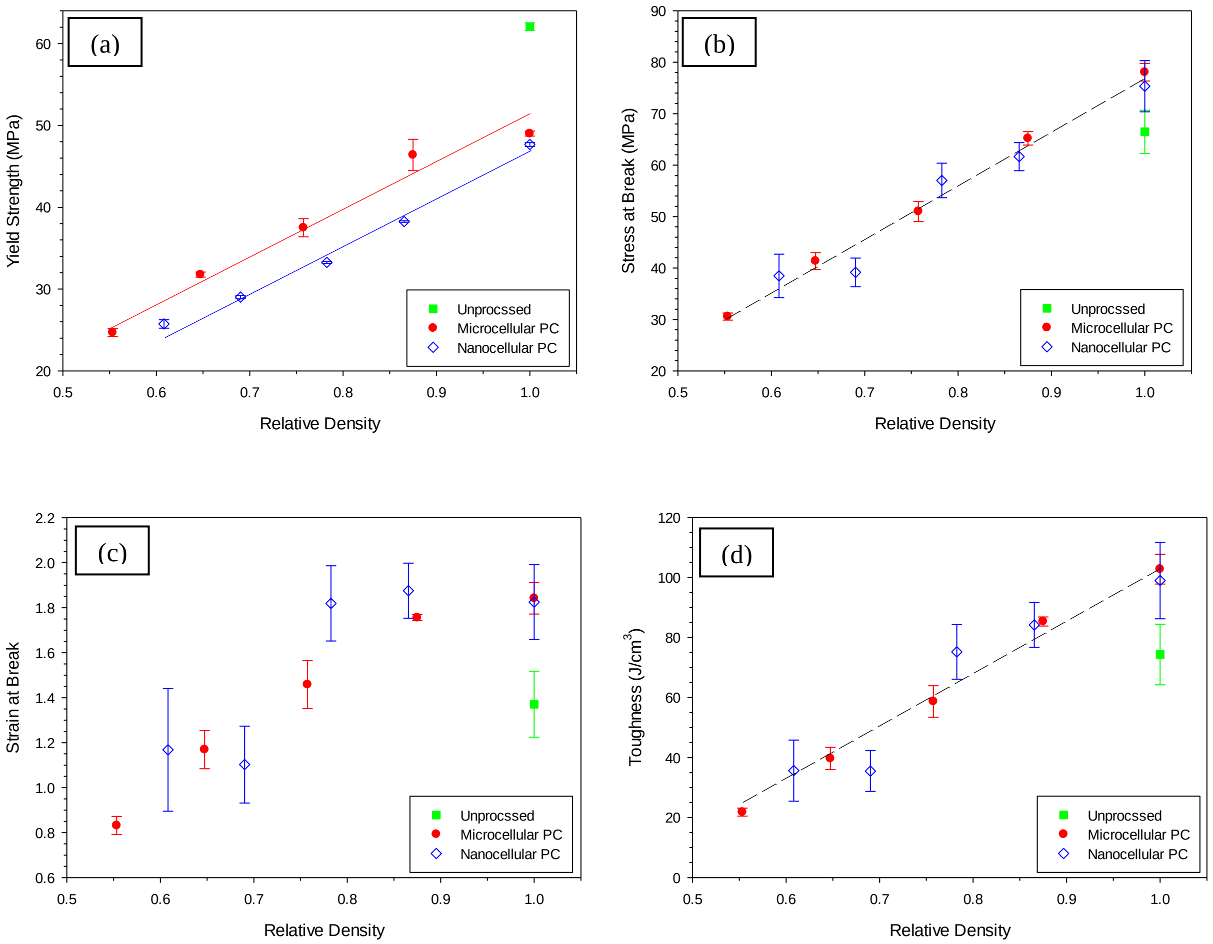

Figure 10.5 Plot of (a) yield strength, (b) stress at break, (c) strain at break, (d) toughness as a function of relative density, for unprocessed, microcellular, and nanocellular PC.

10.3.3 **Impact Property**

Impact test measures the material properties at a very high strain rate. Figure 10.6 shows the impact energy of unprocessed, microcellular, and nanocellular PC. Saturation annealed samples have a similar impact energy to unprocessed PC. Impact energy of microcellular and nanocellular PC seems to decrease linearly with relative density. On the other hand, the cell size doesn't seem to affect the impact energy.

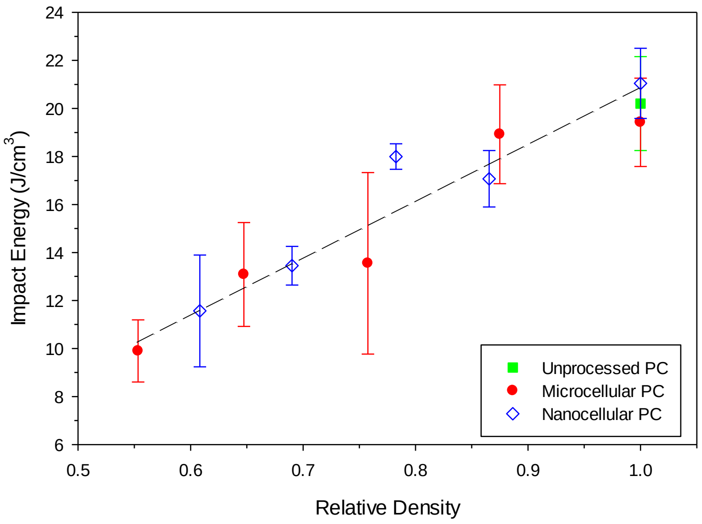

Figure 10.6 Impact energy as a function of relative density.

10.3.4 **Thermal Conductivity**

Figure 10.7 shows the thermal conductivity of unprocessed, microcellular, and nanocelluar PC. The thermal conductivity of both microcellular and nanocellular PC decreases with relative density. Two additional observations can be made. First, at similar densities, nanocellular PC seems to have a lower thermal conductivity than microcellular PC. This is believed to be due to a combination of Knudsen effect and tortuosity effect [3]. Knudsen effect represents the reduced heat conduction through gas phase due to the nanoscale confinement which prevents air molecule from collide with each other. Tortuosity effect represents the reduced heat conduction through matrix due to the much more tortuous nature of the matrix material in the nanocellular foams. Secondly, compared to microcellular PC, nanocellular PC decreases more rapidly with relative density. This is possibly due to the much higher tortuosity at a lower density in nanocellular PC. More experimental data need to be generated for foams with relative density below 0.5. If the rapid decreasing trend continues for nanocellular PC, nanocellular PC represents a new generation of cellular materials with a much lower thermal conductivity and may find many important applications in heat insulation.

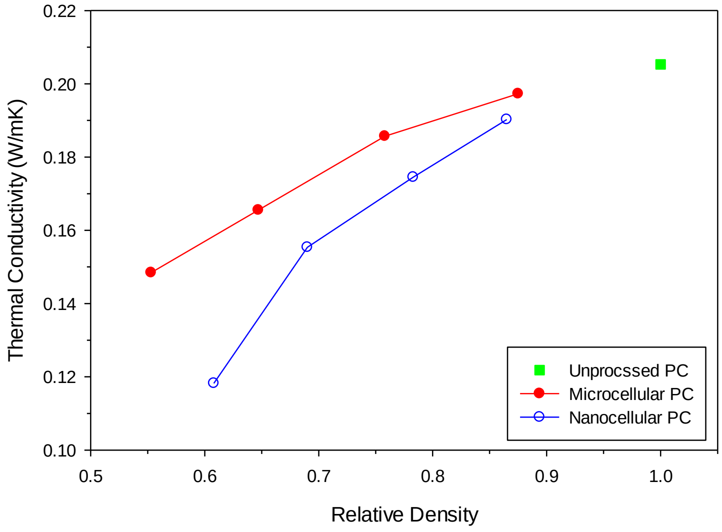

Figure 10.7 Thermal conductivity as a function of relative density for unprocessed, microcellular, and nanocellular PC.

10.3.5 **Glass Transition Temperature**

Interesting results were obtained when measuring the glass transition temperature of the foamed samples. Figure 10.8 shows the glass transition temperature of unprocessed, microcellular, and nanocellular PC.

Compared to unprocessed PC, microcellular PC seems to have a similar T_g.; however, the T_g for nanocellular PC seems to increase with decreasing relative density. A maximum of 4 ℃ occurs at the relative density of 0.6. Previous studies conducted by Miller and Kumar [1] also showed similar phenomenon. In their case, the maximum increase was around 4.5 ℃ in nanocellular PEI at the relative density of 0.55.

A study conducted by Sill et al. [6] showed that the T_g of polystyrene thin film started to increase when the film thickness was below 250 nm and reached a maximum at the thickness of 60 nm (see Figure 10.9). The increase in T_g was due to nanoscale confinement of the polymer chain, where nanoscale thickness dimension limited segmental mobility of the polymer chains.

To substantiate the existence of nanoscale confinement effect in this study, the cell wall structure of the microcellular and nanocellular PC with a similar density are compared in Figure 10.10. The average cell wall thickness for microcellular PC is around 700 nm, whereas it is about 100 nm for nanocellular PC. According to the study by Sills et al. [6], cell wall in microcellular PC will not show the nanoscale confinement effect. However, the cell wall in nanocellular PC will show roughly 3 ℃ increase in T_g, which is in very good agreement with this study and the study by Miller and Kumar. Therefore, the increase in the T_g of nanocellular foams is believed to be due to the nanoscale confinement effect of the cell walls.

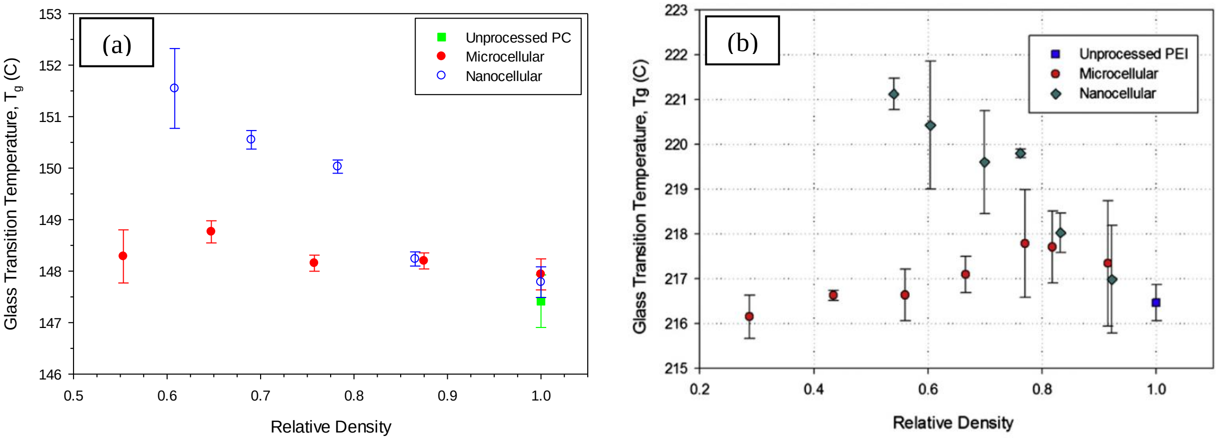

Figure 10.8 Glass transition temperature as a function of relative density for (a) unprocessed, microcellular, and nanocellular PC, and (b) unprocessed, microcellular, and nanocellular PEI as reported by Miller and Kumar [1]. Copyright 2011. Reproduced with permission from Elsevier.

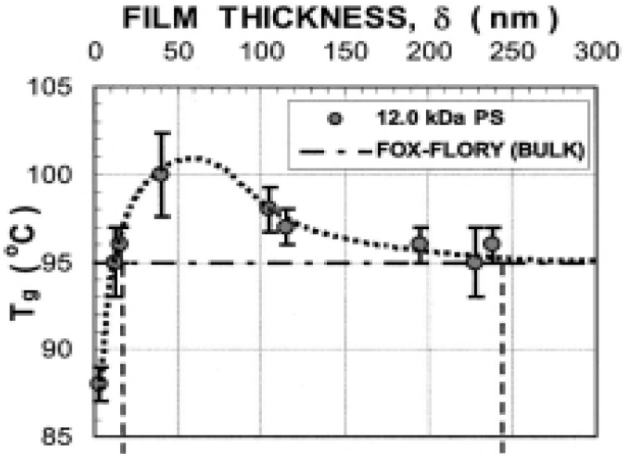

Figure 10.9 Film thickness dependence of the glass transition temperature on polystyrene films (M_w=12 kDa) reported by Sills et al. [6]. Copyright 2004. Reproduced with permission from AIP Publishing.

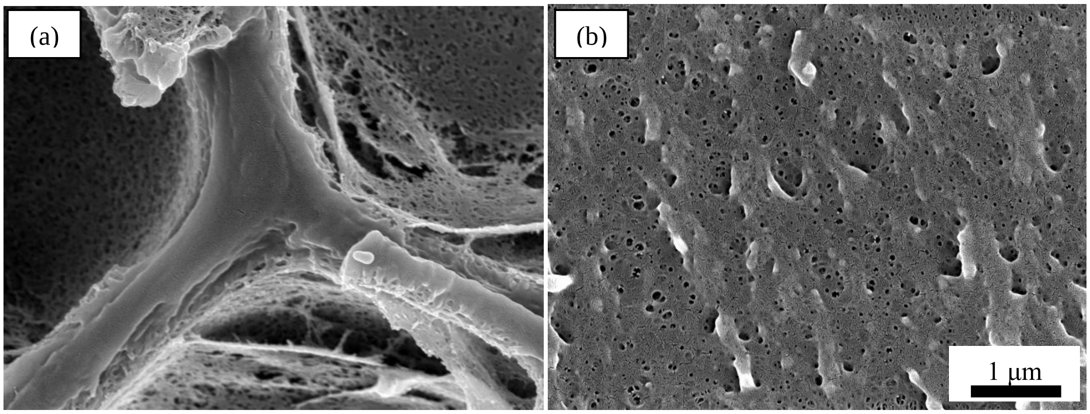

Figure 10.10 Cell wall structures of (a) microcellular PC with RD=0.553, and (b) nanocellular PC with RD=0.608. Both images have the same magnification and scale bar.

10.3.6 **Light Transmittance**

During sample preparation, nanocellular PC seemed to be somewhat translucent. More accurate light transmittance experiments were then conducted to confirm its translucent nature. Different from other property tests, thin film materials were used for the light transmittance experiments. Microcellular and nanocellular PC with 0.41 relative density were prepared. The cellular structures are shown in Figure 10.11. Microcellular PC film has an average cell size of 9 μm and nanocellular PC film average cell size of 28 nm. Figure 10.12 shows the light transmittance of unfoamed, microcellular, and nanocellular PC at difference wavelengths. A significant difference can observed between microcellular and nanocellular PC. Microcellular PC blocks the light in the whole wavelength range, whereas nanocellular PC transmits light for wavelength above 500 nm.

Light transmission in materials can be predicted by Rayleigh scattering theory, when the characteristic length of the material is much smaller than the wavelength. It is expressed as follows:

$$\frac{I}{I_0} = A * \exp(\frac{B}{\lambda^4}) \qquad (2)$$

where I is the intensity of light passing through, I_0 the intensity of the incident light, A the surface scattering coefficient, B the parameter related to sample thickness and microsturctures, and λ the wavelength.

Rayleigh scattering theory is applied to predict the light transmission in nanocellular PC. The model prediction with parameters $A = 1$, $B = 5 \times 10^{11}$ nm^4, match very well with the experimental data.

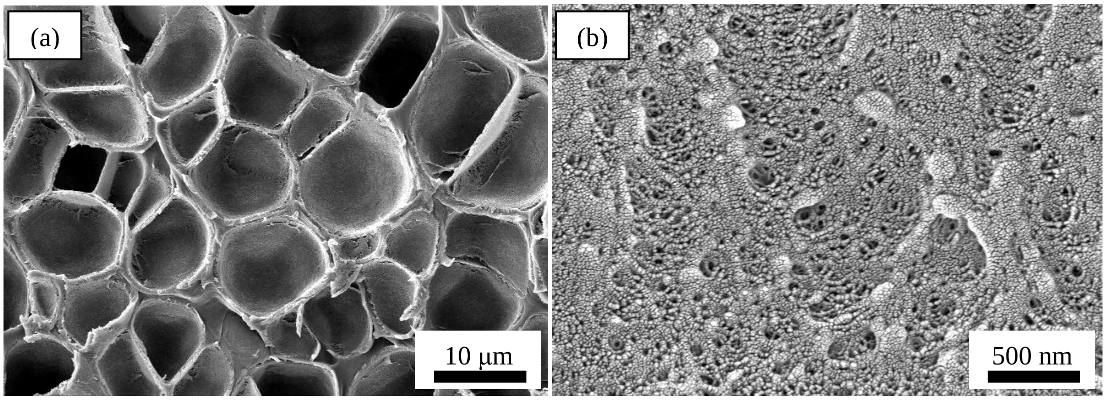

Figure 10.11 Cellular structure of (a) microcellular PC thin film with an average cell size of 9 μm, and (b) nanocellular PC thin film with an average cell size of 28 nm.

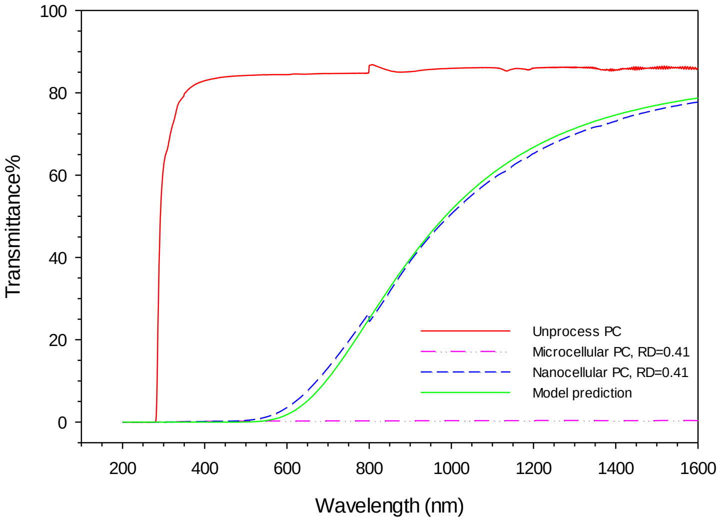

Figure 10.12 Light transmittance of unprocessed, microcellular, and nanocellular PC thin film. Both foamed samples have a relative density of 0.41. Model prediction using Rayleigh scattering theory is also shown.

10.4 **Conclusion**

Flat microcellular and nanocellular PC specimens were successfully fabricated using hot press technique. The established processing conditions enable us to make specimens with appropriate dimensions for property tests. Microcellular PC with cell size in the range of 5-8 μm and nanocellular PC with cell size between 17-25 nm were used for subsequent property tests.

Tensile properties, including Young’s modulus, yield strength, stress at break, strain at break and toughness, as well as impact energy, are a strong function of foam density. Cell size doesn't seem to affect these properties. The reduction in cell size doesn’t bring in an improvement in mechanical properties; on the other hand, there is no degradation in mechanical properties associated with cell size reduction.

Compared to microcellular PC, nanocellular PC has a much lower thermal conductivity, due to a combination of Knudsen effect and tortuosity effect. Also, nanocellular PC seems to decrease more rapidly with relative density. Nanocellular PC represents a new generation of cellular materials with a much lower thermal conductivity and may find many important applications in heat insulation.

Glass transition temperature of nanocellular foam increases with decreasing relative density. The increase in T_g is believed to be due to nanoscale confinement of the polymer chains in the cell walls, which limits the segmental mobility of the polymer chains.

Microcellular and nanocellular PC thin film were compared in the light transmittance measurement. Nanocellular PC thin film shows a significantly improved light transmission than microcellular PC. The light transmission in nanocellular PC can be well described by the Rayleigh scattering theory.

10.5 **References**

1. Miller D and Kumar V. Polymer 2011;52(13):2910-2919.
2. Zhou C, Vaccaro N, Sundarram SS, and Li W. Journal of Cellular Plastics 2012;48(3):239-255.
3. Notario B, Pinto J, Solorzano E, de Saja JA, Dumon M, and Rodríguez-Pérez MA. Polymer 2015;56:57-67.
4. Notario B, Pinto J, and Rodríguez-Pérez MA. Polymer 2015;63:116-126.
5. Gibson LJ and Ashby MF. Cellular Solids: Structure and Properties: Cambridge University Press, 1997.
6. Sills S, Overney RM, Chau W, Lee VY, Miller RD, and Frommer J. The Journal of Chemical Physics 2004;120(11):5334-5338.

Chapter 11

Conclusions and Recommendations

11.1 Conclusions

Several key findings regarding to the fabrication and properties of polymer nanofoams are summarized in this section.

Fabrication

A process using low-temperature saturation to create polymer nanofoams with cell size less than 100 nm has been discovered and studied. Four polymers – PC, PMMA, PSU, PPSU, are investigated using this novel process. Due to its similarity to the well-established solid-state microcellular foaming process, the novel process for making nanofoams can also be scaled up for large scale production.

Lowering the saturation temperature is found to significantly increase the solubility of CO_2 in polymer. The higher CO_2 solubility depresses the T_g of polymer to a lower temperature, even to below 0 °C. The higher solubility also enhances the cell nucleation, which is essential for creating nanofoams.

Nanofoams have been created in all of the four polymer systems investigated. Processing space has been established for each polymer system that relates process parameters to resulting cellular structures.

A critical CO_2 concentration is observed. As the CO_2 concentration increases, the cell nucleation density increases and cell size decreases. However, above a critical concentration, the cell nucleation density increases much more rapidly, and correspondingly, the cell size drops drastically. The critical CO_2 concentration seems to be polymer dependent, with a higer T_g polymer exhibiting a lower critical CO_2 concentration.

There exists a limit for both the cell nucleation density and cell size. It is observed that at a very high CO_2 concentration, nucleation density and cell size levels off when the CO_2 concentration continues to increase. It is found that the smallest cell size is around 20 nm and maximum cell nucleation densities on the order of 10^{15} cells/cm^3.

At higher foaming temperatures, the closed-cellular structure transitions to a porous, interconnected nanoporous structure. The nanoporous nature has been verified using the dye penetration test. The nanoporous structure may be used in many applications, such as filtration, battery separators, etc.

Properties

Flat microcellular and nanocellular PC specimens were successfully fabricated using hot press foaming technique. The established processing conditions enable us to make specimens with appropriate dimensions for property tests. Microcellular PC with cell size in the range of 5-8 μm and nanocellular PC with cell size between 17-25 nm were used for subsequent property tests.

Tensile properties, including Young’s modulus, yield strength, stress at break, strain at break and toughness, as well as impact energy, are a strong function of foam density. Cell size doesn't seem to affect these properties. The reduction in cell size doesn’t bring in an improvement in mechanical properties; on the other hand, there is no degradation in mechanical properties associated with cell size reduction.

Compared to microcellular PC, nanocellular PC has a much lower thermal conductivity, due to a combination of Knudsen effect and tortuosity effect. Also, nanocellular PC seems to decrease more rapidly with relative density. Nanocellular PC represents a new generation of cellular materials with a much lower thermal conductivity and may find many important applications in heat insulation.

Glass transition temperature of nanocellular foam increases with decreasing relative density. The increase in T_g is believed to be due to nanoscale confinement of the polymer chains in the cell walls, which limits the segmental mobility of the polymer chains.

Light transmittance properties of nanocellular and microcellular PC thin films (~127 μm thick) were compared. Nanocellular PC transmits significantly more light than microcellular PC. This result provides some insights to the question whether transparent foams can be created. The much improved light transmittance of nanofoams may render them to be useful for some exciting potential applications, such as packaging films and thermal insulative windows.

11.2 **Recommendations**

Although this study provides many results and insights regarding to the fabrication and properties of nanofoams, there are still many questions that need further investigations in the future.

(1) Investigate the application of the low-temperature saturation method to create nanofoams in other systems, such as other neat polymers, polymer blends, copolymers, and nanocomposites. It is expected that many of candidate polymers in these categories are likely to show nanocellular structures with the much higher CO_2 concentration at lower saturation temperatures. The lower-temperature saturation is more effective in increasing the CO_2 solubility than by increasing the saturation pressure. Therefore, a much mild saturation pressure can be used in order to create nanofoams.

(2) Explore the application of significantly lowering polymer T_g by low-temperature CO_2 saturation. In some cases, the T_g depression of polymers studied was over 100 ℃ and the T_g dropped to below 0 ℃. Potential applications might be developed to utilize this property.

(3) Investigate the mechanism for the critical concentration phenomenon. The solid-state nucleation in polymer is currently not well understood. Critical concentration phenomenon provides additional information regarding to solid-state nucleation and may shed some light on understanding and developing solid-state nucleation theories and models.

(4) Investigate the mechanism that is responsible for the limit of the cell nucleation density and cell size. From thermodynamic point of view, the surface tension might level off at high CO_2 concentration, resulting in the limit of cell nucleation density according to classical nucleation theory. From material point of view, the free volume or microvoids (typically a few nanometers)

intrinsic to the glassy polymers might serve as the limit for the size of any voids generated in the foaming process. Further investigations on these two possible mechanisms are needed.

(5) Study the creation of nanofoams using low-temperature saturation and ultrasound sonication. Some preliminary experiments conducted in the lab showed that when PLA was saturated under 5 MPa and -20 ℃ or -30 ℃, and subsequently treated with ultrasound in room temperature, nanoporous structures were created. More detailed investigations need to be conducted to establish the processing space. Nanoporous biodegradable PLA can potentially be used in scaffold applications. Also, other crystalline polymers, such as PET, LDPE, HDPE, might also show nanocellular or nanoporous structures using the low-temperature saturation and ultrasound sonication.

(6) Investigate other properties of nanofoams, such as fracture, fatigue, and acoustic properties. Microcellular foams were reported to have enhanced fatigue and fracture properties even than the unprocessed polymers. Nanofoams, as a relatively new material, may further enhance these properties, since cells are now much smaller than the crack size and the cells can possibly deter the crack propagation.

(7) Explore the application of nanoporous structures. All the polymers studied – PC, PMMA, PSU, PPSU, showed nanoporous structures under certain conditions. The potential applications of the nanoporous materials are largely unexplored. They may be used as filtration membranes or as templates for creating other nanostructures. The huge amount of internal surface area of nanofoams enables them to be used as a cheap alternative for catalysis support application.

(8) Study phase separation of polymer-CO_2 at very high CO_2 concentration. Solid-state foaming is essentially a type of phase separation. According to typical phase separation theory, at very high CO_2 concentration, polymer phase may nucleate and become the dispersed phase. In fact, in a few preliminary experiments, nanoballs structures were created under certain conditions. For example, when PC was saturated under 5 MPa and -30 ℃, and subsequently foamed at 120 ℃ and 130 ℃, nanoball structures were observed. Similarly, when PPSU was saturated under 5 MPa and 10 ℃,

and then subsequently foamed at 210 ℃, nanostructures were also observed. The nanoball structures are very interesting and potentially very useful for drug delivery application.